

**POLITECNICO DI MILANO**

Facoltà di Ingegneria dei Materiali e delle Nanotecnologie

Laurea Magistrale

Dipartimento di Chimica, Materiali e Ingegneria Chimica

“G. Natta”

**Characterization of Interlaminar Damage  
in Self-Healing Epoxy Smart Structures**



**POLITECNICO  
MILANO 1863**

Relatore: Dott. Ing. Antonio Mattia Grande

Correlatore: Dott. Ing. Paolo Bettini

Elaborato di laurea di:

Nicola Casarini

Matr. n. 905255

Anno accademico 2019/2020



# ABSTRACT

The aim of this thesis work is to introduce a mechanochromic self-healing epoxy resin, fully characterized in previous studies, as a matrix in multi-functional composite materials with glass reinforcing fibres, for future developments and applications in aerospace and biomedical fields. The examined resin embeds dynamic covalent disulphide bridges which provide intrinsic self-healing behaviour, whereas colour variation is directly attributed to mechanical stress. These properties allow for the combination of superior characteristics typical of thermosetting polymers and the possibility to perform re-processing, which is only suitable for thermoplastics. For this reason, the main part of the work is focused on the study of compatibility of resin with fibres and more in general on the entire laminate manufacturing process. Great emphasis is given to curing and post-curing cycles, as cross-linking has a major role on resin final properties, so on the whole composite.

From the mechanical point of view, the study is focused on the material behaviour in response to delamination and on repairing efficiency. This will necessarily impact critical parameters found by mechanical tests. Future developments on the repair cycle and on composite integrity will allow the implementation of optical fibres with sensors as an internal system for direct monitoring of delamination crack growth and consequent dynamic repair.

This thesis work is part of a collaboration project between Politecnico di Milano and Agenzia Spaziale Italiana (ASI), which aspires to design multi-functional materials for aerospace applications.

**Key Words:** *aerospace field; composite materials; epoxy resin; self-healing; mechanochromism; manufacturing; interlaminar fracture toughness; SEM; porosity.*



# SOMMARIO

L'elaborato di tesi in esame mira a inserire una resina epossidica auto-riparante e meccanocromica, precedentemente caratterizzata, come matrice per la realizzazione di materiali compositi multifunzionali con fibre di vetro, per futuri utilizzi in ambito aerospaziale. La resina sfrutta legami covalenti dinamici zolfo-zolfo che permettono la riparazione intrinseca del materiale, mentre l'effetto di variazione di colore è una diretta conseguenza delle sollecitazioni meccaniche. Queste proprietà permettono di combinare le superiori caratteristiche della resina, in qualità di polimero termoidurente, alla possibilità di riprocessare il materiale, tecnica solitamente esclusiva dei polimeri termoplastici. A fronte di ciò, il corpo dell'elaborato si fonda sullo studio delle caratteristiche di compatibilità della resina con le fibre di vetro e sull'intero processo di manufacturing del laminato. Particolare attenzione è stata posta sul ciclo di curing e post-curing, data l'enorme influenza della reticolazione sulle proprietà finali della resina, e di conseguenza del materiale composito nel complesso.

Dal punto di vista meccanico, lo studio si concentra sul comportamento del materiale in risposta alla delaminazione e sulla efficienza della riparazione, che inevitabilmente impatterà sui parametri critici trovati. Studi successivi sulla riparazione e sulla integrità dei compositi porteranno ad implementare fibre ottiche dotate di sensori all'interno del materiale composito al fine di monitorare il processo di delaminazione e la conseguente riparazione dinamica.

Questo elaborato di tesi rientra nel progetto di collaborazione tra Politecnico di Milano ed Agenzia Spaziale Italiana, che mira alla progettazione di materiali multifunzionali per applicazioni in ambito aerospaziale.

**Parole Chiave:** *settore aerospaziale; materiali compositi; resina epossidica; auto-riparazione; meccanocromismo; fabbricazione; tenacità alla frattura interlaminare; SEM; porosità.*



# ACKNOWLEDGEMENTS

*“Never looking back, or too far in front of me  
The present is a gift, and I just wanna be”  
Common*

First and foremost, I would like to express my deep gratitude to my supervisor Dr. Antonio Mattia Grande and co-supervisors Dr. Paolo Bettini and Drs. Daniela Rigamonti, as well as to the entire DAER Laboratory staff, for the whole-hearted guidance and valuable suggestions during the process of doing this research and more in general for giving me the opportunity to be part of this project. Thanks also to Martina Frigerio, who shared the thesis project and the Lab experience with undisputable professionalism and accuracy.

Secondly, I am also grateful towards all the professors from the Department of Chemistry, Materials and Chemical Engineering “Giulio Natta” who took a fundamental role during these five years in Politecnico di Milano. An immense thank goes to all my classmates of Nanotechnology and Materials Engineering and friends in Milan: without you, this satisfying journey would not have been the same. A special mention goes to Margherita, who supported me with unconditional love for almost my entire academic career, giving sincere advices and sharing precious and unique experiences.

Last but not least, I wish to take this opportunity to immensely thank my parents, relatives and friends from Bologna, for mentally and physically encouraging me in any choice I made during my life. Despite the distance during these last years, the sense of unity among us has always been strong, and I owe it to you all for being always present during the tough times.

Everyone played an irreplaceable role in shaping my attitude and creativity during the path of life. Great inspiration came also from basketball and music, a fantastic duo which tuned my emotions in everyday routine and deeply helped in my personal and social growth.

Once more, a heartfelt thanks to all.





# TABLE OF CONTENTS

<b>1</b>	<b>INTRODUCTION .....</b>	<b>13</b>
1.1	Aim of the thesis work.....	15
<b>2</b>	<b>STATE OF THE ART .....</b>	<b>16</b>
2.1	COMPOSITE MATERIALS .....	16
2.1.1	Basic principles.....	16
2.1.2	Main properties.....	17
2.1.3	Polymeric matrices.....	18
2.1.4	Glass fibres reinforcement.....	20
2.2	SMART MATERIALS: SELF-HEALING.....	23
2.2.1	Process and classification .....	24
2.2.2	Extrinsic healing .....	25
2.2.3	Intrinsic healing.....	27
2.2.4	Dynamic covalent chemistry and disulphide bonds.....	30
2.3	LAMINATED COMPOSITES MANUFACTURING: MOULDING.....	33
2.3.1	Introduction and classification of moulding technologies .....	33
2.3.2	Moulding phases .....	35
2.3.3	Polymerization in autoclave.....	38
2.3.4	Polymerization in hot press/oven.....	39
2.4	DAMAGE MODES AND FRACTURE MECHANICS IN COMPOSITE MATERIALS .....	40
2.4.1	Basic principles of Linear Elastic Fracture Mechanics (LEFM).....	42
2.4.2	Delamination .....	43
2.4.3	Damage management in FRPCs .....	44
2.5	STRUCTURAL HEALTH MONITORING FOR COMPOSITES INTEGRITY.....	45
2.5.1	Damage assessment and monitoring in FRPCs.....	47
2.6	OPTICAL FIBRE SENSORS FOR DAMAGE DETECTION AND MONITORING .....	49
2.6.1	Optical fibres.....	50
2.6.2	Fibre Bragg Grating (FBG) sensors .....	52

<b>3</b>	<b>MATERIALS AND EXPERIMENTAL TECHNIQUES .....</b>	<b>54</b>
3.1	DIFFERENTIAL SCANNING CALORIMETRY (DSC) .....	55
3.1.1	Theoretical background .....	55
3.1.2	Laboratory analyses .....	56
3.2	SCANNING ELECTRON MICROSCOPY (SEM) .....	58
3.2.1	Theoretical background .....	58
3.2.2	Laboratory analyses .....	59
3.3	DENSITY TEST .....	61
3.3.1	Theoretical background .....	61
3.3.2	Laboratory analyses .....	62
3.3.3	Equilibrium mathematical approach.....	63
3.4	DOUBLE CANTILEVER BEAM (DCB).....	65
3.4.1	Theoretical background .....	65
3.4.2	DCB Standard Test Method .....	66
3.4.3	DCB test apparatus and elements.....	69
3.4.4	Calculation of critical interlaminar fracture toughness ( <i>GIC</i> ).....	69
3.4.5	Laboratory analyses .....	72
3.5	MANUFACTURING PROCESS.....	74
3.5.1	Matrix phase realization .....	74
3.5.2	Reinforcement phase realization .....	76
3.5.3	Stoichiometric calculations.....	76
3.5.4	Composite mass calculations .....	77
3.5.5	Laminate mould design requirements.....	79
3.5.6	Mould components .....	80
3.5.7	Mould treatment .....	82
3.6	REALIZATION OF THE FIRST COMPOSITE PANEL.....	83
3.6.1	Samples preparation for SEM analysis.....	84
3.6.2	Samples preparation for density test.....	87
3.6.3	Samples preparation for DCB tests.....	88

3.7	REALIZATION OF THE SECOND COMPOSITE PANEL .....	91
3.7.1	Samples preparation for DCB tests.....	92
3.7.2	Autoclave thermal cycle .....	94
3.7.3	Specimens treatment and hinges adhesion .....	95
3.7.4	Resolution of technological issues: DCB hinges endurance .....	96
3.8	HEALING CYCLE ON DCB SPECIMEN.....	99
<b>4</b>	<b>EXPERIMENTAL RESULTS .....</b>	<b>100</b>
4.1	FIRST COMPOSITE PANEL.....	100
4.1.1	Masses calculation.....	100
4.1.2	DSC analysis.....	101
4.1.3	SEM analysis.....	104
4.1.4	Density test analysis.....	109
4.1.5	DCB test analysis.....	112
4.2	SECOND COMPOSITE PANEL .....	114
4.2.1	Masses calculation .....	114
4.2.2	DCB test analysis.....	115
4.3	REPAIR CYCLE: EPOXY RESIN SELF-HEALING .....	141
4.3.1	DCB test analysis.....	142
<b>5</b>	<b>CONCLUSIONS .....</b>	<b>151</b>
5.1	MANUFACTURING PROCESS.....	151
5.2	SEM AND DENSITY TESTS: VOIDS AND DEFECTS ASSESSMENT .....	152
5.3	DOUBLE CANTILEVER BEAM (DCB) MECHANICAL ANALYSIS .....	153
5.4	SELF-HEALING ABILITY OF THE DYNAMIC EPOXY SYSTEM .....	154
5.5	MECHANOCROMISM.....	155
5.6	FBG SENSORS INCORPORATION FOR DAMAGE MONITORING .....	155
<b>6</b>	<b>APPENDIX .....</b>	<b>156</b>
6.1	E-glass fabric data sheet.....	156
6.2	CLT analysis for composite stiffness.....	157
6.3	Aluminium mould CAD representation .....	158



## LIST OF FIGURES

Figure 1: Toughness of some materials used as matrices in advanced fibre composites. [9] .....	17
Figure 2: Summary of the approach for development of a high-performance fibre composite. [9] .	18
Figure 3: Peculiar epoxy group of epoxy resins [11] .....	19
Figure 4: Chemical structure of DGEBA [11] .....	19
Figure 5: Typical mechanical properties of reinforcing fibres. [8].....	21
Figure 6: Chemical composition of the two main glass fibre types. [9].....	22
Figure 7: General mechanism of Diels Alder cycloaddition reaction. [34].....	29
Figure 8: General self-healing systems. [35] .....	30
Figure 9: Synthetic procedure and chemical structure of dynamic epoxy networks and related mechanochromic behaviour. [36].....	32
Figure 10: Basic processes of a laminated composite. [39] .....	33
Figure 11: General comparison of thermoplastic and thermoset composite processing. [39] .....	34
Figure 12: Schematic of a typical vacuum bag form laminate composites. [38] .....	38
Figure 13: Ply-level fracture mechanisms exhibited by continuous fibre-reinforced composites. [40] .....	41
Figure 14: Fracture modes for LEFM. [44].....	42
Figure 15: Sources of delamination at geometric and material discontinuities. [44] .....	44
Figure 16: Schematic of optical fibres. [47] .....	50
Figure 17: Schematic of Bragg grating sensor. [47] .....	52
Figure 18: Distortion of the peak due to applied torsion and tension combined loading. [46] .....	53
Figure 19: Schematic, two-dimensional representation of thermoset cure with four main stages: (a) monomers, (b) branching, (c) gelled incomplete crosslinked network, (d) fully cured thermoset polymer. [48] .....	55
Figure 20: Sample encapsulating press (on the left) and the encapsulated sample (on the right) for DSC analysis.....	56
Figure 21: TA Instruments DSC 2010 CE in DAER laboratory. ....	56
Figure 22: Schematic diagram of a SEM. Two pairs of scan coils are shown, and this double deflection allows the scanning beam to pass through the final aperture. [49] .....	58
Figure 23: Hitachi TableTop SEM (on the left) and a top view of the SEM holder blocking the composite specimen covered with conductive tape.....	60
Figure 24: Westphal-Mohr's balance scheme. [51].....	61
Figure 25: Double Cantilever Beam Specimen (a) with piano hinges, (b) with loading blocks. [52]	66
Figure 26: Delamination Resistance Curve (R curve) from DCB test. [52].....	67
Figure 27: DCB specimen. [40].....	67
Figure 28: Load Displacement Trace from DCB Test. [52] .....	68
Figure 29: Modified Beam theory. [52] .....	70

Figure 30: Compliance Calibration theory. [52].....	71
Figure 31: Modified Compliance Calibration theory. [52].....	71
Figure 32: MTS 858 Mini Bionix II machine supplied by DAER laboratory. ....	72
Figure 33: Proof of the mechanocromic effect (green spots) caused by accidental scratches during manufacturing.....	73
Figure 34: VELP Scientifica ARE magnetic stirrer supplied by DAER laboratory for resin preparation.....	75
Figure 35: Zoomed photo of the E-glass woven fabric used to design the composite panel.....	76
Figure 36: Technical sketch (top view) of the panel and the resulting DCB specimens. ....	80
Figure 37: Overview of the components of the aluminium mould.....	82
Figure 38: Sketch (lateral view) of the panel, stressing out the position of fibres and Teflon.....	83
Figure 39: Hot Press used for curing and post-curing cycles (on the left) and the first produced composite panel with incorporated optical fibres. ....	84
Figure 40: Darker spot detected on the first panel.....	85
Figure 41: Overview of the SEM specimens choice with respect to the position inside the panel. ...	86
Figure 42: Lapping of SEM specimens. ....	86
Figure 43: Comparison between a non-lapped specimen (left) with a lapped one (right).....	86
Figure 44: SEM specimens (P1, P2, P3) plunged in ultrasonic bath. ....	87
Figure 45: DCB specimens preparation: a) sandblasting and cleaning, b) structural adhesive application, c) assembled tapered specimens.....	90
Figure 46: DCB specimens ready for mechanical testing. ....	90
Figure 47: Sketch (lateral view) of the panel, stressing out the position of peel-ply and Teflon. ....	91
Figure 48: From left to right, steel spacers, Ergal plates and composite specimens. ....	92
Figure 49: DCB specimens' preparation: a) assembled tapered specimens, b) pack creation for vacuum bag, c) closed vacuum bag and air sucking. ....	93
Figure 50: Autoclave supplied by DAER laboratory.....	94
Figure 51: AF163 adhesive leakage from DCB specimen.....	95
Figure 52: Assembled DCB specimen secured in the vice. ....	97
Figure 53: Preliminary DCB test to verify the surface treatments adopted for the second panel.....	97
Figure 54: DSC analysis on preliminary dynamic resin, before the realization of the composite panel. ....	102
Figure 55: DSC analysis on dynamic resin from first composite panel.....	102
Figure 56: SEM micrographs of P1 specimen. ....	104
Figure 57: SEM micrographs of P2 specimen.....	104
Figure 58: SEM micrographs of P3 specimen showing a crack tip. ....	105
Figure 59: SEM micrographs of P3 specimen showing the crack growth. ....	105
Figure 60: SEM micrographs of P3 specimen showing the crack initiation. ....	105
Figure 61: SEM micrographs of P4 specimen.....	106

Figure 62: SEM micrographs of P5 specimen (Side 1). .....	107
Figure 63: SEM micrographs of P5 specimen (Side 2). .....	107
Figure 64: SEM micrographs of P6 specimen (Side 1). .....	107
Figure 65: SEM micrographs of P6 specimen (Side 2). .....	108
Figure 66: Evidence of the interface collapse during (on the left) and after (on the right) the DCB test.....	112
Figure 67: Schematization of a DCB specimen setup. ....	115
Figure 68: Frame sequence of P1 specimen under loading. ....	118
Figure 69: Repaired P1 specimen. ....	141
Figure 70: Mid-plane zoomed image of the repairing effect. ....	141
Figure 71: Proof of the abrupt and rapid crack growth during the test. ....	142
Figure 72: First panel (on the left) and second panel (on the right) inside the aluminium mould. ....	151





## LIST OF TABLES

Table 1: Thermal cycle of the DSC analysis.....	57
Table 2: Characteristics of the ingredient of the dynamic epoxy resin. ....	74
Table 3: Aluminium mould components for composite panel realization. ....	80
Table 4: SEM specimens dimensions (P1, P2, P3).....	85
Table 5: SEM specimens dimensions (P4, P5, P6). ....	85
Table 6: Data considered for the realization of the Ergal stiffening plates. ....	89
Table 7: Results obtained according to ASTM D 5528-01. ....	89
Table 8: 121°C-cycle used for the adhesion of Ergal stiffening plates. ....	94
Table 9: First adopted preparation method for the second panel. ....	96
Table 10: Second adopted preparation method for the second panel. ....	96
Table 11: Healing cycle performed on P1 DCB specimen.....	99
Table 12: Results from composite mass calculations.....	100
Table 13: Comparison between theoretical and experimental results.....	100
Table 14: Glass transition temperature comparison with previous results. ....	103
Table 15: biggest defect found in every specimen.....	106
Table 16: Optical fibres measurements on P4, P5 and P6 specimens. ....	108
Table 17: Data employed for density test analysis. ....	109
Table 18: Results obtained with Mohr-Westphal scale. ....	109
Table 19: Voids volume fraction and Young's modulus of the three specimens.....	109
Table 20: Mean value and standard deviation for density test results.....	110
Table 21: Results from composite mass calculations.....	114
Table 22: Comparison between theoretical and experimental results. ....	114
Table 23: DCB specimens measured geometry. ....	116
Table 24: Initial delamination lengths measured before pre-opening and before opening.....	116
Table 25: Main data from opening phase of DCB test. ....	118
Table 26: Parameters related to the methods for data reduction.....	126
Table 27: Interlaminar fracture toughness mean values for every specimen.....	129
Table 28: $G_I$ mean values and standard deviations. ....	129
Table 29: DCB critical points for critical interlaminar fracture toughness.....	131
Table 30: Statistical analysis on the critical fracture toughness values with respect to each method applied.....	136
Table 31: $G_{IC}$ mean values and standard deviations. ....	138
Table 32: Technical data needed for the repair cycle. ....	141
Table 33: Parameters related to the methods for data reduction.....	145
Table 34: Comparison of $G_I$ values found for pristine and repaired P1 specimen.....	146
Table 35: Critical points comparison between pristine and repaired specimen. ....	148

Table 36: Interlaminar fracture toughness decay after healing cycle..... 150

Table 37: Final G assessment for P1 specimen (MBT)..... 150

Table 38: Initial data needed for CLT.....157

Table 39: Fabric obtained with Autodesk Heliux Composite. ....157

Table 40: Stiffness results obtained with CLT analysis.....157

## LIST OF GRAPHS

Graph 1: Autoclave cycle with temperature and pressure variation in time. ....	95
Graph 2: DCB attempt test for surface treatment comparison. ....	98
Graph 3: Mean value and standard deviation for voids volume fraction. ....	110
Graph 4: Mean value and standard deviation for Young's modulus. ....	110
Graph 5: Pre-opening comparison between DCB specimens. ....	117
Graph 6: Crack opening comparison between DCB specimens. ....	119
Graph 7: P1 pre-opening and crack opening comparison. ....	120
Graph 8: P2 pre-openings and crack opening comparison. ....	121
Graph 9: P3 pre-opening and crack opening comparison. ....	121
Graph 10: Crack length behaviour as a function of transverse displacement. ....	122
Graph 11: P1 MBT method application. ....	123
Graph 12: P1 CC method application. ....	123
Graph 13: P1 MCC method application. ....	124
Graph 14: P2 MBT method application. ....	124
Graph 15: P2 CC method application. ....	124
Graph 16: P2 MCC method application. ....	125
Graph 17: P3 MBT method application. ....	125
Graph 18: P3 CC method application. ....	125
Graph 19: P3 MCC method application. ....	126
Graph 20: P1 specimen fracture toughness comparison. ....	127
Graph 21: P2 specimen fracture toughness comparison. ....	127
Graph 22: P3 specimen fracture toughness comparison. ....	128
Graph 23: G <sub>1</sub> statistical analysis conducted on every applied method. ....	130
Graph 24: P1 specimen NL point detection. ....	131
Graph 25: P2 specimen NL point detection. ....	132
Graph 26: P3 specimen NL point detection. ....	132
Graph 27: P1 specimen +5%C <sub>o</sub> point detection. ....	133
Graph 28: P2 specimen +5%C <sub>o</sub> point detection. ....	133
Graph 29: P3 specimen +5%C <sub>o</sub> point detection. ....	134
Graph 30: P1 specimen P <sub>MAX</sub> point detection. ....	134
Graph 31: P2 specimen P <sub>MAX</sub> point detection. ....	135
Graph 32: P3 specimen P <sub>MAX</sub> point detection. ....	135
Graph 33: G <sub>IC</sub> <sup>NL</sup> comparison. ....	137
Graph 34: G <sub>IC</sub> <sup>+5%Co</sup> comparison. ....	137
Graph 35: G <sub>IC</sub> <sup>PMAX</sup> comparison. ....	138
Graph 36: G <sub>IC</sub> <sup>NL</sup> statistical analysis applied on every adopted method. ....	139

Graph 37: $G_{IC}^{+5\%C_0}$ statistical analysis applied on every adopted method.....	139
Graph 38: $G_{IC}^{PMAX}$ statistical analysis applied on every adopted method. ....	140
Graph 39: A comparison between the DCB tests of pristine and repaired P1 specimen.....	143
Graph 40: Repaired P1 MBT method application. ....	144
Graph 41: Repaired P1 CC method application. ....	144
Graph 42: Repaired P1 MCC method application.....	145
Graph 43: Interlaminar fracture toughness trend of repaired P1 specimen. ....	146
Graph 44: Graphical comparison of interlaminar fracture toughness trend for pristine and repaired specimen. ....	147
Graph 45: NL point for repaired P1 specimen. ....	148
Graph 46: $+5\%C_0$ point for repaired P1 specimen.....	149
Graph 47: $P_{MAX}$ point for repaired P1 specimen. ....	149

# 1 INTRODUCTION

In the last 10 years, polymers and polymeric matrix composites (PMCs) have become increasingly widespread in materials R&D of technological-industrial fields such as Aerospace, Aeronautics, Biomedicine and Automotive. As a matter of fact, the combination of the reinforcing phase's load-bearing ability and the tough and ductile protectiveness of the polymeric matrix enhances the possibility to obtain strong, stiff and lightweight materials which are able to transmit the load to and from the reinforcement, showing also higher fatigue and corrosion resistance performances with respect to metallic alloys. For what concerns the Aerospace industry, even if composites manufacturing winds up being problematic, their advantages carry on the possibility to obtain a new generation of larger, but more efficient and sustainable aircrafts, such as Boeing 787 and Airbus models. [1]

However, the main drawbacks concerning PMCs are their weak performances towards impact loading; in addition, their peculiar failure mechanisms, as fibre-matrix debonding, delamination, fibre fracture and microcracking of the brittle (polymer) matrix critically compromise their use as replacement for tougher metal parts. As previously mentioned, composites manufacturing is very expensive and besides, the impossibility to be reshaped, due to their nature, makes repair and recycling be huge problems to deal with.

Beyond the conventional approaches for managing failures (prediction, detection, manual repair and replacement), which need enormous costs and time waste together with frequent inspections during service life, in the last decade material designers and researchers have concentrated their energies and studies towards a new type of "damage management" approach, which goal is to overcome the previously mentioned critical aspects of damage and repair in composite/polymeric materials. [2] [3] By adopting a philosophy which tolerates some damage growth, considerable weight, cost savings and design freedom could be achieved. Furthermore, there are numerous applications in which a component is expected to tolerate significant damage growth yet still be fit for service, that is, to be "damage tolerant" or "fail-safe." If such an approach were coupled with an inherent repairability in composite materials, these materials would be more widely used. [1]

This advanced approach lies on the synergic combination of biomimetic and a new family of smart materials which are able to restore/recover their mechanical and structural integrity after damage: these are called self-healing materials. Their peculiar property enlarges their application field to those where long-term reliability in poorly accessible areas is needed or where the system is prone to damage. Thus, repairing is essential to enhance reliability and lifetime of materials. Though scientists are inspired by the natural process of blood clotting or repairing of fractured bones, trying to incorporate the same concept into engineering materials. [4]

In the aerospace industry, self-healing materials have the ability to repair damages that may have occurred during a flight and increase the lifetime of the components. One key advantage of self-healing composite materials is to repair dynamic damage and maintain impact resistance. Self-healing composites can be used in various capacities (e.g., in aerospace structural parts to prevent damage and increase lifetime, and also in anticorrosion and barrier coatings).

The introduction and diffusion of advanced composite materials in Aeronautics, thanks to their lightness and their peculiar mechanical properties, has opened new perspectives towards Structural Health Monitoring (SHM) techniques. With this term, we refer to the ability to continuously control the structure healthiness, pointing out the presence of cracks and their possible propagation by the insertion of sensors and actuators network. The rise of interest towards these kind of monitoring systems is strongly justified by the increasing development and use of optical fibre sensors, which have numerous advantages in composite materials. The reduced dimensions and weight allow their embedment inside laminates directly during the production phase. Moreover, the high-level sensibility to mechanical stresses makes optical fibre sensors recommended to control the component state of deformation. [5]

## **1.1 Aim of the thesis work**

As presented by *Paolillo S.* [6] in its Master Thesis experience at Aerospace Department of Politecnico di Milano (DAER), a complete characterization of the rheological and mechanical properties of an intrinsically self-healing epoxy polymer network has been done, showing the ability for this system to be reprocessed and consequently recycled despite its thermosetting nature. In the optic of the collaboration between Politecnico di Milano and ASI (Agenzia Aerospaziale Italiana), this Master Thesis work intends to employ the previously obtained results to design multifunctional epoxy based FRPCs for applications in aerospace field.

Few examples of studies regarding this particular epoxy based FRPC have been found. Thus, it is safe to say that this work constitutes a first attempt to design a proper self-healing FRPC and to characterize its functional properties as a function of repair cycles and efficiency.

In Chapter 2, an overview of the theoretical background concerning composite and smart materials is provided to fully understand their relationship with fracture mechanics, damage modes and composite moulding techniques. A brief paragraph is dedicated to optical fibres.

In Chapter 3, standard experimental techniques, namely Differential Scanning Calorimetry, Scanning Electron Microscopy, density and Double Cantilever Beam tests, are reported with mention to theoretical aspects and laboratory experimental activities; moreover, special mention is given to curing and post-curing cycles as a fundamental step of the whole composite design phase.

Chapter 4 includes the quantitative results obtained from the analysis and tests carried out in laboratory and a qualitative counterpart reflects the main technological aspects and evidences from the experimental experience.

Chapter 5 resumes the main aspects developed from this thesis work and, to conclude, it opens a forward-looking discussion on optical fibres implementation for system monitoring and more in general on future developments of multifunctional components in industrial/aerospace field.

## 2 STATE OF THE ART

### 2.1 COMPOSITE MATERIALS

#### 2.1.1 Basic principles

In materials science, a composite material is a heterogeneous body made of, at least, two phases and whose properties are enhanced with respect to those of the separated phases, namely the matrix and the reinforcement. The synergy between the constituents implies the formation of mechanically advanced lightweight materials that are inherently anisotropic, as the fibres are usually arranged at different predetermined angles within discrete two-dimensional stacked layers. The direction orthogonal to the two-dimensional layers is usually unreinforced to avoid compromising in-plane performance, which results in a vulnerability to damage caused by out-of-plane loading (i.e., impact). For this purpose, the load acting on the matrix must be correctly transferred to the reinforcement via the interface, which strength degree is fundamental. A weak interface results in low stiffness and strength, but high fracture resistance, while a too strong adhesion causes the opposite, i.e., brittle behaviour. Other important properties like creep and fatigue resistance, as well as environmental degradation, are affected by interface features, but their relationships are complex and must be supported by large experimental evidence. [1] [7]

Composite materials technology exploits the high specific moduli and strength of reinforcing phase (fibres) to produce low density, high performance structures. For what concerns engineering applications, the most important property of unidirectionally reinforced materials is the anisotropy, therefore it is absolutely relevant to obtain the fibres aligned in the direction of the principal stress. For many applications of epoxy resins, this can be done by stacking prepreg fibrous sheets (i.e. prepreg) to form laminates. Another way to provide quasi-isotropy is to use woven reinforcements or to combine differing fibre placement techniques. The most important fibres are those based on E-glass, carbon and aramid polymers, all available in a wide range of forms and properties. For epoxy resins, the most common fabrication processes incorporate continuous carbon, aramid or glass fibres, as lamination in autoclave or hot compression moulding.

In the case of high-performance carbon-fibre and glass-fibre laminates, they are fabricated by prepreg moulding using the above-mentioned techniques. A “prepreg” consists of collimated fibres or woven cloth prepreg with thermoset or high-performance thermoplastic, modified with a thermoplastic or an elastomeric toughening agent and containing a latent hardener. It is fundamental to emphasize that the complete reaction of the epoxy groups is generally achieved after long times at high temperatures, so that higher-heat-distortion temperatures and chemical resistance can only be reached after appropriate post-curing. The hardener, together with the curing system, is responsible for improving the mechanical properties of the epoxy resin. [8]



The 1<sup>st</sup> generation of composites introduced to aircraft construction in the 1960s and 1970s employed brittle epoxy resin systems, thus creating laminated structures with poor tolerance to low-energy impacts caused by runaway debris or those encountered during manufacture and subsequent servicing operation. Even though scientists are mindful of the lower damage-tolerance of thermosets with respect to thermoplastic materials, the focus seems now to be on affordability. In the effort to improve the through-the-thickness strength properties and impact resistance, composites industry has moved towards toughened epoxies, which have much higher failure strains, comparable to thermoplastic polymers as shown in Figure 1. [7]

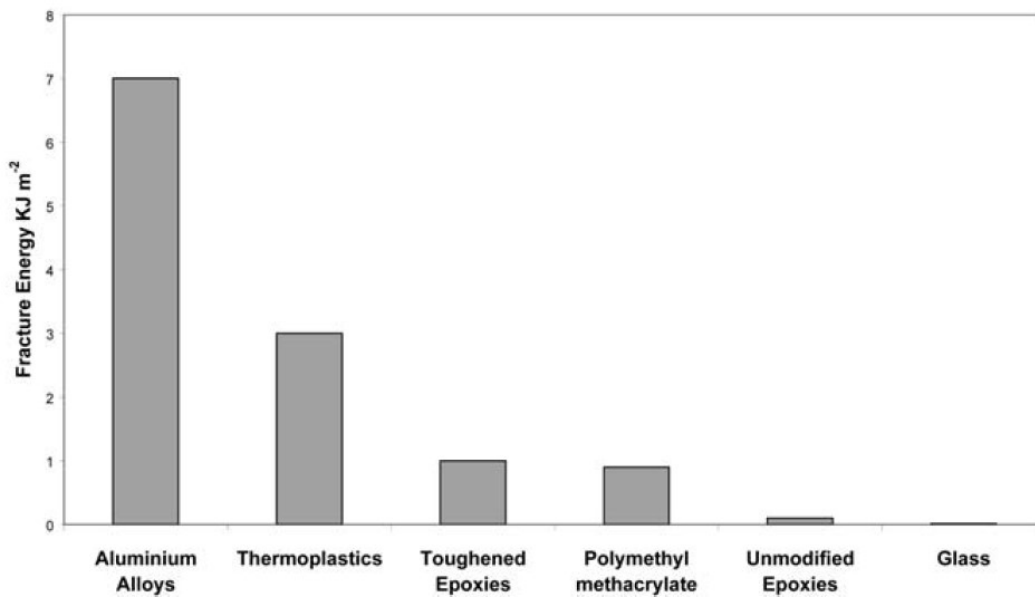


Figure 1: Toughness of some materials used as matrices in advanced fibre composites. [9]

### 2.1.2 Main properties

In composites technology, the matrix serves the following functions:

- 1) transfers load into and out from the fibres;
- 2) separates the fibres to prevent failure;
- 3) protects fibres from environmental damage;
- 4) supports the fibres in the shape of the component.

The mechanical properties which are significantly affected by the matrix characteristics include longitudinal compression strength, transverse tensile strength, and interlaminar shear strength. These are generally called matrix-dominated properties. To be matrices adaptable, polymers must also have resistance to aircraft solvents (i.e., fuel or hydraulic fluids) and to service temperatures typically ranging from 80°C to 150°C respectively for civil and military applications; however, a capability to over 200°C may be required in some cases. [9]

In the production of advanced composites suitable for aerospace applications, it is crucial that the matrix incorporation method does not damage the reinforcement fibres or inadvertently change their orientation. One suitable method is the infiltration of an aligned fibre bed with a low-viscosity liquid that is then converted, by chemical reaction or simply by cooling, to form a continuous solid matrix with the desired properties. The fibre composite approach can provide significant improvements in specific (property/density) strength and stiffness over conventional metal alloys. As summarized in the table of Figure 2, the aim is to use strong, stiff fibres to reinforce a relatively weaker, less stiff matrix.

<ul style="list-style-type: none"> <li>• Fibers</li> <li>– stiff/strong/brittle/low density</li> <li>– high temperature capability</li> <li>– able to carry major load as reinforcement</li> <li>– usually continuous</li> <li>– oriented for principal stresses</li> </ul>	<ul style="list-style-type: none"> <li>• Polymer Matrix</li> <li>– low stiffness and strength ductile or brittle</li> <li>– can be polymer, metal, or ceramic</li> <li>– transmits load to and from fiber</li> <li>– forms shape and protects fiber</li> </ul>	<ul style="list-style-type: none"> <li>• Composite</li> <li>– toughness through synergistic action (woodlike)</li> <li>– high strength and stiffness in fiber direction, weak at angles to fiber axis</li> <li>– tailor fiber directions to optimize properties</li> </ul>
---	--	--

Figure 2: Summary of the approach for development of a high-performance fibre composite. [9]

### 2.1.3 Polymeric matrices

Plastic matrices for fibre composites generally can be divided into thermoplastics and thermosetting polymers; for the latter, it could be useful to differentiate between those requiring additional hardeners, curing agents or catalysts and those that are quenched at a partially reacted state and continue to cure on heating. These two systems satisfy the requirements of an appropriate matrix, which are:

- Low viscosity for fibre impregnation
- High reactivity on curing
- Chemical control of cure without volatile formation
- Good mechanical properties of the cured resin

To sum it up, thermosetting materials are highly cross-linked polymers generated by an irreversible exothermic chemical reaction. In fact, the so-called curing phase involves the generation of a three-dimensional cross-linked molecular structure which is insoluble and inert. The impossibility to recycle or reprocess the material once it has been formed is a direct consequence of its properties. Although, the inadequateness of thermoplastics as possible substitutes has increased the need to investigate a method to efficiently recycle this kind of polymers. Focusing on the aerospace field, it is crucial to obtain reprocessable, recyclable and repairable fibre-reinforced thermoset composites using epoxy resins as matrices. [8]

Epoxies are thermosetting low molecular weight pre-polymers containing more one or more epoxide (also called oxirane) groups, which are rings formed by an oxygen and two carbon atoms. Because of the different electronegativity between them, carbon atoms of the ring are electrophilic, and this arrangement turns to be highly reactive due to their high strain, compared with common ethers. [10] They generally satisfy the above criteria because the curing phase occurs without evolution of volatile organic compounds (VOCs), in a controllable manner and with low shrinkage. For these reasons, epoxy resin-based composite materials generally find application in high performance structures where high specific strength and stiffness dominate, together with perfect damage tolerances, corrosion resistance and long shelf life (aerospace structures or sports goods).

Nowadays, almost 90% of the world production of epoxy resins is based on the reaction between bisphenol-A (BPA) and epichlorohydrin in the presence of a basic catalyst, producing oligomers of di-glycidyl ether of bisphenol A, commonly known as DGEBA. Its properties depend on the number of repeating units, considering that low-molecular-weight molecules tend to be liquids and higher MW ones tend to be more viscous, even solid. When these oligomers react with the hardener, the epoxy resin is cured and becomes a thermosetting polymer. [10]

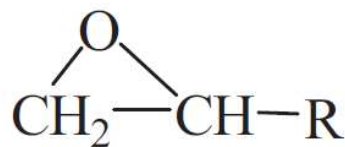


Figure 3: Peculiar epoxy group of epoxy resins [11]

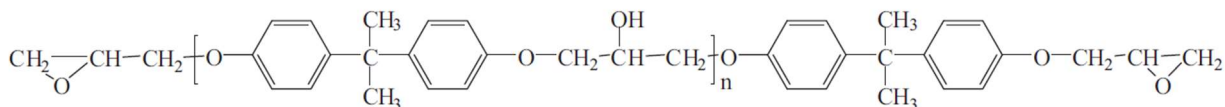


Figure 4: Chemical structure of DGEBA [11]

For what concern hardeners, they are molecules with active hydrogen atoms which can be added to the epoxy group. A focused and careful choice of both the resin blend and the hardener is required to provide a controlled curing phase, because the latter has a great influence on the cured resin properties as a result of the network chains molecular structure. [8] The cure kinetics and glass transition temperature ( $T_g$ ) of epoxy resins are strictly dependent on the molecular structure of the curing agents. Generally, epoxy resins are cured at elevated temperatures with a 2-steps process, thus they obtain higher glass transition points, as well as greater tensile strength, heat and chemical resistance. In detail, glycidyl amides have a higher functionality and higher cross-link densities and  $T_g$ , so they are particularly suitable for aerospace composites. [10] [11]

Apart from the enhanced chemical and mechanical properties, the interest towards epoxies for FRPCs is also accounted for the heat, electrical and water resistance, adhesion strength, availability and the relatively cheap price. Nevertheless, the potential use of epoxy thermosets in many high-performance applications still presents major structural limits as inherent brittleness and rigidity, which are inevitably the primary causes for delamination (ply separation) and a poorly impact resistance behaviour. This is the main reason why, from a generic perspective, epoxies are modified with various additives and fillers, such as oligomeric compounds, plasticizers or nano-fillers, and toughened with thermoplastic polymers, inorganic particles or fibres. Within the aerospace industry, fibres are the first candidates as a toughening method to improve epoxies physical properties, thus overcoming their weak points. [9] [11]

Before proceeding with a reinforcement discussion, it is worth mentioning that recent researches are taking the first steps towards the design of novel bio-based epoxy materials, as in the case of *Liu et al.* [12] As previously stated, the glass transition temperature of a cured epoxy resin is dependent on molecular stiffness and average functionality of the reactants. The epoxy system provided in this study is a biobased tri-epoxy (TEP) synthesized and cured with an anhydride monomer in presence of a zinc catalyst. As the TEP molecule has more epoxy groups than common bisphenol A epoxies molecule on average, the former would favour the formation of a denser cross-linked network, thus showing higher  $T_g$  value ( $> 180^\circ\text{C}$ ). More importantly, the cured epoxy showed mechanical properties comparable to that of bisphenol-A epoxy materials, as well as efficiently heat-activated stress relaxation and self-healing properties. Although these results make TEP a promising alternative to basic BPA epoxies, this work only represents the first attempt to combine renewable feedstocks-derived systems and dynamic chemistry for the design of high service temperature multifunctional materials.

#### **2.1.4 Glass fibres reinforcement**

Reinforcement fibres act as a dispersed phase to assure suitable mechanical resistance and stiffness and they are generally circular cross-section tubes made of elements with low atomic number, like carbon, aluminium and silicon. The peculiar fibrous shape gives highlighted anisotropy due to the strong directionality of interatomic bonds, but the possibility to control it allows to reinforce the materials in the same direction of loading application. The use glass and carbon fibres is widespread in the aerospace industry, due to their enhanced mechanical properties with respect to weight. In most of these cases, therefore, carbon fibre reinforcements are preferred with respect to others. As a matter of fact, by comparing the mechanical behaviour of the previously mentioned potential reinforcing fibres with matrix and bulk materials, the benefits of the former are deeply reflected in their enhanced strength and stiffness, apart from steel.

Even tough efficient structures can be realized with the highest values' fibres, i.e. carbon and high-performance polymeric ones, whenever economic considerations become more important in industrial application, glass fibre-reinforced composites are highly competitive and economic at  $\approx 1/3$  the material cost, thus they are employed for secondary aircraft structure within the aerospace industry, where no heavy loads are applied.

Glass fibres are based on silica ( $\text{SiO}_2$ ) melted with oxides and they are common as PMCs reinforcement thanks to their high strength and low cost. Despite being employed in demanding structural applications such as pressure vessels and rocket casings since the early 1960s, their support in airframes has been limited due to the relatively low specific stiffness. Nevertheless, they are widely diffused in secondary structures and in all those aircraft components where low stiffness is not a design limitation. In Figure 5 the main compositions of glass made into fibres for PMCs are listed. E-glass (calcium alumino-borosilicate) type has enhanced electrical resistivity and lower dielectric constant, thus is the most widely exploited in structural applications because of its relatively low cost and high strength. S-glass (magnesium alumino-silicate) type, where S stands for high-strength grade, has increased stiffness and can withstand higher temperatures, to the detriment of higher costs. [8] [9]

	Relative density	Young's modulus (GPa)	Tensile strength (GPa)	Failure strain (%)	Fibre diameter ( $\mu\text{m}$ )
E glass	2.55	72	1.5–3.0	1.8–3.2	10–16
S glass	2.5	87	3.5	4.0	12
S-2 glass	2.49	86	4.0	5.4	10
Carbon-mesophase pitch	2.02	380	2.0–2.4	0.5	10
Carbon-PAN					
Type A high strength	1.8	220–240	3.0–3.3	1.3–1.4	7
Type A high performance	1.8	220–240	3.3–3.6	1.4–1.5	7
Type A high strain	1.8	220–240	3.7	1.5–1.7	7
Type II high strength	1.8	250	2.7	1.0	7
Type I high modulus	2.0	330–350	2.3–2.6	0.7	7
Intermediate modulus	1.9	280–300	2.9–3.2	1.0	7
SiCO-continuous	2.5	200	3.0	1.5	10–15
SiC-whisker	3.2	480	7.0	–	1–50
SiC Ti C O continuous	2.35	200	2.8	1.4	8–10
Boron	2.6	410	3.4	0.8	100
$\alpha$ -alumina (FP)	3.9	380	1.7	0.4	20
$\beta$ -alumina (Saffil)	3.3	300	2.0	0.5	3
$\delta/\theta$ -alumina (Safimax)	3.3	250	2.0	–	3.1
$\eta$ alumina (Safimax LD)	2.0	200	2.0	–	3.2
$\text{Fe}_{40}\text{B}_{20}$ metallic glass	–	100	3.6	–	–
H.C. steel	7.8	210	2.8	–	250
Polyphenylene terephthalamide					
Aramid – high modulus	1.47	180	3.45	1.9	12
Aramid – intermediate modulus	1.46	128	2.65	2.4	12
Aramid – low modulus	1.44	60	2.65	4.0	12
Aramid – staple fibre (polymetaphenylene-isophthalamide)	1.4	17.3	0.7	22.0	12
Polybenzothiazole (PBT)	1.5	250	2.4	1.5	20
Polyamide 66	1.44	5.0	0.9	13.5	$\approx 10$
Polyethene (theory)	–	200	–	–	–
Solution spun	1.0	100–150	–	–	–
Drawn	$\approx 1$	6–80	–	–	–

Figure 5: Typical mechanical properties of reinforcing fibres. [8]

In comparison to other plastics, the cost of epoxy glass composites is low (except for polyester-based laminates) but where the fabrication rate and the complexity of the moulding dominate, other plastics solutions win out. On a cost for similar stiffness basis, glass fibre laminates still compete effectively with high performance metals such as titanium, but the carbon fibre solution is expensive and fabrication economies or lower running costs (in the case of airlines) need to be considered in the design.

Glass type	Si	Al <sub>2</sub> O <sub>3</sub>	CaO	B <sub>2</sub> O <sub>3</sub>	MgO	Na <sub>2</sub> O K <sub>2</sub> O
E-Electrical	53	14	18	10	5	< 1
S-High strength	65	25	—	—	10	—

Figure 6: Chemical composition of the two main glass fibre types. [9]

Undoubtedly, it is worth mentioning that current manufacturing industries are promoting natural fibre-based bio-composites and hybrid composites as promising materials for automotive, building construction, packaging and aerospace applications. As depicted by *Saba et al.* [10], the introduction of natural fibres reinforcements as an alternative to synthetic ones in epoxy matrices results in even lower density, weight and costs, together with better renewability and biodegradability. These studies have concluded that physical, thermal and mechanical properties of natural fibres-based composites display improved performances for manufacturing of both automotive and aerospace high-performance products and components.

## **2.2 SMART MATERIALS: SELF-HEALING**

Smart materials are generally materials which mechanical, thermal, optical or electromagnetic properties can be tuned and modified in a controlled way whenever an external stimulus is applied. Inspired by living organisms, these materials tend to mirror nature-like functionalities: if compared with human body, the host material seems to possess sensors aimed at processing the received stimuli, thus mimicking nerves and actuators which then responds to the upcoming signals like muscles. To complete the comparison, a sort of data-analysis system has to collect and monitor the received signals, elaborates the acquired information and subsequently generate a suitable reaction, thus behaving as the brain. In brief, smartness embodies the fundamental concepts of “self-sensing” and “self-adaptability”, and the overall versatility of these special materials makes them suitable to face and solve actual engineering problems, thus giving the opportunity to design a new generation of products. A first classification of smart materials can be done on the basis of their working principle as active or passive materials.

- Active materials are able to modify their properties under the application of an electric, magnetic or thermal field by converting energy, in accordance to the First Law of Thermodynamics. The main examples include piezoelectric and magneto-strictive materials, as well as shape memory alloys, polymers and photovoltaics;
- Passive materials cannot transduce energy, but they are able to change a property under a stimulus. Among them, pH-sensitive materials, liquid crystals and fibre optics are very important.

Smartness describes those features which provide numerous possible applications for these materials and structures in aerospace, manufacturing, civil infrastructure systems, biomechanics and environment. By changing their properties, smart materials can detect faults and cracks and therefore they become useful as a diagnostic tool. This characteristic can be utilized to activate the smart material embedded in the host material in a proper way to compensate for the fault. This phenomenon is called self-repairing (or self-healing) effect. [13] [14]

Self-healing is defined as the ability of a material to autonomously heal, recover or repair damages, that is, without any external intervention. In this way, self-healing composites materials are capable of self-repairing upon damage initiation. As we previously mentioned, the early development concept of this peculiar ability relied on the mimicking action of living organisms, which motivated further researches in developing self-healing materials. Historically, the main goal of materials development was to improve them by directly enhancing their properties and optimizing their manufacturing process. Even though the first point has been widely overcome, even smallest defects are inevitably avoidable and that leads to periodical inspections and repairs, which are highly expensive and high-consuming activities. Focusing on FRPCs, they are critical as they suffer extreme internal damage from low velocity impact with no external indication. For that reason, non-destruction inspection (NDI) techniques are tested to check for any possible defect. Whenever a damage is found, no repair technique is applied as standard, because composites undergo different failure modes we have seen before, including fibre breakage, pull out and delamination. The development of self-healing materials therefore means an approach change, which turns from damage prevention to healing, thus from avoiding crack formation to material intrinsic repair. With focus on aerospace industry, self-healing materials offer great advantages when implemented in spacecrafts, as we know that space maintenance, as well as safety and reliability of such structures, is extremely hard and expensive. [4] [15] [16]

### **2.2.1 Process and classification**

The healing process can be generally defined regardless of the material (metals, ceramics or polymers) and its intrinsic properties. Whenever a damage occurs, a crack can initiate and to repair the formed defect, a healing agent is triggered by the damage itself (autonomic materials) or by an external stimulus (non-autonomic materials) and, by acting on the damaged area, it reconnects the crack planes by physical/chemical interactions, thus assuring the repair and restoration of material mechanical properties. Macroscopically, healing proceeds with two different and consecutive steps, including a physical and a chemical process. In the first one, the flow of healing precursors or the chains movement are mandatory for damage repair, thus they are continuously controlled by kinetics and thermodynamics. The repair event is determined by the kinetic energy of chains and entropy changes meanwhile by chains diffusion, thus affecting the overall Gibbs free energy. [17]

Moreover, a proper amount of influence must be placed on the matrix free volume, which is desirable to the mobility of polymer chains; during the mending process, voids and free volume facilitate segmental mobility of chains, preventing rigidity and consequent damage perception to increase. The chemical process is instead dominated by different polymerization reactions of healing precursor, entanglement of polymer chains or reversible covalent bonding, according to the base matrix material. All these stages are balanced by the damage-to-healing rate, defined by various parameters such as loading frequencies, strain rate or stress amplitude. [16]



The incorporation of self-healing properties in materials often cannot perform their recovering action without an external trigger, and thus, self-healing mechanisms can be divided into two main types: extrinsic and intrinsic healing. The first one is characterized by the use of a healing agent as additive, while intrinsic healing involves the branch of supramolecular chemistry, as it considers reversible molecular bonds in the structure of the material. The most diffused methods to develop self-healing composite materials are:

- Repair by liquid agent incorporated in the matrix
- Thermally induced repair carried out by a solid-phase material
- Intrinsic repair by ionomers

Differences between intrinsic and extrinsic self-healing approaches are discussed in the following section. [18]

### **2.2.2 Extrinsic healing**

The extrinsic healing process is based on the use of a liquid healing agent directly incorporated inside the matrix as a separate phase. The agent is usually in the form of microcapsules or hollow fibres, often coupled with a catalyst which can be encapsulated or dissolved in the matrix too. As a consequence of a damage, local capsules are broken, and both the liquid agent and the catalyst are released to rapidly heal the crack and thus prevent its growth and the otherwise unavoidable fracture failure of the whole structure. The main approaches are:

- Healing agents contained in the form of microcapsules, with catalysts dispersed in the matrix. In few cases, the healing agent can react itself and there is no need for a catalyst to initiate the recovering process; [15]
- Healing agent contained in the form of tubes/hollow fibres, which is essentially the same as before, but with varied shape; [19]
- Mesoporous network containing healing agents and delivering them from external reservoirs in case of damage. [20]

Essentially, when the material is damaged, the agent flows into the crack and repair it with the aid of the catalyst. Concerning the encapsulation strategy, great attention is given to the controlled release of the precursor, while in the case of hollow fibres the reinforcement is based on the bleeding ability of bio-systems and the healing agent is delivered into cracks when the damage has already occurred. Anyway, a larger amount of healing agent is provided with respect to encapsulation techniques. To enhance the healing efficiency, a 3D microvascular network inspired from respiratory system is developed into the matrix to store the healing agents for transport in long distance.

Self-healing materials adopting hollow fibres or mesoporous networks are called vascular, but the formers are restricted to one-dimension only while the incorporation of microvascular channels lends added functionality and increased autonomy to polymer composites (i.e., the ability to distribute active healing material for crack healing, which is difficult by conventional methods in monolithic materials). [16]

In a nutshell, the extrinsic healing concept is based on material response after or at the damage onset. Obviously, there is wide evidence of drawbacks concerning this kind of approach. Concerning the autonomous healing technique, a first hurdle could be the reliance on liquid resin delivery system that may lead to a lower strength and a lack of healing repeatability. Within this context, a study on the encapsulation technique with manual catalyst injection brought *Kessler et al.* [21] to recover up to 67% of the virgin fracture toughness of the polymer, but healing repeatability was limited to 3 three cycles only. In addition, it is worth taking care of vessels integrity during the manufacturing process, which is still a major issue in large-scale production. Furthermore, crack propagation needs to break the microcapsules containing the healing liquid and so they must be necessarily in the crack path, as suggested by *Hayes et al.* [22] Moving our attention to vascularized healing systems, healing repeatability up to the 11<sup>th</sup> cycle was obtained with a maximum recovery of 90%. In this case, materials can be vulnerable to cyclic damage at the same location, and in general, it is common knowledge that healing is not possible once the healing agents are used up or containers are empty.

To conclude, in the chance of encountering severe macroscopic damages, these extrinsic autonomous healing schemes would require even more liquid agents to fill macroscopic cracks, as well as empty capsules left behind may act as voids/inclusions, thus becoming detrimental for the structure strength. Due to all these reasons, current research is deeply focused on improvements regarding both the healing agents and the catalysts, and for what concerns new catalyst-free encapsulation techniques. [23]

In fibre-reinforced polymers (FRPs), high fibre stiffness and strength are obtained with high spatial density of strong and non-reversible chemical bonds in the fibre axis direction. Hence, chemical nature of high modulus organic fibres is such that it is intrinsically not possible to embed the healing capability, as the required bond strength in the fibre axis direction will be far too high to replace it by reversible covalent bonds. However, reinforcing fibres can be modified at the expense of their strength to contain a liquid healing agent, as shown by Bond *et al.* [1] with hollow glass fibres, but their work also showed that this insertion deeply lowers the composites intrinsic properties. In addition, two-dimensional and three-dimensional networks of such fibres hardly fit in large-scale production methods of FRPCs and further studies were implemented to minimize invasiveness and implement scalability. The fibre/matrix interface zone plays an essential role in transferring the load between the polymeric matrix and the previously mentioned fibres, as microcracks growing in this region can lead to large scale damage and catastrophic failure due to uncontrolled propagation and coalescence. From this perspective, researchers recently started to apply self-healing methodologies aimed at repairing microscopic interface damage, and provided that the interfacial crack faces are in some form of local contact, healing of such interfaces can also be achieved by intrinsic routes. Moreover, it is commonly known that extrinsic systems already present some inconveniences such as the potential chemical incompatibility between healing agent and composite, the poor design window to introduce the agent in the structure and finally the fact that the healing action is surely connected to the agent presence and quantity leads to singular healing events with limited entity. [24]

### **2.2.3 Intrinsic healing**

Intrinsic healing is based on the own healing capability of the matrix material and more generally on specific properties, such as molecular structure and bonds. In detail, when the material is prone to an internal damage, it can repair itself through dynamic chemical or physical bonds which are sensitive to specific stimulus and selectively reversible under equilibrium conditions. So, intrinsic healing systems are active methods programmed to respond to macroscopic damages with the help of specific properties, and in most of the cases they require human/external stimuli. Three main different modes of intrinsic self-healing have been proposed by *Zhang and Rong* and can be achieved by reversible covalent bonds, thermo-reversible physical interactions or supramolecular chemistry. [25]

### **2.2.3.1 Supramolecular interactions**

Reversible supramolecular interactions are low-energy bonds which influence the overall material properties, if well designed. They are mainly based on interactions which are neither covalent nor physical, including  $\pi$ - $\pi$  stacking, hydrogen bonding or metal coordination. Peculiar systems based on noncovalent interactions have been developed to overcome the need of a thermal trigger, however resulting in relatively inadequate mechanical performance. To deal with the difficulties in their integration in FRPs, the healing process has been kept at ambient temperature, even though higher temperatures would improve it, and novel hybrid systems based on both covalent and noncovalent bonds were created, as shown by *Sordo et al.* [26] with bifunctional (DGEBA) and tetrafunctional (TGMDA) epoxy resins. Despite the inclusion of these systems within FRPs has been demonstrated, as well as their production through conventional manufacturing techniques, the confident results obtained with tensile properties recovery are not balanced by suitable stiffness values essential for structural applications. [27]

### **2.2.3.2 Polymer blends**

A self-healing strategy exploiting existing commercial resin systems seems to be more practically applicable with respect to common covalently bonded ones. Thus, the idea of thermoplastic blending (i.e., thermoplastic phase dispersed within a thermoset host) can facilitate crack healing under heating. For these blends, the healing phenomenon is related to melting and subsequent thermoplastic phase volume expansion, flow of the melt in the damage volume and characteristic physical or chemical steps at molecular level. The latter can consist of chain re-entanglement of the thermoplastic melt or the formation of reversible noncovalent bonds in the thermoplastic phase. This mechanism was demonstrated by *Hayes et al.* [22] [28] with a solid-state epoxy resin of DGEBA and Epikote 828, which allowed chain entanglement at the crack faces after damage through heating at 130°C.

Thermo reversibility of physical interactions has been studied on the ionomeric copolymer ethylene methacrylic acid (EMAA), whose ionic species form reversible clusters and enhance mobility within the polymeric structure. The interest towards EMAA for systems embedding a thermoplastic phase in a thermoset matrix resides in the strong adhesion with epoxy during the curing phase and its thermal expansion which is 7 times greater than that of epoxy. Thus, an inclusion of 15 vol% EMAA particles within an epoxy resin has led to a 25% increase in the load to failure thanks to the strong adhesion between the two components, as proved by *Meure et al.* [29] Moreover, after thermal healing, fracture toughness recovery up to 85% was certainly achieved due to the huge expansibility of EMAA which creates pressure gradients and fill better the cracks. Despite the potential of ionomers in FRPs, EMAA is inevitably sensitive to humidity and its application development has slowed down. [30] [31]

### 2.2.3.3 Reversible covalent bonds

Reversible covalent chemistry, which represents a versatile strategy towards FRPCs repair, implies the dissociation and reassociation of covalent bonds under damage. Covalently bonded disulphide groups within an epoxy network have been introduced, thus providing reversible crosslinks which could be activated upon heating while maintaining suitable mechanical properties (Young's modulus ranging between 800 – 1200 MPa). As a result, recent studies produced GFRP based on disulphide-containing thermoset matrices with fibre volume fractions of about 50%, showing full recovery of mechanical properties after thermal treatment. The most widely used reaction for such systems is based on the Diels-Alder (DA) reaction, where a high density of crosslinks are generated by the reaction of electron-rich dienes and electron-poor dienophiles. Despite several researches have confirmed the ability of these systems to heal repeatedly, it is important to remind that healing is performed above the glass transition point. Therefore, repair may be less appropriate for some structures with residual stresses which can undergo a loss of integrity. [32] [33]

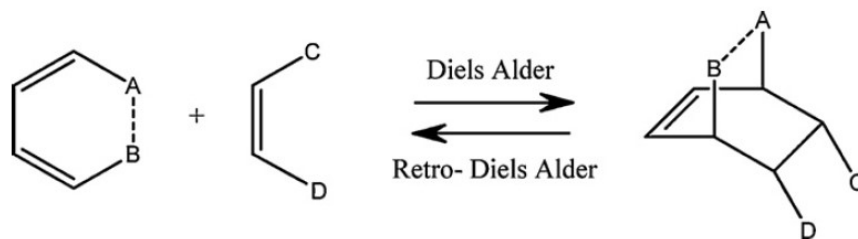


Figure 7: General mechanism of Diels Alder cycloaddition reaction. [34]

According to *Banshiwal* [16], two additional categories of intrinsic healing systems combining physical/chemical approaches can be included: shape memory polymers and polymer blends. To sum up the intrinsic healing concepts, the healing process depends on the ability of the polymer matrix to acquire sufficient molecular mobility upon the application of an external or internal trigger such as temperature, pH or light induction. Intrinsically, healing polymers have the advantages that no external healing entities are required, and local damage healing can take place multiple times. As the main repair systems integrated into structural composites have been described, it is crucial to clarify that, to date, only the matrix repair has been demonstrated and so, if fibres are fractured, there is no remedial action available. To conclude, the integration of a self-repair function within a high fibre volume fraction FRP is highly challenging as the embedded function must compete for volumetric space with the fibres themselves, which typically occupy > 50% of the total volume. [24] [35]

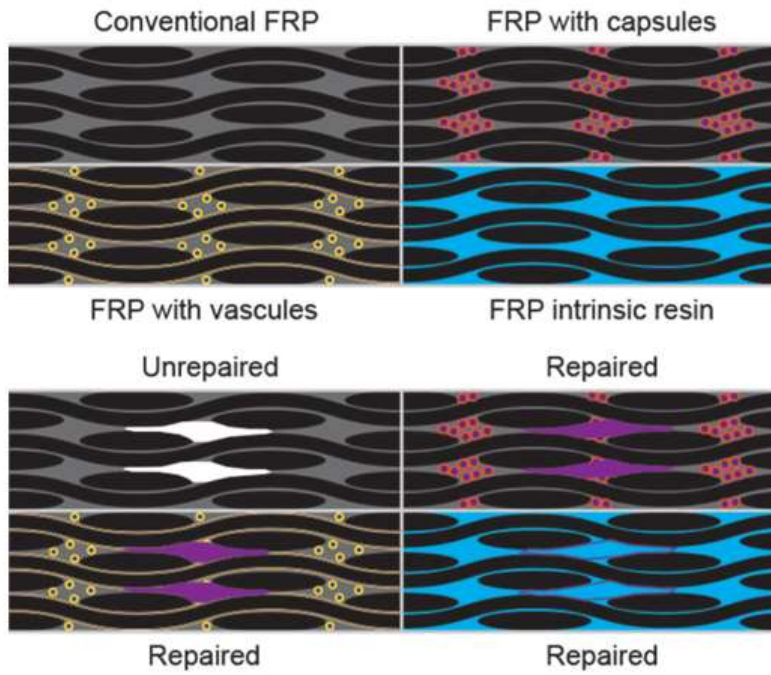


Figure 8: General self-healing systems. [35]

Naturally, as expressed by *Cohades et al.* [35] the effectiveness of healing in composites is predicted on the question of how healing and recovery is characterized, and the performance is commonly discussed in terms of healing efficiency ( $\eta$ ). This is a dimensionless value expressed as a percentage in terms of strength, stiffness, or toughness and, more generally, can be written as:

$$\eta = 100 \cdot \left[ \frac{\text{healed property} - \text{damaged property}}{\text{pristine property} - \text{damaged property}} \right]$$

#### 2.2.4 Dynamic covalent chemistry and disulphide bonds

Blending of conventional matrix polymers and polymers with intrinsic healing potential has been proposed as a promising route to polymer matrices combining some healing capability with acceptable mechanical properties, exploiting crucial concepts like Dynamic Supramolecular Chemistry and reversible covalent bonds. Taking into consideration this category, polymers based on the DA–rDA reaction have already been employed in fibre-reinforced composites, as well as in self-healing hybrid nanocomposites to overcome the long inspection times and consequent high maintenance costs. Disulphide bonds being part of a conventional epoxy-based thermoset represent an interesting alternative reversible covalent chemistry. [24] [33]

Cross-linked polymer networks possess enhanced mechanical properties as well as thermal and chemical resistance with respect to their not cross-linked counterpart, but it is proved that the high cross-links density and consequent stiffness increase the susceptibility to mechanical damage. Stimuli-responsive systems are achieved by incorporating some dynamic covalent functionalities into the matrix backbone or in side chains, so as to improve service life, energy efficiency and impact resistance. [16] As seen in *Paolillo's* thesis work [6], as disulphide bonds are weaker than carbon bonds, the mechanical scission is much easier and the possibility to exploit this point has helped in developing new and various self-healing polymers based on disulphide compounds. In order to design a polymer network able to heal at room temperature with no stimuli needed, aromatic disulphides were preferred with respect to aliphatic ones, as the exchange mechanism of the former is likely to occur at room temperature, while the latter requires the presence of catalysts or UV light. Among the aromatic disulphides, the most popular one is 4-aminophenyl disulphide (4-AFD), which is the one selected for the previous characterization part of this work, showing both vitrimer-like and mechanochromic behaviours.

The vitrimer-like behaviour, as reported by *de Luzuriaga et al.* [36], shows stress relaxation at high temperatures, thus allowing to use the resin for the manufacturing of reprocessable, repairable, recyclable fibre-reinforced thermoset composites. In a simpler way, they combine the advantages of both thermoplastic and thermosetting polymers, since they have mechanical and thermal properties typical of thermosets together with the possibility of being moulded upon heating like thermoplastics. Moreover, mechanochromic properties are mainly attributed to the formation of sulfenyl radicals, which disappears in a day at room temperature or in a few seconds if the glass transition point is crossed. It is foreseen that such an effect will find fundamental practical applications in terms of damage detection and failure monitoring, which are surely essential while dealing with FRPCs. Previous studies by *de Luzuriaga et al.* [37] already demonstrated that, since the resulting DGEBA/4-AFD network does not have any thiols or catalyst that can lead to thiolate ions, healing and reshaping ability stems from disulphide homolyses and radical exchange reactions. Moreover, tensile tests performed on both reference and dynamic epoxy resins outlined that their thermal and mechanical properties turn out to be comparable.

The use of 4-AFD instead of classical diamine hardeners does not, in principle, alter the resulting epoxy thermosets performances and so, concerning future potential industrial applications, it would not affect the final components.

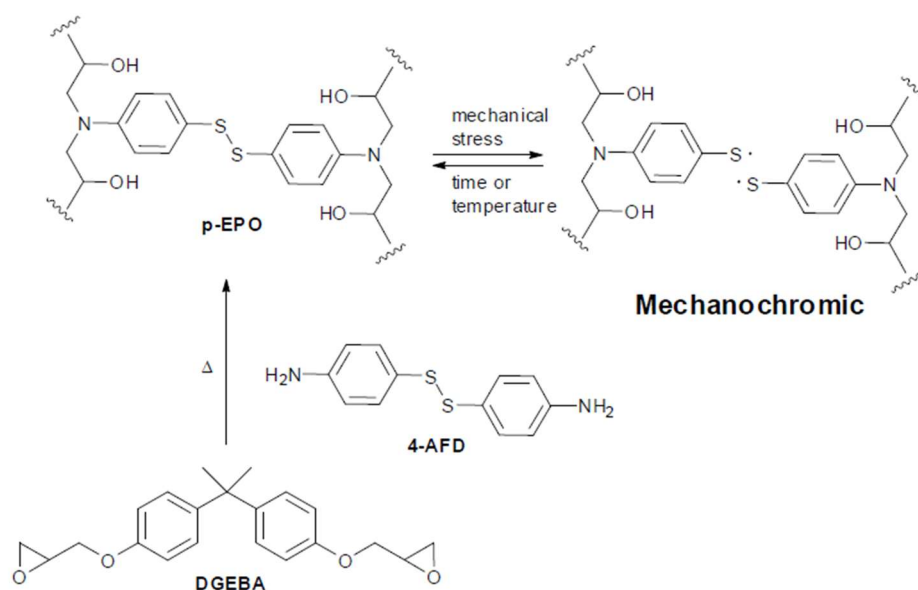


Figure 9: Synthetic procedure and chemical structure of dynamic epoxy networks and related mechanochromic behaviour. [36]

Most of the literature is concentrated on 4-AFD as it undergoes spontaneous homolyses at room temperature, thus applying as good candidate for future research as matrix material for aerospace composites. The combination with DGEBA leads to an epoxy vitrimer with very fast relaxation times and low activation energy, in good agreement with the fact that aromatic disulphide exchange does not require heat. Furthermore, dynamic properties include reprocessing, reshaping and recycling, which are by far the main drawbacks of thermosetting polymers. The main problems are still related to large-scale use for the previously mentioned mechanical reasons and due to the high-temperature and high-pressure healing, as well as 4-AFD expensiveness which is still one of the major issues. In his thesis work, *Paolillo* confirmed these studies and addressed the experimental efforts towards impact tests and scratching attempts, thus differentiating damages depending on the mechanochromic effect. Besides, known that repairing by disulphide bond reorganization requires temperatures above  $T_g$ , post-curing has been proven to enhance toughness and strength, as well as extend glass transition temperature above  $170^\circ\text{C}$ , which is a great issue if compared with previous results. To conclude, mechanical reprocessing was successfully performed and resulted materials still showed both mechanochromic and self-healing features.



## 2.3 LAMINATED COMPOSITES MANUFACTURING: MOULDING

### 2.3.1 Introduction and classification of moulding technologies

It is commonly known that manufacturing technologies can be subdivided on the basis of the composite matrix nature, which can be thermoset or thermoplastic. In accordance to this, the 75% of composite manufactures for commercial applications are made with thermoset resins, which are fundamental in the aerospace field. As resins are commonly in liquid state at the beginning of the process, thermosets-based composites require lower working pressure; moreover, glass transition temperatures are generally lower compared to those of thermoplastic materials, thus allowing for simpler systems and lower energy costs. Among the advantages, it should be noted that resins' low viscosity raises the wettability of fibres, thus reducing porosity and voids fraction. Among technologies for the manufacturing of composites with thermoset matrices, moulding technologies are the most diffused, with special mention to autoclave and hot press processes in aerospace industry.

Moulding includes all those production processes characterized by the deposition of composite on a suitable mould, which gives the desired shape after the polymerization process. In general, these technologies can be divided with respect to the way fibres are deposited. The so-called Lay-Up processes are based on superimposition of multiple layers, gradually made by continuous fibres which can be organized in fabrics or be unidirectional. If these fibres sheets are already impregnated with resin (*prepreg*), the processes are called Dry Lay-Up, while if they are manually wetted during deposition, processes are named Wet Lay-Up. A third but negligible family that of Spray-Up processes, based on the simultaneously spraying of matrix resin and discontinuous fibres; these last involve the realization of mechanically poor manufactures which are not suitable for aerospace field. From the other hand, prepreg allows for very high mechanical properties and the production of components with complex shapes. [38]

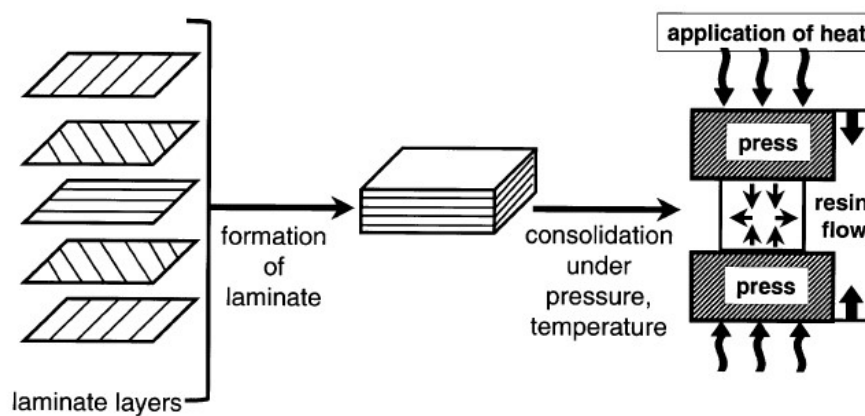


Figure 10: Basic processes of a laminated composite. [39]

<i>Thermoplastic processing</i>	<i>Thermoset laminate processing</i>
High viscosity at processing temperature	Lower viscosity at processing temperature
Shear thinning, extensional, viscoelastic flow	Primarily Newtonian flow
Significant effect of matrix shear on fibers	Primary flow mechanism: percolation
Short cycle times	longer cycle based on cure kinetics

*Figure 11: General comparison of thermoplastic and thermoset composite processing. [39]*

No matter which processing method is used, there are several points in common for all these technologies, which are explained below. First, it is fundamental to distribute the fibres uniformly in every part of product according to design requirements. As some properties of fibre composites mainly depend on the distribution state and the content of fibres, any inadequate content or uneven distribution will lead to weak links in local places, thus affecting the final performances of the product. This holds true also for the resin, which good distribution allows for an adequate curing process, thus ensuring improved mechanical properties to the composite material. Moreover, the amount of air bubble must be reduced as much as possible, thus improving compactness of products. Generally speaking, the volatile gases cannot be removed completely during the preparation of fibre composites. The content of pores is presented by void ratio, i.e., the percentage of void accounting for the total volume of composite. Any presence of voids will reduce performances and long-term properties.

During the design phase it is fundamental to suitably oversize both the product and the associated mould, and this can be done by evaluating the shrinkage of the composite material. To prevent the formation of residual stresses in the final product, CTE of product and mould have to be similar, even though for a process carried out at room temperature this aspect can be considered as negligible. As moulding phases require adequate pressure levels, the mould must be rigid enough to avoid any kind of deformation. Moreover, the level of surface finishing affects the choice of the mould type, its material and the technology to produce it. Other parameters which must be considered are draft angles and radii of curvature.

To conclude, the main requirements for moulding tools are:

- Stability at exercise temperature and pressure
- High wear resistance
- Ease of design, production and compatibility with production plant
- High surface finishing
- High resistance to solvents, to uniform heating rates
- Ease of release agents' application
- Lightweight

Aluminium alloys are lightweight and have an improved thermal conduction coefficient. With respect to steel, machine workability is favoured while it is harder to perform welding. The main disadvantages related to Al alloys are the susceptibility to scratches and dents, and the high CTE, but fortunately these are not crucial point for this thesis work. [41]

### **2.3.2 Moulding phases**

Although several phases can be automated, moulding technologies are basically manual processes with low production volumes and high production costs. For all of them, the whole cycle can be subdivided in three main steps: cutting, lamination and polymerization. The cutting phase is aimed at obtaining the laminate with desired dimensions and shape, lamination is the phase which allows the deposition of layers on the mould and finally the polymerization process is the complete crosslinking/curing of the resin, thus conferring the final properties to the composite component.

In the case of wet lay-up processes (which is our case), it should be noted that it is not possible to lay down unidirectional-only fibres as, in absence of the resin, is the woven pattern of weft and warp which holds fibres together. Nevertheless, it is commonly known that fabrics impart lower mechanical properties to laminates with respect to UD fibres, where reinforcement is monodirectional, and the need of the former is still a major limit to these processes. To conclude, although dry lay-up processes are favoured wherever high performances are required, wet lay-up is generally simpler and largely employed in several fields. [42] [43]

### **2.3.2.1 Cutting of fibres/fabrics**

The cutting of fabrics can be completely automated or fully manual. In the latter case, the operator makes use of a special table equipped with a suitable non-contaminant and hard cover, which allows to minimize the inclusions produced by the cutting tool (commonly the so-called cutter). With the help of templates, it is possible to perform precise cuts, thus obtaining fabrics layers with the desired shape. More complex tools employed for harder geometries can be carbide-covered iron blades, blades with alternated motion or shears. Similarly, systems based on ultrasound blades work with mechanical vibrations at elevated frequencies produced by an integrated source, thus reducing thermal dissipation especially for prepreg. Finally, die cutting systems allow for a complete automation of these procedures, with extremely high production rates.

### **2.3.2.2 Lamination process**

Lamination is the deposition phase and, like the previous one, can be manual as well as completely automated. In the aerospace field, it is fundamental to laminate inside the clean room to avoid interlaminar inclusions. Before lamination, it is necessary to apply a release agent to the mould surface to avoid the possible adhesion with matrix resin. There exist various release agents differing in chemical composition, application mode or functional range, but generally liquid agents are sprayed onto the surface or directly applied with a cotton cloth. Otherwise, for simple geometries it is possible to coat the mould with a thin non-adhesive film of PTFE®. Laminate sheets deposition is sometimes preceded by the application of an additional sheet called peel-ply, which is a thin nylon fabric (available in several grammages) aimed at giving the optimal surface roughness to the laminate for the bonding phase.

In this case, the peel-ply can trap volatile substances derived from the polymerization process and for this reason it is strictly removed before the bonding operation to avoid any type of contamination. The crucial point for lamination is the correct positioning of the sheets, which is even harder in case of manual lamination and strongly depends on the viscosity of the matrix resin. To increase the production rate, the lamination phase can be automated at different levels. When the very deposition of sheets is done by the operator and only some steps are automated, lamination is called mechanically assisted: sheets are moved on conveyor belts with an integrated cutting system. On the other hand, when the operator does not participate at all, lamination is completely automated, as in the case of automatic tape laying machines.

### **2.3.2.3 Polymerization/Curing Phase**

As previously stated, polymerization, or curing, is the manufacturing phase which simultaneously acts on temperature and pressure to confer the final properties to the composite component. The raising of temperature supports the crosslinking, and for every resin system there exists an optimal curing cycle (with related temperature) for complete crosslinking and improved mechanical and physical properties. Although, to reach very high mechanical performances, a reduction of voids fraction is required: for example, the interlaminar shear strength is reduced by 7% for every 1% of voids content. As argued above, air bubbles and volatile substances evacuation can be effectively obtained with an external pressure and the help of the vacuum bag.

The general effect of adding pressure in plastics processing is to let them flow, that is, to overcome the viscous flow resistance of plastic itself and friction generated by relative motion between plastics and mould (e.g., flowing through thin cast path, flow in the process of filling mould etc.). The second reason is obviously the complete compaction to get dense and uniform products. For some thermosetting resin, there are amounts of volatiles components that escape during curing. So, after mould closes, the additional pressure is needed to resist the pressure generated by volatile components and to ensure the compactness of product. In the processing of fibre composites, a crucial point is the adoption of resin formulations that can be processed under low pressure.

The character of such resin systems is that there are negligible volatile components released per unit time when curing. So, the pressure used to resist the pressure generated by volatiles can be reduced. The unsaturated polyester resin and epoxy resin with low viscosity are best among these kinds of resins since they need no solvent when impregnating fibres. All components reside in composites after curing. The curing of high-viscous epoxy resin is of addition polymerizing. Although the reaction itself does not generate any volatile components, the residual solvent in fillers will produce some of it during the moulding.

In moulding processes, the vacuum bag has three main tasks: evacuate air bubbles in the laminate; evacuate all the volatiles substances in the resin (prepreg); promote adhesion between laminate sheets. Although proper attention must be paid during superimposition of sheets, small air bubbles can still be trapped between layer. For this reason, the employment of the vacuum bag during the curing process is more effective as the resin fluidifies with rising temperature and allows for better air conveyance. The same happens also for volatile substances, which give contribution to the laminate voids fraction. The main difference is that the latter cannot be removed with compaction because they are trapped by resin at intralaminar level. Once these substances come out the laminate, they are aspirated: the suction action of the bag produces a resin flux from the mould toward the external surface, through the laminate thickness. Resin fluidity promotes this flux, thus favouring the adhesion of the resin between layers. A typical vacuum bag is composed by different layers of consumables aimed at different tasks, as shown in Figure 12 below. The very vacuum bag is a strongly expandable polymeric film (nylon) which can easily adapt to the mould-laminate assembly.

Valves for air emission are connected to it, and common plasticine is employed to seal the bag to the mould. Finally, the vacuum bag is provided with temperature transducers and pressure taps for the retroactive control of the polymerization process. One or more thermocouples are distributed inside the bag, directly connecting the laminate to the external environment. Sometimes, several dams (made of metallic bars or PTFE, neoprene, silicon) are positioned around the laminate to limit the resin leakage. [38]

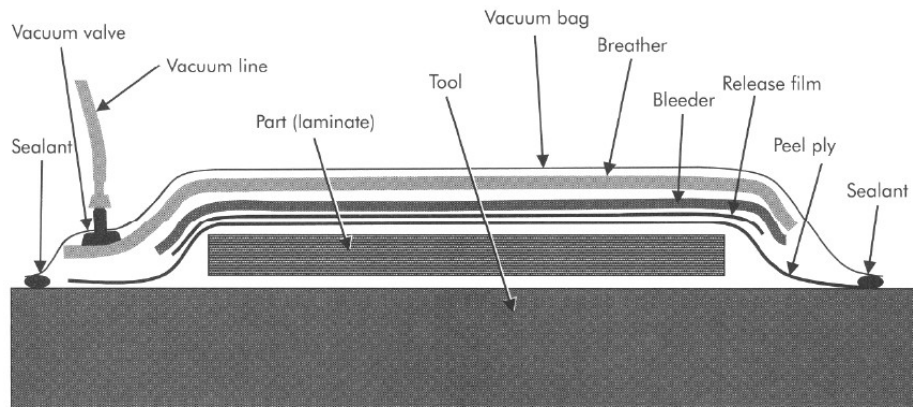


Figure 12: Schematic of a typical vacuum bag form laminate composites. [38]

### 2.3.3 Polymerization in autoclave

The autoclave is a pressure tank with three main variables: temperature, pressure and vacuum level. The laminate undergoes a curing cycle in temperature, while a hydrostatic pressure is simultaneously applied: the latter is the crucial point which verifies the best condition for plies compaction. Therefore, the obtained manufacture exhibit the best mechanical characteristics and for this reason autoclave moulding is the most widespread technology in aerospace field. Independently of the obtained vacuum level, the bag guarantees the pressure difference, so the insulation of the internal volume from the external atmosphere. So, in the autoclave technology the vacuum bag as an additional task with respect to those stated before. Typical autoclaves for composites with thermoset matrix have temperature range up to  $200^{\circ}\text{C}$  and up to  $10\text{ bar}$  of pressure, which allows to control the plant costs. Together with the low production rate, this is considered the main disadvantage, as it becomes harder to paid off the initial investments. To partially reduce the costs, it is often recommended to cure more components simultaneously and to perform co-curing cycles, where bonding and polymerization are carried on together (common with prepreg). During the standard cycles, the autoclave chamber is pressurized by air. As curing is a strongly exothermal process with auto-combustion probability, sometimes it is recommended to use inert gases, especially if curing temperatures rise above  $180^{\circ}\text{C}$ , laminates thickness is very high or if the mould is thermally active.

#### **2.3.4 Polymerization in hot press/oven**

As an alternative to the autoclave, polymerization carried out in hot press or oven is mainly designed for situations where no high mechanical performances are required. These are simpler systems with respect to the autoclave and consequently costs are largely reduced. The hot press is largely preferred for the production of planar panels and laminates of simple geometric form, which is the case of our thesis work. The hot press works by means of couples of planar moulds and counter-moulds and it is characterized by the application of a distributed vertical force for the compaction. The upper part of the machine is composed of four plates. The first one is refractory and provides thermal insulation of the adjacent parts; the second one, in Al-alloy, represents the real heat exchanger of the cooling system, which allows the coolant flowing; the third one heats the laminates through five electrical resistances, while the last one is the support of the mould/material. The temperature is controlled by several thermocouples linked to the third plate in (Al-alloy too). The heating system has three main elements: resistances, thermocouples and the electronic control system. Every thermocouple connected to a resistance transmits the temperature value to the control system, which in turn compares the measured value with the temperature imposed by the operator, thus regulating the current intensity in the resistance. The cooling system has two heat exchangers and pipes which link the former to the external hydraulic plant, thus obtaining a forced cooling with room temperature water (regulated by valves). [38]

## 2.4 DAMAGE MODES AND FRACTURE MECHANICS IN COMPOSITE MATERIALS

As laminated composites are becoming the preferred material system for a cut of industrial applications in aeronautical and aerospace structures, it is fundamental to give a good measure of their modes of failure and evolving technologies for the progressive enhancement of their performance.

To quantify the damage tolerance of a composite structure, it is essential to predict the conditions under which a defect/crack in the structure starts to propagate and subsequently lead to complete failure. Fracture toughness testing addresses this situation by providing material properties in the form of critical stress intensity factors, describing the local stress state around the crack tip, and critical strain energy release rates, thus giving a global description of the fracture process. In order to totally characterize a material, these properties are obtained for all three fracture modes and their combinations. Figure 13 shows the internal structure of a laminated continuous fibre reinforced composite, which is why the ply-level fracture characteristics can be divided into three main categories:

- *Interlaminar fracture.* Despite composites show great in-plane strengths, their laminated structure makes them suffer from relatively poor out-of-plane properties and an unavoidable tendency to delaminate.
- *Intralaminar fracture.* Crack propagation within the matrix can occur between the fibres through the laminate thickness, rather than between the plies. A consequent feature would be the large-scale bridging; when this phenomenon happens, the resistance curve (R-curve) concerning the fracture toughness of the material as a function of crack length, is no longer a material property.
- *Translaminar fracture.* Fibre-breaking cracks represent the mechanisms with the highest amounts of energy dissipation within composites, and fracture toughness values are typically several order of magnitudes larger with respect to those related to interlaminar and intralaminar failure modes. [40]



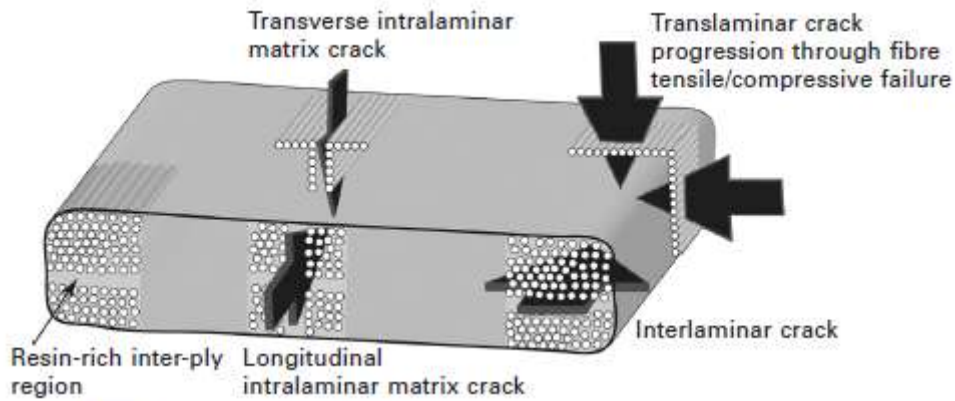


Figure 13: Ply-level fracture mechanisms exhibited by continuous fibre-reinforced composites. [40]

It is common knowledge that the principal mode of failure and consequent cause of yielding in layered composites is delamination, defined as the separation along the interfaces of the layers due to the complex tridimensional stress state they are subjected to during structures operating conditions. This mechanism is induced by interlaminar tension and shear that develop due to multiple factors such as free edges effects, structural discontinuities, working conditions obstacles, adverse temperature and moisture and internal failure mechanism (i.e., matrix cracking). As this phenomenon is hardly predictable during design and analysis phases due to the complexity of the 3D stress state and the presence of defects from production processes, composites lamination follows precautionary procedures (damage tolerance) towards the delamination growth. A complete understanding of composite delamination requires an appreciation for the fundamental principles of fracture mechanics, which have been extended from the original concepts developed for isotropic materials to include the peculiar anisotropy of composite ones. From this perspective, huge importance is given to the fundamental interlaminar fracture mechanisms, which allows to evaluate the damage tolerance of structures. [44]

### 2.4.1 Basic principles of Linear Elastic Fracture Mechanics (LEFM)

Theoretically, any complex deformation of the crack faces in a homogeneous isotropic linear elastic infinite plate can be described by a combination of three fracture modes, shown in Figure 14:

- Mode I represents the opening mode of the crack faces (peeling);
- Mode II represents the sliding mode (shearing);
- Mode III represents the out-of-plane shear mode (tearing).

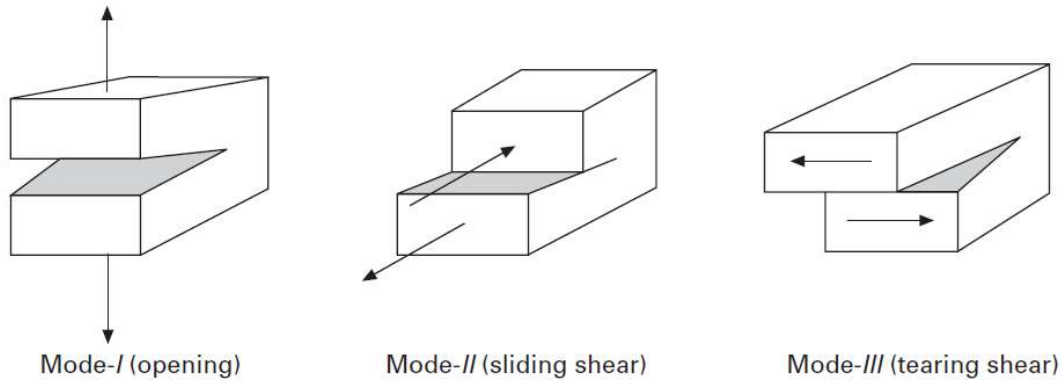


Figure 14: Fracture modes for LEFM. [44]

While in 1920 Griffith submitted an energetic approach towards the fracture mechanics studies, Westergaard and Irwin tried to mathematically solve the equations of the two-dimensional stress field around the crack tip with the help of polar coordinates  $(r, \theta)$ . The main result was the introduction of a constant  $K$  that we know as stress-intensity factor ( $K_I, K_{II}, K_{III}$ ), that linked the stress field to the geometry of the problem, respectively for every fracture mode:

$$\lim_{r \rightarrow 0} \sigma_{ij}^{(I)} = \left( \frac{K_I}{\sqrt{2\pi r}} \right) f_{ij}^{(I)}(\theta)$$

$$\lim_{r \rightarrow 0} \sigma_{ij}^{(II)} = \left( \frac{K_{II}}{\sqrt{2\pi r}} \right) f_{ij}^{(II)}(\theta)$$

$$\lim_{r \rightarrow 0} \sigma_{ij}^{(III)} = \left( \frac{K_{III}}{\sqrt{2\pi r}} \right) f_{ij}^{(III)}(\theta)$$

In 1957, Irwin calculated the work ( $W$ ) required to close a crack of length  $a + \Delta a$  to a length  $a$ , arguing that in a brittle material the whole energy supplied externally is directed in the creation of new crack surfaces as these materials undergo little or no plastic deformations. So, the work required to extend the crack will be the same as the one required to close it. Irwin obtained the strain energy release rate,  $G$ , as

$$G = \lim_{\Delta a \rightarrow 0} \frac{W}{2\Delta a}$$

Direct correlation between  $G$  and  $K$  is given by:

$$G = G_I + G_{II} + G_{III} = \frac{K_I^2}{E'} + \frac{K_{II}^2}{E'} + (1 + \nu) \frac{K_{III}^2}{E}$$

where  $\nu$  is the Poisson's ratio of the material,  $E = E'$  in plane stress,  $E' = E/(1 - \nu)^2$  in plane strain, and  $E$  is the Young's modulus of the material. For what concerns cracks in orthotropic or anisotropic materials, a similar situation exists at the crack tips, but the stress distributions are more complicated and involve material properties. Even though the stress-intensity factors and strain energy release rates are defined in a similar manner, relationships between  $K$  and  $G$  involve complex numbers. [44]

### 2.4.2 Delamination

We have previously seen that modern composite materials use high-strength fibres in a resin matrix and these elements are combined to form a single ply. Composite laminates are formed by stacking plies of different orientations with a selected sequence and curing the laminate under high temperature and pressure. As properties in fibre direction are different from the other two orthogonal directions, a unidirectional ( $0^\circ$ ) ply can be mechanically modelled as an orthotropic material, thus its properties can be obtained through UD properties and the fibre angle. Therefore, we can consider a composite laminate with multi-oriented plies as an anisotropic medium which can suffer from delamination between plies. Consequently, this can be viewed as an interface crack between two anisotropic materials.

The most common causes of delamination are material and structural discontinuities leading to interlaminar stresses, as shown in Figure 15. When delamination occurs, all three failure modes previously listed are present: this happens at stress-free edges due to mismatch in properties of the individual layers, at ply drops where thicknesses must be reduced and in region subjected to out-of-plane bending.

Although significant progress has been made in adapting fracture mechanics to the characterization and prediction of delamination fatigue failure, several difficulties have demonstrated a substantial difference with respect to the well-known damage tolerance assessment of metallic structures. Among these doubts, it is worth highlighting the propensity for cracks to propagate in a mixed-mode way, probably because delamination is forced to grow between composite layers and do not immediately turn toward the opening mode direction as typically happens for metals. The interlaminar fracture toughness associated to each mode must be characterized and the corresponding  $G$  associated with the configuration must be calculated to predict the onset and growth of delamination. [44]

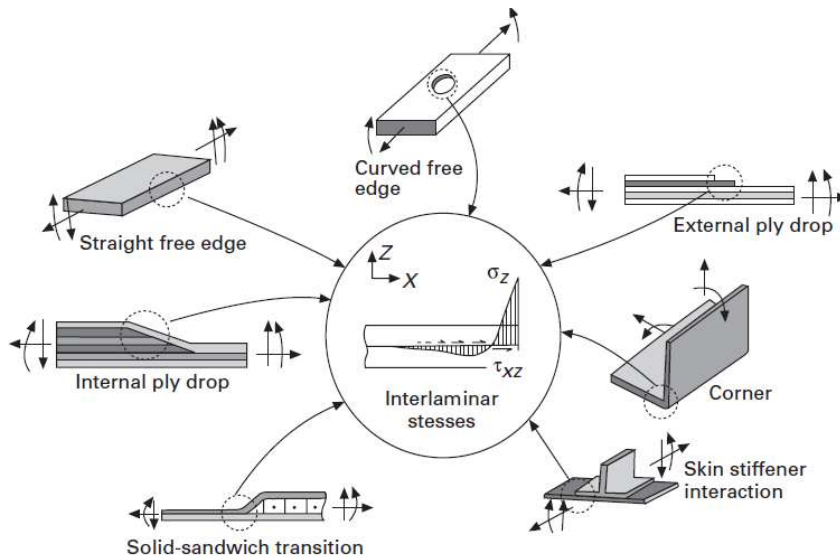


Figure 15: Sources of delamination at geometric and material discontinuities. [44]

### 2.4.3 Damage management in FRPCs

FRPs are especially susceptible to matrix microcracking when subjected to repeated thermomechanical loading. When these microcracks coalesce, other damage modes including fibre/matrix debonding and ply delamination develop within the composite material. The damage is difficult to detect and even more difficult to repair because it often forms deep within the structure and once developed, the integrity of the structure is greatly compromised. The result is a long-term degradation of material properties. Nowadays, composite parts that have been damaged in service are first inspected manually to determine the extent of damage. For critical parts this inspection may include such non-destructive testing (NDT) techniques as ultrasound, infrared thermography or X-ray tomography. If the damage is too severe, the design of a repairing process is senseless, and the structural component must be entirely replaced. On the other side, for less extensive damage, a repair process is attempted. If localized delamination has occurred, it may be repaired by injecting resin via an access hole into the failed area. Another common repair method is the use of a reinforcing patch bonded or bolted to the composite structure. Numerous studies regarding these and other composite repair methods have been published, yet all require time-consuming and costly manual intervention by a trained technician. One area of composites that opens up to new application possibilities is multifunctionality. Multifunctional composites are composite systems providing a variety of functions beyond the role of acting exclusively as a structure, for example by embedding structural health monitoring (SHM) or active fibre composites for suppression of vibration and acoustic control. [44]

## 2.5 STRUCTURAL HEALTH MONITORING FOR COMPOSITES INTEGRITY

Damage identification is carried out in conjunction with five closely related disciplines that include SHM (Structural Health Monitoring), condition monitoring, non-destructive evaluation, statistical process control and damage prognosis. Typically, SHM is associated with online–global damage identification in structural systems such as aircraft and buildings.

SHM is the process of automating condition assessment of aerospace, civil and mechanical engineering infrastructures by observing and interpreting their in-service responses. Typically conducted on structures under normal operational conditions, SHM has the potential to enable early damage detection and condition-based maintenance, thus limiting the needs for periodic inspections and allowing for an optimal allocation of public funds dedicated to infrastructure maintenance. This process involves the observation of a structure or mechanical system over time using periodically spaced measurements, the extraction of damage-sensitive features from these measurements and the statistical analysis of these features to determine the current state of system health. For long-term SHM, the output of this process is periodically updated information regarding the ability of the structure to continue to perform its intended function in light of the inevitable aging and damage accumulation resulting from the operational environments. Under extreme events SHM is used for rapid condition screening, which is intended to provide, in near real-time, reliable information about system performance during such extreme events and the subsequent integrity of the system. As a result of economic issues, these civil, mechanical and aerospace structures are being used in spite of aging and the associated damage accumulation. Therefore, the ability to monitor the health of these structures is becoming increasingly important. [44] SHM is based on the concepts of:

- *Condition-based maintenance*: a sensing system on the structure will monitor its response and notify the operator if damage has been detected. Life-safety and economic benefits associated with such a philosophy will only be realized if the monitoring system provides sufficient warning such that corrective action can be taken before the damage evolves to a failure level;
- *“Damage tolerance”*: the component is designed according to the presence of imperfections, defects and minor damages, which do not constitute a source of danger but must be controlled in real time.

In conjunction with these developments, SHM has received considerable attention in the technical literature. The aerospace community began to study the use of vibration-based damage identification during early 1980s (together with the development of the space shuttle). This work has continued with current applications being investigated for the National Aeronautics and Space Administration’s space station and future reusable launch vehicle designs. Since the mid-1990s, studies of damage identification for composite materials have been motivated by the development of a composite fuel tank for a reusable launch vehicle.

The failure mechanisms, such as delamination caused by debris impacts, and corresponding material response for composite fuel tanks are significantly different to those associated with metallic structures. Moreover, the composite fuel tank problem presents challenges because the sensing systems must not provide a spark source. This challenge has led to the development of SHM based on fibre optic sensing systems. SHM can be defined in terms of a six-step statistical pattern recognition process:

- I. *Operational evaluation* begins to set the limitations on what will be monitored and how the monitoring will be accomplished, by tailoring the damage identification process.
- II. *Data acquisition process* involves the selection of the excitation methods, the sensor types, number and locations, and the data acquisition/storage/transmittal hardware. Economic considerations will play a major role in making these decisions.
- III. *Data normalization* is the process of separating changes in sensor reading caused by damage from those caused by varying operational and environmental conditions.
- IV. *Data cleansing* is the process of selectively choosing data to pass on to or reject from the feature selection process. It is usually based on the knowledge gained by individuals directly involved with the data acquisition. The area of the SHM process that receives the most attention in the technical literature is the identification of data features that allows one to distinguish between the undamaged and damaged structure.
- V. *Feature selection and information condensation* are inherent in the feature selection process, and the best features for damage identification are, again, application specific. One of the most common feature extraction methods is based on correlating measured system response quantities, such as vibration amplitude or frequency, with the first-hand observations of the degrading system. The operational implementation and diagnostic measurement technologies needed to perform SHM produce more data than traditional uses of structural dynamics information, for this reason a condensation of the data is advantageous and necessary in case of comparisons of many feature sets obtained over the lifetime of the structure. Also, because data will be acquired from a structure over an extended period of time and in an operational environment, robust data reduction techniques must be developed to retain feature sensitivity to the structural changes of interest in the presence of environmental and operational variability.
- VI. *Statistical model development for feature discrimination* is concerned with the implementation of the algorithms that operate on the extracted features to quantify the damage state of the structure.

To conclude, SHM concerns the extent of the operating life of components, by verifying the continuous maintenance of performances and by preserving the integrity of the entire system. Recalling the main benefits, the transition from scheduled maintenance to on-condition one allows for a reduction of maintenance times and a reduction of life cycle costs, together with the possibility to use less invasive techniques during the inspections. Despite this, initial investment costs are high due to the complexity of the system and technological aspects related on sensors accuracy and host materials.

Therefore, an increasing number of research studies related to damage identification are aimed at facing many technical and common challenges concerning the adaptation of SHM. These challenges include the development of methods to optimally define the number and location of the sensors; identification of the features sensitive to small damage levels; the ability to discriminate changes in these features caused by damage from those caused by changing environmental and/or test conditions; the development of statistical methods to discriminate features from undamaged and damaged structures; and performance of comparative studies of different damage identification methods applied to common datasets. Finally, a significant challenge for SHM is to develop the capability to define the required sensing system properties before field deployment and, if possible, to demonstrate that the sensor system itself will not be damaged when deployed in the field. If the possibility of damage exists, it will be necessary to monitor the sensors themselves. This monitoring can be accomplished either by developing appropriate self-validating sensors or by using the sensors to report on each other's condition. Sensor networks should also be 'fail-safe'. If a sensor fails, the damage identification algorithms must be able to adapt to the new network. This adaptive capability implies that a certain amount of redundancy must be built into the sensor network. [45]

### **2.5.1 Damage assessment and monitoring in FRPCs**

The evolution of a matrix crack as the initial stage of damage, followed by delamination, is also true for composites subjected to impact load and in most of the damage models reported in literature consider three main stages (transverse matrix cracks, splitting, and delamination), with the degradation of effective elastic modulus of damaged laminates as the damage parameter. So, the final stage of damage progression identified as "delamination," which is the failure of the interface between two plies, is caused by normal and shear tractions acting on the interface, which may be attributed to transverse loading, free edge effect, ply-drop-off, or local load introduction. Delamination can significantly reduce the structural stiffness and the load carrying capacity and, therefore, is considered as one of the critical failure modes in laminated composites.

With the recent developments in the advanced composite applications, utilization of FRP composites for primary aircraft structures, such as wing leading-edge surfaces and fuselage sections, has increased. Impact from flying objects, excessive vibration, and loading can cause damage such as delamination and matrix cracking to the FRP composite structures. Moreover, the internal material damage in the FRP composite structures can be invisible to the human eyes. In some cases, delamination and cracks remain closed while the structure is under no loaded condition. With the intention of regularly monitoring advanced composites structures, structural health monitoring (SHM) technique has recently been developed for FRP composite structures majorly for aerospace structures. During past few decades monitoring of structural health of composites began with damage detection techniques such as vibration and damping methods. Then sophisticated and expensive offline non-destructive testing (NDT) methods were developed for the safe operation of composite structures. However, with the increasing complexity of structures, inspection for damage and clear insight into the structural integrity become difficult using currently available evaluation methods. Indeed, offline NDT was criticized as insufficient and developments of proper SHM systems became vital.

The SHM system developed to monitor FRP composite structures must be capable of identifying the multiple failure criteria of composites. Since the behaviour of most composites is anisotropic, multiple numbers of sensors must be in service to monitor these structures under multidirectional complex loading conditions. The layered structure of the composites makes it difficult to predict the structural behaviour by using surface mounted sensors only. To address this issue embedded sensors need to be used, and these must be robust enough to service the structure's lifetime, as it is impossible to replace them after the fabrication of the parts. The next section discusses about sensors for damage detection and the introduction of optical fibres. [46]



## **2.6 OPTICAL FIBRE SENSORS FOR DAMAGE DETECTION AND MONITORING**

Fibre-reinforced composites have been widely used for load bearing structures because of their good specific stiffness and strength as well as excellent fatigue and corrosion resistance. However, they are susceptible to damage mainly because of the lack of reinforcement in the through-the thickness direction. Detrimental barely visible impact damage (BVID) usually caused by low-energy impact is a particular case, and it could significantly degrade structural performance due to induced interior delamination. As previously mentioned, most conventional NDE techniques such as ultrasonic C-scan, x-ray, thermography and eddy current are limited as they require structural components of complex geometry to be taken out of service for a substantial length of time for post-damage inspection and assessment.

For continuous and in situ monitoring of realistic structures, the use of surface-bonded resistive foil strain gauges offers a potential method. Fibre optic sensors have a proven strain measuring capability with such characteristics as light weight, small size, immunity to electromagnetic interference and capacity for multiplexing sensors in a single optical fibre. They can be easily integrated into composite structures to produce so-called smart composite structures, in order to access interior material and structure locations where other sensing methods cannot easily probe. Research results have demonstrated that embedded fibre optic sensors performed in the same way as either non-embedded sensors in terms of failure stresses or resistive foil strain gauges in tension and compression, although there are stress and strain concentrations around the embedded fibre optic sensor.

These sensors can be developed into fibre optic damage detection and assessment systems (FODDAS) to evaluate the effects of damage from impacts or induced by quasi-static loads on the structural performance. The principle behind them is to measure local and global changes in strengths and stiffness, which are the main damage types in smart structures, via one of the optical properties: intensity, wavelength, phase/state of polarization. Indeed, any of these properties can be linearly related to mechanical axial strain. For the development of FODDAS, it is crucial to be familiar with various types of FO sensor and associated optical properties which are employed to measure mechanical strains. [47]

### 2.6.1 Optical fibres

An optical fibre consists of a central core surrounded by an annular cladding with a protective coating. The core guides the light along the optical fibre, while the cladding physically protects the core. Both layers are substantially made of silica, but sometimes plastic materials are employed. Finally, the coating, mainly made of polyacrylate, polyimide or organic modified ceramic materials, gives enhanced protection and mechanical properties to the fibre itself. A schematic of optical fibres is shown in Figure 16.

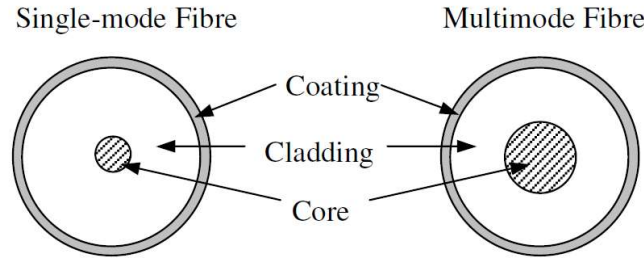


Figure 16: Schematic of optical fibres. [47]

Optical fibres working principle is based on waveguide light propagation due to the difference in refractive indexes between core and cladding. While the cladding has a lower refractive index, the core is a higher refractive index layer able to confine light within itself with minimal loss over a long distance. So, the core layer takes advantage of the total internal reflection (TIR) phenomenon occurring at the interface with the cladding and ruled by Snell's law:

$$n_1 \sin(\theta_1) = n_2 \sin(\theta_2)$$

Where  $n$  is refractive index and  $\theta$  the light ray angle, respectively for core and cladding. Condition for TIR is  $\theta_2 \geq 90^\circ$  and so the critical angle can be evaluated as:

$$\theta_1 = \theta_c = \arcsin \frac{n_2}{n_1}$$

since  $n_{CORE} > n_{CLADDING}$ , if  $\theta_1 > \theta_c$  the incident light undergoes TIR.

The overall diameter for a FO varies between 120 and 250  $\mu m$ ; when the core diameter is around 10  $\mu m$ , the optical fibre may carry only one mode of the light wave and for this reason is termed as *single-mode fibre*. If diameter is between 50 and 100  $\mu m$ , FO allows more than one light mode to propagated and so it is named "multimode". Either a single-mode or multimode optical fibre can be used to construct an individual FO sensor, with the former being much more sensitive and so more suitable for strain measurements. As announced before, single-mode sensors can detect a local area around 40 – 50 mm away from them; although, requiring higher light intensity, multimode sensors could reach greater areas but with lower accuracy. For this reason, to ultimately evaluate the effects of damage on large smart structures, a state of induced stress or strain must be determined.

This consequently requires multiple strain measurements, which can be provided only by fibre optic sensor networks: for example, in a fully distributed sensing system a large number of sensing points can be selected along the individual optical fibres.

Several requirements must be satisfied to precisely detect damages: embedded sensors must have a good mechanical bonding with host composite structures in order to experience the same strain gradient. Then, they must also be located near the region where the damage occurs, but on the other hand they must have sufficient strain resolution if damages are located far away from them. Moreover, optical fibres have a strain-at-failure value as high as that of the reinforcing fibres of the host composites. Obviously, if fracture of the optical fibres is used for an indication of damage, strain measurements may not be needed after all. Major individual fibre optic strain sensors are subdivided into intensity, interferometric and polarimetric sensors according to which optical property will be modulated by the external load.

- Intensity-modulated sensors are the simplest optical sensors based on modulation of light intensity in a multimode optical fibre (greater intensity); although they are easy to construct and do not require complex instrumentation or signal processing, intensity-modulated sensors provide only limited information, as they require knowledge on damage location. However, if a large number of intensity-modulated sensors are employed in a network for damage detection, they could be useful due to their low cost;
- Interferometric sensors measure phase changes either in a single-mode optical fibre or developed between two optical fibres, which is related to mechanical strain. It has high sensitivity and so it is useful for the evaluation of damage effects on the structural performance of the hosts;
- Polarimetric sensors are based on single-mode or elliptical core two-mode birefringent polarization-preserving optical fibres. birefringence is induced either by a residual strain field across the core or by an asymmetry in core geometry. [46] [47]

### 2.6.2 Fibre Bragg Grating (FBG) sensors

For what concerns the SHM of aircraft fibre-reinforced polymer structures, fibre Bragg grating (FBG) sensor is of great interest. This is based on a single-mode optical fibre with a set of intermittent reflective Bragg gratings along fibre length, written into the core surface by exposing the side of the fibre to an intense interference pattern of ultraviolet radiation. In this way, they offer a periodic modulation of refractive index of FO core and thus they act as a region of sensing. This periodically varying refractive index region reflects only a narrow band of light corresponding to the Bragg wavelength  $\lambda_B$ , which is related to the grating period  $\Lambda_0$ :

$$\lambda_B = \frac{2n_0\Lambda_0}{k}$$

where  $k$  is the order of grating and  $n_0$  the initial refractive index of the core material before strain application. Once the strain  $\varepsilon$  is applied, a change in wavelength  $\Delta\lambda_B$  occurs. Then, any physical change in the fibre profile will cause a variation of refractive index.

A typical length of a FBG sensor varies from 2 – 20 mm and it can be embedded into composites during composite parts manufacturing with no adverse effect on strength due to sensor reduced size. Again, when an embedded FBG sensor is subjected to the external load, induced changes in the wavelength of its gratings can thus be related to mechanical strain. Furthermore, this sensor is suitable for networking as it has a narrowband response with wide wavelength operating range, hence it can be highly multiplexed (multiplexing capability is the possibility to take multiple measurement points per fibre). Moreover, it is nonconductive so it can also operate in electromagnetically noisy environments without any interference. Finally, as the signal has low transmission loss, the sensor signal can be monitored from longer distances allowing for remote sensing.

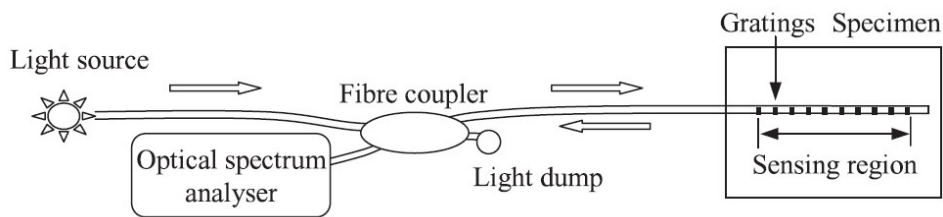


Figure 17: Schematic of Bragg grating sensor. [47]

To resume, a FBG sensor is a wavelength filter which is photoinduced into a fibre core due to intensive UV light. When the fibre is stressed, grating period undergoes a variation and consequently the central wavelength of the reflected spectrum shifts to another value which can then be determined by spectral techniques. So, during the fabrication of FBG sensors, the pitch spacing of their gratings can be individually controlled in such a way that the wavelength shift of a series of individual FBG sensors can be tracked simultaneously for multiplexing. It is obvious that the distortion of FBG sensors depends on the type of loading.

The effect of the twist and micro bending of FBG sensors under multiaxial loading has been identified as the causes for this discrepancy. The change of section geometry of the FBG sensor due to micro bending and twisting, leads to a variation of the refractive index of the FBG core material which causes distortion of the FBG response spectra.

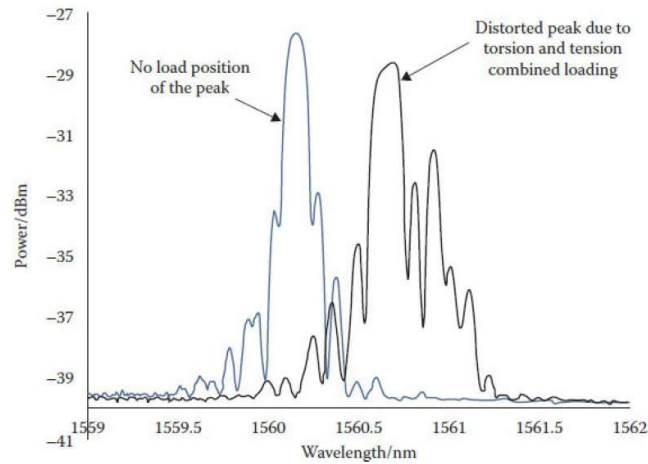


Figure 18: Distortion of the peak due to applied torsion and tension combined loading. [46]

The FBGs' capability of detecting stress gradients along its grating length can be used to identify the stress variations in the FRP composites by means of chirp in the reflected spectra of the FBG sensor. This phenomenon can be used to detect damage in the composite structures. The majority of research work on FBG sensors in SHM of composite structures has focused on investigation of the spectra of FBG sensor embedded in the vicinity of damage. Observations of the distorted sensor spectra due to stress concentrations caused by delamination and cracks have been used to estimate the damage conditions. A major advantage of using FRP composites is the possibility of deciding on the number of layers and layup orientation based on the required structural behaviour. In an FRP composite aerospace structure there are several layers with multiple orientations, which are placed one on top of the other and hence it is possible to embed FBG sensors in any layer during the manufacturing of the structure.

So, after their appearance in late 1970s, the FBG sensors had been using for SHM of composite materials efficiently for more than two decades and recent advances have provided great opportunities to develop more sophisticated in situ systems. Although FBG sensors are a popular choice in smart structure applications thanks to attractive properties such as small size, immunity to electromagnetic fields, and multiplexing ability, potential drawbacks related to complex three-dimensional measured strains and sensitivity to temperature must be considered for further SHM and sensors improvements. [46] [47]

### **3 MATERIALS AND EXPERIMENTAL TECHNIQUES**

As previously specified in Par. 2.4.1, fracture mechanics rules the behaviour of materials which contain flaws and cracks, and its main goal is to discover the maximum stress value that the material can bear in the above-mentioned conditions. This occurs with the introduction of the fracture toughness, an indicator of the ability of a material to bear an applied load. Our study is mainly focused on linear elastic fracture mechanics (LEFM), which mainly deals with sharp cracks in elastic bodies, just considering the hypothesis of a small ductile region around the crack tip.

The study of failure in composite materials is strongly related to the degree of bonding between fibres and matrix, which can lead to voids formation and delamination onset. Indeed, when cracks terminate at the interface between fibres and matrix, the crack tip acts as a stress concentration site, thus weakening the interfaces between adjacent layers and leading to delamination. In this section, all the tests carried out in laboratory are discussed from a theoretical point of view and focusing on the equipment and methods employed during the experimental part of the thesis work. In particular, the following techniques will be discussed:

- Differential Scanning Calorimetry (DSC) analysis (Par. 3.1);
- Scanning Electron Microscopy (SEM) analysis (Par. 3.2);
- Density test (Par. 3.3);
- Double Cantilever Beam (DCB) mechanical test (Par. 3.4);

The second part of this section will deeply focus on the whole manufacturing process of the fibre-reinforced composite panels and on the aspects considered for all the above-mentioned tests and analyses.

### 3.1 DIFFERENTIAL SCANNING CALORIMETRY (DSC)

#### 3.1.1 Theoretical background

Differential Scanning Calorimetry (DSC) is one of the most used and versatile thermal analysis techniques that covers the determination of transition temperatures and enthalpies of fusion and crystallization of polymers, provided these are fabricated in a shape from which it is possible to cut an appropriate specimen (usually milligram quantities). During the analysis, the test material undergoes a controlled temperature program with a specified gas (i.e., nitrogen) and the difference in the heat flow rate between the specimen and a reference body over time (due to energy variation in the material) is monitored with a sensing device. The key in this technique is that when chemical reactions physically alter the sample, it will take a certain amount of heat to keep the temperature of the sample increasing at the same rate as the reference. Such measurements provide quantitative and qualitative information about endothermic (heat absorbed) or exothermic (heat evolved) processes, as well as changes in heat capacity. The heat flow-temperature data provides many information on physical and chemical properties of thermosetting materials, including glass transition temperature ( $T_g$ ) and all aspects related to curing (onset, heat, maximum rate, heat capacity) [6]. For this reason, DSC is a highly valuable analytical tool for the analysis and characterization of thermosetting materials, such as epoxies and polyesters, and directly describes the growth and branching of chains occurring during the curing phase, as seen below (Figure 19).

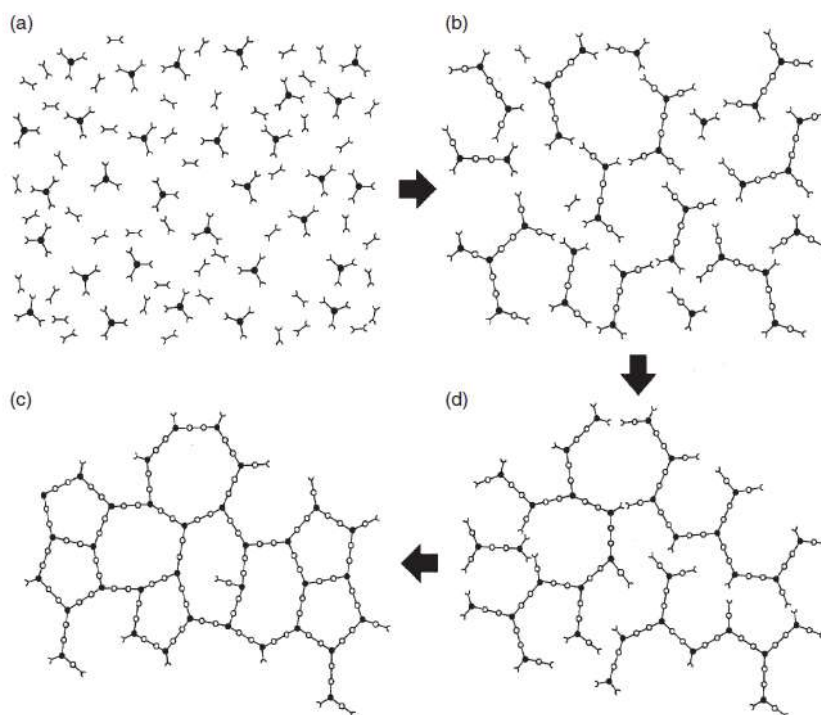


Figure 19: Schematic, two-dimensional representation of thermoset cure with four main stages: (a) monomers, (b) branching, (c) gelled incomplete crosslinked network, (d) fully cured thermoset polymer. [48]

### 3.1.2 Laboratory analyses

Samples for DSC measurements were taken from epoxy leaked from aluminium mould so as to confirm the previous  $T_g$  results obtained in *Paolillo's* thesis work [6]. These samples consist in several aluminium pans containing a scrap of the already mixed and cured epoxy, which are prepared and weighted; then, the lid is aligned with the pan and consequently crimped to it by using the TA Instruments Sample Encapsulating Press, as shown in Figure 20.

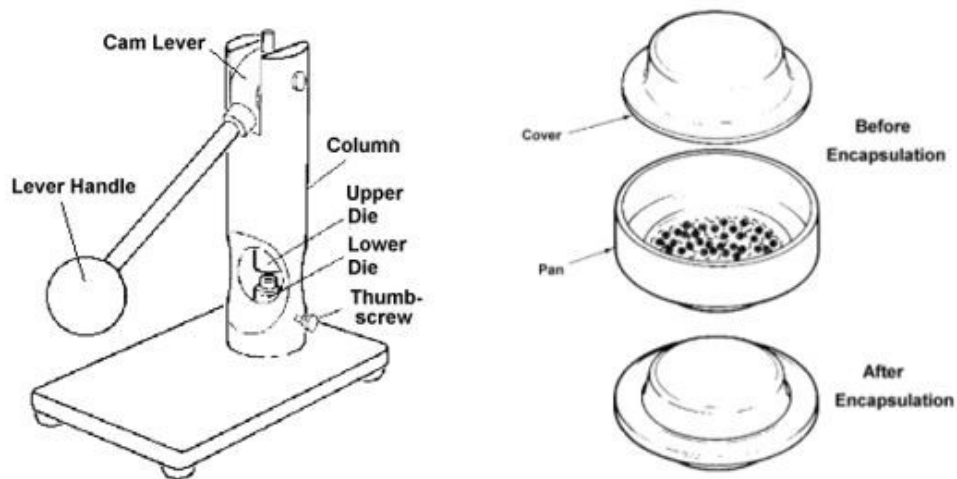


Figure 20: Sample encapsulating press (on the left) and the encapsulated sample (on the right) for DSC analysis.

The calorimeter at the disposal of Politecnico di Milano (DAER) is called TA Instruments DSC 2010 CE. As shown in Figure 21, it is composed of two main parts: the 2010 CE instrument containing the electronics and software needed to run experiments and for data storage, and the DSC cell where sample and reference pans are positioned on platforms on a disc, beneath which thermocouples are placed to control differential heat flow.



Figure 21: TA Instruments DSC 2010 CE in DAER laboratory.



For what concerns this thesis work, the test consists in two different heating/cooling cycles at fixed temperature rate under nitrogen flow ranging from 30 to 40  $mL/min$ . The sample is sandwiched in between a metal cover (pan) to ensure good heat transfer and then placed into the DSC cell at room temperature together with an empty pan (reference); then, the test starts by heating with different temperature rate after equilibrating cell temperature at  $-10^{\circ}C$  with the help of the TA Refrigerated Cooling System. The temperature cycle adopted for this test is shown in Table 1.

	<b>Initial Temperature [<math>^{\circ}C</math>]</b>	<b>Final Temperature [<math>^{\circ}C</math>]</b>
<b>1<sup>st</sup> heating cycle</b>	20 $^{\circ}C$	220 $^{\circ}C$
	1 min isotherm	
<b>1<sup>st</sup> cooling cycle</b>	220 $^{\circ}C$	20 $^{\circ}C$
<b>2<sup>nd</sup> heating cycle</b>	20 $^{\circ}C$	220 $^{\circ}C$
	1 min isotherm	
<b>2<sup>nd</sup> cooling cycle</b>	220 $^{\circ}C$	20 $^{\circ}C$
<b>Temperature rate [<math>^{\circ}C/min</math>]</b>	20 $^{\circ}C/min$ (constant)	

Table 1: Thermal cycle of the DSC analysis.

Difference in the heat flow between sample and reference is plotted against temperature. Curing is observed as a significant broad exothermic peak, which area can be integrated to give the heat of cure:

$$\Delta H_{CURING} = \frac{1}{m_{SAMPLE}} \int_{t_i}^{t_f} dH_{PEAK}(t)$$

where  $t_i$  and  $t_f$  are respectively the initial and final reaction times which correspond to the initial and final temperatures of the exothermic peak, while  $m_{SAMPLE}$  is the resin sample mass and  $dH_{PEAK}$  is the heat exchanged in the peak time range. Complete curing is not always achieved, so the parameter  $\alpha$  is introduced to quantify the degree of cure:

$$\alpha = \frac{\Delta H_{CURING}}{\Delta H_{TOTAL}}$$

where  $\Delta H_{TOTAL}$  is the total heat of reaction. The degree of cure, which is fundamental to assess various material's properties, is both characterized by the increment in  $T_g$  and the decrease of the heat of cure. When thermoset materials are completely cured, the residual heat of cure is almost zero and the glass transition temperature reaches a constant value, as it depends on the material chemistry. With mention to data analysis, once the test has been completed, DSC measurements on epoxy resin were collected using TA Instruments Universal Analysis and TRIOS software to confirm the transition temperature of the resin. [6] Evidence of the comparison will be briefly shown in Par. 4.1.2.

## 3.2 SCANNING ELECTRON MICROSCOPY (SEM)

### 3.2.1 Theoretical background

Scanning Electron Microscopy (SEM) is the most widely used imaging technique for the study of both short and continuous fibre composites. The nature of the adhesion between the matrix and the resin and information relating structure to mechanical properties can be obtained by SEM assessment of the composite fracture surface, which undoubtedly helps in detecting possible composites failure mechanisms. SEM is a high-resolution diagnostic tool which forms an image by scanning a probe (i.e., a focused electron beam), across the specimen. The probe then interacts with a thin surface layer of the specimen, in the order of few micrometres at most. The working principle of a conventional SEM is schematized in Figure 22 below. [49]

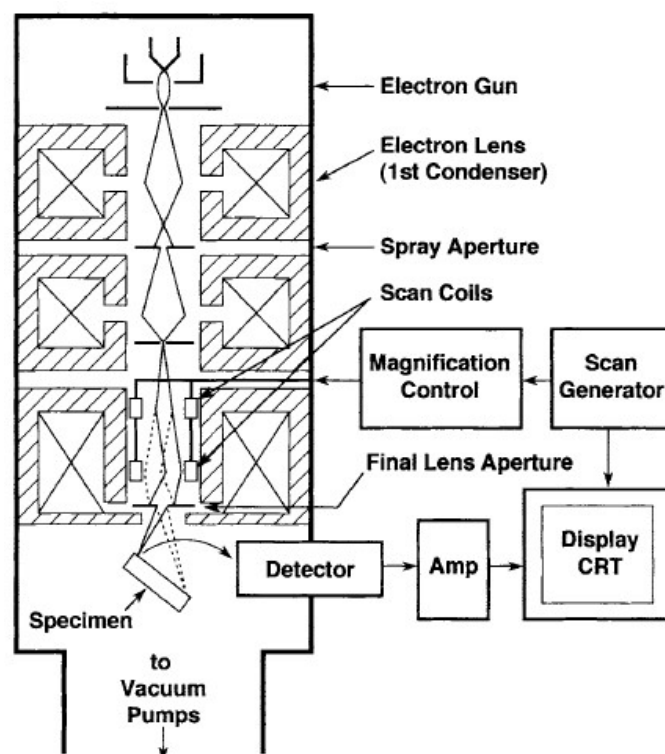


Figure 22: Schematic diagram of a SEM. Two pairs of scan coils are shown, and this double deflection allows the scanning beam to pass through the final aperture. [49]

The electron gun creates an electron flow which is accelerated towards the specimen through several lenses. In this way, the beam is controlled by the scan generator which deflects it all over the sample surface, thus the image of the electron source is created in the specimen plane. The primary electrons generate likewise secondary electrons on the specimen sample which are detected by the electron collector and subsequently amplified to enable its display. A cylindrical vacuum column is strongly required for electrons to travel without collisions with air molecules and so to avoid electron scattering and image distortion.

Compared with incident light optical microscopy, the SEM has higher resolution and a much larger depth of field, so this means that a larger area of the specimen is brought into focus at the same time. Using microscopy analysis, the complete cross-section can be produced in multiple images, which can be meshed together to create a complete cross-sectional image at a sufficient 100x magnification.

Samples for SEM analysis must undergo a series of pre-treatment operations. First, a deep cleaning of the sample surface is important to remove possible undesired particles like dusts and contaminants related to the source of materials and previous practical operations. Then, as the specimen chamber is large, samples with a diameter of several inches can be accommodated. Their preparation is generally quite simple, and materials must be completely dry in order to withstand high vacuum. Specimens are mounted on holders inserted into the SEM chamber, which is generally large to accommodate samples with several inches diameter, but in case of composites the restrictions on size and geometry of the chamber can be seen as a limiting factor. Specimens are typically mounted on metallic stubs, so the orientation must be properly chosen before to prevent any kind of motion while scanning and consequent damages to the specimen itself. Nonconductive materials, such as most polymers, require either conductive coatings, low accelerating voltages, or variable pressure to prevent them from charging up in the electron beam. Proper coatings are made of a thin layer of gold or platinum.

### **3.2.2 Laboratory analyses**

Before the mechanical assessment of the laminate, the samples obtained by hand lay-up lamination were observed by Scanning Electron Microscopy (SEM) with Hitachi TableTop Microscope TM3000, allowing the analysis of specimens' thickness, internal defects/voids, optical fibres diameter and technological defects (delamination) caused by pressing.

A sanding technique has been employed to prepare the surface and make it flat, flush and clean. For this purpose, a Bitech Europe lapping machine from DAER was used, together with different grain sandpapers (P320, P600 and P1200). Samples were blocked onto the holder inside the SEM chamber, after being covered with a layer of conductive adhesive tape (Figure 23). The evaluation of voids content by image analysis has been done through the Hitachi related software on sets of multiple micrographs taken at different locations. On the heels of optical fibres, their mean diameter has been recorded together with the dimensions of their shell.

Normal SEM images are easy to interpret qualitatively:

- fibres are presented as luminous white filaments;
- matrix as shades of grey;
- voids/defects are in black.



*Figure 23: Hitachi TableTop SEM (on the left) and a top view of the SEM holder blocking the composite specimen covered with conductive tape.*

For what concerns the internal defects assessment, a good contrast between void and matter must be assured to balance the qualitative and the quantitative analyses. Then, a complete scanning along the whole length of every sample is carried out in order to distinguish the non-negligible internal defects or voids, under the assumption of small void dimensions ( $< 100 \mu m$ ) and low void content ( $< 10\%$ ). In conclusion, microscopy is a visual and destructive analysis technique that allows the void size, shape and distribution to be analysed. The method is widely used in industry due to its visual characterisation advantage, but also has an inherent section-bias error associated with analysing two dimensional (2D) cross-sections of the sample, thus being not representative of the whole three-dimensional sample.

Concerning the final reading, it is clear how the analysis strongly depends on the operator which performs the test, as software magnification, focus and contrast are all personal choices related to sample positioning. Moreover, the evaluation of the 2D analysis could induce reading errors while evaluating voids of different nature all around the sample. Due to all these restrictions and due to the uncertainty on the mass fractions of matrix and fibres sheet during the production of the laminate, a deep microscopy voids assessment is beyond the purpose of this thesis work.

### 3.3 DENSITY TEST

#### 3.3.1 Theoretical background

Void content/porosity, delamination, matrix cracks and impact damage are just some of the composite material defects. These defects need to be identified and characterised for determination of the ‘quality’ of a composite structure, as these parameters have a significant effect on the mechanical properties of the material and can act as failure initiation points. Density or Archimedes’ test is a conventional composite void characterisation technique, which calculates the samples actual density using the Archimedes’ principle. Then, the void volume fraction is calculated using the theoretical density of the sample with no voids present. The technique relies on accurate knowledge of the fibre and matrix density and weight fraction values of the laminate. The method can give a negative void fraction, which is theoretically impossible and generally it must be said that it provides results of limited accuracy and/or reliability due to inherent testing errors. [50]

As we previously stated, mechanical properties in composites are highly influenced by the fibre reinforcement volume fraction. The assessment of this value is performed by measuring the density of the composite (or the specific gravity), and for this reason it is crucial to perform this test before the very mechanical treatment. In our case, specific weight/density measurements were taken with the help of a Mohr-Westphal’s balance, which is one of the most common methods and it is based on Archimedes’ principle: the upward buoyant force that is exerted on a body immersed in a fluid is equal to the weight of the fluid that the body displaces. A general scheme of the Westphal’s balance is shown below. [17]

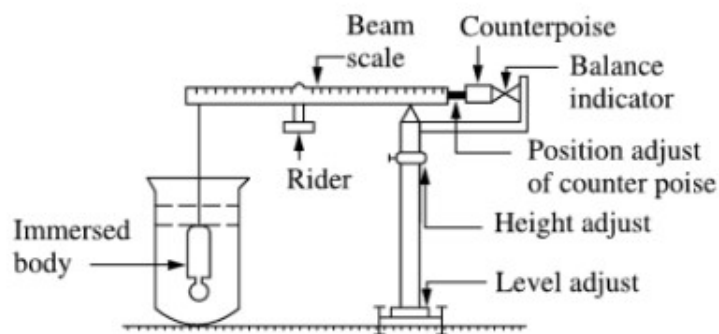


Figure 24: Westphal-Mohr's balance scheme. [51]

### 3.3.2 Laboratory analyses

The balance in DAER laboratory consists of a height adjustable primary structure on which a double-armed shaft is assembled. The arms are both calibrated: the short one is used to calibrate the balance and the longer one holds different weights (actually 9) needed to measure the actual weight of the submerged sample. Distilled water is used as a reference liquid and put in a jar together with the specimen to create a non-equilibrium state. This setting allows to obtain highly accurate results as the known weights are placed on the calibrated arm in specific positions until a new equilibrium state is reached: every notch position determines a decimal value (up to 3) of specimen's weight in water. By knowing the apparatus and specimen weights, the final value of voids volume fraction is recorded through proper mathematical relations reported in Para 3.3.3 .



*Figura 24: Westphal balance (on the right) and Branson ultrasound bath (on the left) at the disposal of DAER laboratory.*

Three specimens from a lateral scrap part of the composite panel were taken into consideration for this analysis. A Branson 2210 Ultrasonic bath from Tecnovetro S.r.l. was used to plunge specimens in water for 10 minutes before density tests were performed. After drying, air weight was taken for all of them with an analytical scale from Gibertini Elettronica. This aspect is of crucial importance for the following reasons. As the experiment is carried out with complete immersion of the plate and the specimen, several side aspects must be taken into account, like friction between plate and jar, liquid drops all around and air bubbles on the specimen. A deep and accurate cleaning of the specimen, followed by immersion in distilled water is needed to wet the specimen surface, thus limiting the formation of bubbles.

### 3.3.3 Equilibrium mathematical approach

Going back to the equilibrium condition set once the plate is immersed in water, it is possible to read the weight of the specimen inside the liquid and evaluate the composite's density  $\rho_C$  according to the following formula:

$$\frac{\rho_C}{\rho_{H_2O}} = \frac{w_{air}}{w_{air} - (w_{balance} - w_{M-W})}$$

Where  $w_{air}$  is the weight of the specimen in air measured before testing,  $w_{M-W}$  is the scale reading, and  $w_{balance}$  is the equipment weight (in our case equal to 20 g). Finally,  $\rho_{H_2O}$  is the density of distilled water, equal to 1 g/cm<sup>3</sup> as the test is performed at room temperature.

Since this thesis work is deeply focused on mechanical properties, it would be helpful to qualitatively compare the results obtained with density test and the theoretical Young's modulus. By assuming a perfect laminate, from the rule of mixtures we know that that the theoretical composite density  $\rho_{C,TH}$  and Young's modulus  $E_{C,TH}$  are both functions of fibres (subscript  $F$ ) and matrix (subscript  $M$ ) density and volume:

$$\begin{cases} \rho_{C,TH} = \rho_F f + \rho_M (1 - f) \\ E_{C,TH} = E_F f + E_M (1 - f) \end{cases}$$

Being  $f$  the fibres volume fraction equal to (see Data Sheet in 6.1):

$$f = \frac{V_F}{V_M + V_F} = 0.55$$

the voids volumetric fraction can be calculated as a relative error on composite density:

$$V_{voids}(\%) = \frac{\rho_{C,TH} - \rho_{C,SAMPLE}}{\rho_{C,TH}}$$

or by the following equation:

$$V_{voids}(\%) = 100 - \rho_{C,SAMPLE} \left( \frac{m_M}{\rho_M} + \frac{m_F}{\rho_F} \right)$$

where  $m_M$  and  $m_F$  are respectively the mass fractions of matrix and fibres, while  $\rho_F = 2.9$  g/cm<sup>3</sup> and  $\rho_M = 1.2$  g/cm<sup>3</sup>. Using Archimedes principle, the actual density ( $\rho_{C,SAMPLE}$ ) of the sample is determined, with the sample first being weighed in air and then while submerged in water. Considerations on the obtained results will be done in a second moment on the basis of the concepts related to small voids dimensions (< 0.1  $\mu m$ ) and low content (< 10%).

The Young's modulus accounting for voids fraction can be predicted as:

$$E_C = E_F f + E_M (1 - f - V_{voids}) + E_{voids} V_{voids}$$

with  $E_{voids}$  referring to air trapped voids is equal to 0 *GPa*. To conclude we can evaluate the final error by considering again an ideal composite with no voids or imperfections:

$$ERROR = \left( \frac{E_{C,TH} - E_C}{E_{C,TH}} \right) \cdot 100$$



## 3.4 DOUBLE CANTILEVER BEAM (DCB)

### 3.4.1 Theoretical background

As damage modes and the main principles of fracture mechanics were deeply explained in Par. 2.4, here the purpose is to concentrate our attention on mechanical testing. American Society for Testing of Materials (ASTM) standards have been developed for Mode I (Double Cantilever Beam, DCB), the one we will focus on, and for mixed-Mode I and II (mixed-mode bending, MMB). Then, other methods were recently tested for pure Mode II (end notched flexure test, ENF) and III (edge cracked torsion, ECT). [44]

The possibilities offered by numerical tools to model the presence of interlaminar cracks in composite material and to evaluate their possible propagation are very promising for the development of SHM (Structural Health Monitoring) systems. Quasi-static fracture tests are widely used to assess performances of self-healing FRPs and double cantilever beam (DCB) configuration (and its tapered and width-tapered variants) is by far one of the most common sample geometries. Following the intrinsic approach, this work is focused on previous results from literature, performed by *Hayes et al.* [28] with poly(bisphenol-A-co-epichlorohydrin) as solid healing agent in a commercial epoxy resin demonstrating a fracture strength recovery up to 70% after a thermal healing cycle at 140°C and then carried on by *Paolillo S.* [5] [6]

Susceptibility to delamination is one of the major weaknesses of many advanced composite structures and so, a complete knowledge of their resistance to this kind of fracture can be useful for product development and material selection. For this reason, major efforts are made to fully study and understand the Mode I opening of specimens through DCB tests, for the estimation of interlaminar fracture toughness ( $G_I$ ) and its related critical value  $G_{IC}$ , thus showing the importance of fiber bridging phenomena in the interlaminar fracture between glass reinforced plies. The general aim is to develop delamination failure criteria for damage tolerance and durability analyses, while our main purpose is to compare quantitatively the related values of  $G_{IC}$  for composite materials undergoing repairing cycles. A full explanation of the standard technique, the apparatus and various aspects related to DCB tests is given below.

### 3.4.2 DCB Standard Test Method

In the past, much more attention has been given to Mode I interlaminar fracture, as in this case the fracture occurs at much lower stress values with respect to other modes. DCB standard test method, issued under the fixed designation ASTM D 5528-01 [52] describes the crack opening/peeling mode (Mode I), in which the delamination faces open away from each other. DCB specimen is the most widely used specimen for the measurement of mode I interlaminar fracture toughness,  $G_{IC}$ , which is the critical value of  $G$  for delamination growth as a result of an opening load or displacement. This test method is limited to composites with unidirectional carbon/glass fiber tape laminates with brittle and tough single-phase polymer matrices.

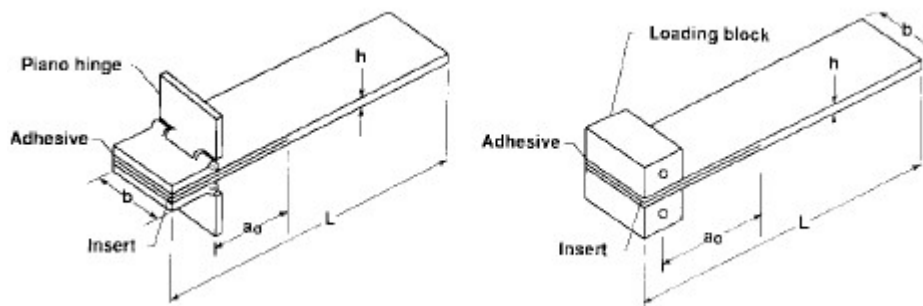


Figure 25: Double Cantilever Beam Specimen (a) with piano hinges, (b) with loading blocks. [52]

The DCB shown in Figure 25 consists of a rectangular, uniform thickness, unidirectional laminated composite specimen; a thick non-stick film is previously placed between the central plies during curing cycle to introduce a pre-crack. Opening forces are applied by means of hinges (a) or blocks (b), bonded to one specimen. The ends are opened by controlling either the displacement or the crosshead movement, and the load and delamination length are recorded. Before the test, the sides of the specimen are usually marked with a millimetric scale to quantitatively track the crack growth.

For what concerns the applicability of ASTM D 5528-01, DCB specimens shall be at least 125 mm long and 20 – 25 mm nominally wide, inclusive. Required thickness must be between 3 – 5 mm, while Teflon insert length corresponds to an initial delamination length of 50 mm, plus an extra length required for hinges/blocks application. A polymer film is recommended for the insert to avoid problems with folding or crimping at the cut end of the insert and concerning epoxy matrix composites cured at temperatures around 170°C, a thin film of polytetrafluoroethylene (PTFE) is suggested. A second fundamental point is the bonding of the hinges to the specimen, which shall be performed immediately after surface preparation with a room temperature cure adhesive.

In the DCB test, as the delamination grows from the insert, a resistance-type fracture behavior usually develops where the calculated  $G_{IC}$  first increases monotonically, and then stabilizes with further delamination growth.

The main reason behind delamination resistance is the development of a phenomenon called fiber bridging, which results from growing the delamination between two 0° unidirectional plies; fibers between adjacent laminates oppose to the specimen opening, acting like a bridge and thus enhancing its toughness. From this perspective, the advantage of a 0° ply interlaminar is to prevent the crack to move out of the middle-specimen plane and prevent any form of crack hopping phenomena. In this test method, a resistance curve (*R curve*) depicting  $G_{Ic}$  as a function of delamination length will be generated to characterize the initiation and propagation of a delamination in a unidirectional specimen, as show below in Figure 26.

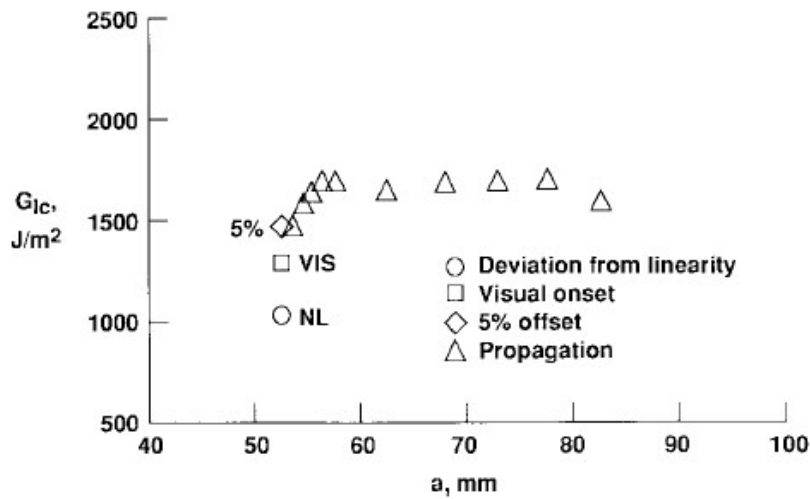


Figure 26: Delamination Resistance Curve (*R curve*) from DCB test. [52]

As load is applied, the delamination length  $a$  is measured on one side of the specimen. The initial delamination length  $a_0$  is the distance from the load line to the end of the insert. When the specimen is loaded, the length of the initial delamination is determined by graduation marks generally applied on the same side of the specimen; then, readings are taken for the next 1 mm increments of delamination growth.

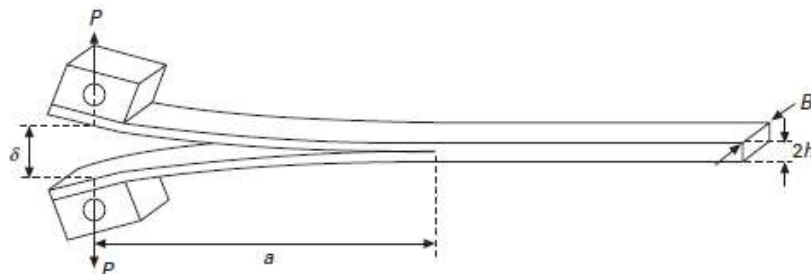


Figure 27: DCB specimen. [40]

Recordings of loading and unloading conditions are showed through the generation of a  $P$  vs.  $\delta$  graph (Figure 28). This represent, together with the  $R$  curve, the main data processing output resulting from DCB tests.

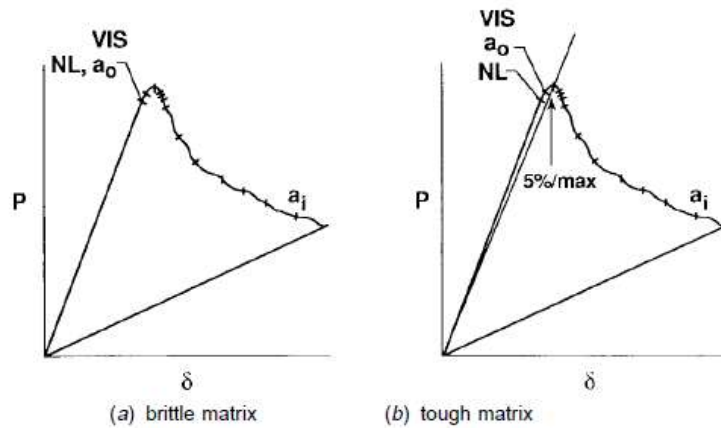


Figure 28: Load Displacement Trace from DCB Test. [52]

Linear elastic behavior is assumed in the calculation of  $G$  used in this test method: this prediction is valid whenever the damage zone or nonlinear deformation at the delamination front is small relatively to the smallest specimen dimension (typically its thickness). Load grows linearly with respect to displacement in the first segment, up to the point where crack propagation begins. Then, the crack advances up to a second point, where the specimen is unloaded by reversing the machine movement. The area included in the three-segments graph represents the energy dissipated during the crack propagation phase. [40]

### 3.4.3 DCB test apparatus and elements

According to ASTM D 5528-01, the equipment for a proper DCB test should include:

- *Testing Machine*: a properly calibrated test machine shall work in a displacement control mode with a constant displacement rate varying from 0.5 to 5 mm/min;
- *Load Indicator*: it indicates the total load carried by the test specimen with great accuracy, minimizing the inertia;
- *Opening Displacement Indicator*: opening displacement may be estimated as the crosshead separation, with the specimen grips attached, provided that machine deformation is less than 2% of the opening displacement of the test specimen;
- *Load Versus Opening Displacement Record*: an X-Y plotter shall be used to record the load versus opening displacement during the test. Alternatively, the data may be digitally stored and then post-processed;
- *Optical Microscope*: the optical microscope or equivalent magnifying devices are strongly recommended to observe the delamination front from one side of the specimen as it extends along one edge during the test.

### 3.4.4 Calculation of critical interlaminar fracture toughness ( $G_{IC}$ )

The ASTM D 5528-01 standard mentioned before provides three specific points to define the instant of crack initiation, the corresponding critical load and opening displacement (of the machine crossbeams). These evaluations have to be carried out on a  $P$  vs.  $\delta$  graph seen before.

- *Deviation from linearity (NL)*: it is the onset value for  $G_{IC}$ , calculated from the load and displacement at the point of deviation from linearity, also called onset of nonlinearity (NL). This calculation assumes that the delamination starts growing from the insert in the interior of the specimen at this point, thus NL value represents a lower bound value for  $G_{IC}$ . Visually, it is the first point of the  $P$  vs.  $\delta$  curve not belonging to the linear section tangent;
- *Visual observation (VIS)*: it is the visual initiation value for  $G_{IC}$  corresponding to the load and displacement for the first point at which the delamination is visually observed to grow from the insert or from the crack tip, at the test onset;
- *5% Offset / Maximum Load (5% / Max)*: it is a value of  $G_{IC}$  calculated by determining the intersection of the load-deflection curve, once it has become nonlinear, with a line drawn from the origin and offset by a 5 % increase in compliance from the original linear region of the load-displacement curve. If the intersection occurs after the maximum load point, the maximum load should be used to calculate this value.

Finally, four main methods of data reduction are available for calculating  $G_{IC}$  values, that were evaluated by a round-robin test:

- Beam theory (BT);
- Modified beam theory (MBT);
- Compliance calibration method (CC);
- Modified compliance calibration method (MCC).

The methods of calculating the strain energy release rate ( $G$ ) are all based on the following equation:

$$G = \frac{P^2}{2b} \frac{dC}{da}$$

Where  $P$  is the applied load,  $B$  is the specimen width,  $C$  is the specimen compliance, the ratio between displacement and applied load, and  $a$  is the crack length.

#### 3.4.4.1 Beam Theory (BT) and Modified Beam Theory (MBT) methods

The beam theory expression for the strain energy release rate of a DCB is showed below:

$$G_I = \frac{3P\delta}{2ba}$$

Where  $P$  is the load,  $\delta$  is the load point displacement,  $b$  the specimen width and  $a$  the delamination length. To overcome the possible overestimation of  $G_{IC}$  due to rotation at the delamination front, it is suggested to consider a slightly longer delamination,  $a + |\Delta|$ , where  $|\Delta|$  can be determined by depicting a least squares plot of the cube root of compliance,  $C^{1/3}$ , as a function of delamination length (Figure 29). Remember that the compliance  $C$  is the ratio between the load point displacement and the applied load,  $\delta/P$ . So, Mode I interlaminar fracture toughness can be determined as follows:

$$G_I = \frac{3P\delta}{2b(a + |\Delta|)}$$

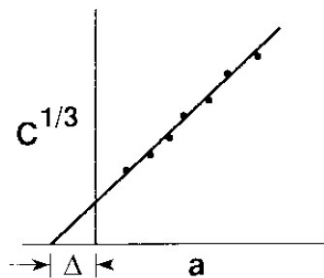


Figure 29: Modified Beam theory. [52]

### 3.4.4.2 Compliance Calibration (CC) method

This method generates a least squares plot of  $\log(\delta_i/P_i)$  versus  $\log(a_i)$  using the visually observed delamination onset values and all the propagation values. The exponent  $n$  from the slope of the best-fitting straight line is calculated according to  $n = \Delta_y/\Delta_x$ , where both  $\Delta$  are defined in Figure 30.  $G_{IC}$  is calculated as:

$$G_I = \frac{nP\delta}{2ba}$$

$$n = \Delta_y/\Delta_x$$

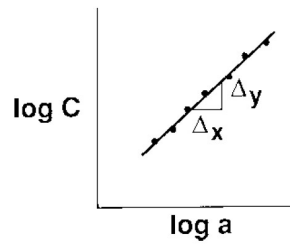


Figure 30: Compliance Calibration theory. [52]

### 3.4.4.3 Modified Compliance Calibration (MCC) method

The last method generates a least squares plot of the delamination length normalized by specimen thickness,  $a/h$ , as a function of the cube root of compliance,  $C^{1/3}$  (Figure 31). The slope of the line is called  $A_1$  and the interlaminar fracture toughness is found as:

$$G_I = \frac{3P^2C^{2/3}}{2A_1bh}$$

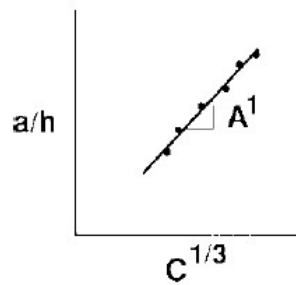


Figure 31: Modified Compliance Calibration theory. [52]

To conclude, intercept  $\Delta$ , slope  $n$  and slope  $A_1$  for the respective methods are used to reduce the data. As clearly stated in ASTM standard, all these reduction methods differ by no more than 3%, so none of them is considered superior. However, MBT method gave the most conservative  $G_{IC}$  outcomes for 80% of the specimens tested, hence it is the most recommended. Consequently, the classic BT method has to be considered not acceptable.

### 3.4.5 Laboratory analyses

Once the laminate design has been accomplished, three specimens were cut and employed for DCB test, according to the preparation method that will be explained in Par. 3.6 for the first panel and in Par. 3.7 for what concerns the second panel. First, the measure of initial delamination length  $a_0$ , namely the distance between load line and the end of Teflon ® film, has been taken. Then, the hinges were fixed on the testing specimen and on the loading machine, assuring symmetry and alignment of the apparatus and the sample for a clearer load reading. The specimen is fixed to the lower crossbeam of the machine and before fixing it to the upper one, it is necessary to reset the load for reading calibration.

Tests in DAER laboratory at Politecnico di Milano have been performed by using a MTS 858 Mini Bionix ® II machine (Figure 32), imposing a loading and unloading displacement rate equal to  $0.5 \text{ mm/min}$ .



Figure 32: MTS 858 Mini Bionix II machine supplied by DAER laboratory.



For the second composite panel, a pre-opening of few millimeters in every specimen has been attempted, then a real opening was performed trying to reach a pre-determined specimen length (1<sup>st</sup> specimen: 40 mm; 2<sup>nd</sup> specimen: 30 mm; 3<sup>rd</sup> specimen: 50 mm). The choice of opening specimens to three different lengths is justified by the fact that the primary purpose of this thesis work is to evaluate the quality of the resin repairing ability and the possibility to state that healing is not influenced by the size of the damaged area would be a huge step forward on the final composite assessment. After unloading, a video for every specimen was recorded with great attention to assure an almost perfect synchronization between video starting and DCB test onset.

In a second moment, photo frames were extrapolated from videos to evaluate the crack opening length with GIMP software. Different opening crack lengths were recorded and measured from specific frames. In the meantime, data files of load, opening displacement and time of acquisition were obtained directly from the machine software and re-elaborated with Microsoft Excel software. These constituted the main phases of data processing for the evaluation of the interlaminar fracture toughness ( $G_I$ ) and its related critical value ( $G_{IC}$ ).

It is worth mentioning that the results presented in the following Section (Par. 4) are meant to be considered only in a qualitative way, as the tested specimens do not satisfy the dimensions regulated by ASTM standard. Some modifications are implemented also on applied load and on loading/unloading rates due to technological reasons. A deeper discussion will follow in the next paragraph. To conclude, it is important to state that the whole experimental set-up did not allow to concretely verify the mechanochromic effect of the resin, which has showed during the manufacturing process before undergoing mechanical testing.



*Figure 33: Proof of the mechanochromic effect (green spots) caused by accidental scratches during manufacturing.*

### 3.5 MANUFACTURING PROCESS

In this paragraph the whole manufacturing process is extensively explained, starting from epoxy resin and fibres until the realization of the final composite panels. In a second moment, all the mentioned tests carried out on the panels will be mentioned together with their technological and experimental aspects.

#### 3.5.1 Matrix phase realization

For the realization of the matrix phase of the composite panel, a dynamic resin was created by mixing together our prepolymer and hardener in controlled quantities. As earlier explained in Section I, epoxy resins are the main class of thermosetting polymers employed for this purpose and they consist of a resin prepolymer and a hardener, the latter acting as the curing agent. Once mixed, they submit a curing and post-curing process to link one to each other and finally form a three-dimensional network, as the rings of the resin react with hydrogen atoms from the hardener thus creating covalent intermolecular bonds (see Par. 2.2.4). The main advantages and features of epoxy resins are otherwise described in Par. 2.1.3. In this thesis work, the following materials were employed for the realization of the dynamic resin.

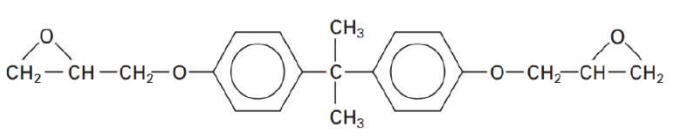
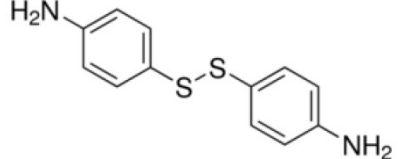
Prepolymer (non-crosslinked)	Hardener
<b>Commercial name</b>	
D.E.R. <sup>TM</sup> 332 di-glycidyl ether of bisphenol-A epoxy (DGEBA) purchased from Sigma-Aldrich	4-aminophenyl disulphide (4-AFD, 98%) purchased from Sigma-Aldrich
<b>Molecular weight</b>	
<b>340.41 g/mol</b>	<b>248.37 g/mol</b>
<b>Chemical formula</b>	
<b>C<sub>21</sub>H<sub>24</sub>O<sub>4</sub></b>	<b>(H<sub>2</sub>NC<sub>6</sub>H<sub>4</sub>S)<sub>2</sub></b>
	

Table 2: Characteristics of the ingredient of the dynamic epoxy resin.

As previously mentioned, a significant aspect that must be taken into account during the design phase is that curing and post-curing processes strongly affect the final structure and properties of the resin, mainly from a mechanical point of view. Hence, absolute attention has been paid for the choice of a suitable and optimal curing pathway, thus assuring that the strong relationship between structure and properties will entail proper final performances of the entire composite. For the purpose of this thesis work, the results concerning materials amount and curing/post-curing processes of the resin obtained by *Paolillo S.* [6] were taken as a good starting point to realize the composite panel. More specifically, by considering a resin density  $\rho = 1.2 \text{ g/cm}^3$ , it was shown that for every 100 g of DGEBA resin, 36.48 g of 4-AFD hardener were needed for a correct mixing.

Prepolymer and hardener were accurately mixed while constantly heating the mixture at  $80^\circ\text{C}$  with a VELP Scientifica ARE magnetic stirrer (Figure 34). A strict control on temperature was performed with the help of an external thermocouple, while the slow mixing allowed for the removal of air bubbles inside the resin which can compromise its homogeneity. The mixture was then poured into a pre-designed metallic mould (its realization is explained in Par. 3.5.5) to impregnate the plies of dry glass-fibres fabric through a hand lay-up process (Par. 3.6 and 3.7).



Figure 34: VELP Scientifica ARE magnetic stirrer supplied by DAER laboratory for resin preparation.

### 3.5.2 Reinforcement phase realization

The reinforcement phase of the composite under examination is HexForce® - Hexcel® 01102 1000 TF970 E-glass woven fabric [0°/90°], purchased by Hexcel® Composite S.r.l. It has nominal weight 290 g/m<sup>2</sup> and thickness 0.23 mm (its data sheet is provided in Appendix 6.1).



*Figure 35: Zoomed photo of the E-glass woven fabric used to design the composite panel.*

Cutting dry fabrics is extremely difficult because the friction between fibres and the cutting tool can damage the texture and fray the fabric at the cutting edges. For this reason, scotch tape stripes were preliminarily applied to outline and carefully measure the region to be cut, then a cutter was used to obtain our fibres layers. Six layers with dimensions 80 mm x 150 mm were cut out for every composite panel. As the long sides of the panel were previously considered as scrap regions of the entire composite, scotch tape stripes have been left attached during the lamination phase, while short sides have been left free.

### 3.5.3 Stoichiometric calculations

As suggested in Par. 2.2.4, the epoxy group is the site of the cross-linking reaction and it is truly relevant to deeply understand the nature of the epoxy and of the curing system, on which the properties of the cross-linked polymer strongly depend. It is common knowledge that amines are the most diffused among the main curing systems for epoxies. In this case, one of the amine hydrogens reacts with the epoxy ring to form a hydroxyl group which can then react (i.e., addition reaction) with another group to cross-link the chains with no by-product. Primary amines ( $R - NH_2$ ), which contain two active amine hydrogens, are therefore capable of reacting with two epoxy groups and achieving a greater cross-linking density (number of cross-links per polymer) than single functional hardeners, which would inevitably improve physical properties, although to the detriment of flexibility. If the amine is aromatic, overall stiffness, low shrinkage, and temperature capability are improved, although toughness is sacrificed.

For thorough cross-linking, the hydrogens of the primary and secondary amines should be matched 1:1 with the epoxy groups. The desired stoichiometric quantity of amine in weight parts per 100-gram epoxy resin (phr) is calculated as:

$$\begin{aligned} \text{equivalent weight of amine} &= \frac{\text{amine MW}}{n^\circ \text{ of active H atoms}} \\ \text{equivalent weight of epoxy resin} &= \frac{\text{epoxy resin MW}}{n^\circ \text{ of epoxy groups}} \\ \text{phr} &= \frac{\text{equivalent weight of amine}}{\text{equivalent weight of epoxy resin}} \cdot 100 \end{aligned}$$

To sum up, the molecular weight of the DGEBA epoxy resin is 340.41 *g/mol* (with 2 epoxy groups), while, for what concerns 4-AFD as curing agent for the dynamic network, its molecular weight is 248.37 *g/mol* (with 4 active hydrogen atoms). Thus, *phr* value is the following:

$$\text{phr}_{DGEBA/4-AFD} = \frac{\frac{248.37}{4} \text{ g/mol}}{\frac{340.41}{2} \text{ g/mol}} \cdot 100 = 36.48\%$$

This finally means that, for every 100 *g* of DGEBA resin, 36.48 *g* of 4-AFD are needed. It is important to say that the expensiveness of the hardener carried weight on the choice of panel (and consequently the DCB specimens) dimensions. Indeed, for every panel three specimens dimensionally smaller than ASTM Standard (but still suitable to perform DCB tests) were obtained.

### 3.5.4 Composite mass calculations

To design the composite panel from which DCB specimens will be obtained, in addition to the stoichiometric resin/hardener ratio calculated above, we considered that:

- The density of the composite matrix (DGEBA and 4-AFD) is 1.2 *g/cm<sup>3</sup>*;
- From HexForce® data sheet, woven glass fabric occupies 55% of the epoxy laminate total volume and is 0.23 *mm* thick;
- With reference to ASTM D 5528-01 and previous thesis works [5] [53] [54], we chose to design a 6-ply panel with the dimensions: 150 *mm* x 80 *mm*, where singular ply thickness was 0.25 *mm*.

From given measurements, 1-ply laminate total volume will be:

$$V_{PLY} = b \cdot L \cdot th \text{ [mm}^3\text{]}$$

where  $b$ ,  $L$  and  $th$  are respectively the width, the length and the thickness of the ply. Then the rule of mixtures is applied as follows:

$$f = \frac{V_F}{V_M + V_F}$$

where  $f$  is the fibres volume fraction, which is known from data sheet, and  $V_M$  and  $V_F$  are respectively the volume occupied by matrix and reinforcement. Consequently (still considering only 1 ply):

$$V_M = V_{PLY} \cdot (1 - f)$$

$$V_F = V_{PLY} \cdot f$$

So, the matrix total mass for an  $n$ -plies laminate is given by:

$$M_{M,TOT} = nV_M\rho_M$$

with  $n = 6$  in this case. Finally, by considering that the ratio between DGEBA and 4-AFD is 100:36.48, the total mass for the realization of the 6-plies laminate is subdivided as:

$$M_{DGEBA,TOT} = M_{M,TOT} \cdot \frac{100}{136.48}$$

$$M_{4-AFD,TOT} = M_{M,TOT} \cdot \frac{36.48}{136.48}$$

Then, an increase of +15% in DGEBA e 4-AFD masses has been considered for future resin leakage during the curing and post-curing phases. Reformulating the rule of mixtures, theoretical density can be calculated. Rule of mixtures is generally applied in materials science, especially in the composites field, since it theoretically delimits the values of properties such as the elastic modulus or the density. It consists on a volume-weighted mean which considers both the properties of the matrix and the fibres. In the present case, the rule can be described as:

$$\rho_{CTH} = \rho_F \cdot f + \rho_M(1 - f)$$

The resultant value will be later compared to the measured density value, so to assess the presence of voids within the material.

### 3.5.5 Laminate mould design requirements

Before understanding how the mould has been realized, it is fundamental to illustrate some technological aspects related to the production phase of the panel and the incorporation of optical fibres, as attempted for the first laminate. As, previously said, the main phases are the hand lay-up lamination and the curing/post-curing cycles. Here is a list of the obstacles we ran into during this part of the manufacturing process:

- Limit the generation of air bubbles both during prepolymer-hardener mixing and during impregnation, mainly to assure a good degree of compaction between layers;
- Minimize inclusions of undesired materials due to the limits in the accuracy of hand cleaning of surfaces and various tools used in laboratory;
- Keep the panel thickness constant, as the leakage of resin from the mould edges did not guarantee a complete uniformity of the resin layer for the entire panel area;
- Preserve the correct texture of dry fabrics during the application of the resin, avoiding damages, twisting or wrinkling;
- Achieve a correct and homogeneous impregnation of the fibres, as hand lay-up necessarily generates wetter or drier areas of the panel;
- Limit the intrusiveness of optical fibres incorporated in the composite laminate, so that they do not bring additional embrittlement or unwanted cracks onset points;
- Protect optical fibres from resin leakage at the exit points of the laminate, and from temperature and pressure levels employed during the curing phase and processing;
- Insert the optical fibres inside the laminate, due to its reduced thickness. It had been taken into account that our laminate would have been about 1.5 *mm* thick, but the optical fibres, incorporated between the fourth and fifth lamina, would have been at a height of about 1 *mm* from the surface of the lower plate of the mould. This entailed the need to raise the entire panel in order to allow the holes in the lateral short dams of the mould to accommodate the optical fibres. This point will be better explained further on.

Then, post evaluations on the realization of the first panel have suggested that there was a substantial resin leakage, thus representing a non-negligible waste of material due to the high cost of the hardener. In order to reduce this loss, the gaps left between the mould and the lateral dams were sealed with plasticine stripes of size 80 *mm* x 7.5 *mm* x 3 *mm* before the realization of the second panel. Moreover, two components of the mould were downsized to the same length as the produced composite to allow a better positioning of the containing rubber.

### 3.5.6 Mould components

The mould was realized with the main purpose of limiting material waste and assuring homogeneity and uniformity of the final composite panel. 7000 Class aluminium purchased from Migliari Alluminio S.r.l was used to realize the various components. The aluminium mould designed to process the whole laminate is constituted by the pieces listed in Table 3 (CAD two-dimensional representations reported in Appendix 6.3).

Component	Dimensions [mm]	Details
lower plate	200 x 310 x 10	it hosts the side dams and the base on it
stamp	155 <sup>(*)</sup> x 80 x 10	it closes the mould with pressure application
base	155 <sup>(*)</sup> x 80 x 2	it is the part onto the composite is laminated
short-side L-shaped dams (2)	150 x 25	they have holes for bolts fixing and smaller holes for fibres hosting
long-side L-shaped dams (2)	155 x 25	they only have holes for bolts fixing

Table 3: Aluminium mould components for composite panel realization.

The lengths of the base and stamp were reduced to 150 mm for the realization of the second panel.

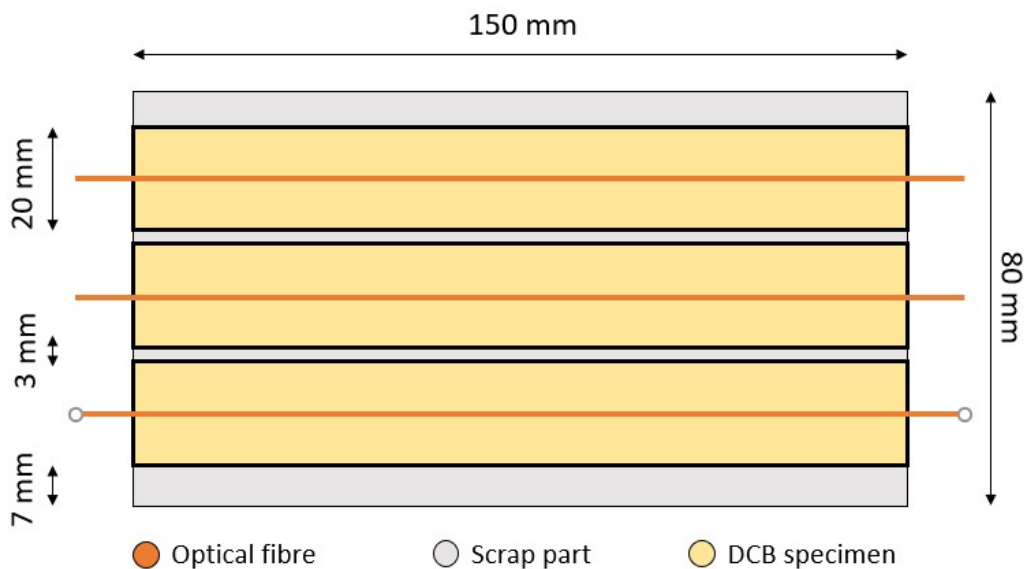


Figure 36: Technical sketch (top view) of the panel and the resulting DCB specimens.



From the open mould schematized above (Figure 36) we can recognize:

- Three DCB specimens of dimensions  $20\text{ mm} \times 150\text{ mm}$ ;
- Two lateral scrap parts of  $7\text{ mm} \times 150\text{ mm}$ ;
- Two inner scrap parts of  $3\text{ mm} \times 150\text{ mm}$ .

While the inner scrap parts help in sample cutting, the lateral ones have been designed to assure that no scotch tape is found inside the specimen and to reduce the edges damage. The scheme in Figure 36 is feasible for both the first and the second panel, even if, as we mentioned before, optical fibres were inserted only in the first one to test their incorporation and adaptability inside the composite material. Despite this, we will discuss later in Par. 3.6 the fact that all the specimens from the first panel encountered various obstacles during DCB testing, and for this reason we designed a second composite panel to solve every processing problem in view of the mechanical assessment. Indeed, the setting up of a valid and correct design phase has been a primary concern of ours with respect to the embedment of optical fibres. Regarding the thickness of the derived composite panel, various measurements have been taken throughout the specimen surface and statistically it came out that the mean value was  $1.5\text{ mm}$ .

### 3.5.7 Mould treatment

Every piece was produced and assembled in Politecnico di Milano DAER building. A preparatory treatment was given to the assembly by applying a holes-filling product (2 layers, interval of 15 – 20 *minutes*) and a release agent (6 layers, interval of 15 – 20 *minutes*), 24 hours before lamination process.

- Marbocote® RS415 ECO is designed as a mould sealer for glass reinforced polyester (GRP), vinyl ester, epoxy or metal moulds. The resin both seals micro-porosity and fills minor scratches on the mould surface;
- Marbocote® 75 ECO is an advanced polymeric resin in a non-chlorinated organic solvent blend which is designed to release epoxy, polyester, vinyl ester, phenolic and other thermosetting resins. It provides a durable film capable of giving many releases per application and will not contaminate the released surface.

Some small strips of plasticine (for the second panel only) have been prepared in order to fill the residual volume provided by the mould.



*Figure 37: Overview of the components of the aluminium mould.*

### 3.6 REALIZATION OF THE FIRST COMPOSITE PANEL

Regarding the production of the first composite panel, we proceeded in pre-treating the aluminium mould as discussed in Par. 3.5.7 and cutting the dry fabric to size (as seen in Par. 3.5.2). Then, the dynamic network has been prepared by mixing the suitable quantities of resin and hardener (increase by 10 – 15% to deal with human error and processing losses) and heating the mixture at 70 – 80°C with a VELP Scientifica ARE magnetic stirrer. The temperature is set in order to make the resin more viscous and let it properly mix with the hardener. The dynamic epoxy was then poured directly into the previously designed aluminium mould and manually laid up over each of the 6 E-glass plies using a regular metallic spatula to enhance resin distribution over fibre fabric. This manual process must be as slow and accurate as possible to minimize the formation of voids in the resin, which badly affect the final laminate processing and properties.

After the 3<sup>rd</sup> ply (at half the thickness), a Teflon® (PTFE) layer of dimensions 50 mm x 80 mm has been placed as crack initiator, as recommended in ASTM standard. Moreover, three optical fibres have been inserted between the 4<sup>th</sup> and the 5<sup>th</sup> plies in order to longitudinally cross the whole laminate. Each of them was then wrapped in a 45°-cut protecting shell. This peculiar incision is necessary to simplify the application of a second transparent commercial bi-component PATTEX® epoxy at the optical fibre exit point, aimed at filling the space between fibre and shell. Indeed, this commercial epoxy is workable only for 5 minutes and its consequent solidification (with no expansion/shrinkage) prevents our DGEBA dynamic resin to enter the shell during the curing/post-curing process. The protecting shells were inserted in each hole of the lateral dams, making sure they entered the laminate for about 1 cm, by keeping them in tension and slightly adherent to the underlying ply. A sketch of the panel set up is shown below in Figure 38.

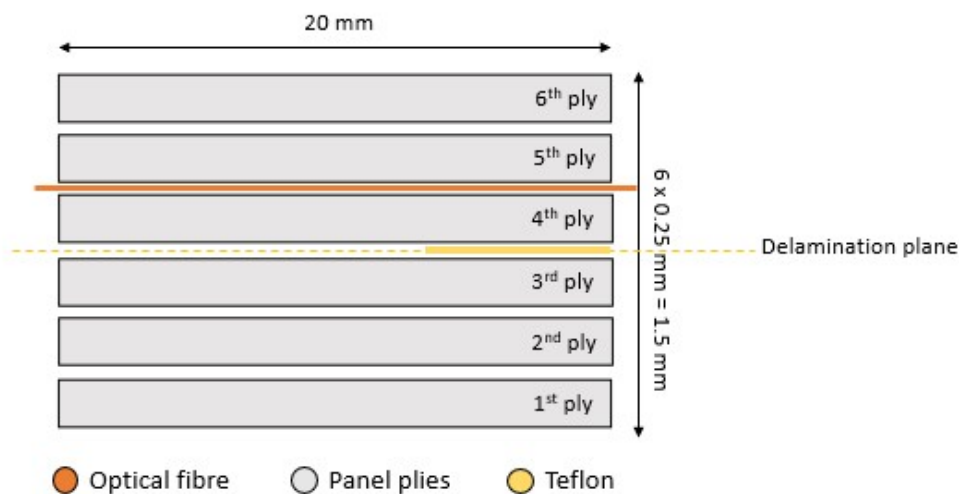
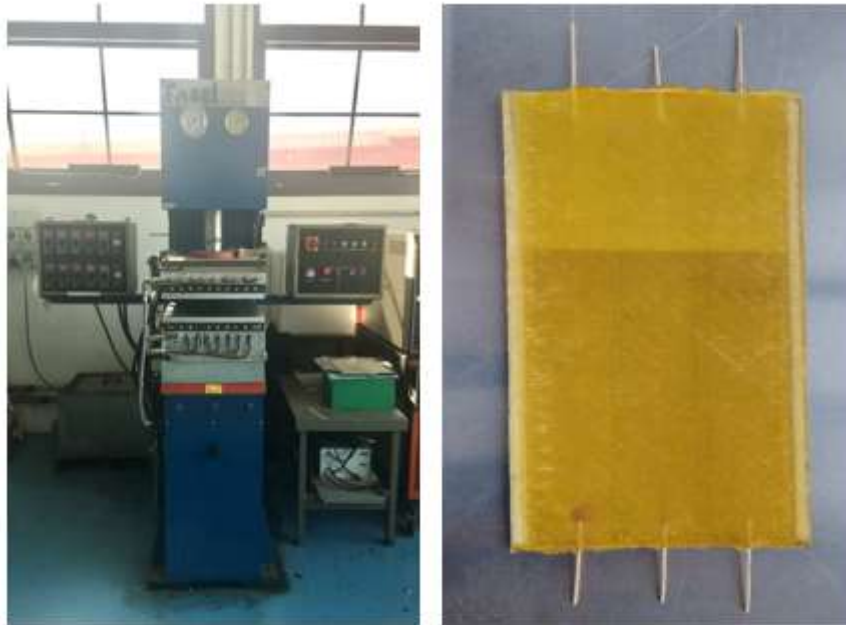


Figure 38: Sketch (lateral view) of the panel, stressing out the position of fibres and Teflon.

Finally, the stamp was closed and positioned in the FASEL Hot Press from Aermacchi S.p.A., so that the resin could undergo curing ( $120^{\circ}\text{C}$  for  $2\text{ h}$ ) and then post-curing ( $150^{\circ}\text{C}$  for  $2\text{ h}$ ) with a minimum pressure up to  $P = 2\text{ bar}$ . Once cooled down to room temperature, the mould has been removed from the press as show below in Figure 39, then opened to extract the first produced panel.



*Figure 39: Hot Press used for curing and post-curing cycles (on the left) and the first produced composite panel with incorporated optical fibres.*

### **3.6.1 Samples preparation for SEM analysis**

As this is a first attempt to employ this dynamic epoxy resin in the contest of FRPCs, it has been considered appropriate to implement a SEM analysis. Indeed, there is almost little knowledge on the resin behaviour in fibre-reinforced composites, especially for what concerns fibres impregnation. Moreover, as hand lay-up impregnation cannot be extremely precise, it has been crucial to understand the efficiency and the overall quality of the results regarding the possible presence of voids, defects or internal breaks.

A third reason for the need of a SEM analysis deeply regards the integrity of the embedded optical fibres. Definitely, it is fundamental to understand if the fibres are damaged at the entrance and exit points of the laminate, and along the entire panel. In detail, a small darker spot in correspondence of the optical fibre protective shell has been detected as the only visible point of non-homogeneity in the first produced panel (present near all the six protective shells, but only this has a non-negligible dimension).

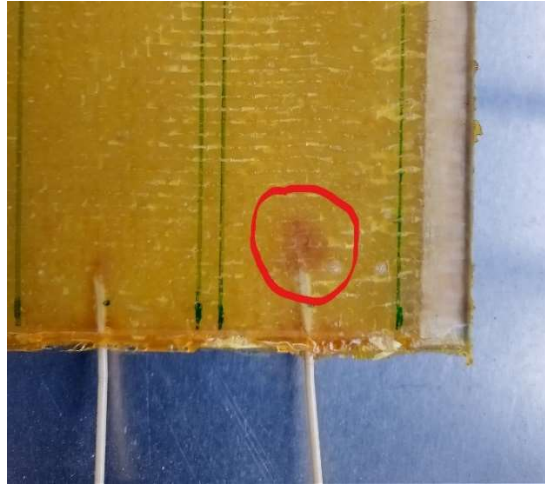


Figure 40: Darker spot detected on the first panel.

The specimen's choice for SEM analysis is schematized below (Figure 41) with the following criteria:

- P1, P2, P3 were chosen to be suitable also for density tests. A special mention has to be done for P3 specimen, which has been chosen because a detachment was observed between the 3<sup>rd</sup> and 4<sup>th</sup> plies, extended for near half of the length. This gap is probably due to the scotch tape left after the cutting phase. As seen in the Figure 41, they have been cut out from a lateral scrap part of the panel;

	<b>P1</b>	<b>P2</b>	<b>P3</b>
<b>Length [mm]</b>	39	40	39
<b>Width [mm]</b>	6	5	5
<b>Thickness [mm]</b>	1	1	1

Table 4: SEM specimens dimensions (P1, P2, P3).

- P4 was chosen to observe the resin darker (orange) spot, probably due to a leakage of the sealing commercial resin. Consequently, P5 was chosen to compare the side with the darker spot and the side where only the DGEBA epoxy resin is present. P6 choice is justified by the fact that the optical fibre is here clearly visible, and any fracture detection can be important if compared to areas where optical fibres are absent. Both sides of P5 and P6 specimens have been investigated. These specimens have been cut out from one of the future DCB samples, so only two were then available for the mechanical assessment.

	<b>P4</b>	<b>P5</b>	<b>P6</b>
<b>Length [mm]</b>	20	20	20
<b>Width [mm]</b>	11	5	10
<b>Thickness [mm]</b>	1	1	1

Table 5: SEM specimens dimensions (P4, P5, P6).

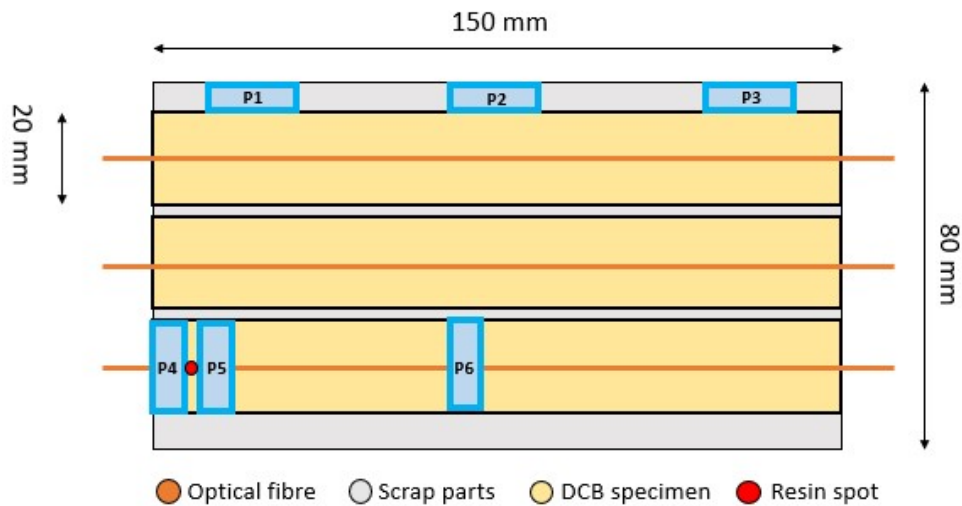


Figure 41: Overview of the SEM specimens choice with respect to the position inside the panel.

As mentioned before, different grain sandpapers (P320, P600, P1200 from the largest to the finest grain) have been used to lap up the specimens' surface, while diamond paste was not taken into consideration due to matrix softness and the reduced dimensions of the panel. Images of the technique and resulting lapped specimens are provided below. To conclude, the specimens have been covered with a thin layer of conductive silver-coloured adhesive tape in order to slowly acquire electric charge, then they were mounted on the microscope support to start the analysis.



Figure 42: Lapping of SEM specimens.



Figure 43: Comparison between a non-lapped specimen (left) with a lapped one (right).

### 3.6.2 Samples preparation for density test

Once the SEM analysis has been terminated, we chose P1, P2 and P3 samples to perform a density test. A preliminary cleaning has been done for 10 minutes by means of an ultrasonic bath: they were placed in a glass container and placed in water inside the bowl of Branson 2210 Tecnovetro machine, finally they were left in distilled water for few minutes to complete the preparation before the test. A picture of the specimens cleaning phase is shown below.



*Figure 44: SEM specimens (P1, P2, P3) plunged in ultrasonic bath.*

Then, every specimen was poured inside a beaker full of water and weighed following the Archimedes' principle and theoretical and practical aspects explained in Par. 3.3.2 and 3.3.3.

### 3.6.3 Samples preparation for DCB tests

As anticipated before, the obtained panel has a thickness of at least  $th = 1.5 \text{ mm}$ . This value does not fulfil the dimensional requirements of DCB ASTM standard stressed out in Par. 3.4.2 and, if tested with no external reinforcement, it would inevitably break when mechanically loaded. For this reason, six stiffening plates of dimensions  $20 \text{ mm} \times 150 \text{ mm}$  were cut from an Ergal 7000 aluminium panel (Al 7075) purchased from Migliari Alluminio S.r.l., with following sandblasting and acetone cleaning. For what concerns the determination of the thickness of Ergal stiffening plates, two fundamental mechanical hypotheses have to be concurrently verified:

- Ergal aluminium must not yield, so the plates behaviour cannot deviate from the elastic field;
- A rigid opening of the specimen must be guaranteed, so as to limit excessive rotation at the crack tip.

According to ASTM D 5528-01 standard, the interlaminar fracture toughness can be predicted as:

$$G_I = \frac{12(P \cdot a)^2}{Eb^2h^3}$$

where  $b$  is the specimen length,  $a$  is the delamination length,  $h$  is half of the specimen thickness,  $E$  is the Young's modulus and  $P$  the applied load. A bending moment acts on the specimen and it is equal to:

$$M_f = P \cdot a = \sqrt{\frac{G_I E b^2 h^3}{12}}$$

If we consider the mid-plane of the panel as the one hosting delamination phenomena, the problem can be considered as symmetric and consequently the maximum bending moment at the specimen average thickness (after three plies) can be evaluated as:

$$M_{f,MAX} = \sqrt{\frac{G_I E b^2 (h/2)^3}{12}}$$

This generates a maximum stress component distribution equal to:

$$\sigma_{MAX} = \frac{M_f \cdot h_{MAX}}{2I} = \frac{6M_f}{bh^2}$$

where  $I$  is called moment of inertia of the section and is defined as:

$$I = \frac{bh^3}{12}$$

In conclusion, the condition to be satisfied for the plate not to yield is:

$$\sigma_{MAX} < \sigma_{yielding, Al}$$



which means to impose a limit on the aluminium thickness equal to:

$$h > \sqrt{\frac{6M_f}{b\sigma_{yielding, Al}}}$$

In the case of this thesis work, the following data have been considered:

Al 7075 Young Modulus [ <b>MPa</b> ]	<b><i>E</i></b>	<b><math>7 \cdot 10^4</math></b>
Al 7075 Yielding Stress [ <b>MPa</b> ]	<b><math>\sigma_{yielding, Al}</math></b>	<b>400</b>
Interlaminar Fracture Toughness [53] [ <b>N/mm</b> ]	<b><math>G_I</math></b>	<b>3</b>
Half-thickness [ <b>mm</b> ]	<b><math>h/2</math></b>	<b>0.75</b>
Width [ <b>mm</b> ]	<b><math>b</math></b>	<b>20</b>

Table 6: Data considered for the realization of the Ergal stiffening plates.

So, it turned out that:

Bending moment [ <b>N · mm</b> ]	<b><math>M_f</math></b>	<b>607.58</b>
Al 7075 thickness [ <b>mm</b> ]	<b><math>h</math></b>	<b>&gt; 0.675</b>

Table 7: Results obtained according to ASTM D 5528-01.

With these results, we initially considered an aluminium thickness  $h \approx 1 \text{ mm}$ . As  $h$  is the average thickness and the problem has considered by symmetry only half of the specimen, the obtained result should be doubled ( $h \approx 2 \text{ mm}$ ). The value of  $G_I$  found in literature and previous thesis works [53] turned out to be an uncertain data, for this reason we considered a suitable value of  $h = 3 \text{ mm}$  for Ergal plates thickness in order to match the previously mentioned requirements. In particular,  $3 \text{ mm}$  thick Ergal was used for the first panel while the specimens from the second panel were created with a  $5 \text{ mm}$  thick Ergal stiffening.

Regarding the first panel, the Ergal plates have been sandblasted and cleaned with acetone (Figure 45a), then the Ergal-composite sandwich was created by applying 3M™ Scotch-Weld™ Structural Adhesive Film AF 163-2 on the surface (Figure 45b). As this material is a matrix, complete adhesion occurs only upon heating, so the film was applied with the help of a hairdryer. Finally, the whole pack was covered with insulating adhesive tape to limit material waste (Figure 45c); indeed, an excess of structural adhesive can contaminate the specimens and can laterally glue the Ergal plates, thus vanishing any attempt of a correct DCB test because any output data would not concern only the epoxy resin inside the composite, but a mixture of different involved materials.

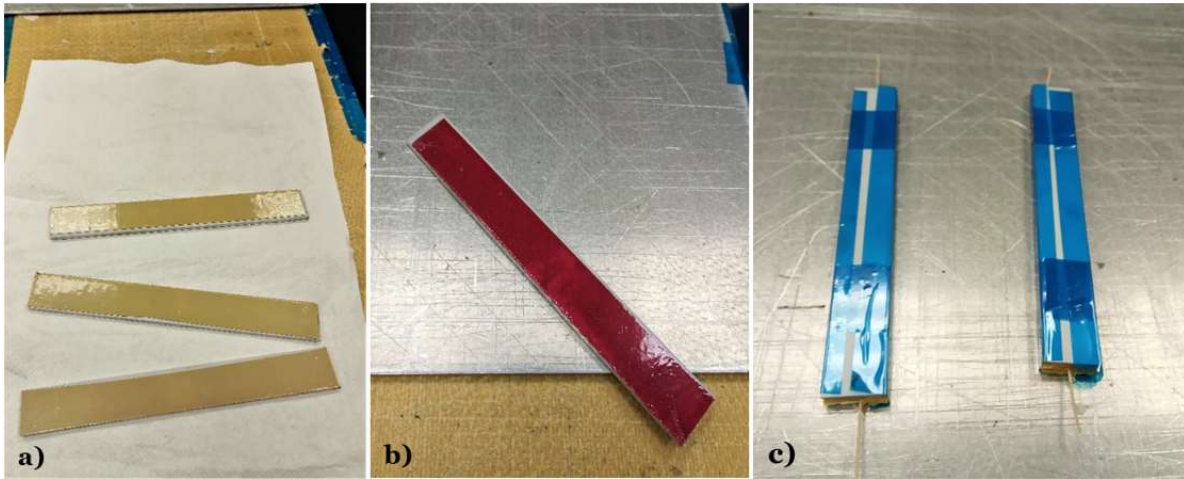


Figure 45: DCB specimens preparation: a) sandblasting and cleaning, b) structural adhesive application, c) assembled tapered specimens.

The specimens have been put in press for one hour at  $125^{\circ}\text{C}$  with a light pressure applied, as the only need was to keep the pieces together during AF163 crosslinking phase. After the extraction, the adhesive tape has been removed, but a substantial structural adhesive leakage has been detected. Therefore, all the edges of the future DCB specimens were trimmed to eliminate any kind of contamination. At this point, the external surface of the Ergal plates was carefully cleaned with acetone in order to correctly apply the hinges required for the DCB test: in this respect, Araldite 2015 from Huntsman® was applied and specimens have been secured in the vise and kept at rest for 24h to allow cross-linking. The last step was the application of a white powder developer (SKD S-2 from Magnaflux Spotcheck®) needed to highlight the crack opening by marking equally spaced notches along on edge of the specimen. This will allow us to measure the crack growth in the second phase of image acquisition and DCB data processing. The final DCB specimens ready to be tested are shown below (Figure 46).

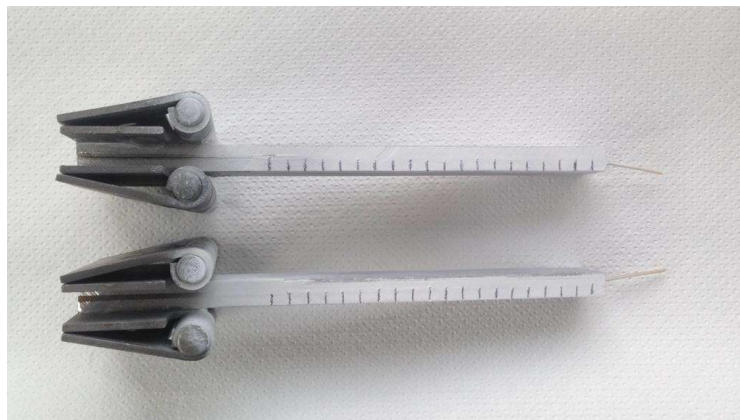


Figure 46: DCB specimens ready for mechanical testing.

As already anticipated, all the tests conducted on the specimens from the first panel were rejected and give no useful mechanical results, therefore some technological and manufacturing modifications have been designed and directly applied to a second composite panel.

### 3.7 REALIZATION OF THE SECOND COMPOSITE PANEL

The second composite panel was designed with the same hand lay-up process explained in Par. 3.5. In this case, all the technological problems faced during the realization of the first panel, which inevitably brought DCB test to failure, have been solved, thus postponing the embedment of the optical fibres inside the composite material. Moreover, two components of the mould were downsized to the same length as the produced composite (150 mm) to allow a better positioning of the containing rubber and a more suitable sealing of the mould. The production process of the second panel is schematized below for simplicity:

- The aluminium mould has been treated and assembled as explained in Par. 3.5.6; the dimensions of the base and the stamp were reduced to prevent any further resin loss.
- A 80 x 150 mm peel-ply lamina was applied before the 1<sup>st</sup> and after the 6<sup>th</sup> ply. This is a thin nylon fabric which assures the optimal laminate surface roughness needed for the bonding phase. Indeed, the smoothness of the first panel surface should probably contribute to the failure of DCB tests, and for this reason the aim of the second panel was to increase its roughness and assure an enhanced adhesion;
- Teflon® deposition has been actuated as for the first panel, but this time it was not aligned with the edges, but sticking out of the laminate to simplify pre-opening during DCB test;
- Deposition and impregnation of the laminate plies has been conducted as explained in Par. 2.3.2.2;
- As previously said, the gaps left between the mould and the lateral dams were sealed with plasticine stripes of size 80 mm x 7.5 mm x 3 mm;
- Curing and post-curing cycle have been carried out as normally.

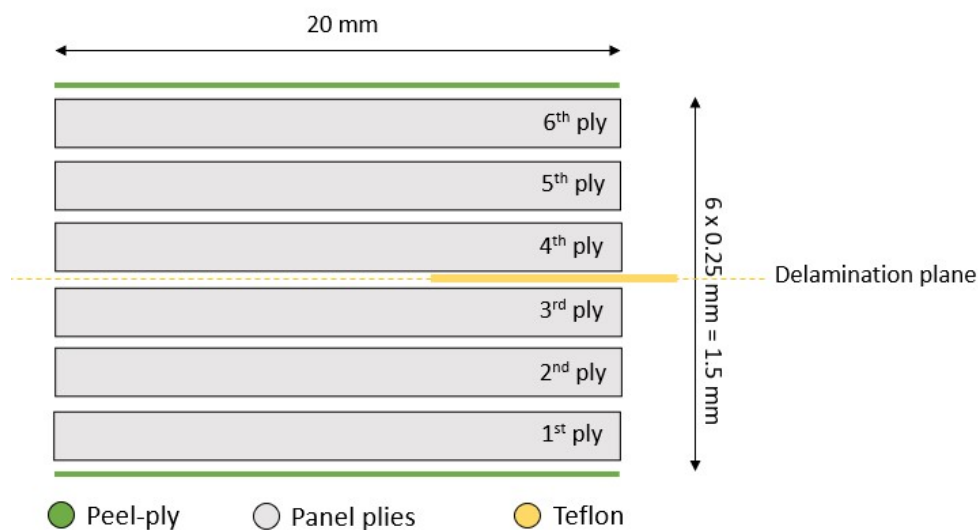


Figure 47: Sketch (lateral view) of the panel, stressing out the position of peel-ply and Teflon.

### 3.7.1 Samples preparation for DCB tests

From the second composite panel, three DCB specimens were obtained. It is important to specify that, due to the previous failure regarding the first laminate, only DCB tests were conducted on these specimens, and no attention has been paid to density tests nor SEM analysis. As mentioned before, the Ergal stiffening plates were, in this case, 5 mm thick. The following procedure has been chosen:

- Three specimens with dimensions 150 mm x 20 mm and six Ergal plates (with same dimensions) were cut;
- Peel-ply layers were removed from the specimens;
- Ergal plates have been cleaned and sandblasted;
- Four steel spacers with smoothed edges were realized to overcome the possibility to pierce the vacuum bag and to hold the specimens in their position. They have been placed between the specimens and covered with Teflon®.

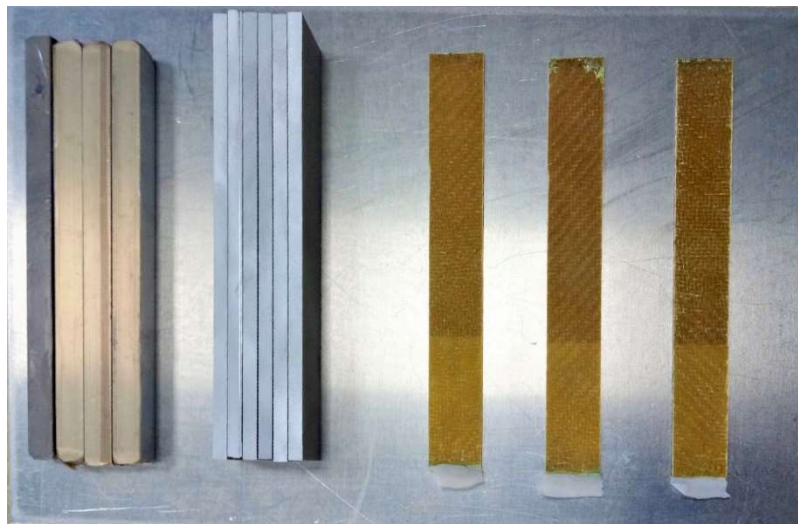


Figure 48: From left to right, steel spacers, Ergal plates and composite specimens.

Again, the Ergal-composite sandwich was created by applying structural adhesive and insulating adhesive tape as described in Par. 3.6.3; this is shown in Figure 48a below. Once the whole packing was ready (Figure 48b), two thermocouples were connected to control the temperature in the autoclave and finally the vacuum bag was closed and air sucked (Figure 48c) as explained in literature. The previous activities were strictly performed inside the clean room in D.A.E.R at Politecnico di Milano, which is a clean room of class 1000 (the air dustiness level is maintained within a thousand particulates for every cubic metre) provided with a double-entry system to prevent any type of contamination. To assure a controlled polymerization of the structural adhesive film and to avoid the obstacles encountered with the hot press, the autoclave technology has been adopted.

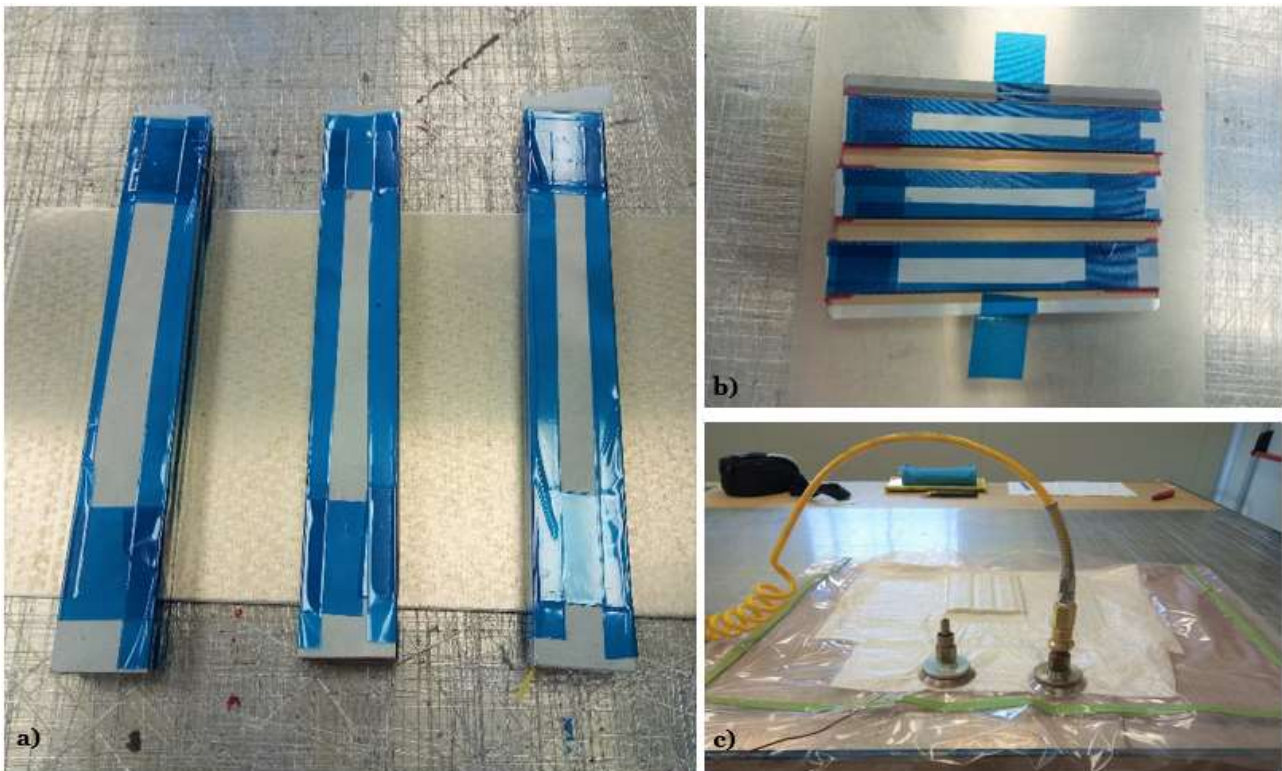


Figure 49: DCB specimens' preparation: a) assembled tapered specimens, b) pack creation for vacuum bag, c) closed vacuum bag and air sucking.

### 3.7.2 Autoclave thermal cycle

The autoclave in D.A.E.R department of Politecnico di Milano has a quick-acting carbon steel cylindrical chamber, provided with horizontal axis. Its exercise pressure is 15 bar, while the maximum temperature is 450°C, with a maximum gradient of 10°C/min. The tank is divided into two main blocks: the first is represented by the chamber, compressors and service/auxiliary systems. The second block is mainly the electrical control panel which manages the whole system by setting the desired cycle and by regulating the parameters.



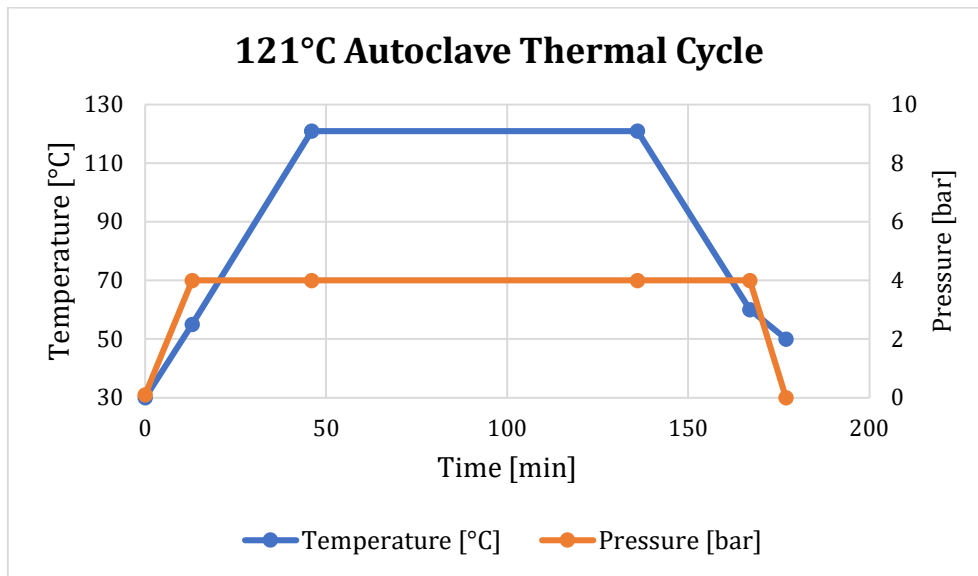
Figure 50: Autoclave supplied by DAER laboratory.

The curing cycles for epoxy resins are generally given by the material manufacturer, and the table below shows the 121°C-cycle used for this thesis work.

	<b>1</b>	<b>2</b>	<b>3</b>	<b>4</b>	<b>5</b>	<b>6</b>
<b>Temperature [°C]</b>	30	55	121	121	60	50
<b>Pressure [bar]</b>	0.1	4.0	4.0	4.0	4.0	0.0
<b>Vacuum</b>	-1	-1	-1	-1	-1	0
<b>Time [min]</b>	/	13	33	90	31	10
<b>Rate [°C/min]</b>		+2	+2	/	-2	-1

Table 8: 121°C-cycle used for the adhesion of Ergal stiffening plates.

A graph of the autoclave cycle is here showed for sake of completeness.



Graph 1: Autoclave cycle with temperature and pressure variation in time.

### 3.7.3 Specimens treatment and hinges adhesion

After performing thermal treatment in autoclave, the vacuum bag was opened, and the three specimens were trimmed to avoid bridge effects by adhesive AF-163. Ergal external surfaces were deeply cleaned to eventually remove all the possible resin/material residuals from previous manufacturing, then sandblasted and cleaned with compressed air. Moreover, they were rubbed with P-60 sandpaper and degreased with acetone. The unwanted leakage of AF-163 adhesive has been reduced with respect to the first composite panel.

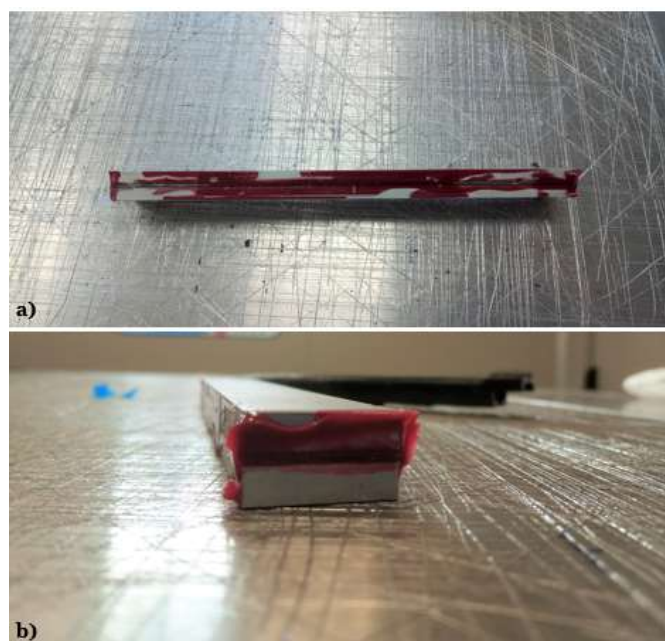


Figure 51: AF163 adhesive leakage from DCB specimen.

### 3.7.4 Resolution of technological issues: DCB hinges endurance

In this case, more attention was paid due to the technological obstacles encountered during the production of the first panel, for which the interface between the composite and aluminium has collapsed. The three new DCB specimens from the second panel were firstly tested at the MTS machine, demonstrating an improved adhesion between composite and Ergal, but at this time the interface between the hinges and stiffening Ergal has given up. This inconvenience has immediately been linked to the possibility of formation of an oxide layer on Ergal surface, which necessarily affect roughness and adhesion.

For this reason, a more careful check on their endurance was performed to assure the complete integrity of the specimens for the mechanical assessment. In this connection, two preparation methods were tested to assure a correct bonding degree: the first based on sandblasting and sandpaper, while the second one on surface sandblasting only, as schematized below.

<b>1<sup>st</sup> METHOD: SANDBLASTING AND SANDPAPER</b>		
	<b>Hinges surface</b>	<b>Ergal aluminium surface</b>
1	deep cleaning in acetone bath	remove remains from previous processes
2	remove remains from previous processes	sandblasting
3	sandblasting with a sandblaster	remains removal and 2 <sup>nd</sup> sandblasting
4	remains removal and 2 <sup>nd</sup> sandblasting	tide up with compressed air
5	tide up with compressed air	rub with P-60 sandpaper
6	rub with P-60 sandpaper	tide up with compress air
7	tide up with compress air	degrease with acetone
8	degrease with acetone	apply a uniform layer of bicomponent adhesive on the interested area
9	apply a uniform layer of bicomponent adhesive on the interested area	/

Table 9: First adopted preparation method for the second panel.

<b>2<sup>nd</sup> METHOD: SANDBLASTING</b>		
	<b>HINGES SURFACE</b>	<b>ERGAL ALUMINUM SURFACE</b>
1	Repeat from 1 to 5	Repeat from 1 to 4
2	<b>NO rubbing with P-60 sandpaper after sandblasting</b>	
3	Repeat from 7 to 9	Repeat from 6 to 8

Table 10: Second adopted preparation method for the second panel.



Again, the adhesive, namely bicomponent 3M™ Scotch-Weld™ Epoxy Adhesive DP460, was applied on both surfaces of every of specimen, glued in between the hinges. It is important to slowly mix the bi-component adhesive to prevent the formation of air bubbles. Once the specimen and hinges have been put in contact, they were secured in the vice for at least 24h, with detailed attention on what concerns the orthogonality between the aligned hinges and the vertical axis of the specimen. As last pre-treatment step, one side of the specimen was sprayed with white water paint and notches have been marked every 0.5/1 cm from the end of PTFE layer.

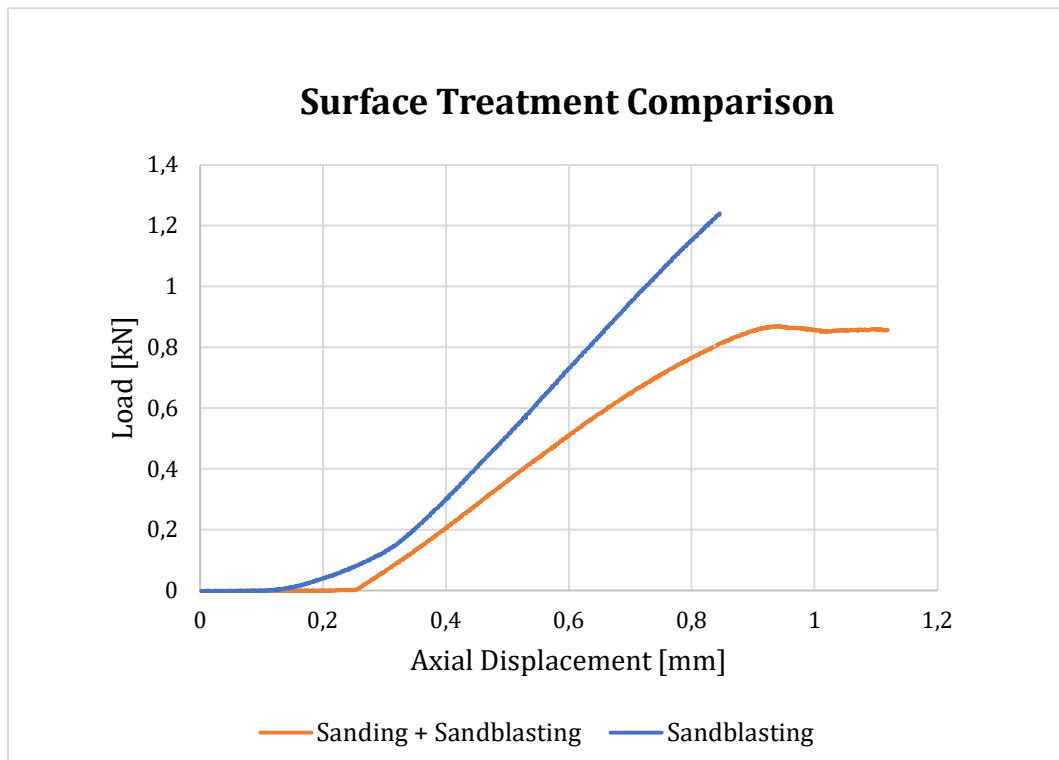


*Figure 52: Assembled DCB specimen secured in the vice.*

It was found out, thanks to a preliminary rough DCB test, that sandblasted Ergal withstand a load above 1200 N, while the sanded one barely bore 900 N ( $\approx 870$  N). The comparison between the loading curves for the two methods can be seen in the chart below.



*Figure 53: Preliminary DCB test to verify the surface treatments adopted for the second panel.*



Graph 2: DCB attempt test for surface treatment comparison.

For this reason, to prevent the possibility of detachment between specimen and hinges, it was preferred to utilise only sanding (the 2<sup>nd</sup> method) as a pre-treatment over aluminium surfaces before performing DCB tests. Indeed, the first method including sandpaper created deep scratches in the specimens, which necessarily required a greater amount of adhesive to reach the same adhesion level. In this regard, it is essential to secure the specimens immediately after sandblasting as, in this way, aluminium surface has no time to oxidize. Moreover, to prevent eventual remains or dust from affecting the delaminated area, the specimens have been covered with adhesive tape on their perimeter before sandblasting, and the protection has been removed after it.

### 3.8 HEALING CYCLE ON DCB SPECIMEN

The repairing phase was performed after DCB tests on the three specimens obtained from the second composite panel, bearing in mind that this represents a first attempt to study and characterize the healing ability of this epoxy resin in a fibre-reinforced composite. For this reason, only the first specimen (P1) was tested by undergoing the following temperature/pressure cycle in the hot press (Table 11).

Phase	Initial Temperature [°C]	Final Temperature [°C]	Pressure [bar]
Heating	25	200	4
Repair	200°C for 10 minutes		4
Cooling	200	25	4

Table 11: Healing cycle performed on P1 DCB specimen.

Once again, much effort has been invested to guarantee:

- A homogeneous heating at the interface where the PTFE sheet was inserted, in order to let the entire epoxy resin self-heal across the entire surface area;
- Constant pressing to the specimen from the very beginning to avoid the oxidation of the cracked surface.

The pressure has been calculated on the basis of the specimen area, considering that the metallic hinges needed for the DCB test were left attached to it. An external thermocouple directly connected to the specimen mid-plane has been employed to fulfil the first point.

Once the interlaminar fracture toughness values were obtained, the mechanical assessment has concluded with the calculation of the relative error:

$$\Delta G_I = \left( \frac{\Delta G_{I,pristine} - \Delta G_{I,repared}}{\Delta G_{I,pristine}} \right) \cdot 100$$

to investigate the deterioration of the specimen characteristics after the second DCB test. The same has been performed for every  $G_{IC}$  obtained with the mentioned critical points (Par. 3.4.4).

## 4 EXPERIMENTAL RESULTS

### 4.1 FIRST COMPOSITE PANEL

#### 4.1.1 Masses calculation

With mention to Par. 3.5.4 and by considering the DGEBA:4-AFD ratio found before, the masses for the realization of the first composite panel were obtained with the following results (also considering a +15% on the total amount of material due to future manufacturing losses).

		1 ply	6 plies	+15% losses
<b>Total volume</b> [ $mm^3$ ]	$V_{PLY}$	3000	18000	/
<b>Fibres volume</b> [ $mm^3$ ]	$V_F$	1650	9900	/
<b>Matrix volume</b> [ $mm^3$ ]	$V_M$	1350	8100	/
<b>Matrix mass</b> [g]	$M_{M,TOT}$	1.620	9.720	11.180
<b>Resin mass</b> [g]	$M_{DGEBA,TOT}$	1.187	7.122	8.190
<b>Hardener mass</b> [g]	$M_{4-AFD,TOT}$	0.433	2.598	2.990

Table 12: Results from composite mass calculations.

The values contained in the last column (+15% losses) have been used to create the first composite panel and here below they are compared with the real amount of materials used.

		+15% losses	Experimental amount
<b>Matrix total mass</b> [g]	$M_{M,TOT}$	11.180	11.255
<b>Resin total mass</b> [g]	$M_{DGEBA,TOT}$	8.190	8.250
<b>Hardener total mass</b> [g]	$M_{4-AFD,TOT}$	2.990	3.005

Table 13: Comparison between theoretical and experimental results.

After the curing and post-curing cycles, the panel has been extracted from the aluminium mould and the leaked cross-linked resin was collected and weighted, thus obtaining a value of  $M_{M,LEAKED} = 3.340$  g. This means that the actual loss of resin for what concerns the first panel equals to:

$$LOSS: \frac{M_{M,LEAKED}}{M_{M,TOT}} \% = \frac{3.340}{11.255} \cdot 100 = 29.68 \% \cong 30 \%$$

The first produced panel was visually homogeneous, taking into account the questionable reliability of the hand lay-up process. The loss of about a third of the total resin mass has expressed several doubts on the materials quantity needed. Initially it was envisaged to re-organize the mass calculation based on seven plies (as the last ply had little scarce resin with respect to the others) or to consider a bigger % error, but the substantial resin loss moved the concept of reducing the mould dimensions and to employ some plasticine strips to contain the material leakage (Par. 3.7).

#### 4.1.2 DSC analysis

DSC results are here obtained from the analysis of the normalized heat flow – temperature curve, where it is possible to observe two different runs of the same heating-cooling cycle (Par. 3.1). We have seen that the DSC cure of epoxy resin is characterized by a broad exothermic peak, and with increasing heating rate the height of the exotherm increases as well.

As discussed previously,  $T_g$  is actually a temperature range, rather than a specific temperature, but the convention, however, is to report a single temperature defined as the midpoint of the temperature range, bounded by the tangents to the two regions before and after the sudden decrease in heat flow. This process is manually done with TA Instruments TRIOS software, by roughly choosing the initial and the final value of the temperature range. In some cases, it is possible that the first thermal cycle interferes due to some DSC chamber vibrations, by causing an incorrect transition or by eliminating it. Where it has been shown that this effect is present, the first thermal cycle (1<sup>st</sup> Run) is not taken into consideration in order to obtain reliable temperature readings. Moreover, as the choice of the temperature range is purely manual, a certain degree of dispersion in the results is unavoidable.

For this reason, the glass transition temperature was estimated with the second heating cycle applied to the sample pan as the midpoint temperature related to the curve tangent, as depicted in Figure 54 and Figure 55. As the only 2<sup>nd</sup> scan is concerned, no residual exothermic peak was found as a proof that complete curing has been achieved for the epoxy system. A preliminary DSC analysis was conducted on a specimen ( $m = 13\text{ mg}$ ) of totally cross-linked dynamic resin to verify the glass transition temperature ( $T_g$ ) obtained in the previous thesis work [6].

A section of the heating/cooling cycle showing the  $T_g$  is shown in here below.

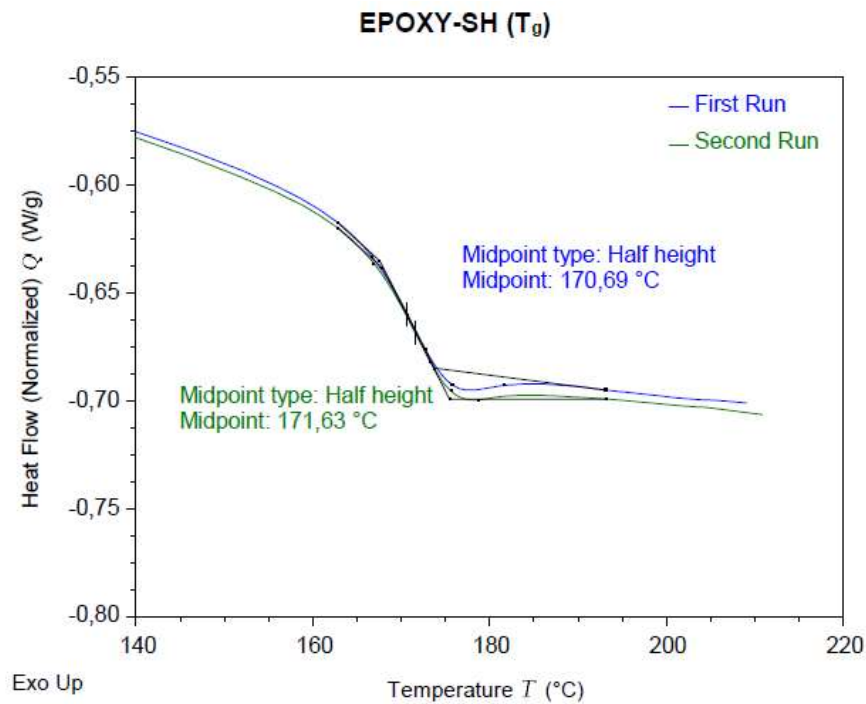


Figure 54: DSC analysis on preliminary dynamic resin, before the realization of the composite panel.

In a second moment, a scrap of leaked dynamic resin ( $m = 13 \text{ mg}$ ) from the first composite panel has been analysed again. As discussed before, a reliable proof of possible chamber vibrations during the 1<sup>st</sup> scan is observed in Figure 55.

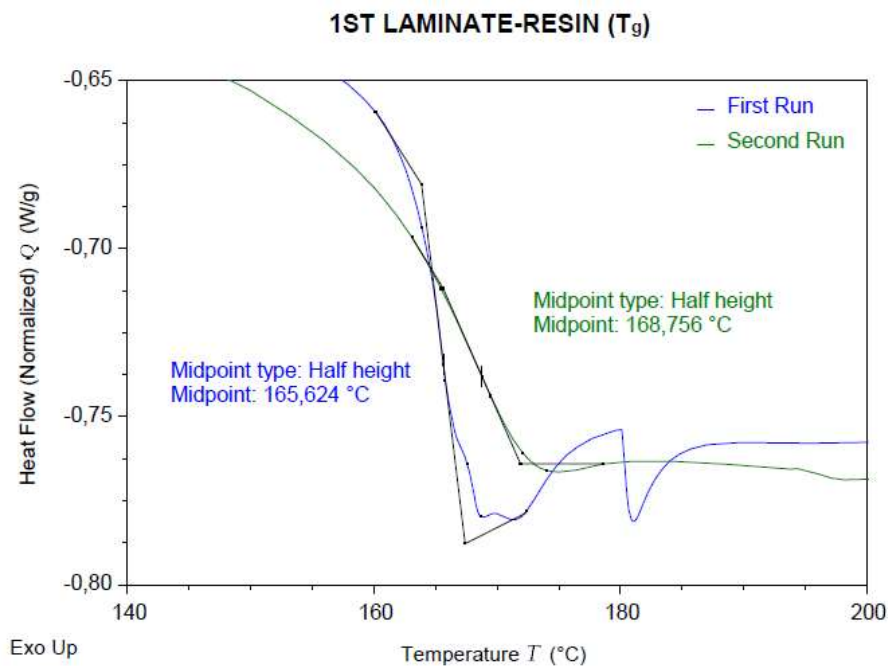


Figure 55: DSC analysis on dynamic resin from first composite panel.

Table 14 includes the obtained  $T_g$  values compared previous results on the same dynamic epoxy resin and related epoxy composite.

<b>Dynamic Epoxy Glass Transition Temperature <math>T_g</math> [°C]</b>				
	<b>Previous Results</b>		<b>Experimental Results</b>	
	Dynamic Epoxy [6]	Dynamic Composite [17]	EPOXY-SH	1 <sup>ST</sup> LAMINATE-RESIN
<b>Only cured</b>	144.19	/	/	/
<b>Post-cured, 1<sup>st</sup> scan</b>	166.23	/	170.69	165.62
<b>Post-cured, 2<sup>nd</sup> scan</b>	171.39	167.04	171.63	168.76

Table 14: Glass transition temperature comparison with previous results.

Since the definition of glass transition temperature is somehow ambiguous in itself, the values showed in Table 14, all differing by no more than 7°C, can be considered comparable one with the others and for this reason they are consistent with the comparative study developed in *Paolillo's* thesis work for dynamic epoxy and in Garcia's thesis work for dynamic composite. Indeed, a glass transition temperature around 170°C for the post-cured DGEBA-4AFD dynamic epoxy resin has been confirmed, noticing once again the substantial difference with the values (around 130°C) found in previous paper taken as reference. [36]

As suggested in [6], this discrepancy is ascribed to the stoichiometry assessment described in Par. 3.5.3, on which we based our calculations on the required materials amount for the realization of the composite panel. As a matter of fact, in previous studies a greater amount of 4-AFD hardener was embedded in the same epoxy system, thus reducing the resin extent and consequently requiring less time and lower temperatures to complete the glass-to-rubber transition.

To complete the  $T_g$  assessment, the comparison with Garcia's dynamic composite demonstrates that the presence of the fibres should not markedly affect the resin crosslinking process and therefore its glass transition temperature.

### 4.1.3 SEM analysis

As far as the Scanning Electron Microscopy analysis is concerned, we chose six specimens taken from different parts of the first composite panel, as clarified in Par. 3.2.2. In general, we can define two main locations where defects are present. The first one corresponds to areas rich in matrix away from fibres. Voids encountered in this location are completely surrounded by the epoxy matrix, and their shapes are mostly circular. The second location is defined as areas rich in interface, primarily composed of reinforcing fibres and where the shapes of voids are more elliptical or of different irregular geometry.

The most significant SEM micrographs for P1, P2 and P3 taken from the lateral scraps of the composite are reported here below. The whole length of every specimen was scanned with  $\times 100$  magnification in order to detect possible defects, cracks and delamination phenomena.

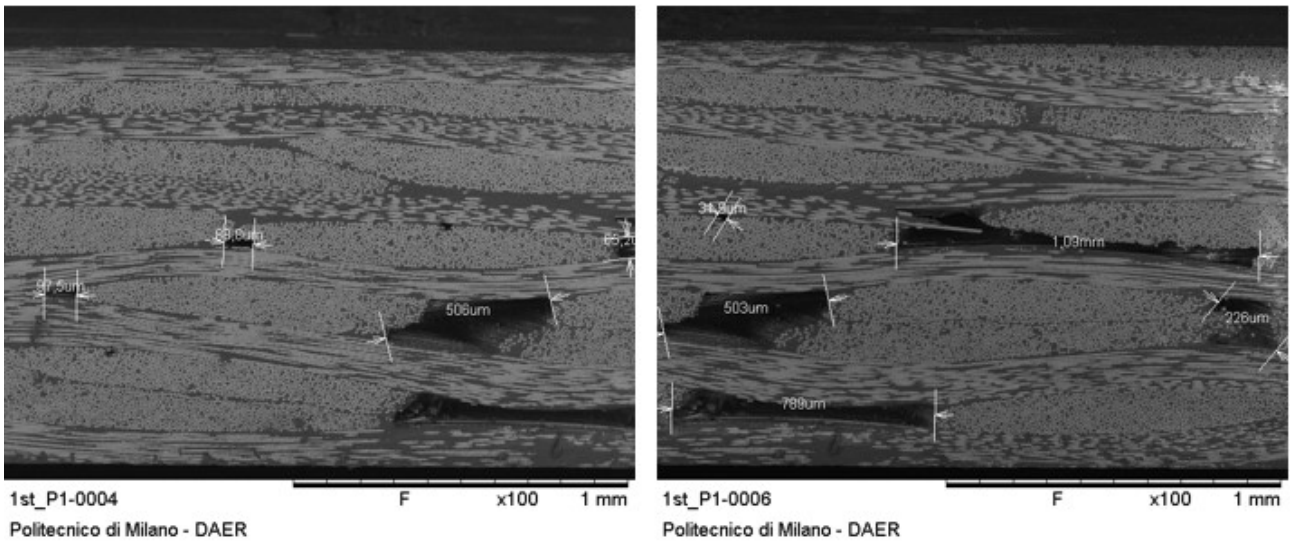


Figure 56: SEM micrographs of P1 specimen.

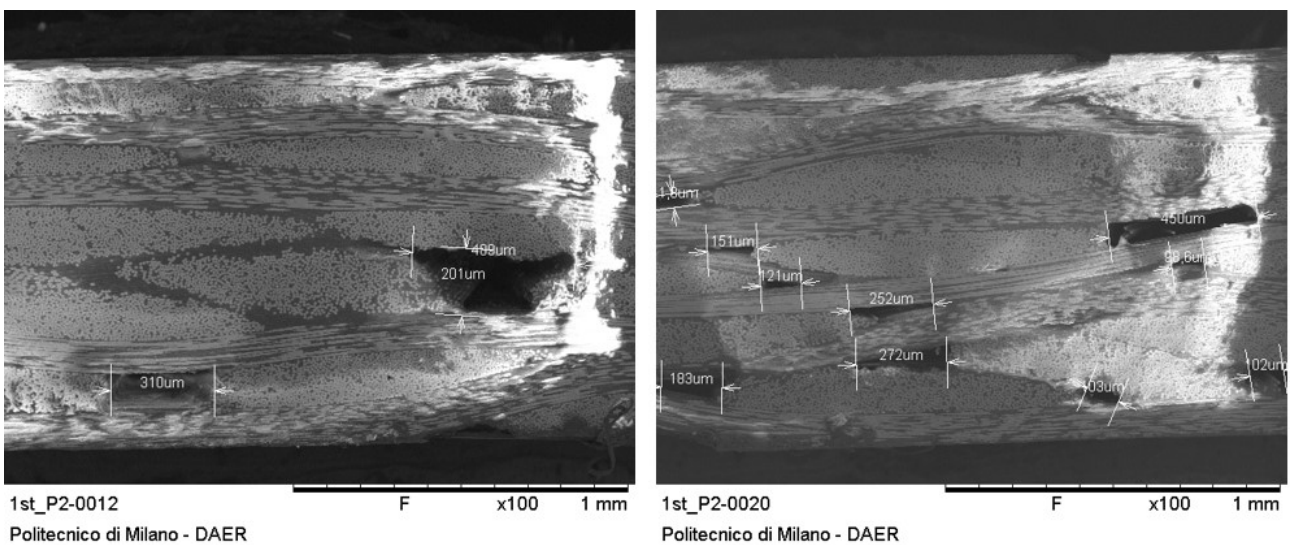
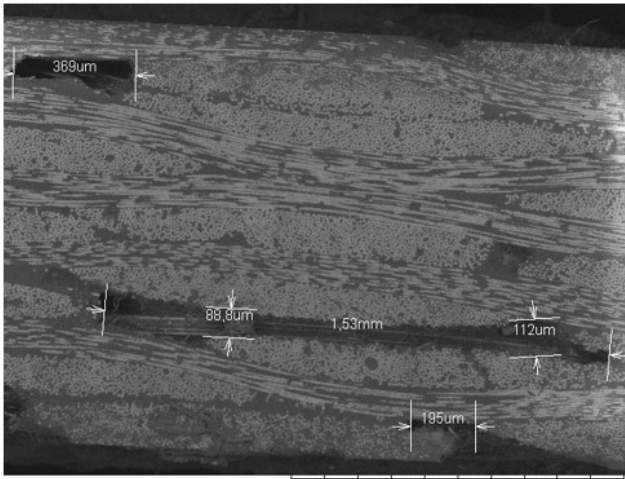
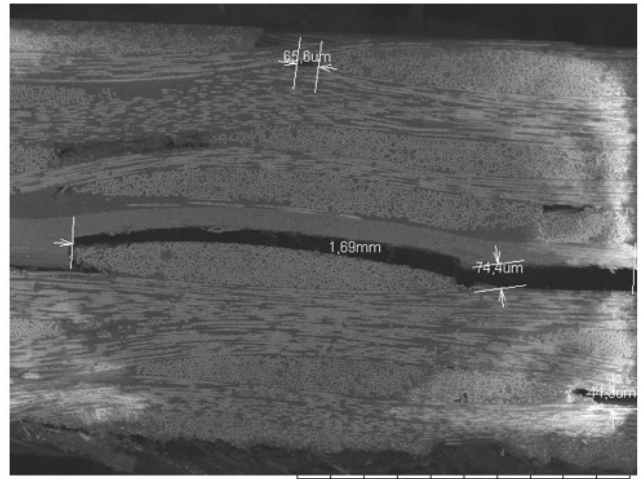


Figure 57: SEM micrographs of P2 specimen.



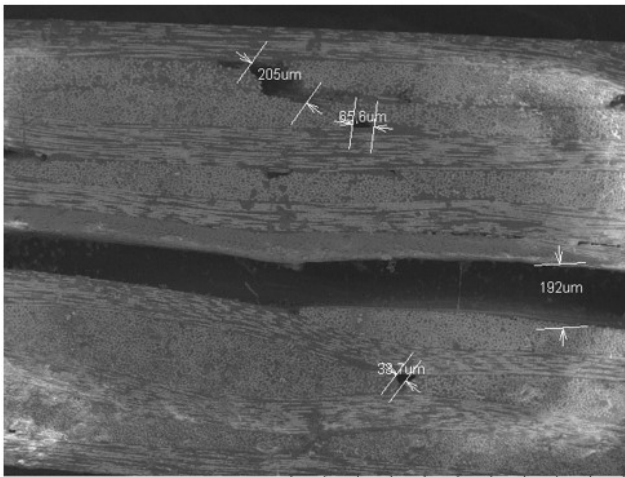


1st\_P3-0010  
Politecnico di Milano - DAER  
F x100 1 mm

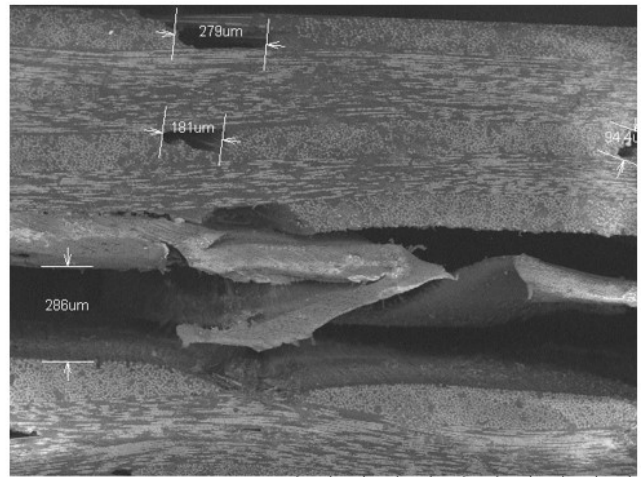


1st\_P3-0016  
Politecnico di Milano - DAER  
F x100 1 mm

Figure 58: SEM micrographs of P3 specimen showing a crack tip.

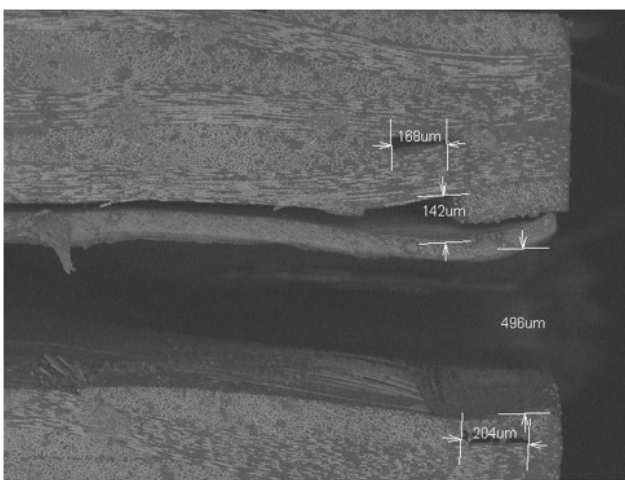


1st\_P3-0018  
Politecnico di Milano - DAER  
F x100 1 mm

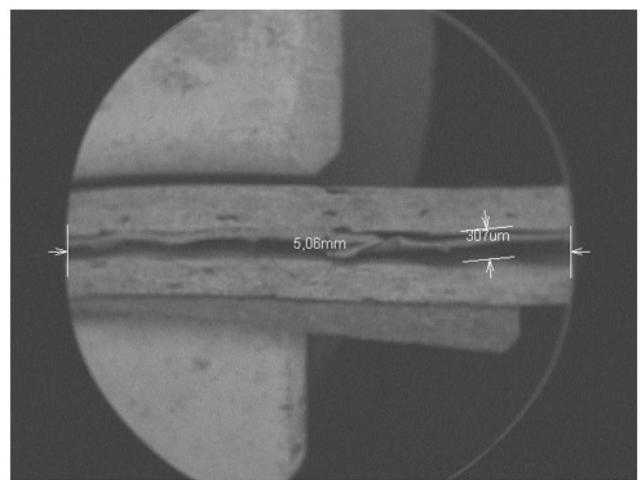


1st\_P3-0022  
Politecnico di Milano - DAER  
F x100 1 mm

Figure 59: SEM micrographs of P3 specimen showing the crack growth.



1st\_P3-0024  
Politecnico di Milano - DAER  
F x100 1 mm



1st\_P3-0026  
Politecnico di Milano - DAER  
F x30 2 mm

Figure 60: SEM micrographs of P3 specimen showing the crack initiation.

As easily detectable from the SEM micrographs above, P1, P2 and P3 specimens have shown non-negligible defects with big voids and significant delamination. Indeed, P3 specimen is affected by a huge delamination extending to almost half the total length of the specimen, roughly between the 3<sup>rd</sup> and the 4<sup>th</sup> plies, due to the presence of the scotch tape applied during the fabric cutting phase. This is clearly visible in Figure 58, Figure 59, Figure 60. A summary of the biggest defects for every specimen is listed in the Table below.

<b>Biggest void, crack or delamination [<math>\mu\text{m}</math>]</b>	
<b>P1</b>	1090
<b>P2</b>	1530
<b>P3</b>	5060

*Table 15: biggest defect found in every specimen.*

Certainly, these phenomena are a direct consequence of the fact that these specimens were taken from lateral scrap parts of the first composite panel, and therefore they are more prone to structural imperfections and edge effects.

Here we report the most important SEM images concerning specimens P4, P5 and P6 which were chosen as explained in Par. 3.2.2. Again, they were scanned with  $\times 100$  magnification in order to observe the integrity of the optical fibres on both sides.

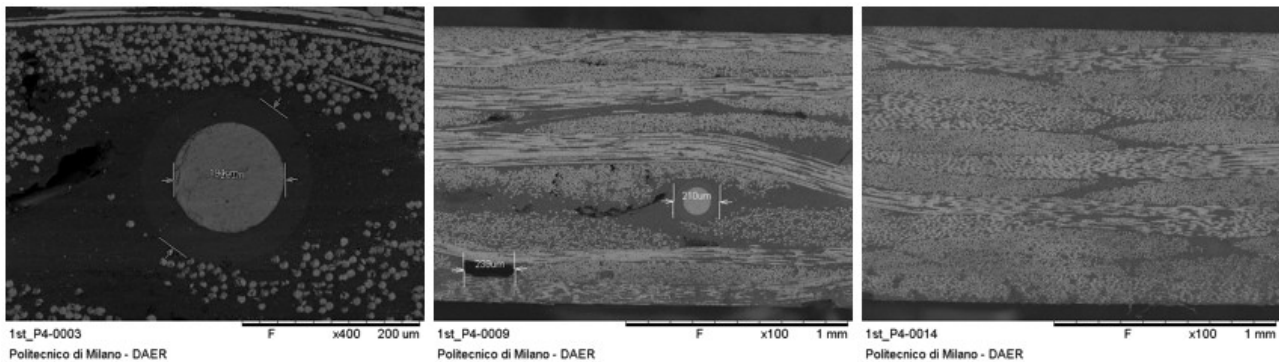


*Figure 61: SEM micrographs of P4 specimen.*

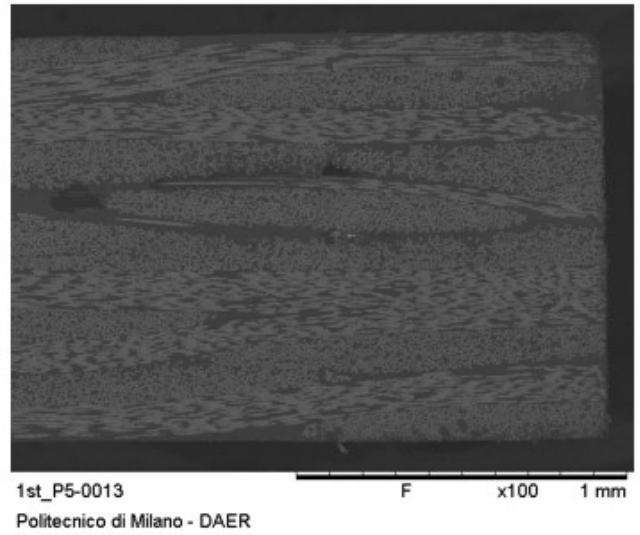
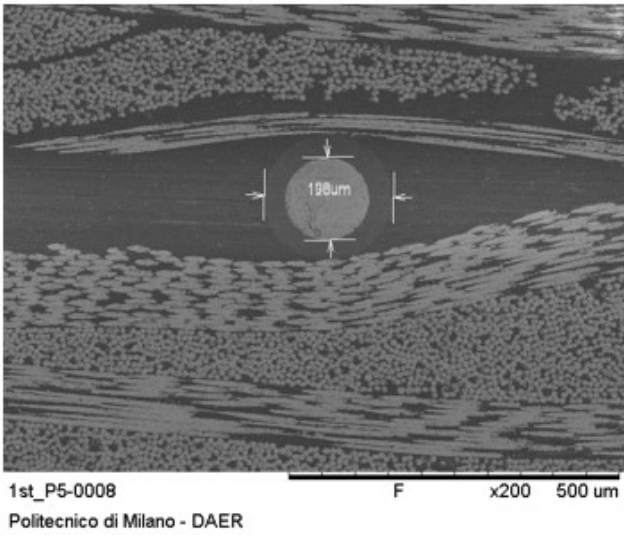


Figure 62: SEM micrographs of P5 specimen (Side 1).

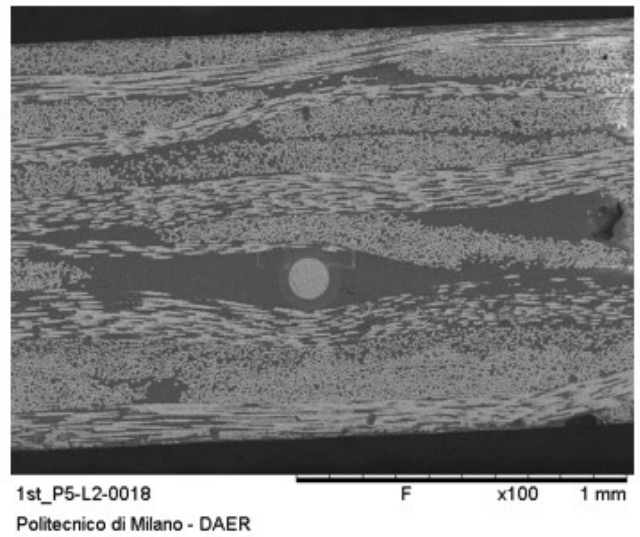
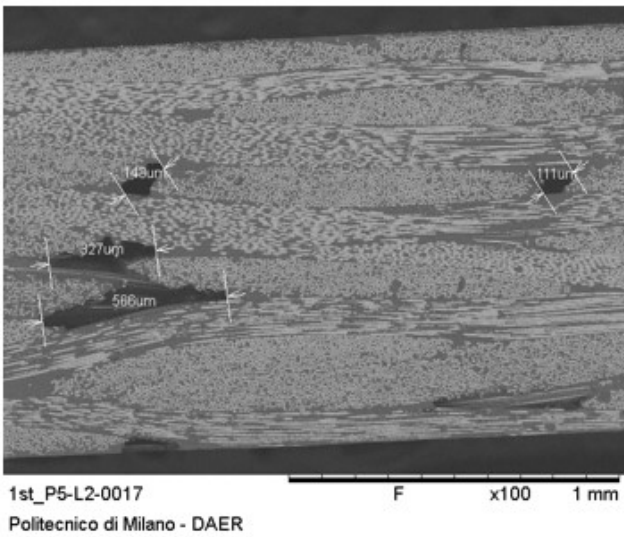


Figure 63: SEM micrographs of P5 specimen (Side 2).

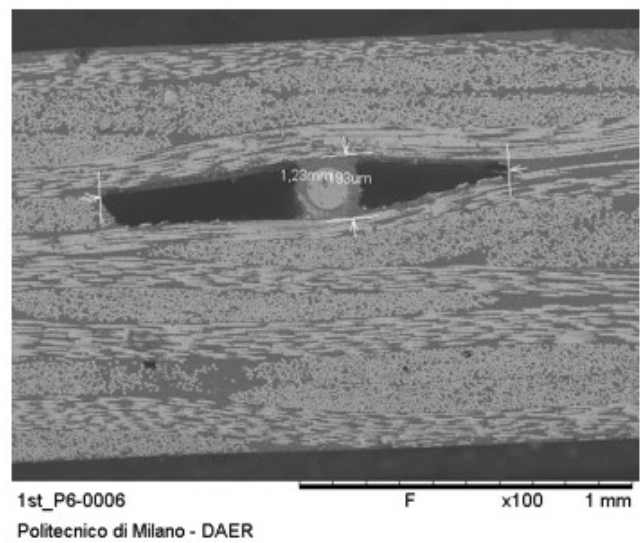
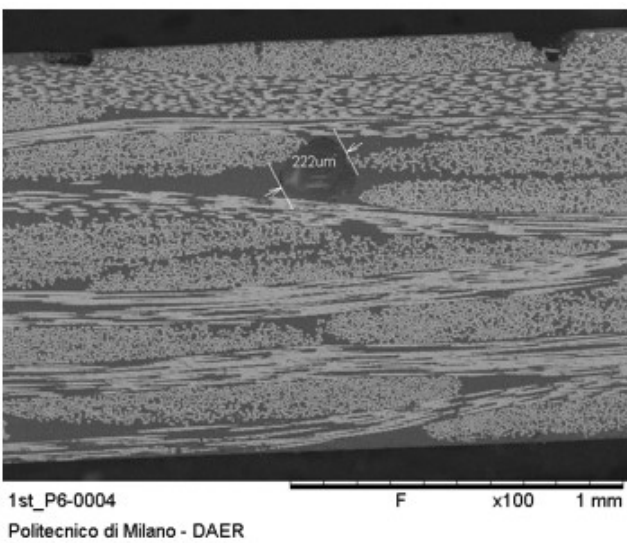


Figure 64: SEM micrographs of P6 specimen (Side 1).

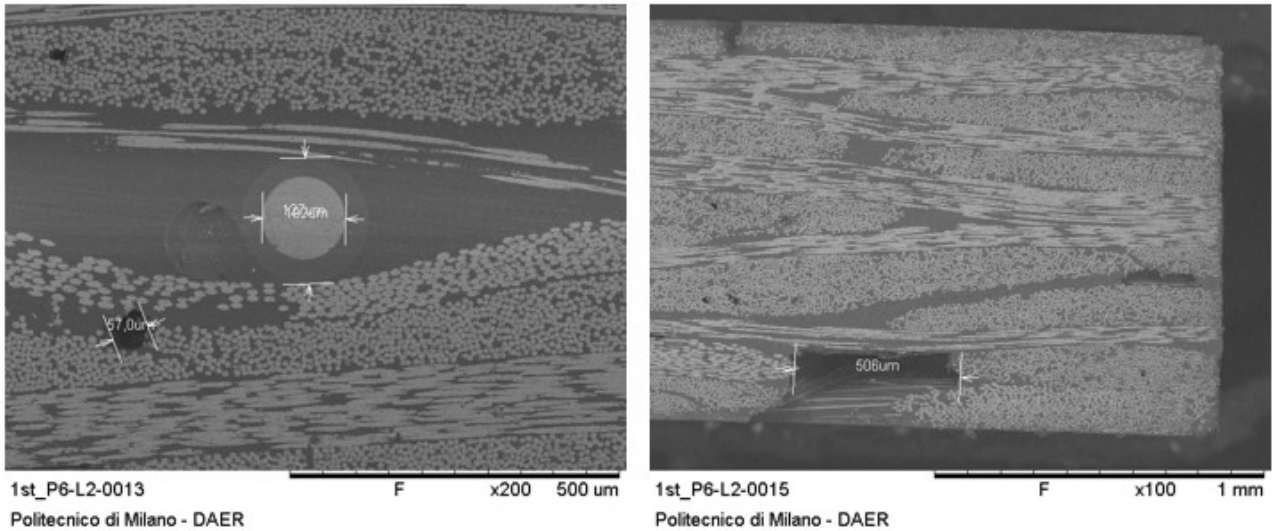


Figure 65: SEM micrographs of P6 specimen (Side 2).

By focusing on the SEM scan images above (Figure 61, Figure 62, Figure 63, Figure 64, Figure 65), it is possible to notice that these specimens present a reduced number of voids and imperfections, which are less extended too if compared to the previous specimens. As P4, P5 and P6 were obtained from a central area of the first composite panel, the hand lay-up process seems to be more effective with respect to the edges. Moreover, it was also possible to investigate the embedment of the optical fibres inside the panel; cladding and fibres diameters are reported in the Table 16.

	P4	P5	P6	
			Side 1	Side 2
<b>Cladding diameter [<math>\mu\text{m}</math>]</b>	194	196	201	192
<b>Optical fibre diameter [<math>\mu\text{m}</math>]</b>	126	126	124	127

Table 16: Optical fibres measurements on P4, P5 and P6 specimens.

More specifically, P4 specimen shows a good manufacturing quality in its central part, with no particularly bigger voids or other dangerous imperfections. P5 specimen seems to be homogeneous too. Last but not least, P6 specimen has been chosen because the optical fibre was not visible to the naked eye for the entire specimen length. Although it has an overall medium quality, it is worth mentioning that the optical fibre is clearly visible on both sides (Figure 64, Figure 65) and this fact unavoidably excludes the possibility of breakage. This evidence agreed with the fact that the impossibility to clearly see the optical fibre along the entire length can be due to a scarce compaction of the panel plies around the fibre itself, or more probably due to several resin excesses which obstruct its visibility. To conclude, the measurements in Table 16 confirm that any of the three optical fibres has been damaged, broken or generally affected by the manufacturing process.

#### 4.1.4 Density test analysis

A density analysis has been performed on P1, P2 and P3 SEM specimens, starting with the data in Table 17 below.

Fibres volume fraction	$f$	<b>0.55</b>
Fibres density [ $g/cm^3$ ]	$\rho_F$	2.90
Fibres Young's modulus [ $MPa$ ]	$E_F$	$7.20 \cdot 10^4$
Matrix volume fraction	$(1 - f)$	0.45
Matrix density [ $g/cm^3$ ]	$\rho_M$	1.20
Matrix post-cured Young's modulus [ $MPa$ ]	$E_M$	$3.83 \cdot 10^3$
Water density [ $g/cm^3$ ]	$\rho_{H_2O}$	1
Balance weight [ $g$ ]	$w_{balance}$	20
Theoretical composite density [ $g/cm^3$ ]	$\rho_C$	2.135
Theoretical composite Young's modulus [ $MPa$ ]	$E_C$	41324

Table 17: Data employed for density test analysis.

With mention to the formulas presented in Par. 3.3, Table 18 shows the obtained results.

		<b>P1</b>	<b>P2</b>	<b>P3</b>
Air weight [ $g$ ]	$w_{air}$	0.539	0.564	0.532
Scale reading [ $g$ ]	$w_{M-W}$	19.752	19.743	19.757
Composite density [ $g/cm^3$ ]	$\rho_C$	1.852	1.837	1.841
Voids volume fraction	$V_{voids}$	0.132	0.140	0.138

Table 18: Results obtained with Mohr-Westphal scale.

Then, the voids volume fraction and related composite Young's modulus referred to the relative error and the formula adopted in Par. 3.3.3 are reported here below.

<b>Specimen</b>	<b>Voids volume fraction</b>		<b>Composite Young's modulus [<math>MPa</math>]</b>	
	<b>Relative error</b>	<b>Formula</b>	<b>Relative error</b>	<b>Formula</b>
<b>P1</b>	0.132	0.223	40816	40469
<b>P2</b>	0.140	0.371	40789	39904
<b>P3</b>	0.138	0.348	40796	39990

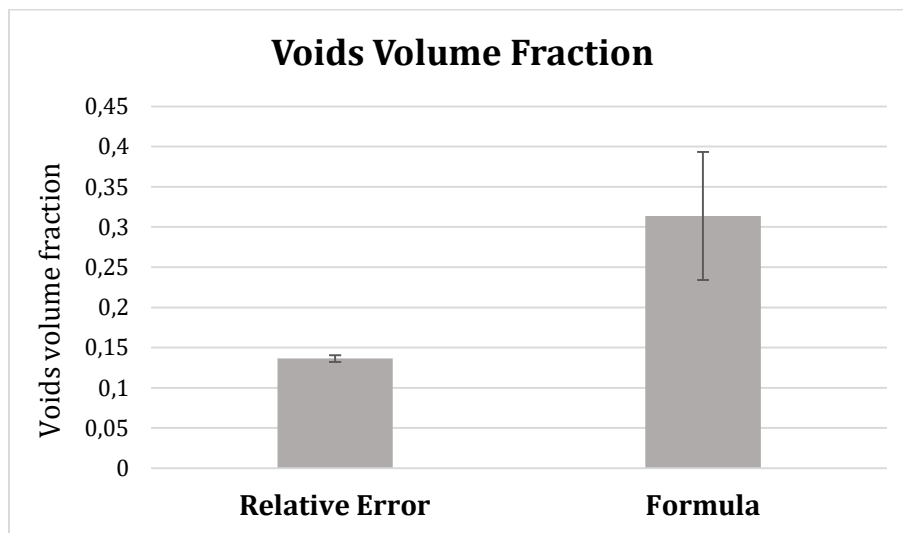
Table 19: Voids volume fraction and Young's modulus of the three specimens.

The values of density, voids volume fraction and Young's modulus for the three specimens are comparable as a result of the fact that they have similar dimensions and they were taken from the same composite panel. Moreover, as the physical features are similar, this applies also to the mechanical properties.

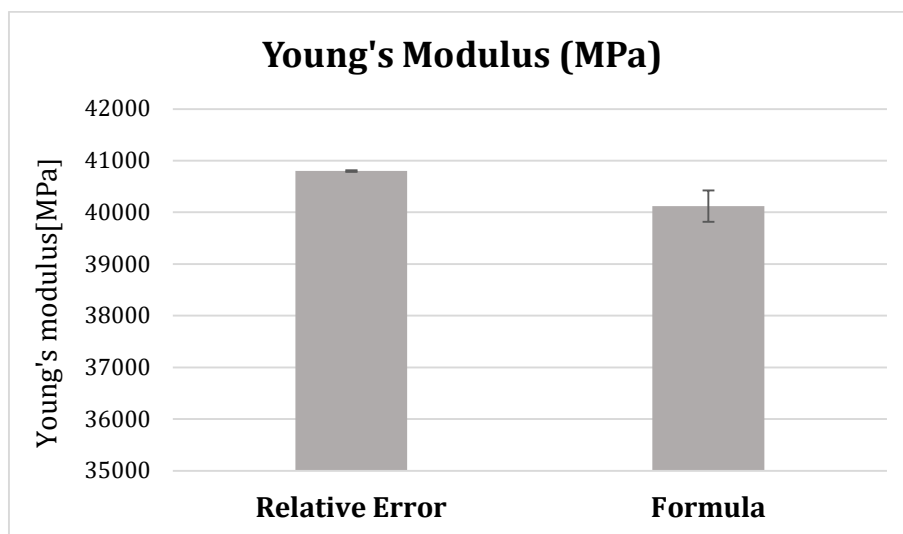
By considering that the relative error method is quite unrefined, the obtained results are consistent with the SEM micrographs exposed in Par. 4.1.3. A statistical analysis has been carried out on the three specimens by measuring the mean value and standard deviation for each adopted method, which results are here exposed.

	Voids volume fraction		Composite Young's modulus [MPa]	
	Mean value	Standard dev.	Mean value	Standard dev.
<b>Relative Error</b>	0.137	0.004	40800	14.012
<b>Formula</b>	0.314	0.080	40121	304.429

Table 20: Mean value and standard deviation for density test results.



Graph 3: Mean value and standard deviation for voids volume fraction.



Graph 4: Mean value and standard deviation for Young's modulus.

As the specimens were taken from a lateral scrap part of the composite panel, the voids volume fraction is inevitably  $> 10\%$ . If mean values of voids volume fraction and Young's modulus are known, the error with respect to the Young's modulus obtained from the rule of mixture can be calculated. Indeed, this last is considered as a theoretical value ( $E_{c,TH}$ ), therefore its value is higher with respect to  $E_c$  of the three specimens reflecting the real composite condition. Therefore:

$$ERROR = \frac{41324 - 40800}{41324} \cdot 100 \cong 1.27 \%$$

$$ERROR = \frac{41324 - 40121}{41324} \cdot 100 \cong 2.91 \%$$

The negligible discrepancy between the experimental results and the values theoretically obtained confirm the consistency of the rule of mixture.

Nevertheless, the exact dynamic matrix density value is unknown as it depends on the cross-linking between hardener and epoxy resin. While glass fibres density is constant, the chosen matrix density depends on the quantity of hardener and DGEBA mixed during the manufacturing of each composite panel. As far as the first panel is concerned, the 30% of resin has leaked during the curing and post-curing phases, so the exact stoichiometric ratio may have undergone a variation from the initial value. As the degree of uncertainty is given by several aspects, by choosing an undefined density matrix value contradicts the previously stated premise that the density values must be accurately known. For this reason, more accurate techniques which are out of the scope of this thesis could be implemented to improve the results reliability.

#### 4.1.5 DCB test analysis

As anticipated in Par. 3.6.3, the double cantilever beam (DCB) tests conducted on the specimens obtained from the first composite panel have all failed due to the collapse of the interface between the composite resin and the Ergal stiffening plates. This undesirable phenomenon is shown in the Figure 66 below.



*Figure 66: Evidence of the interface collapse during (on the left) and after (on the right) the DCB test.*

The interfacial adhesion showed to be very scarce as the entire specimen was detached from the Ergal plate simply by hand, demonstrating that the onset of test failure was mainly linked to several manufacturing faults including:

- Scarce attention during the sanding treatment;
- Poor performance or incorrect mixing of Araldite glue;
- Excessive smoothness of the composite surface;
- Irregularity in the panel thickness;
- Scarce planarity of the Ergal plates;
- Human errors while securing the specimen in the vice, mainly related to the application of the glue, to the orthogonality of the specimen itself with respect to the hinges and to the vice and finally to the applied pressure.



The possibility of any of these phenomena to happen has inevitably led to specimens' areas where the bonding level between aluminium and resin was not sufficient to carry out the mechanical tests. All the remedies adopted for what concern the technological and manufacturing process were already discussed in Par. 3.7 and are here briefly reported:

- Introduction of the peel-ply layers to increase the panel surface roughness;
- Modification of the hinges bonding method and employment of autoclave instead of hot press.

Regarding the uniformity and homogeneity of the composite itself, great efforts were employed during the manufacturing process of the second panel, especially during the hand lay-up phase (resin pouring and fibres sheet arrangement). Among all the suggested technological problems related to DCB failure, this is most probably the one with the highest margin of error because is directly connected to a series of factors including the quality and integrity of the reinforcement fibres, the correct resin preparation and, last but not least, the human manual skills, knowledge and experience.

## 4.2 SECOND COMPOSITE PANEL

### 4.2.1 Masses calculation

With regards to Par. 3.5.3 and by considering the adopted methods to overcome the technological problems encountered before, the masses for the realization of the second composite panel were obtained with the following results (peel-ply layers count as two additional plies).

		<b>1 ply</b>	<b>8 plies</b>	<b>+15% losses</b>
Total volume [ $mm^3$ ]	$V_{PLY}$	3000	24000	/
Fibres volume [ $mm^3$ ]	$V_F$	1650	13200	/
Matrix volume [ $mm^3$ ]	$V_M$	1350	10800	/
Matrix mass [g]	$M_{M,TOT}$	1.620	12.960	14.904
Resin mass [g]	$M_{DGEBA,TOT}$	1.187	9.496	10.920
Hardener mass [g]	$M_{4-AFD,TOT}$	0.433	3.464	3.984

Table 21: Results from composite mass calculations.

Again, the theoretical values contained in the last column have been used as the base for the realization of the second panel and here below they are compared with the real amount of materials used at the moment of the hand lay-up manufacturing process.

		<b>+15% losses</b>	<b>Experimental amount</b>
Matrix total mass [g]	$M_{M,TOT}$	14.904	14.990
Resin total mass [g]	$M_{DGEBA,TOT}$	10.920	11.000
Hardener total mass [g]	$M_{4-AFD,TOT}$	3.984	3.990

Table 22: Comparison between theoretical and experimental results.

Once the post-curing cycle ended, the panel was extracted, and the leaked cross-linked resin collected and weighted. A value of  $M_{M,LEAKED} = 1.616 \text{ g}$  was obtained, and so the actual loss of resin was reduced to:

$$LOSS: \frac{M_{M,LEAKED}}{M_{M,TOT}} \% = \frac{1.616}{14.990} \cdot 100 = 10.78 \% \cong 11 \%$$

Surprisingly, the size modification in the aluminium mould and the implementation of the plasticine stripes as control measures have proven to be satisfactory and the material loss was reduced by one third with respect to the first attempt.

#### 4.2.2 DCB test analysis

Recalling what has been reported in Par. 3.7.1, for every specimen belonging to the second composite panel, called respectively P1, P2, P3 (not to be confused with those employed for density tests), the DCB test was actuated by imposing a loading and unloading speed of  $0.5 \text{ mm/min}$ . The two main phases of the test are reported below and deeply explained in the following paragraphs.

- A first attempt of pre-cracking was performed to verify the so-called initial delamination length ( $a_0$ ), which is the value of the crack when the vertical displacement between the two strips of the specimen ( $\delta$ ) is maximum, averagely considering the PTFE pre-cracking length.
- A second, more precise and long-lasting attempt of cracking was performed again to let the crack reach a pre-fixed length (beyond the PTFE length) on each specimen.

##### 4.2.2.1 Pre-opening

Pre-opening was carried out to ensure that the delamination started by the PTFE sheet, which is  $0.05 \text{ mm}$  thick, continued in the material in order to get reliable results as closer as possible to the real operating condition of the composite panel in adequate applications. The Figure 67 reports the DCB configuration, thus showing the distance between the left free edge of the specimen and the hinges axis, and the PTFE total length.

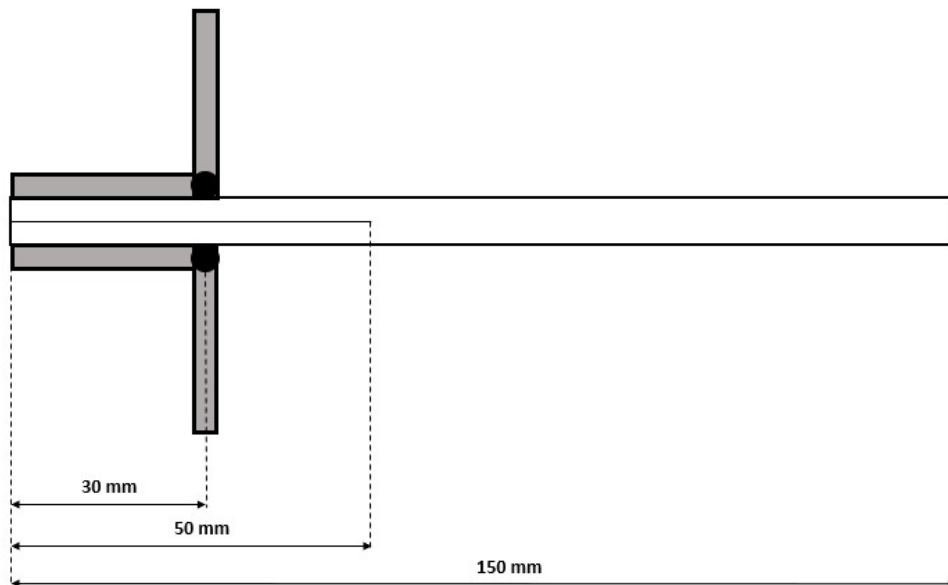


Figure 67: Schematization of a DCB specimen setup.

Every specimen was directly measured after the manufacturing process and the results are here below. It is important to remember that the length of every specimen can vary from the initial one (150 mm) due to the trimming action performed to remove the structural adhesive in excess.

<b>Specimen</b>	<b>Thickness [mm]</b>	<b>Width [mm]</b>	<b>Length [mm]</b>
<b>P1</b>	11.00	19.00	150.00
<b>P2</b>	11.00	19.00	149.00
<b>P3</b>	11.00	19.00	149.00

*Table 23: DCB specimens measured geometry.*

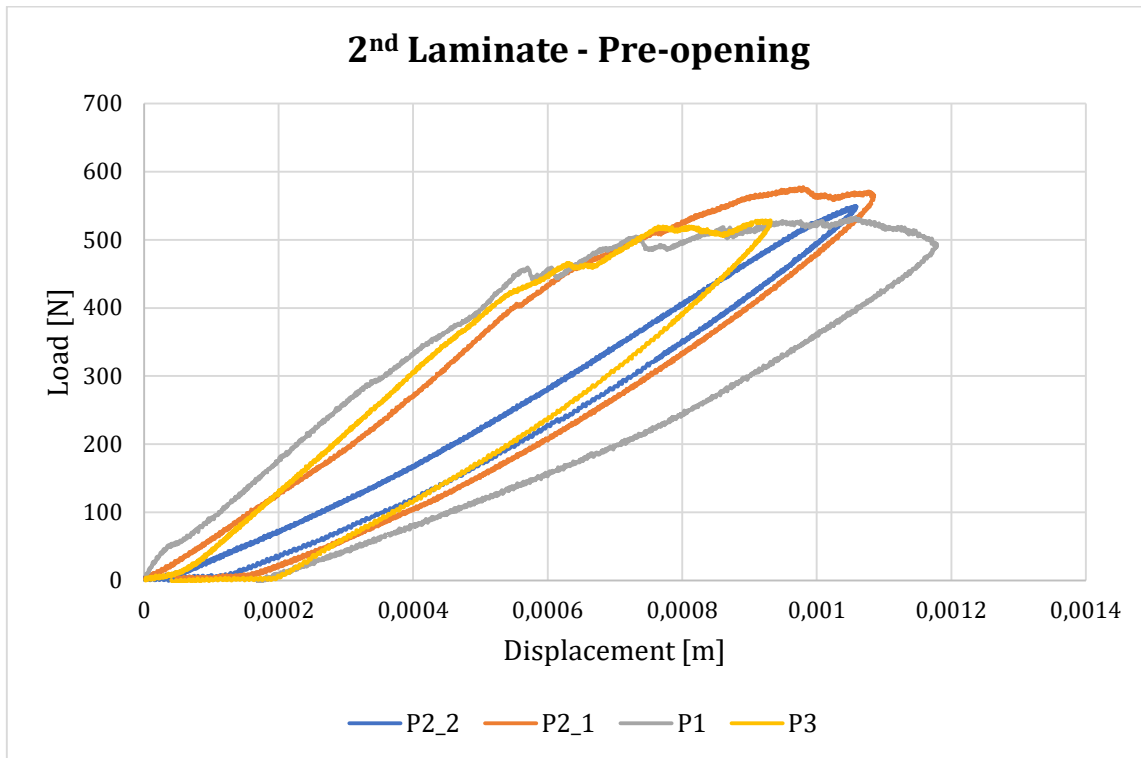
Even though the initial intention was to carry out a single pre-opening and a single opening for each specimen, this is not true for specimen P2. Due to some technological problems related to the recording camera, we will consider two pre-openings for P2 as, fortunately, during the first opening attempt the crack propagated for no more than 1 mm, such as to be considered as a second pre-opening.

Table 24 shows the initial delamination length for the three specimens before pre-opening, considered as the distance between the hinges axis – where the load is applied – and the end of the PTFE sheet inside the specimen (nominally 20 mm long), and before opening, considered as the distance between the hinges axis and the crack tip reached with pre-opening. These distances are both called  $a_0$ .

<b>Initial delamination length <math>a_0</math> [mm]</b>		
<b>Specimen</b>	<b>Before pre-opening</b>	<b>Before opening</b>
<b>P1</b>	20.00	22.72
<b>P2</b>	20.00	23.99
	22.99	/
<b>P3</b>	20.00	22.34

*Table 24: Initial delamination lengths measured before pre-opening and before opening.*

After the data acquisition and elaboration, it was possible to generate a chart for the comparison of specimens pre-opening, as showed here below.



Graph 5: Pre-opening comparison between DCB specimens.

The typical trend of DCB output graphs is depicted, with displacement linearly increasing with the load in the first section. The second phase, even though is not markedly outlined, starts when the load tends to stabilize, thus showing a flatter displacement increase with respect to it. In particular, P1 (grey line) and P3 (yellow line) specimens both show an extremely fragmented pattern, while the pre-openings for P2 (orange and blue lines) have a softer trend. With mention to the second pre-opening, the test was so short that the second phase had no time to develop and subsequently the curve is very narrow.

Then, the third and last phase corresponds to the specimen unloading, with the curves that regress up to the graph origin. While P2 and P3 specimens seem to correctly “close” their curve, this does not happen for what concern P1. Indeed, probably in relation to the specimen installation in the MTS machine, P1 curve does not achieve a perfect closure as secondary dissipation phenomena apart from crack growth originated during the test.

#### 4.2.2.2 Opening

As anticipated in Par. 3.4.5, every specimen underwent an opening phase up to a pre-fixed crack length before being unloaded, beyond the PTFE sheet length. This has been done to study the behaviour of the composite under quite different tensile loading conditions. The measurements were taken with the help of a video camera and a software (GIMP) to extract the frames from the recording. Regarding this, a mean value over all the marked notches was taken to convert the pixel reading from the software to the actual value in millimetres. Initial delamination length ( $a_0$ ) values were recorded by converting the software reading on the frame taken at the times related to  $\delta_{MAX}$  point in the  $P - \delta$  output data. The results are shown in the table below.

Specimen	Pre-fixed crack length [mm]	$\delta_{MAX}$ [mm]	$a_{MAX}$ [mm]
P1	40.00	3.94	60.66
P2	30.00	2.68	51.68
P3	50.00	4.46	69.96

Table 25: Main data from opening phase of DCB test.

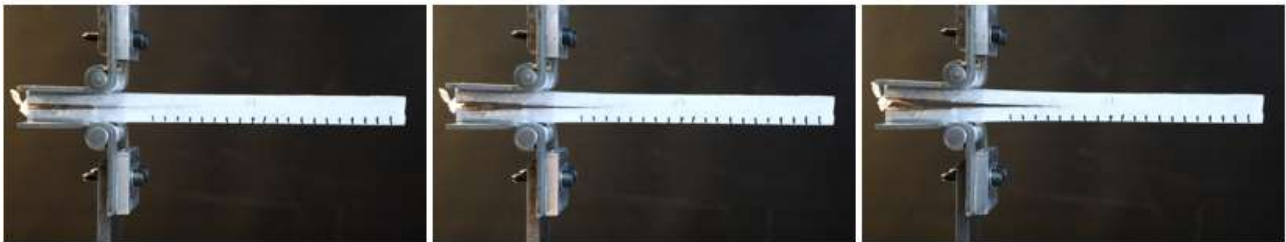
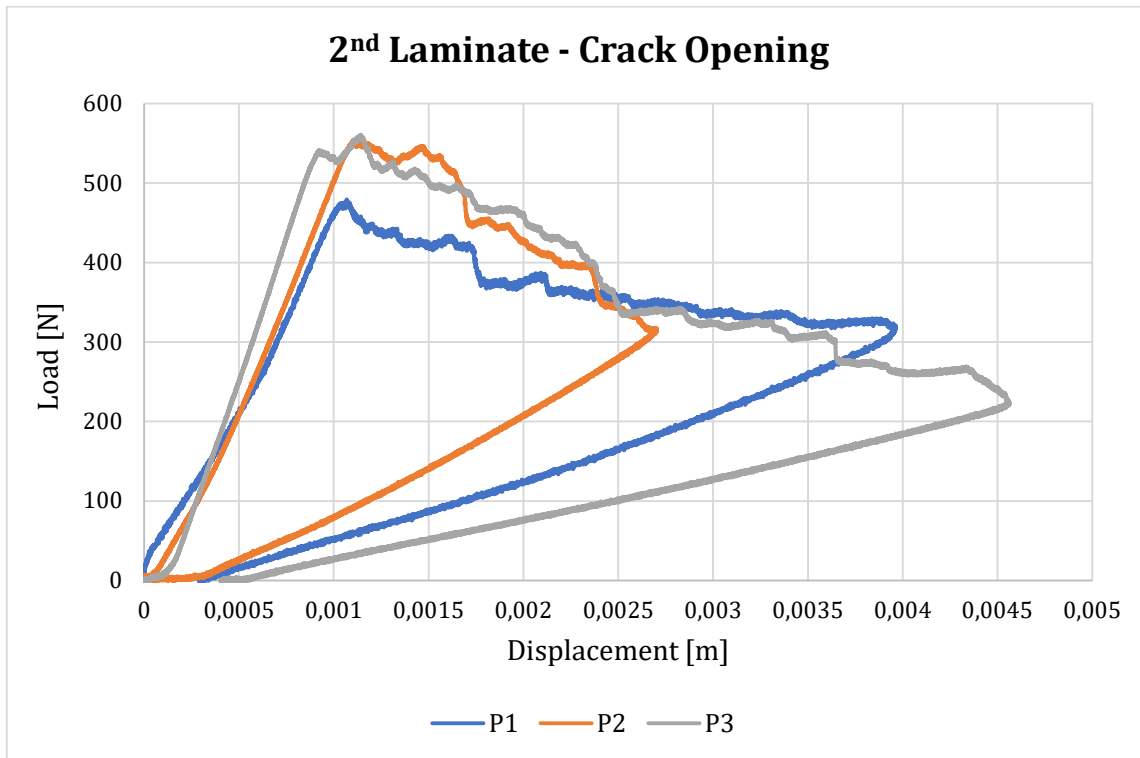


Figure 68: Frame sequence of P1 specimen under loading.

Again, the crack opening Load vs. Displacement charts for every specimen were created from the data acquired, as demonstrated here below.



Graph 6: Crack opening comparison between DCB specimens.

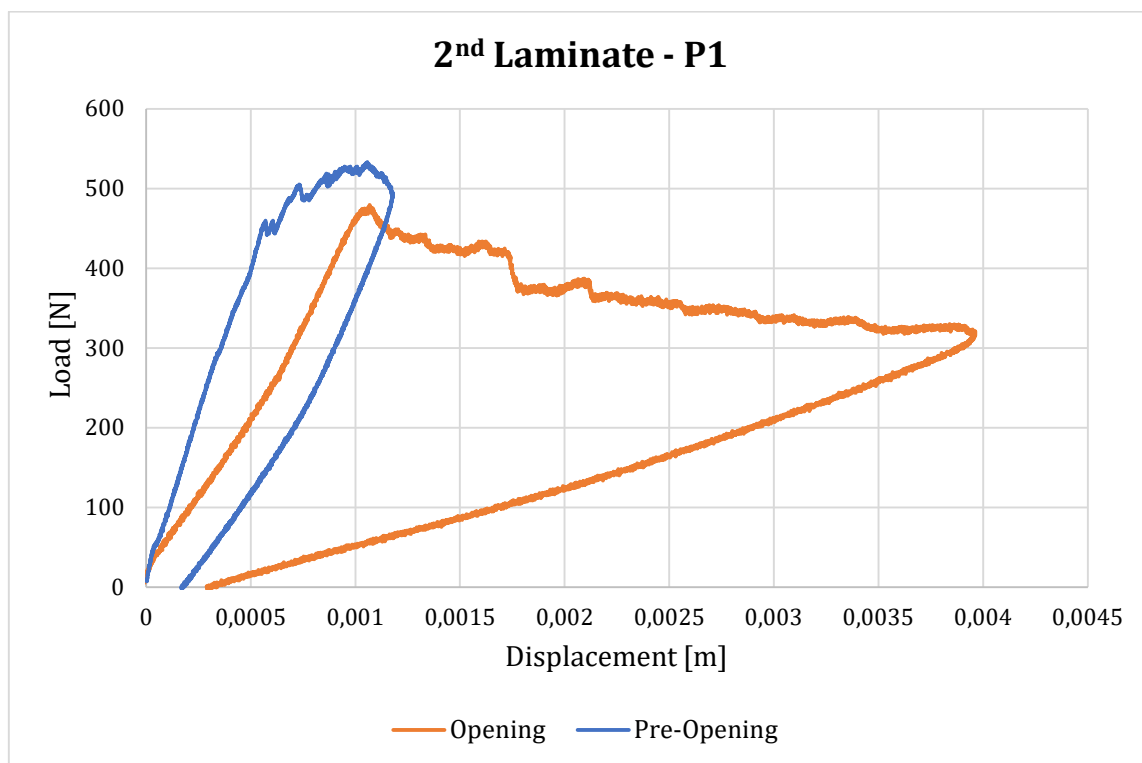
The typical triangle-shaped load-displacement curve for the specimens opening is visibly recognized with three main phases. In the first linear phase, the load linearly grows with the displacement, then a second phase follows, where the load generally tends to stabilize itself with slowly decreasing trend. A final phase corresponds to the specimen unloading, where the curve regresses back to the origin, thus creating a sort of triangle. Every specimen curve is now analysed in detail.

Regarding P1 curve, the first segment approximately starts from the origin, then it seems to undergo a sort of slope variation. Moreover, this specimen is clearly the one bearing the lower maximum loading condition. The second segment is jagged, while the third one does not “close” the triangle probably due to the onset of secondary energy dissipation phenomena. As far as P2 specimen concerns, the first segment has constant slope, similar to that of P3 specimen. The second segment is jagged too and particularly accented in its first part, while the third one succeeds in “closing” the triangle rather well. P3 curve is quite similar to the P2 one in its first segment, and also in the first part of the second segment. Here the second segment is longer and for this reason P3 specimen displacement is nearly doubled with respect to the previous one, even though the triangle closure (third segment) is again badly affected by secondary dissipation phenomena.

This last concept is explained as follows and it is best applied to Ergal, which is the elastic regime. Technically, if the condition of non-yielding is satisfied (Par. 3.6.3), there is no reason for the specimen to store a residual deformation once the unloading phase has ended. In this optimal condition, the curve will have a closed triangle-shaped trend, but in some cases the experimental tests have shown a worse situation where the unloading segment of the curve does not end at the origin as expected. The reasons behind these energy dissipation phenomena and the variation of the material behaviour are beyond the purpose of this work. A non-negligible role is probably played by the settling effects on the specimen fixed to the MTS machine during the initial phase of the DCB test. Accordingly, we may say that the initial acquired data are not representative of the real behaviour of the material.

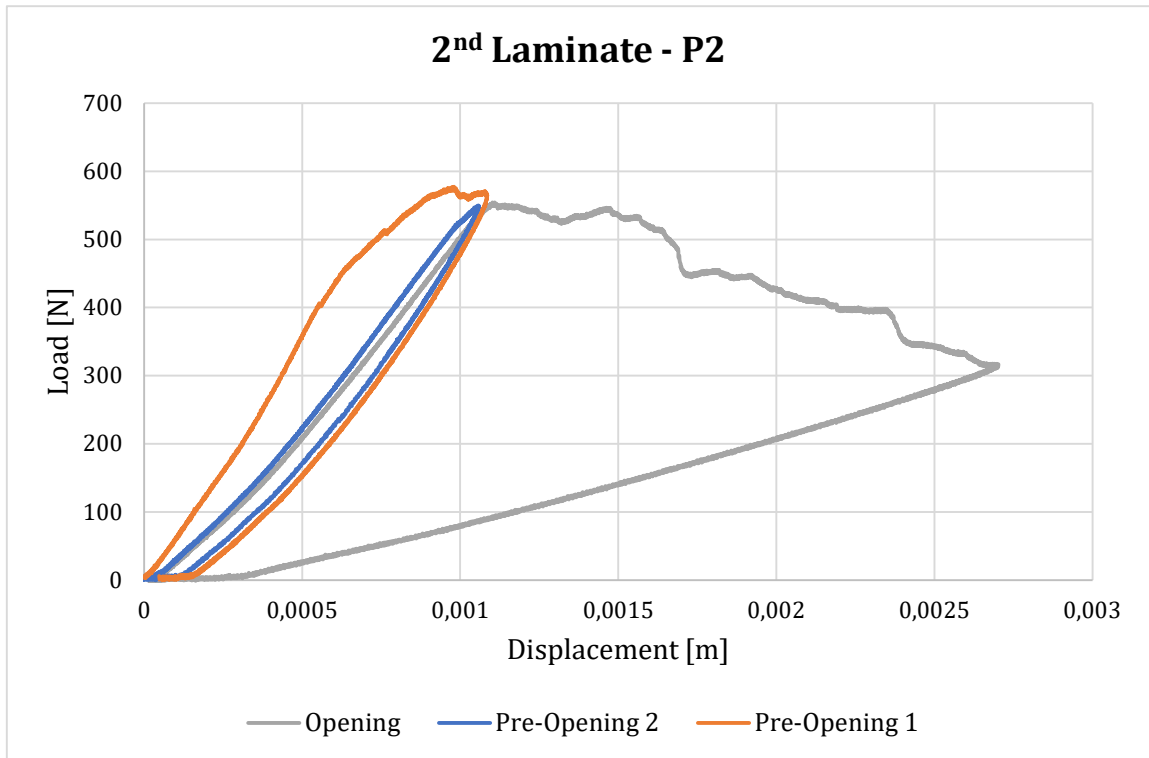
As a first visual assessment on the curves trend in their entirety, it is possible to observe that the extent of the area below the curves is perfectly consistent with the choice of the pre-fixed opening length. Indeed, P1 specimen curve has an intermediate extent between P2 (the smallest) and P3 (the largest), as well as their opening values follow the same trend.

For the sake of completeness, a chart with the comparison between pre-opening and opening curves is reported here below for every studied specimen.

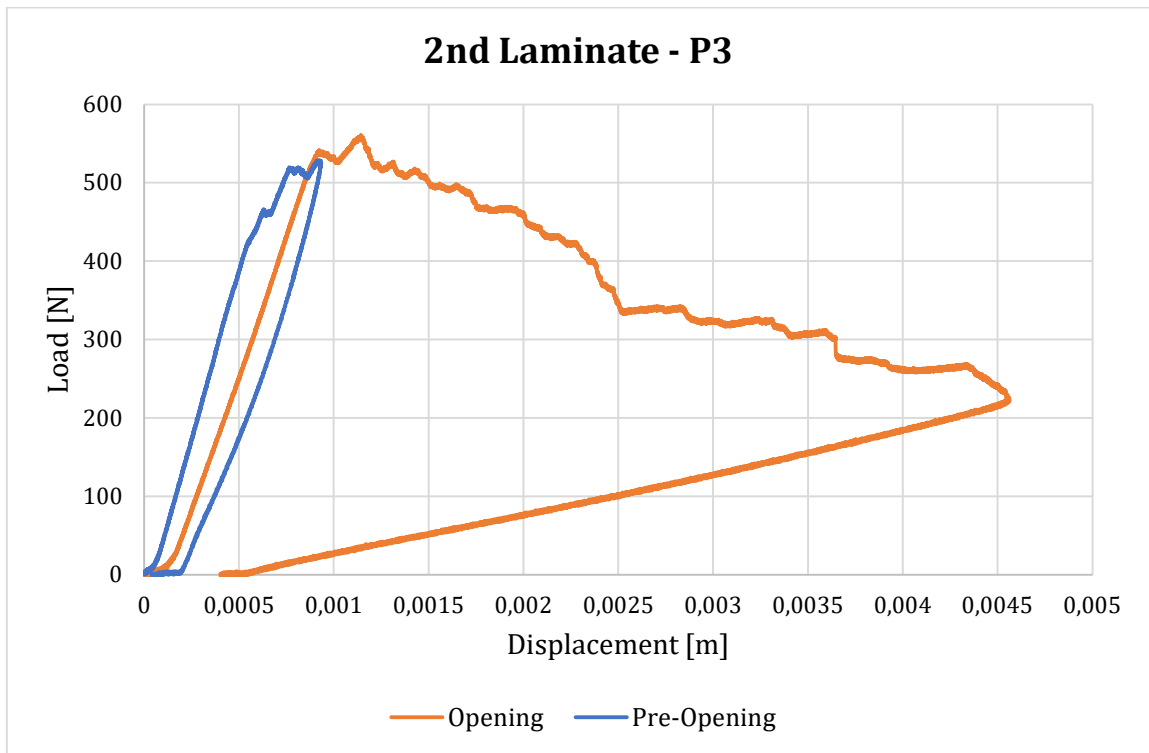


Graph 7: P1 pre-opening and crack opening comparison.





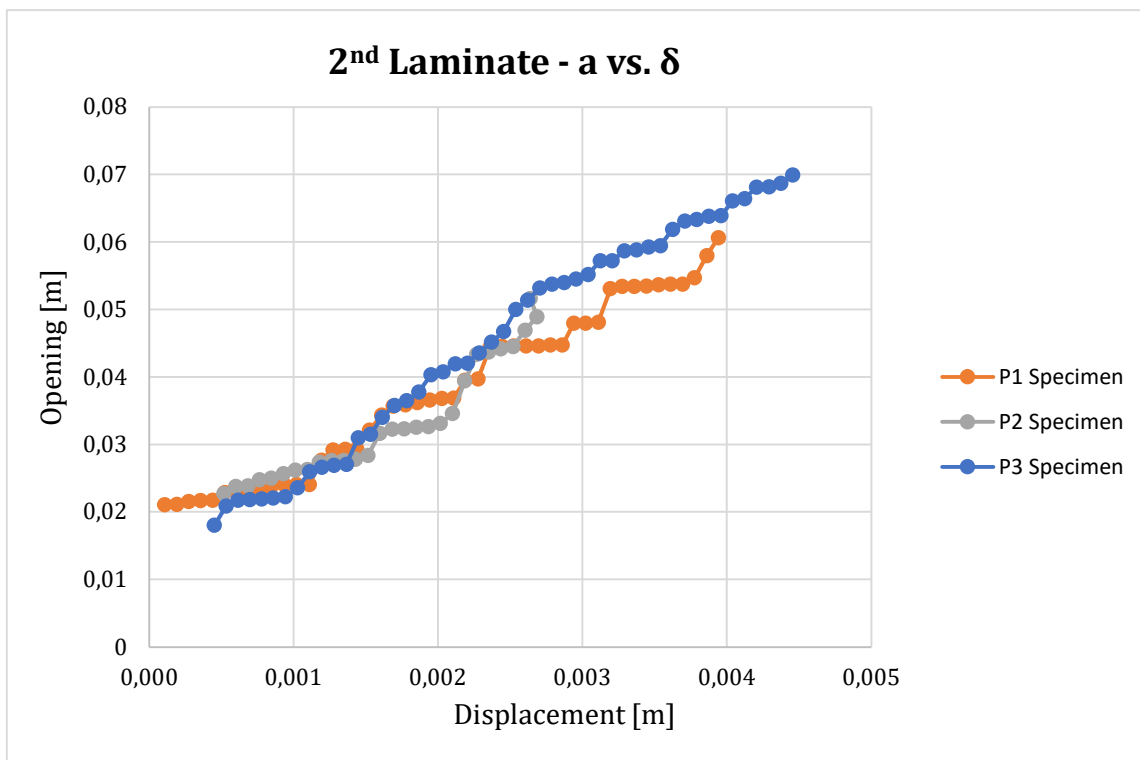
*Graph 8: P2 pre-openings and crack opening comparison.*



*Graph 9: P3 pre-opening and crack opening comparison.*

What has been observed so far for each of the three specimens is confirmed, adding that in each of the three cases the increasing line of the load-displacement curves corresponding to the openings is approximately parallel to the decreasing line of the pre-opening curves. Indeed, the specimens are not dismantled between the pre-opening and the opening test, thereby it is legitimate to expect that in normal (ideal) conditions the mechanical test does not affect the chemistry and the behaviour of the material. This is the reason behind the fact that the closing phase of pre-opening must match with the opening loading phase as much as possible, considering that possible hysteresis or friction effects can inevitably shift the curve segment.

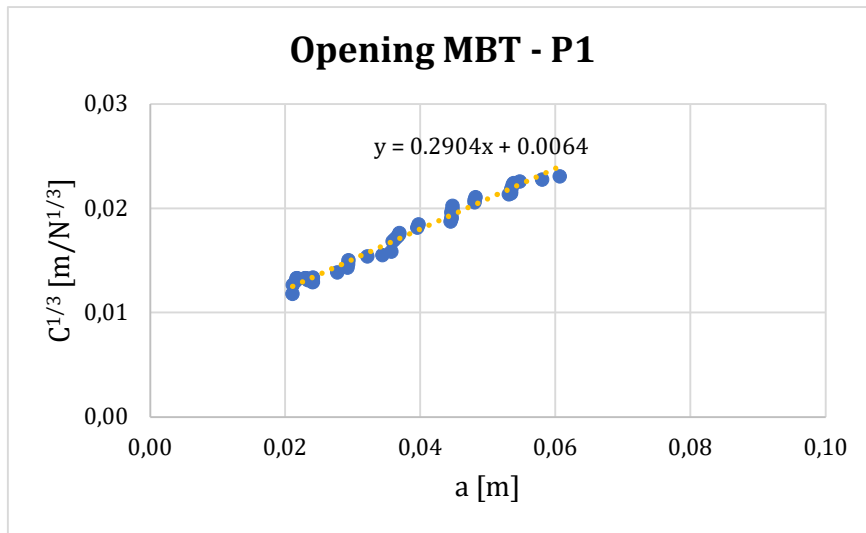
Moreover, an additional chart was generated to compare the trend of crack length as a function of the transverse displacement for each specimen, as shown below (Graph 10).



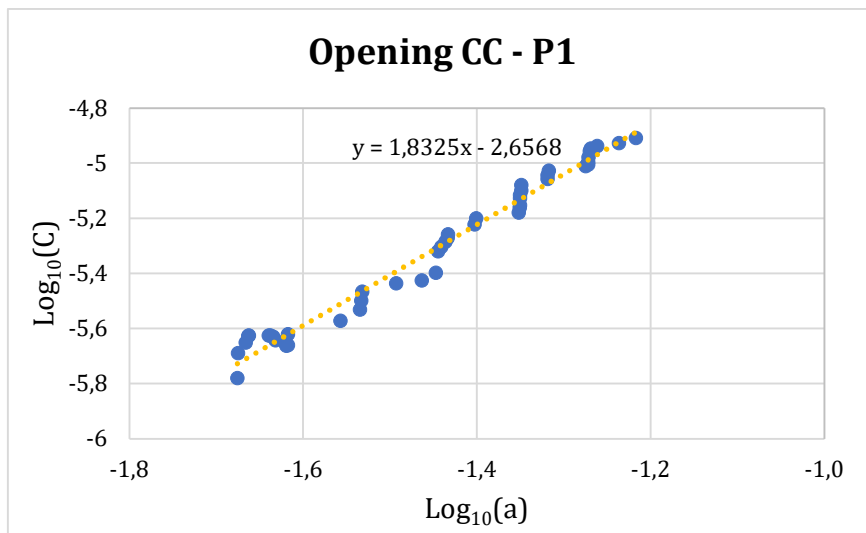
Graph 10: Crack length behaviour as a function of transverse displacement.

The main trend is markedly jagged and non-linear. As a confirmation factor for this observation, it is fundamental to notice that, during the test, the crack did not seem to follow the specimen mid-plane, probably due to planarity inconsistencies originating from composite hand manufacturing. Furthermore, for the data acquirement we chose to examine the cracking tests by pulling frames every 10 seconds out of the video camera and consequently by reading the exact delamination length at that times. Precisely in this context, in the interval between one acquired frame and the next, sometimes the crack advanced quickly, while in other moments it stood constant in time.

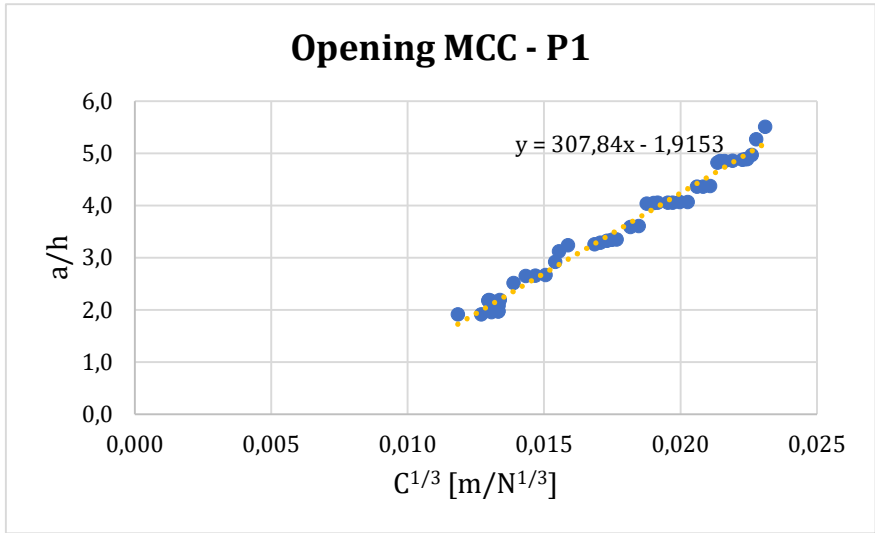
By accurately matching every  $a$  value to the respective machine time and load entities, Mode I interlaminar fracture toughness  $G_I$  was calculated on the basis of dedicated ASTM standard, precisely by following the Beam Theory (BT), Modified Beam Theory (MBT), Compliance Calibration (CC) and Modified Compliance Calibration (MCC) methods, described in (Par. 3.4.4.1). The main results will be discussed in the following section.



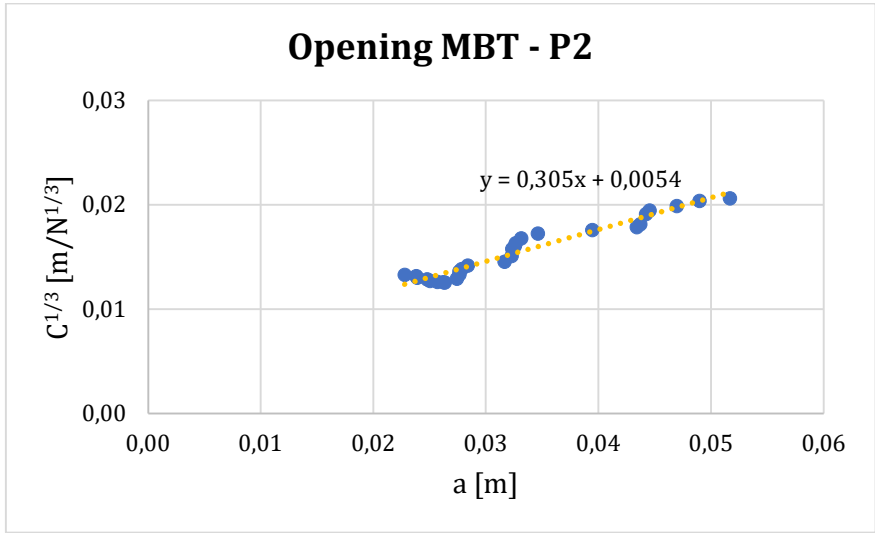
Graph 11: P1 MBT method application.



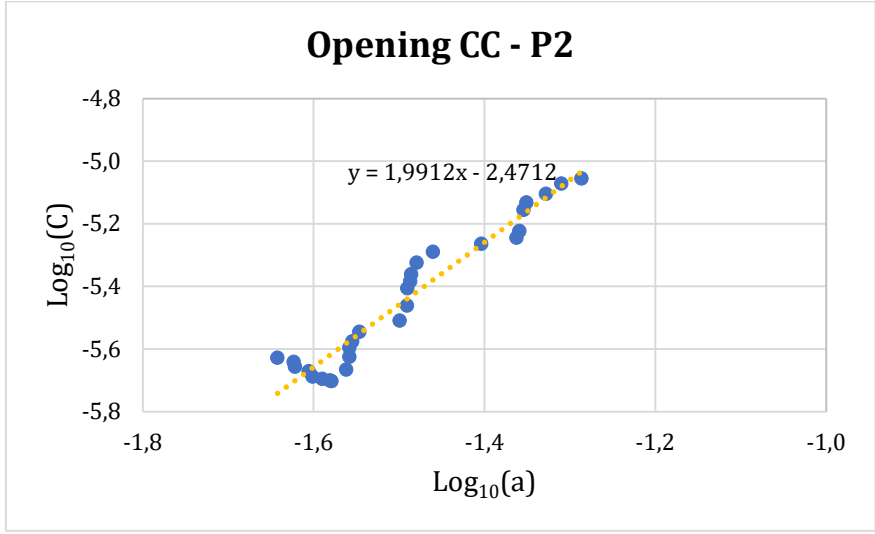
Graph 12: P1 CC method application.



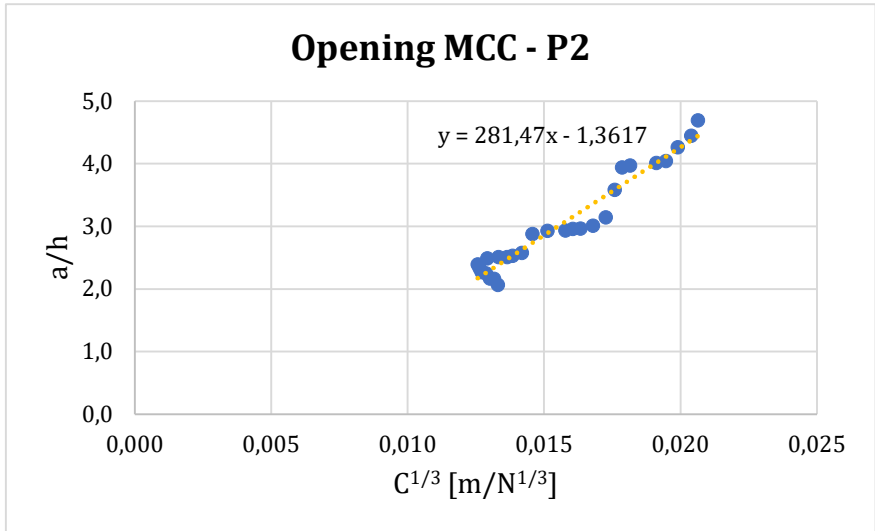
Graph 13: P1 MCC method application.



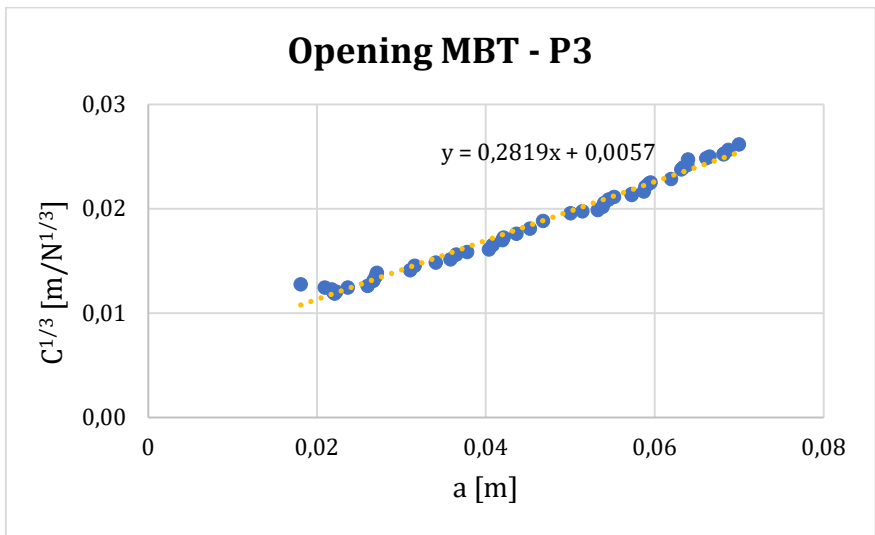
Graph 14: P2 MBT method application.



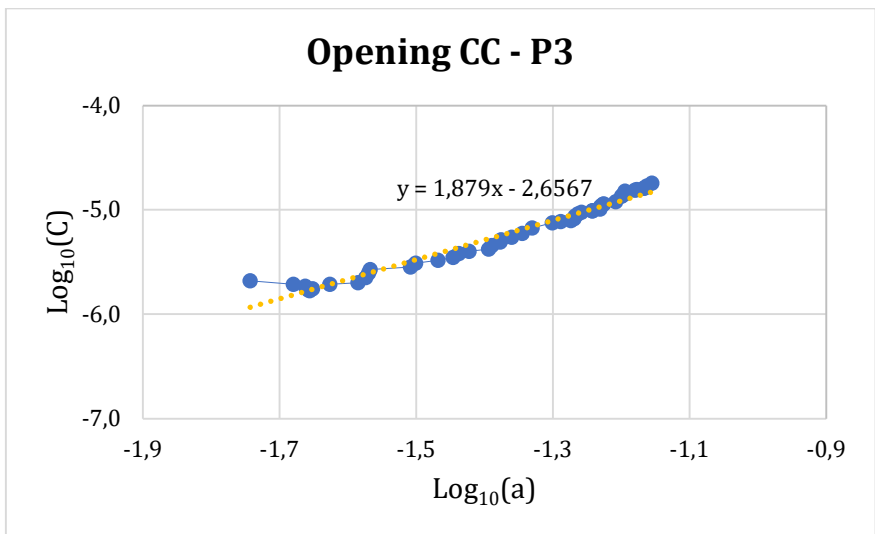
Graph 15: P2 CC method application.



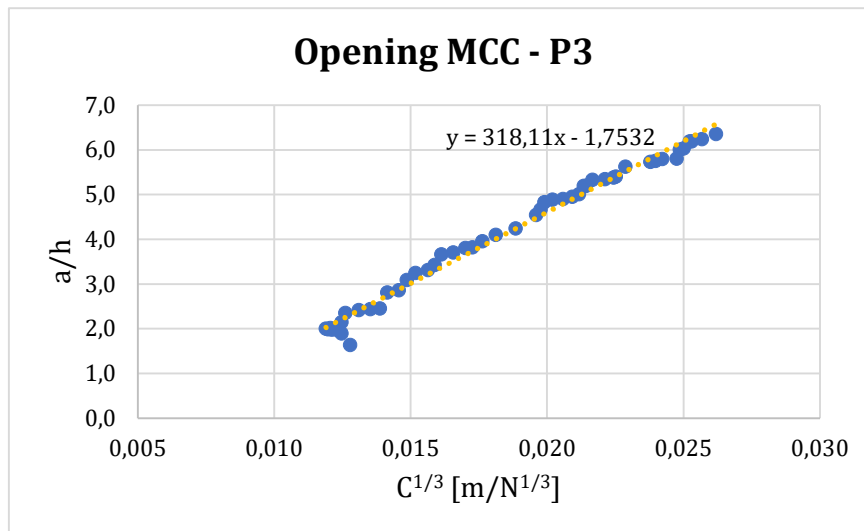
*Graph 16: P2 MCC method application.*



*Graph 17: P3 MBT method application.*



*Graph 18: P3 CC method application.*



Graph 19: P3 MCC method application.

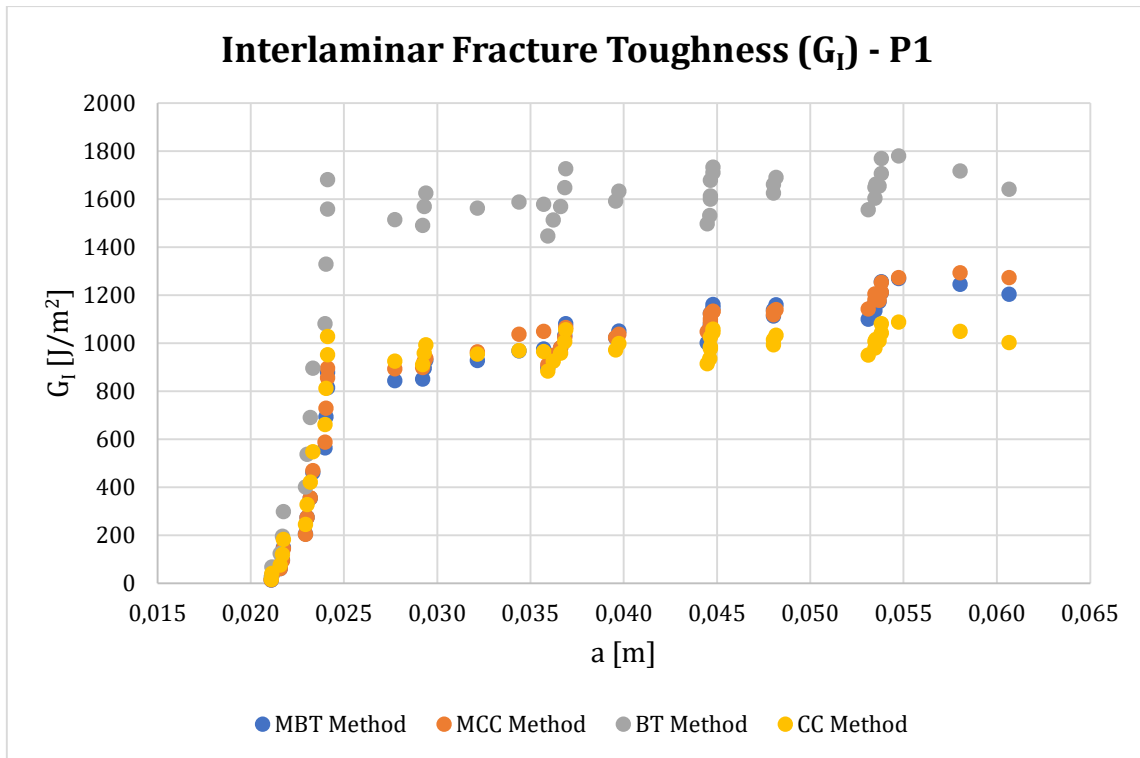
Comparing all the charts above, regarding the Modified Beam Theory method, it is worth mentioning that data from P3 specimen are better distributed and the trend lines interpolate them with a lower margin of error with respect to P1 and P2. For the latter, the graphs where Compliance Calibration method is applied show a more concentrated distribution. Then, for what concerns Modified Compliance Calibration method, it can be noted that the distribution is much more dispersed with respect to the other methods, however, qualitatively the best interpolation belongs again to specimen P3.

Table 26 below shows the quantitative parameters associated with every method applied.

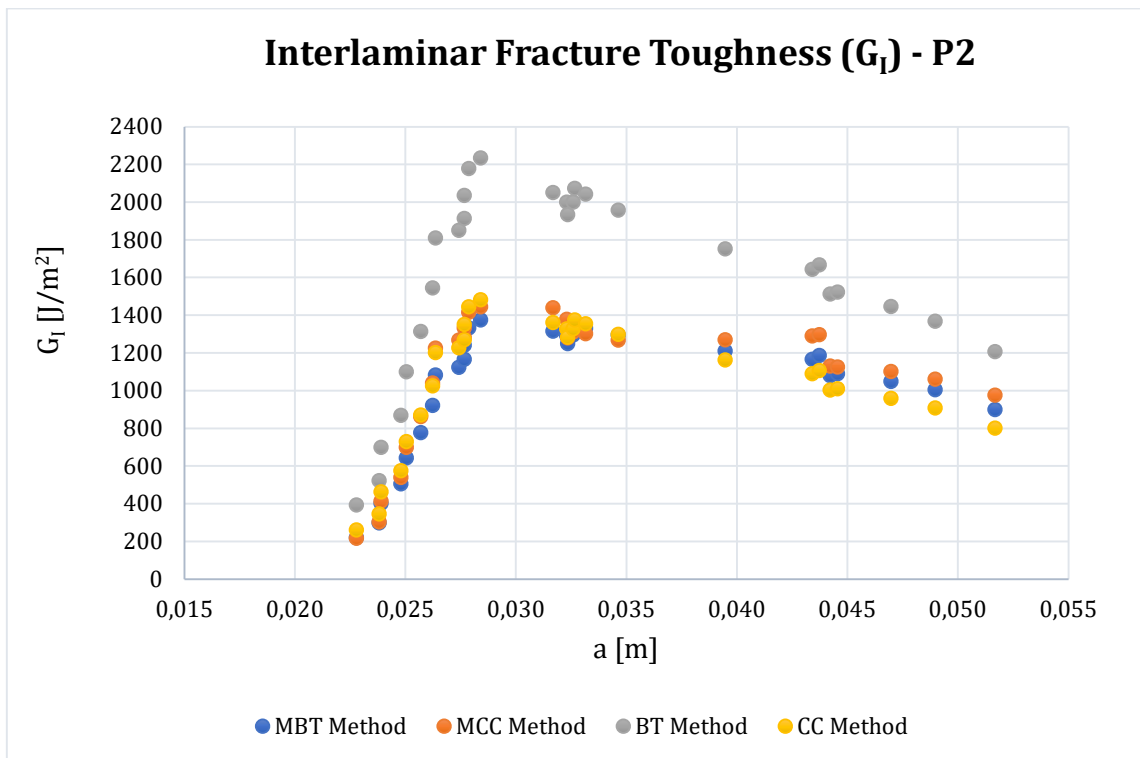
Specimen	$ \Delta $	$n$	$A_1$
P1	0.0220	1.8325	307.84
P2	0.0177	1.9912	281.47
P3	0.0202	1.8790	318.11

Table 26: Parameters related to the methods for data reduction.

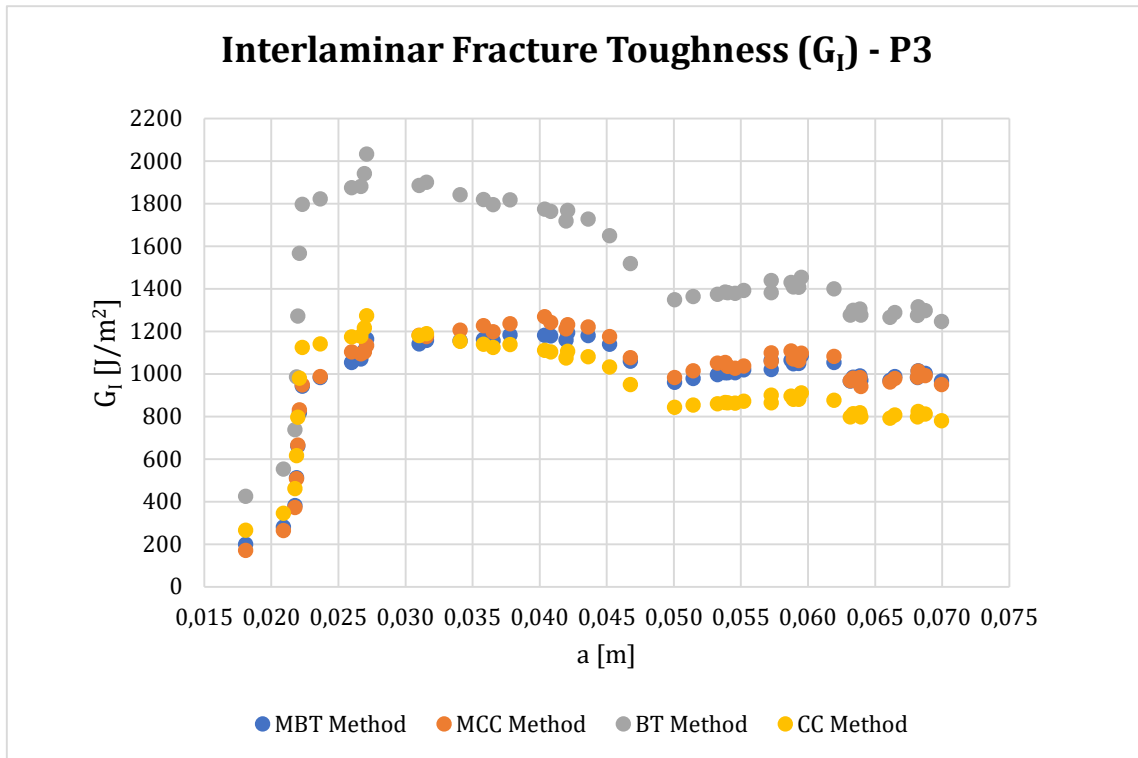
At this point, we finally traced the charts showing the interlaminar fracture toughness ( $G_I$ ) trend for each specimen and each method applied, as explained and graphically showed below.



Graph 20: P1 specimen fracture toughness comparison.



Graph 21: P2 specimen fracture toughness comparison.



Graph 22: P3 specimen fracture toughness comparison.

The first consideration that must be underlined is that, as confirmed by ASTM D 5528-01 [52], the Beam Theory (BT) method overestimates the value of the interlaminar fracture toughness, and for this reason it is not taken into account. Then, from the charts it is possible to observe that, generally, the values obtained with the Modified Beam Theory method lies in between the Compliance Calibration as lower limit, and the Modified Compliance Calibration as the upper one.

Regarding P1 specimen, it is clearly visible that  $G_I$  grows more rapidly in correspondence with the delamination due to the presence of the PTFE sheet, more or less until  $a = 25 \text{ mm}$ . Then it stabilizes around a mean value with a slow increase due to the crack propagation inside the composite panel. This trend is similar for P3 specimen too, especially for the first part, while the main difference is that here a drop in the  $G_I$  average value for  $a = 45 - 50 \text{ mm}$  is encountered, after which a slight increase occurs. Finally, with regard to P2 specimen, the trend undergoes a significant variation with respect to P1 and P3: indeed, it exhibits a sort of  $G_I$  peak after the rapid growth, then followed by a more rapid decrease if compared to the other specimens. This happens for a value of delamination length ranging from 25 to 35 mm.



Recalling that the specimens studied in this thesis work do not comply with the DCB ASTM Standard, the obtained results are mainly qualitative and for this reason the mean values calculated over each data-reduction method applied are presented below.

<b>Interlaminar Fracture Toughness <math>G_I</math> [<math>J/m^2</math>]</b>				
<b>Specimen</b>	<b>BT</b>	<b>MBT</b>	<b>CC</b>	<b>MCC</b>
<b>P1</b>	1362.28	871.19	832.13	887.07
<b>P2</b>	1596.01	1033.63	1059.32	1094.86
<b>P3</b>	1475.86	989.43	924.38	1008.80

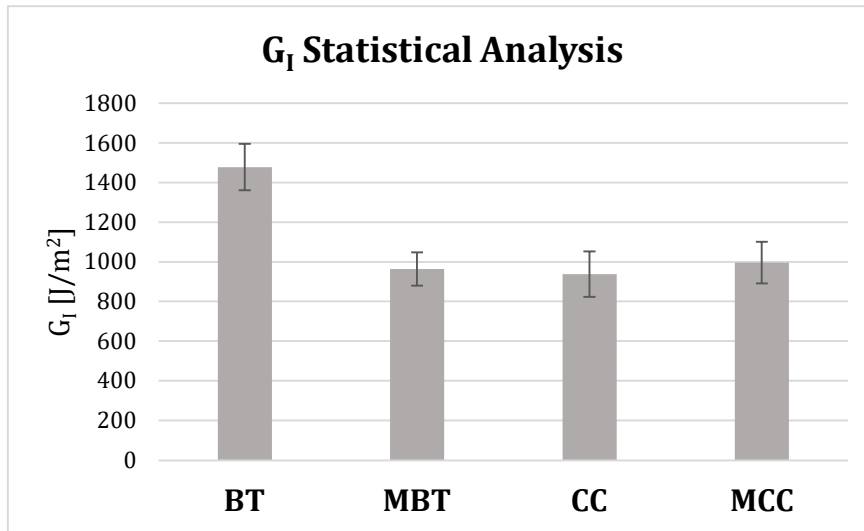
*Table 27: Interlaminar fracture toughness mean values for every specimen.*

The mean values too confirm the Beam Theory overestimation and inadequacy, then the MBT, CC and MCC trend previously described is here almost demonstrated. Recalling the limits and imperfections of the hand lay-up process, it is very promising that the highest  $G_I$  mean values are those belonging to P2 specimen, which occupied the central position in the produced composite panel. Indeed, this indicate that the resin has a better distribution and compactness in that area, then the overall panel homogeneity reached a suitable level, probably because the heat applied by the hot press was more uniform and no edge effects affected the product.

To complete the analysis on the interlaminar fracture toughness, a statistical survey was carried out on every adopted analytical method, a summary of which is depicted in Table 28 and Graph 23.

<b>Interlaminar Fracture Toughness <math>G_I</math> [<math>J/m^2</math>]</b>		
<b>Method</b>	<b>Mean value</b>	<b>Standard deviation</b>
<b>BT</b>	1478.05	116.88
<b>MBT</b>	964.75	83.99
<b>CC</b>	938.61	114.26
<b>MCC</b>	996.91	104.40

*Table 28:  $G_I$  mean values and standard deviations.*



Graph 23:  $G_I$  statistical analysis conducted on every applied method.

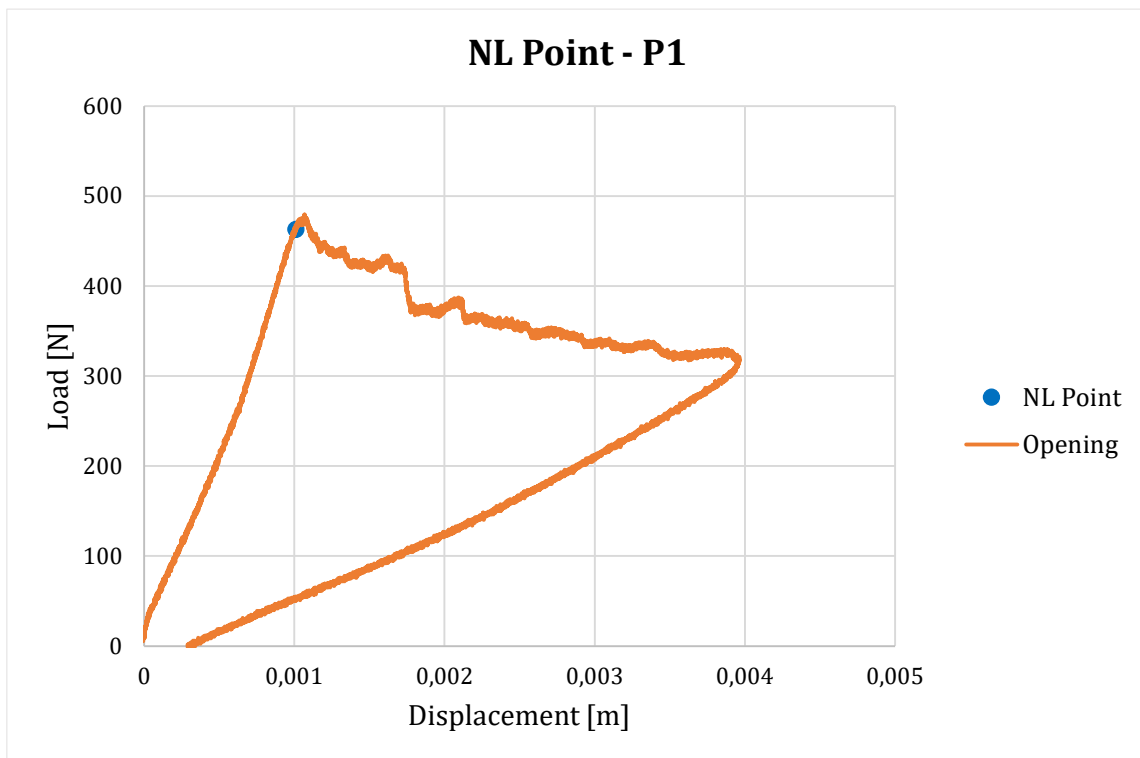
Again, this statistical analysis is a further confirmation of the excessive overestimation applied by the Beam Theory approach, and it still recognize that the MBT values averagely lie in between those belonging to CC and MCC methods, with the least data dispersion among all.

### 4.2.2.3 Determination of the Critical Interlaminar Fracture Toughness ( $G_{IC}$ )

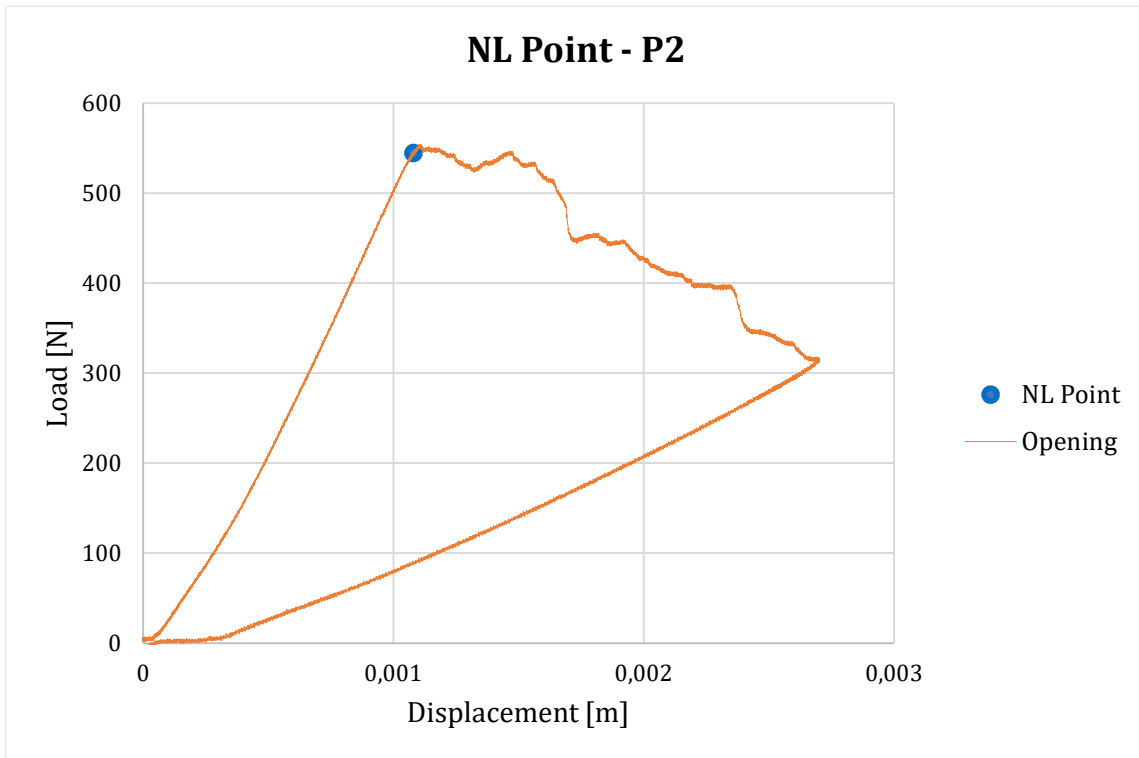
To conclude the mechanical assessment,  $NL$ ,  $+5\%C_0$  and  $P_{MAX}$  critical points were evaluated, while the VIS point was not taken into consideration because the employed experimental apparatus did not allow to detect it.  $P_{MAX}$  point has been studied as an alternative to the  $+5\%C_0$  point for the reason below. As easily noticeable from Graph 25 and Graph 26, both P2 and P3 curves do not start exactly from the origin but their onset is shifted to the right, and this aspect strongly influenced the data processing phase, precisely for the investigation of  $+5\%C_0$  and  $P_{MAX}$  points. For the sake of simplicity, the  $+5\%C_0$  line was found by interpolating the machine data up to the NL point chosen before, thus obtaining a proper linear region of the load-displacement curves, even in the case where their onset is shifted from the origin. The critical points results are showed in Table 29, while their identification is depicted in the charts.

Specimen	$NL$		$+5\%C_0$		$P_{MAX}$	
	$P_C$ [N]	$\delta_C$ [m]	$P_C$ [N]	$\delta_C$ [m]	$P_C$ [N]	$\delta_C$ [m]
<b>P1</b>	463.313	0.0010	468.569	0.0011	479.513	0.0011
<b>P2</b>	544.518	0.0011	552.733	0.0012	554.681	0.0011
<b>P3</b>	539.026	0.0009	541.934	0.0009	560.671	0.0011

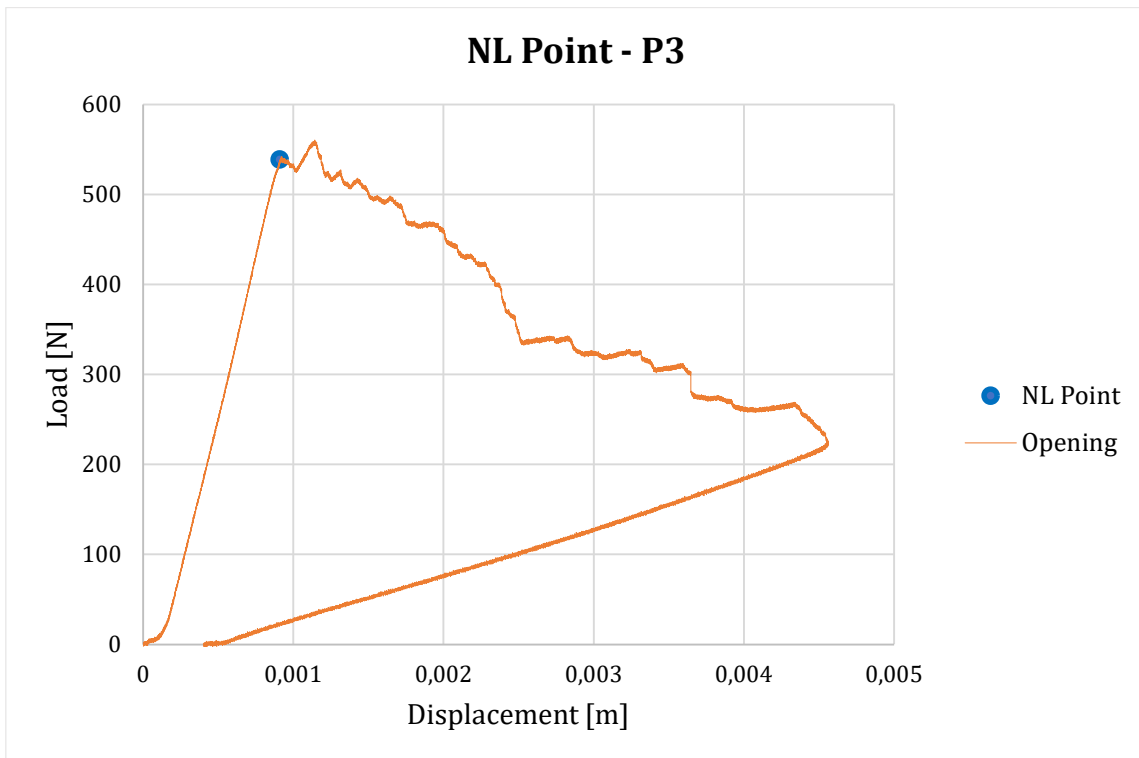
Table 29: DCB critical points for critical interlaminar fracture toughness.



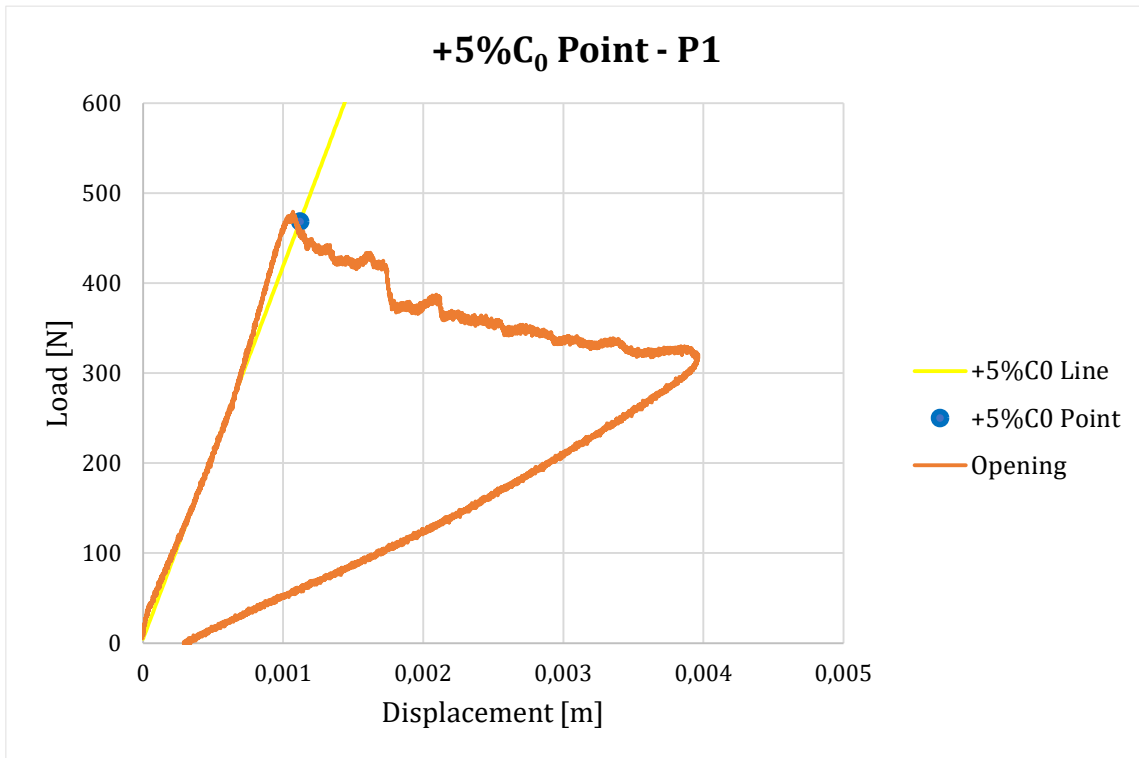
Graph 24: P1 specimen NL point detection.



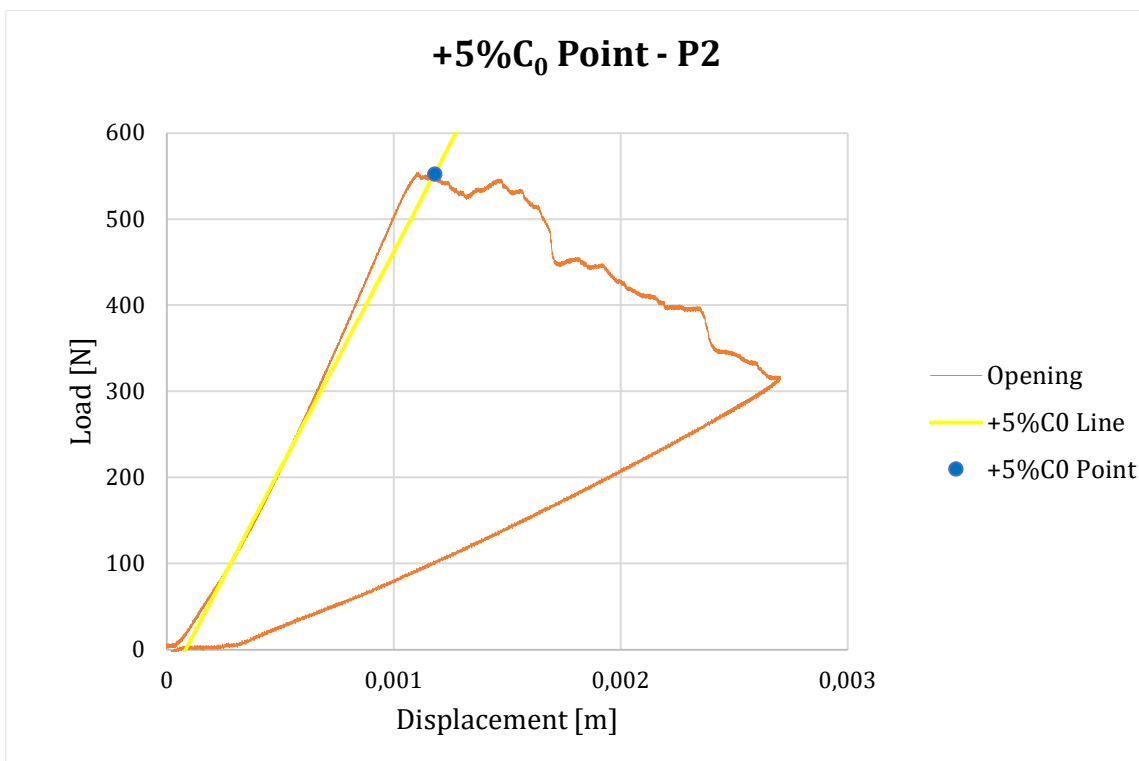
Graph 25: P2 specimen NL point detection.



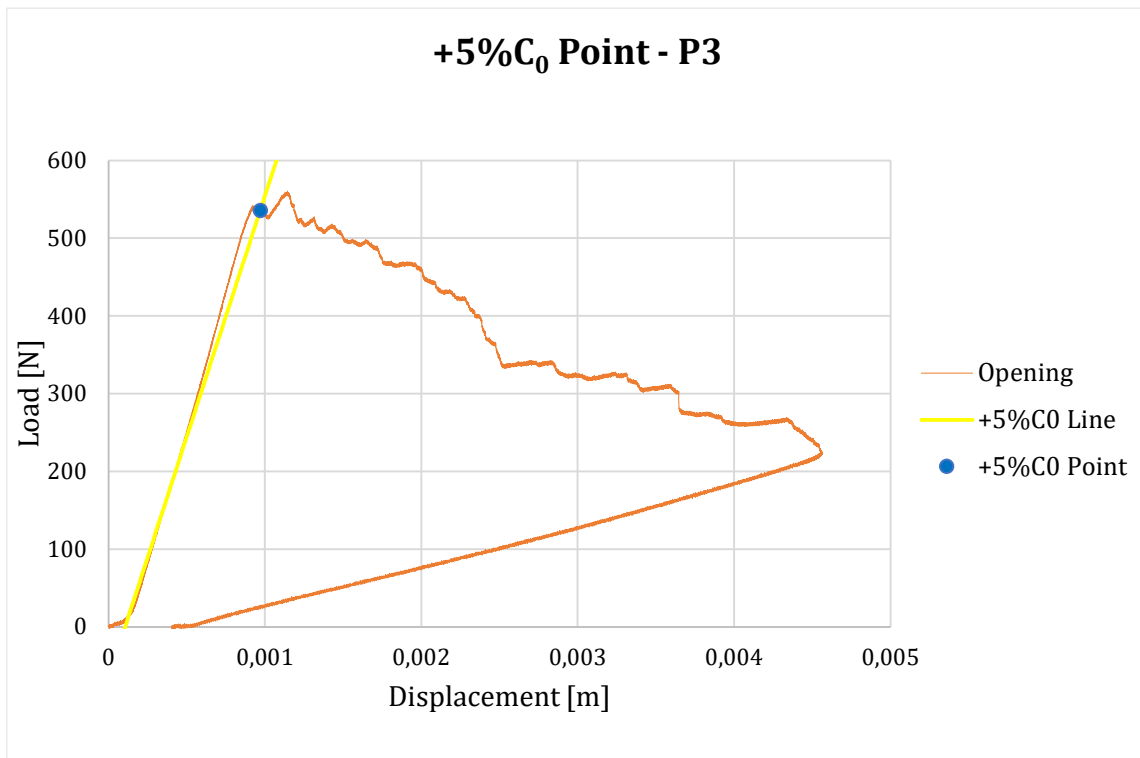
Graph 26: P3 specimen NL point detection.



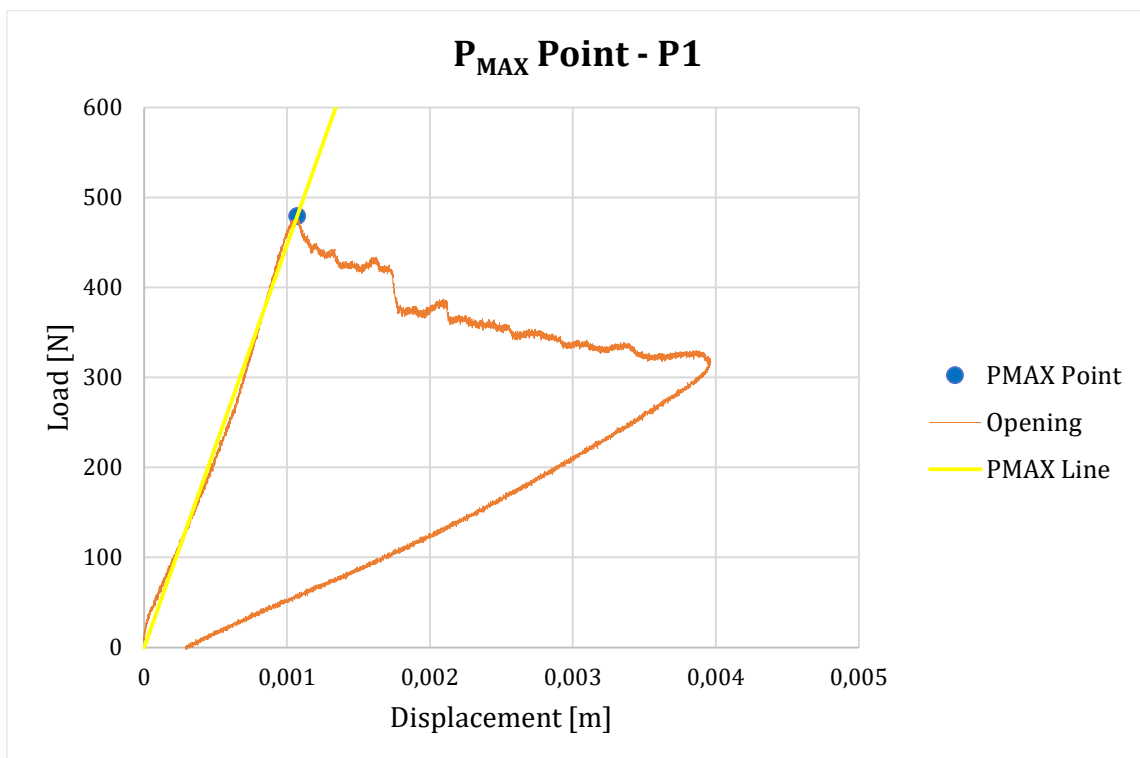
Graph 27: P1 specimen +5% $C_0$  point detection.



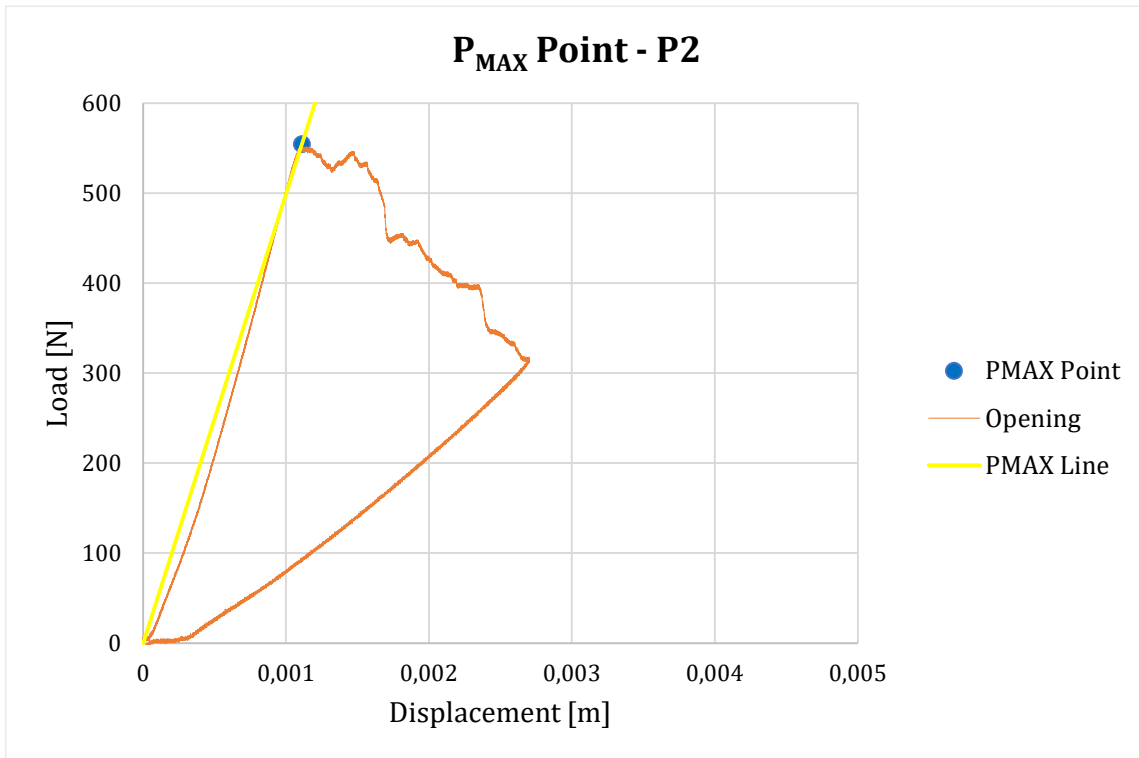
Graph 28: P2 specimen +5% $C_0$  point detection.



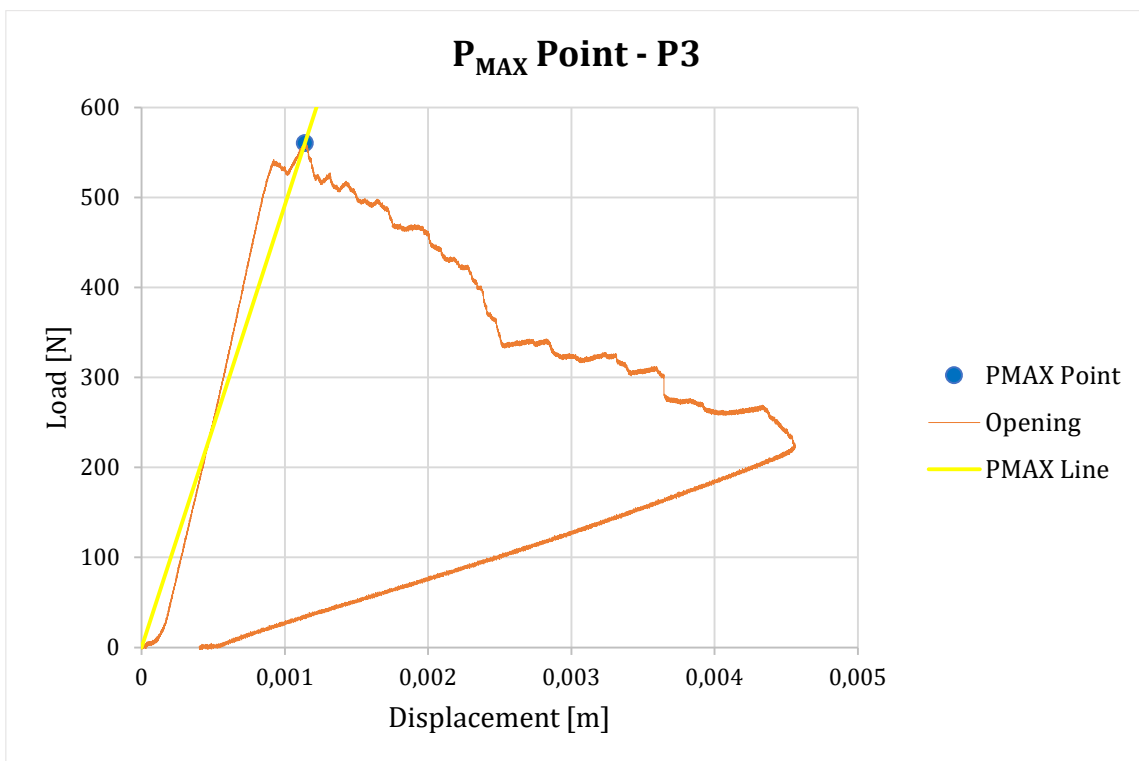
Graph 29: P3 specimen +5% $C_0$  point detection.



Graph 30: P1 specimen  $P_{MAX}$  point detection.



Graph 31: P2 specimen P<sub>MAX</sub> point detection.



Graph 32: P3 specimen P<sub>MAX</sub> point detection.

From the graphs above, it can be observed that for P1 and P2 specimens the points obtained with the  $+5\%C_0$  and  $P_{MAX}$  methods practically coincide (a bigger difference in the first specimen can be due to the fact that the  $+5\%C_0$  method was delineated to overcome the problems related to the linear region of P2 and P3 curves, as explained before). Moreover, for P1 they are much close to the  $NL$  point, while for P2 specimen they are almost perfectly matched. Regarding P3 specimen, the  $+5\%C_0$  point is more similar to that obtained with  $NL$  method than the one obtained with  $P_{MAX}$  approach. All these behaviour discrepancies are probably related to the second segment of each curve, which tends to differ much more among the three specimens. For example, it is possible to observe that the transition between the first and second segment of P1 and P2 specimens averagely happens at the maximum point, while this is graphically not true for P3, where the transition precedes the achievement of the maximum load by the machine. Also in this case it is worth mentioning that the central specimen, P2, has showed the least error between the values found with these three different approaches, again demonstrating its superior quality with respect to the others.

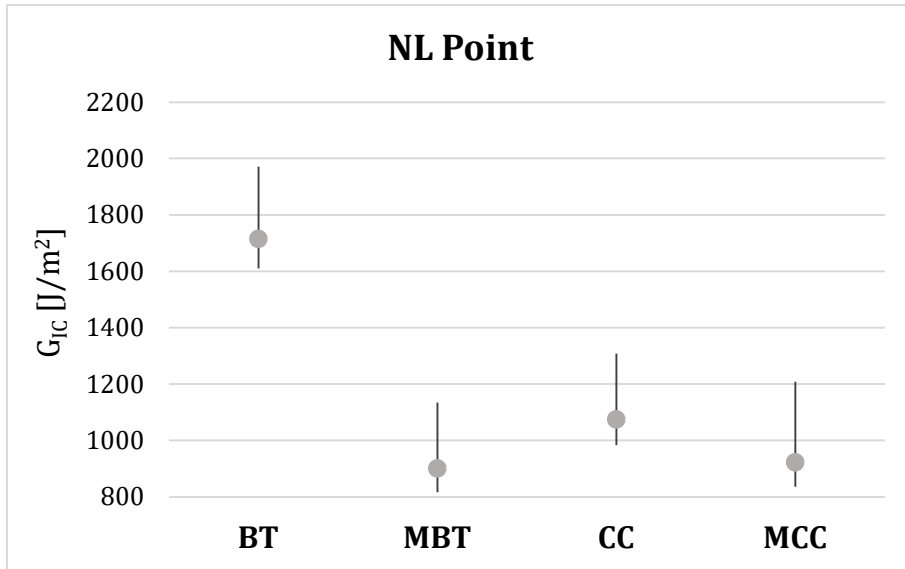
To conclude this last analysis, the average values of the critical interlaminar fracture toughness ( $G_{IC}$ ) for the previous critical points are evaluated and presented in the Table below.

<b>Critical Interlaminar Fracture Toughness <math>G_{IC}^{NL}</math> [J/m<sup>2</sup>]</b>				
<b>Specimen</b>	<b>BT</b>	<b>MBT</b>	<b>CC</b>	<b>MCC</b>
<b>P1</b>	1609.92	817.19	983.39	835.83
<b>P2</b>	1971.12	1134.26	1308.30	1208.16
<b>P3</b>	1715.15	900.52	1074.25	922.59
<b>Critical Interlaminar Fracture Toughness <math>G_{IC}^{+5\%C_0}</math> [J/m<sup>2</sup>]</b>				
<b>Specimen</b>	<b>BT</b>	<b>MBT</b>	<b>CC</b>	<b>MCC</b>
<b>P1</b>	1791.00	909.11	1094.00	904.16
<b>P2</b>	2182.75	1256.04	1448.76	1306.13
<b>P3</b>	1724.40	905.38	1080.05	929.23
<b>Critical Interlaminar Fracture Toughness <math>G_{IC}^{P_{MAX}}</math> [J/m<sup>2</sup>]</b>				
<b>Specimen</b>	<b>BT</b>	<b>MBT</b>	<b>CC</b>	<b>MCC</b>
<b>P1</b>	1832.83	930.34	1119.55	932.43
<b>P2</b>	2007.91	1155.43	1332.71	1238.32
<b>P3</b>	2180.47	1144.84	1365.70	1111.49

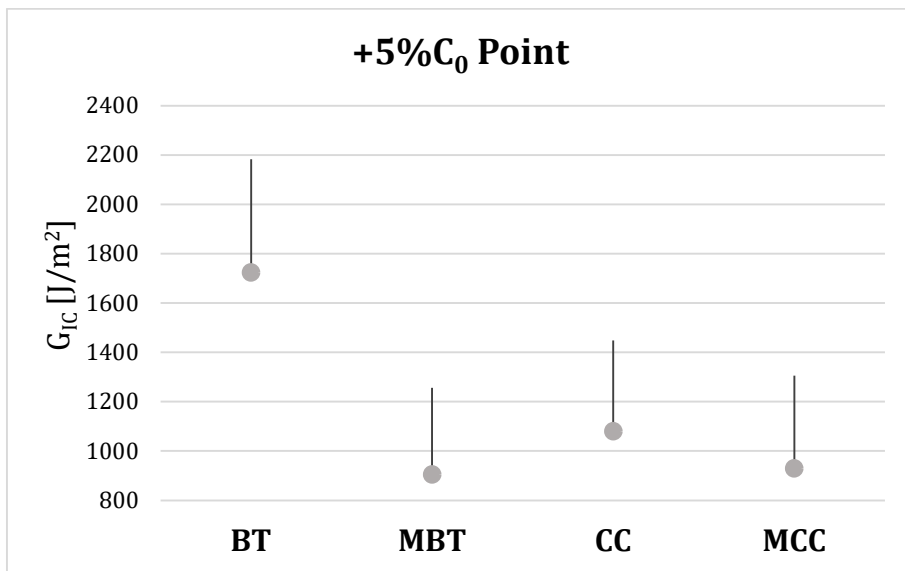
Table 30: Statistical analysis on the critical fracture toughness values with respect to each method applied.



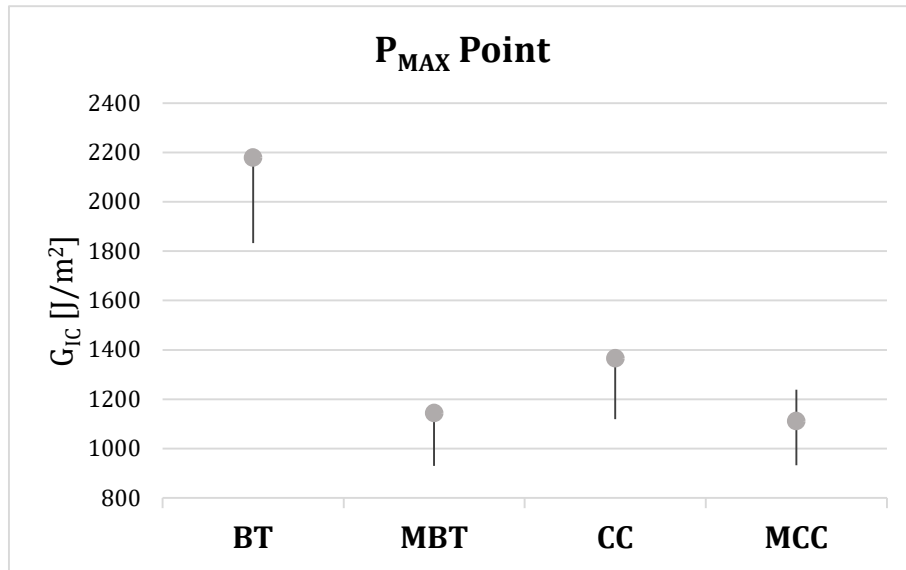
As already demonstrated for the previous  $G_I$  values, the Beam Theory approach applies an excessive overestimation. Then, the best-fitting data regarding the two most reliable methods (MBT and MCC) belongs to the specimen P2, which again possesses the highest values for  $G_{IC}$ . A graphical representation of the trends is show here below.



Graph 33:  $G_{IC}^{NL}$  comparison.



Graph 34:  $G_{IC}^{+5\%C_0}$  comparison.



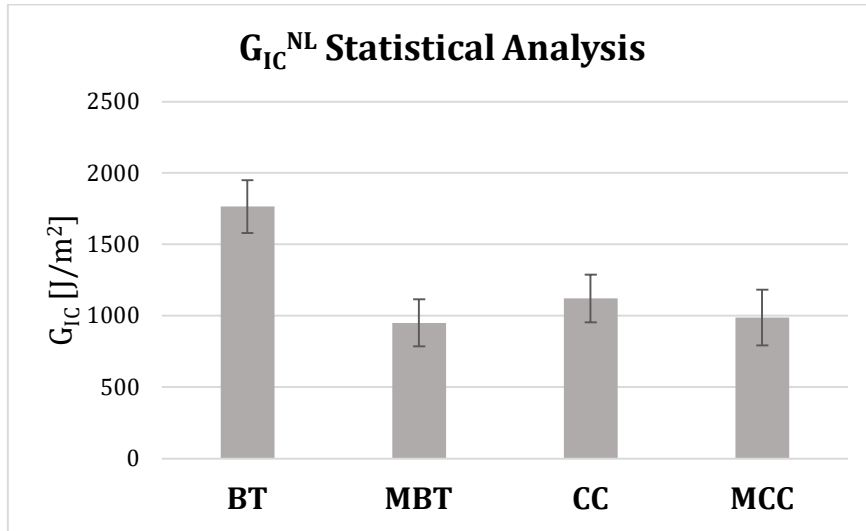
Graph 35:  $G_{IC}^{P_{MAX}}$  comparison.

A statistical survey has been conducted on the obtained results, thus showing again the mean values and standard deviations with respect to each analytical method applied for data reduction.

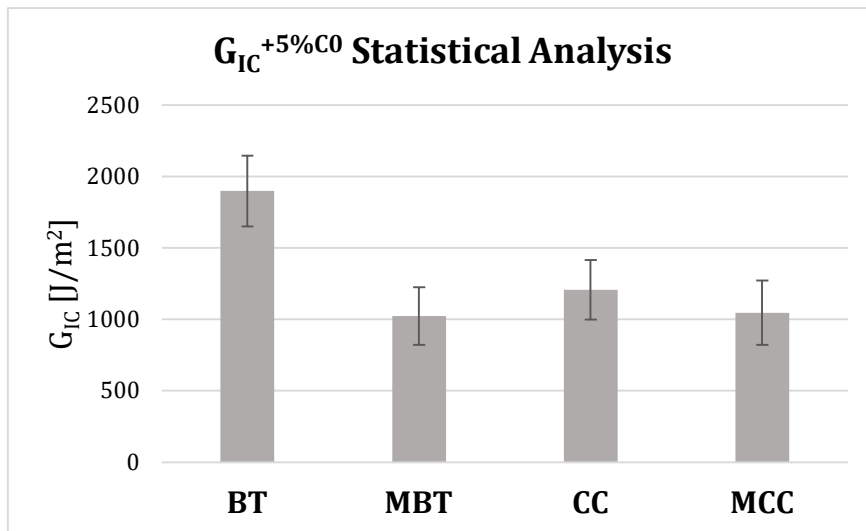
Critical Interlaminar Fracture Toughness $G_{IC}^{NL}$ [J/m <sup>2</sup> ]		
Method	Mean value	Standard deviation
BT	1765.39	185.77
MBT	950.66	164.37
CC	1121.98	167.63
MCC	988.86	194.81
Critical Interlaminar Fracture Toughness $G_{IC}^{+5\%C_0}$ [J/m <sup>2</sup> ]		
Method	Mean value	Standard deviation
BT	1899.38	247.65
MBT	1023.51	201.39
CC	1207.61	208.97
MCC	1046.51	225.19
Critical Interlaminar Fracture Toughness $G_{IC}^{P_{MAX}}$ [J/m <sup>2</sup> ]		
Method	Mean value	Standard deviation
BT	2007.07	173.82
MBT	1076.87	127.01
CC	1272.66	133.61
MCC	1094.08	153.69

Table 31:  $G_{IC}$  mean values and standard deviations.

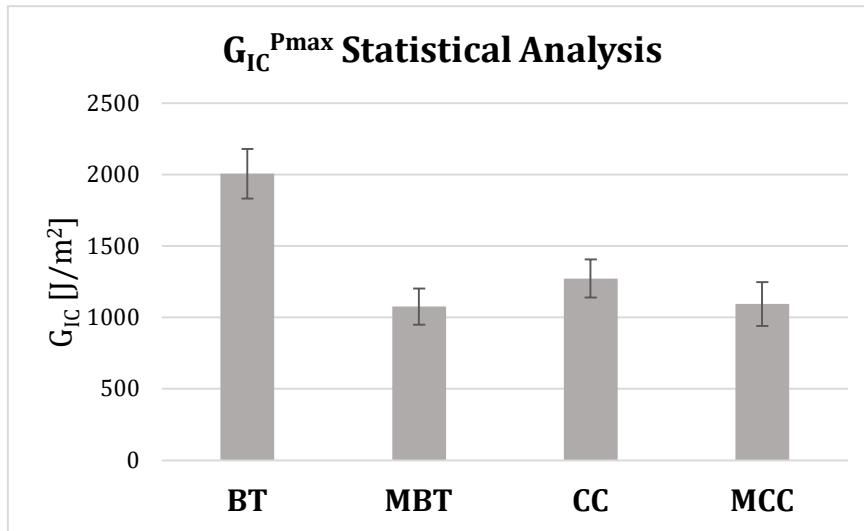
Data shown in Table 31 demonstrate that even for the critical interlaminar fracture toughness, the Modified Beam Theory approach has the least dispersed trend, as shown in Graph 36, Graph 37 and Graph 38.



Graph 36:  $G_{IC}^{NL}$  statistical analysis applied on every adopted method.



Graph 37:  $G_{IC}^{+5\%CO}$  statistical analysis applied on every adopted method.



Graph 38:  $G_{IC}^{Pmax}$  statistical analysis applied on every adopted method.

The final analysis on critical fracture toughness obtained with every analytical method and for the previously seen critical points once again stresses the inadequacy of the Beam Theory approach and the fact, as noted before, that the MBT results are averagely intermediate with respect to CC and MCC approaches

### 4.3 REPAIR CYCLE: EPOXY RESIN SELF-HEALING

The repair cycle was applied to P1 specimen after the DCB test analysis, by placing it in hot press with the exclusion of the surfaced covered by the hinges. The data shown in must be taken into consideration for this phase.

<b>Repair cycle</b>	Temperature [ $^{\circ}\text{C}$ ]	$T$	<b>200</b>
	Time interval [ $\text{min}$ ]	$t$	10
Specimen Area under pressure [ $\text{mm}^2$ ]		$A_{P1}$	2185
Hot press pressure cylinder area [ $\text{mm}^2$ ]		$A_{CYLINDER}$	15625
Hot press minimum pressure [ $\text{bar}$ ]		$P_{CYLINDER}$	3
Actual machine pressure [ $\text{bar}$ ]		$P_{P1}$	30

Table 32: Technical data needed for the repair cycle.

A full-length image of the repaired specimen is shown below, together with magnified picture of the specimen area where the hinges were applied, and the crack initiated. Via visual inspection, the P1 specimen seemed completely repaired since the epoxy resin has fully healed the crack along its entire length.



Figure 69: Repaired P1 specimen.



Figure 70: Mid-plane zoomed image of the repairing effect.

### 4.3.1 DCB test analysis

To carry out a comparison between the pristine and the repaired specimen, a second DCB test was performed on P1 with the same procedure explained in Par. 3.7.1. Here below two frames extracted from the recording video are reported.

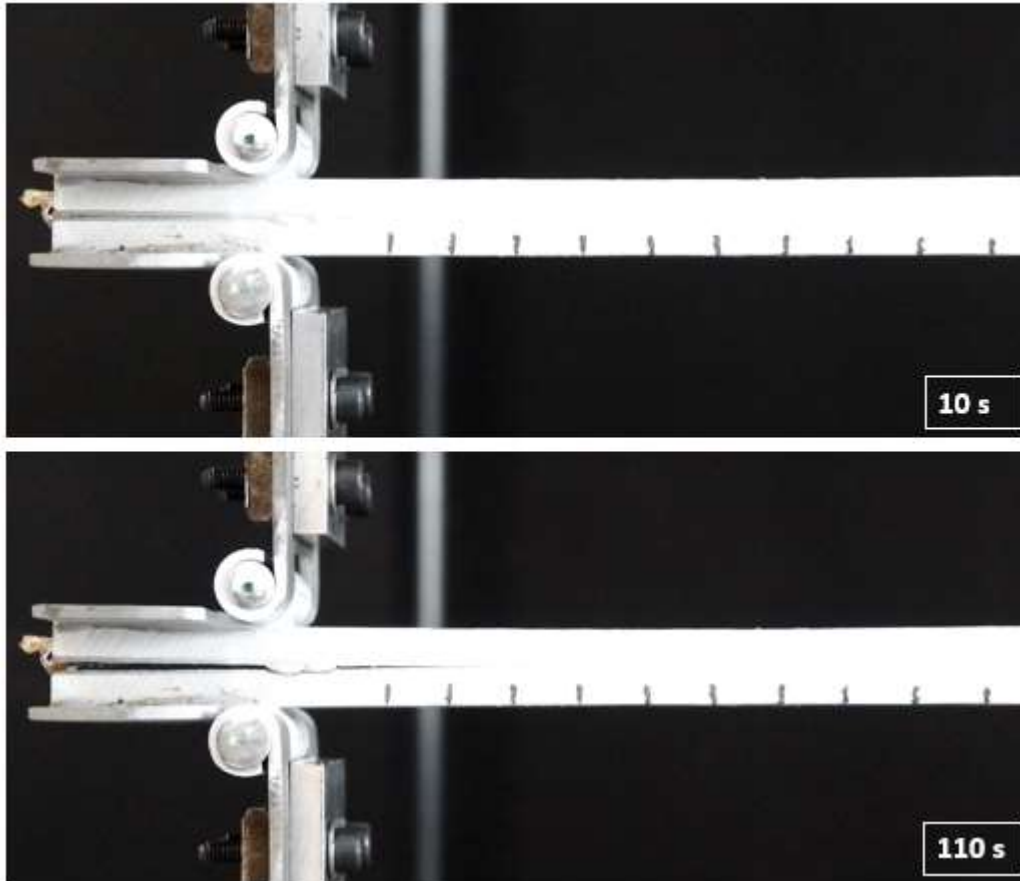


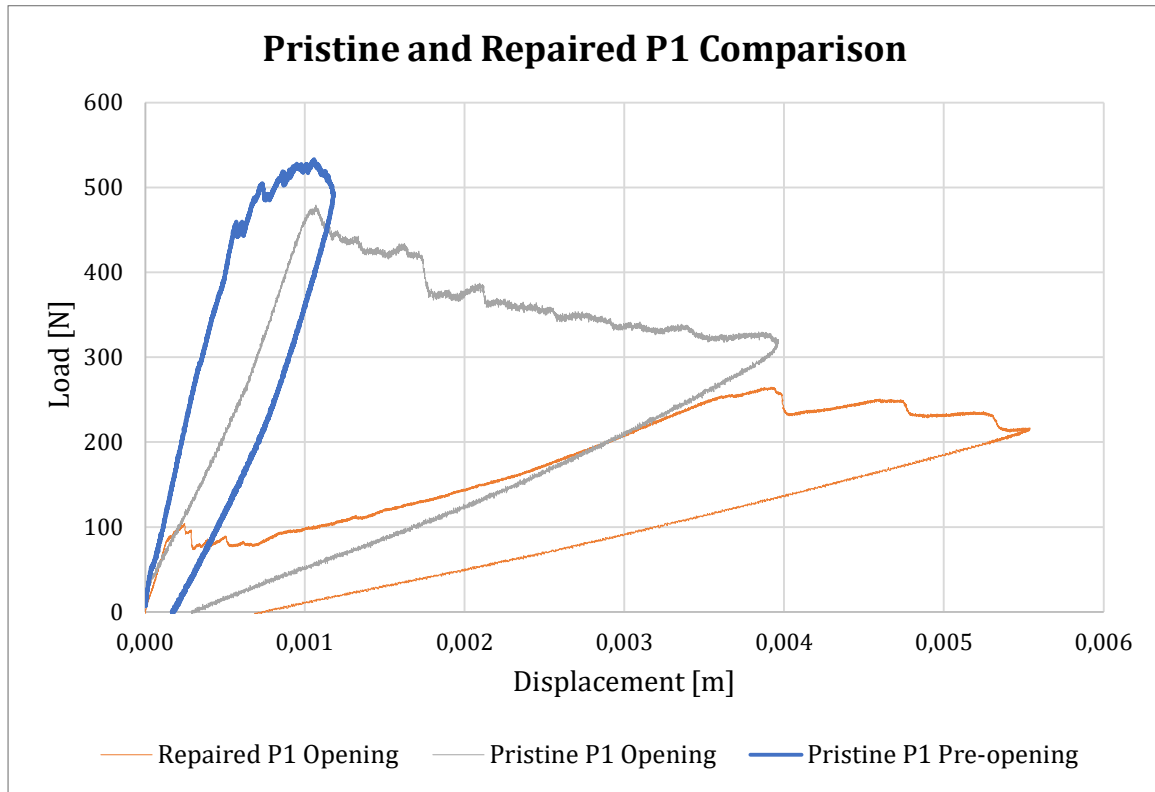
Figure 71: Proof of the abrupt and rapid crack growth during the test.

#### 4.3.1.1 Pre-opening

After more or less a couple of minutes, the crack growth was so rapid and abrupt that the possibility to perform the pre-opening test was denied (Figure 71). These visual results suggest that the specimen did not completely heal throughout its whole interface area; probably due to a non-constant heating of the hot press, the internal region of the specimen has not reached the desired temperature of  $200^{\circ}\text{C}$  for the required period of time (10 seconds). Moreover, a non-negligible margin of error on the applied pressure must be absolutely taken into account as the value of the area of the hot press cylinder was only supposed from its diameter. As a consequence, the disulphide bonds of the dynamic epoxy resin, which are weakly dynamic covalent bond that can undergo bond exchange reactions under heating conditions, had no sufficient time to tightly reform in the inner region, thus acting as an onset for the crack to quickly reach its previous  $a_0$  length.

#### 4.3.1.2 Opening

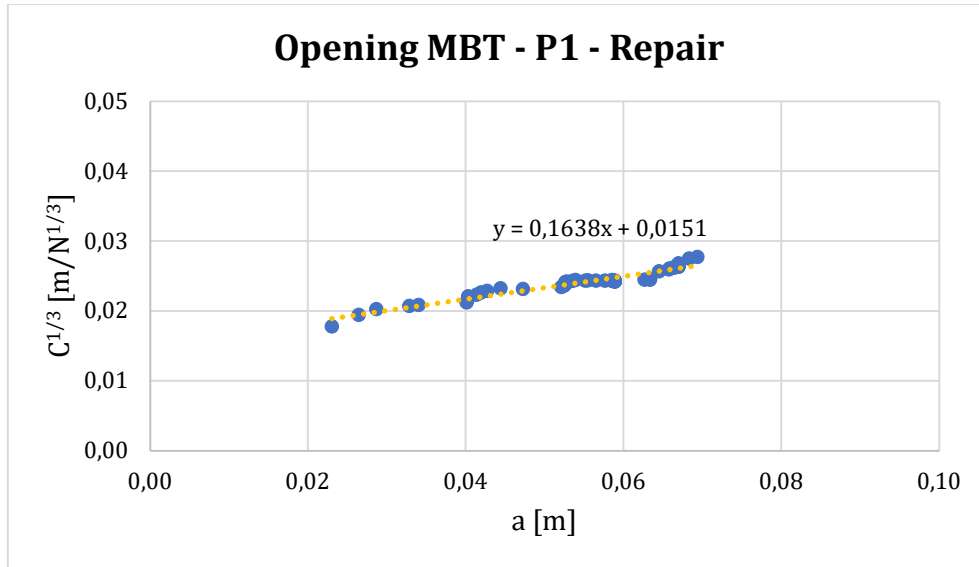
The opening phase of the DCB test was conducted and monitored as for the pristine specimens, and due to the unexpected visual results of the pre-opening attempt, a comparison has been done between the previous data collected for P1 and the ones achieved after repair. This is visible in Graph 39.



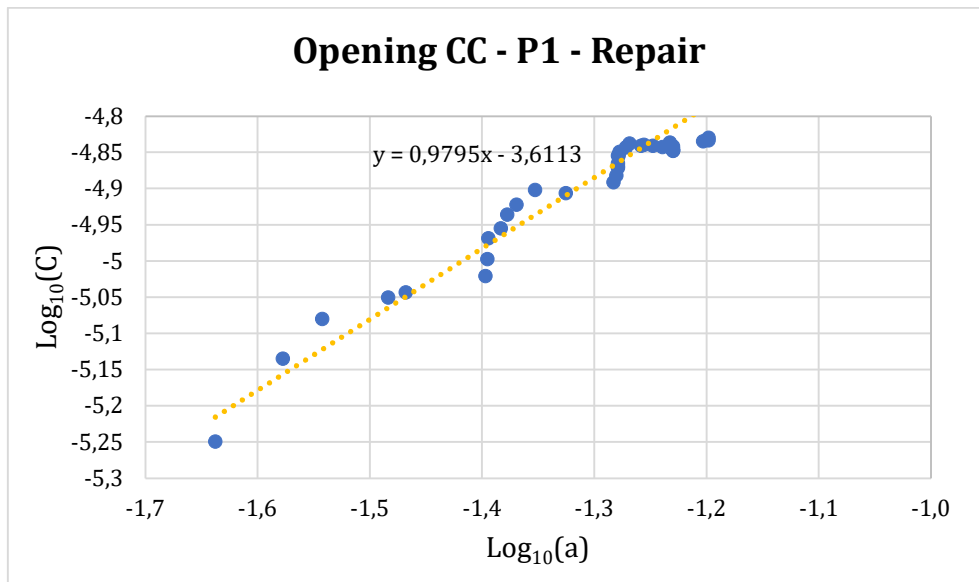
Graph 39: A comparison between the DCB tests of pristine and repaired P1 specimen.

For the reasons explained above, the material repair was only partial, probably concentrated along the specimen perimeter. The first segment of the curve initially follows the opening profile of the pristine specimen while, in a second moment, the crack induced in the previous DCB test grows rapidly with a huge initial axial displacement. This aspect has enormously affected the accuracy of the  $+5\%C_0$  line, which will be examined shortly. Moreover, in this case is quite senseless to compare the trend of crack length as a function of the transverse displacement for P1 specimen, as the two plots have  $\delta$  values of different orders of magnitude. The second segment is generally steadier and less jagged with respect to the ones previously observed, but the residual  $\delta$  value has almost doubled, probably due to secondary dissipative phenomena and the scarce healing efficiency.

By accurately matching every delamination length ( $a$ ) value to the respective machine time and load entities, Mode I interlaminar fracture toughness  $G_I$  was calculated on the basis of dedicated ASTM standard, precisely by methods described in Par. 3.4.4. The adopted methods are depicted in the following graphs.

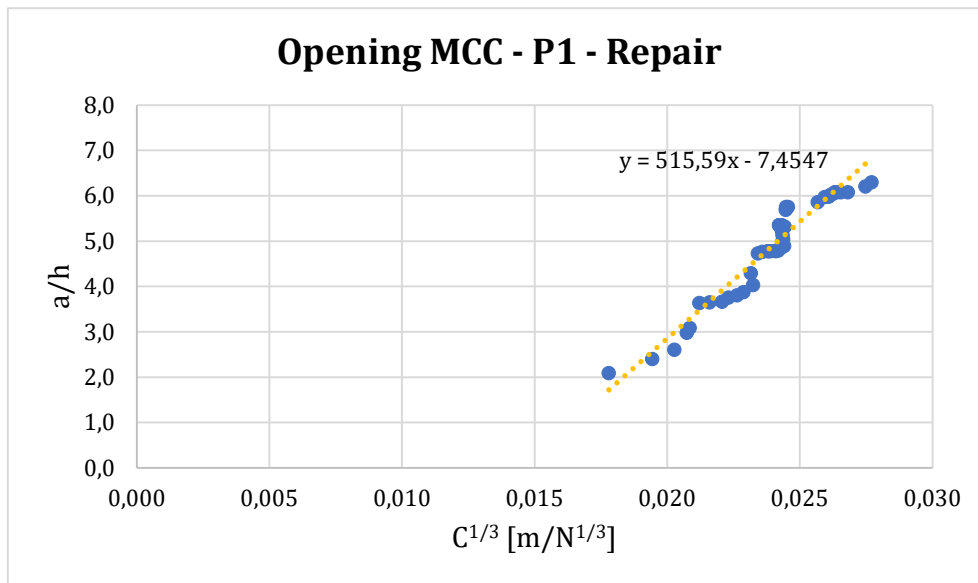


Graph 40: Repaired P1 MBT method application.



Graph 41: Repaired P1 CC method application.





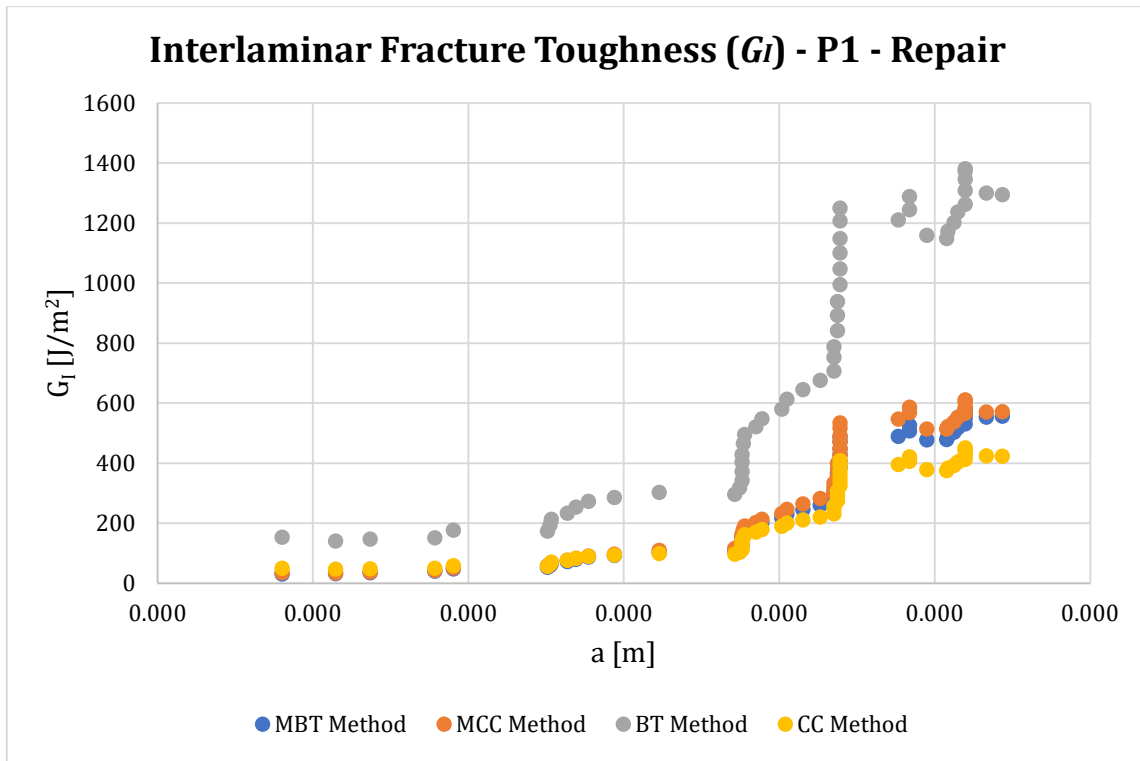
Graph 42: Repaired P1 MCC method application.

The table below shows the quantitative parameters associated with every method applied, compared to the pristine specimen.

Specimen	$ \Delta $	$n$	$A_1$
P1	0.0220	1.8325	307.84
P1 - Repair	0.0922	0.9795	515.59

Table 33: Parameters related to the methods for data reduction.

At this point, we finally traced the charts showing the interlaminar fracture toughness ( $G_I$ ) trend for each method applied, as explained and graphically showed below.



Graph 43: Interlaminar fracture toughness trend of repaired P1 specimen.

After the repair cycle, the interlaminar fracture toughness trend has changed; averagely, the value of delamination length equal to  $a = 50 \text{ mm}$  divides the plot in two regions, where  $G_I$  respectively grows more slowly and rapidly. This phenomenon is directly linked to the alternation, during the DCB test, of regions of abrupt crack growth and moments where it is stalled.

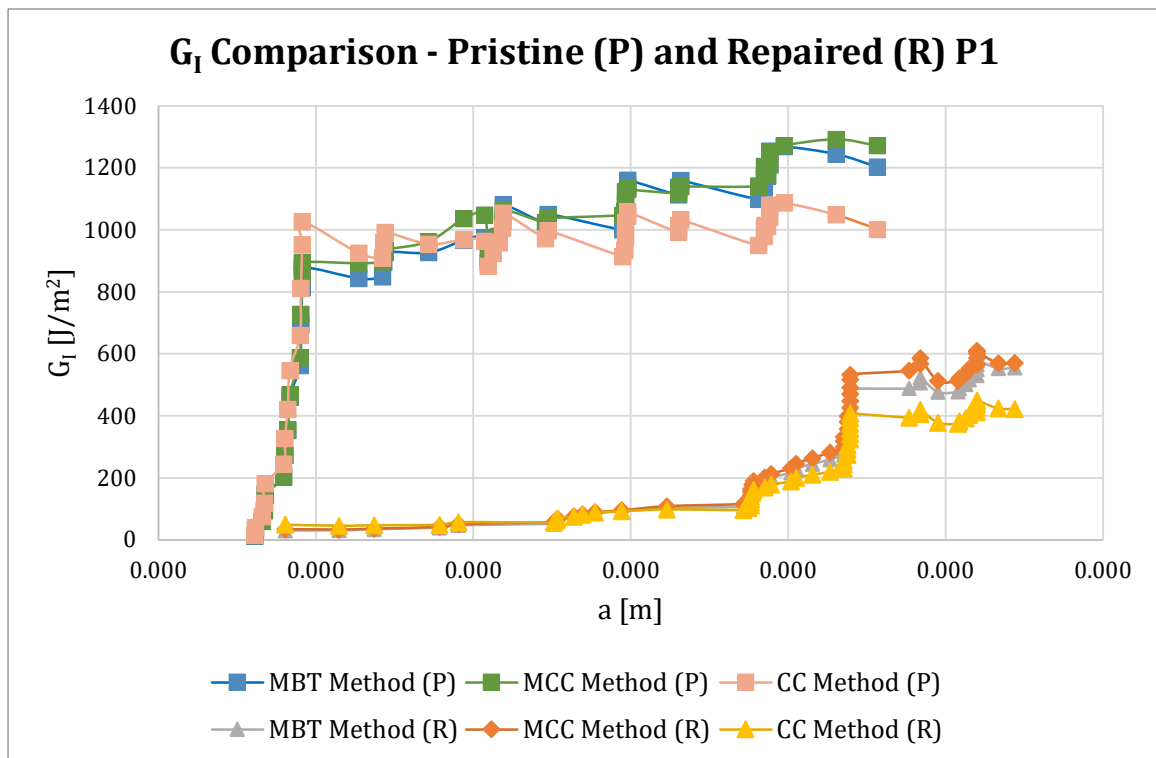
Recalling that the specimens studied in this thesis work do not comply with the DCB ASTM Standard, the obtained results are mainly qualitative and for this reason the mean values calculated over each data-reduction method applied are presented below.

Interlaminar Fracture Toughness $G_I$ [ $\text{J}/\text{m}^2$ ]				
Specimen	BT	MBT	CC	MCC
P1	1362.28	871.19	832.13	887.07
P1 - Repair	740.74	291.11	241.82	313.53
$\Delta G_I$ %	46%	67%	71%	65%

Table 34: Comparison of  $G_I$  values found for pristine and repaired P1 specimen.

With the exception of BT, the other methods display significantly similar values: in this event too, Modified Beam Theory method lies in between CC as lower bound and MCC as upper bound, thus confirming the previously discovered trend. For what concerns the healing efficiency (here displaced as a relative error between the pristine and the repaired value), the reduction of about two thirds of the pristine  $G_I$  values is consistent with the quality of the repair.

A final chart is proposed to display the trend comparison between the pristine and the repaired specimen for the three most reliable methods adopted for data reduction.



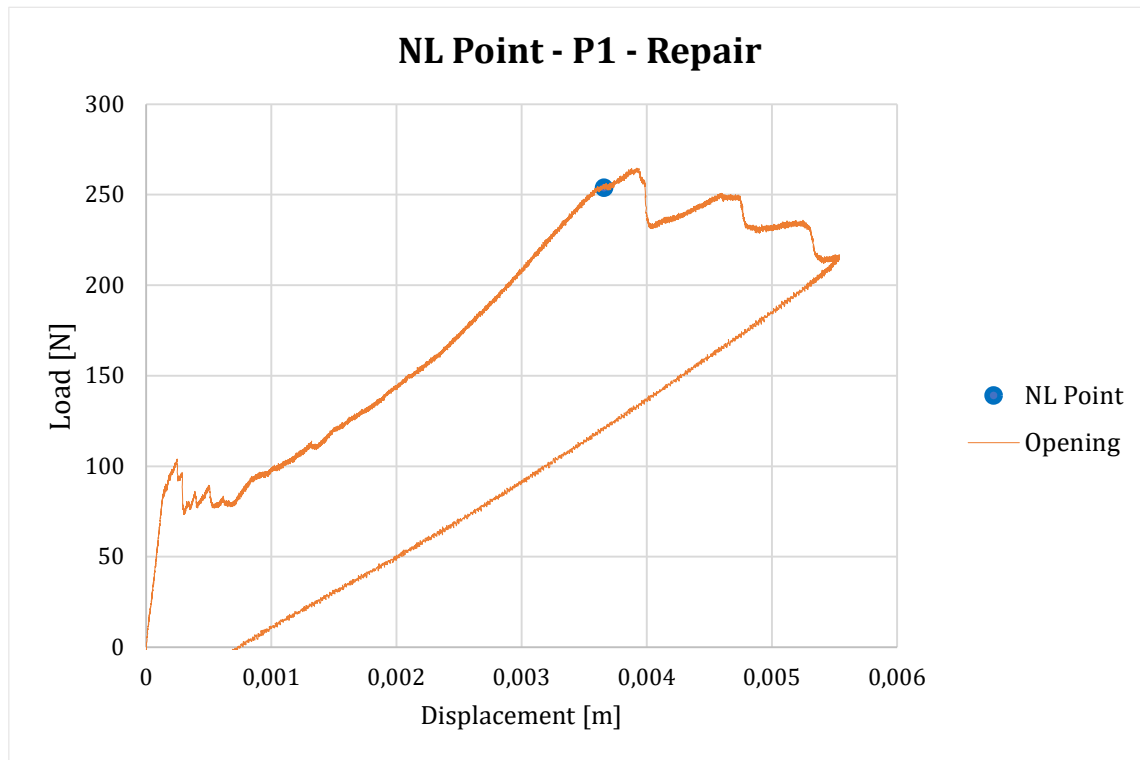
Graph 44: Graphical comparison of interlaminar fracture toughness trend for pristine and repaired specimen.

### 4.3.1.3 Determination and comparison of $G_{IC}$

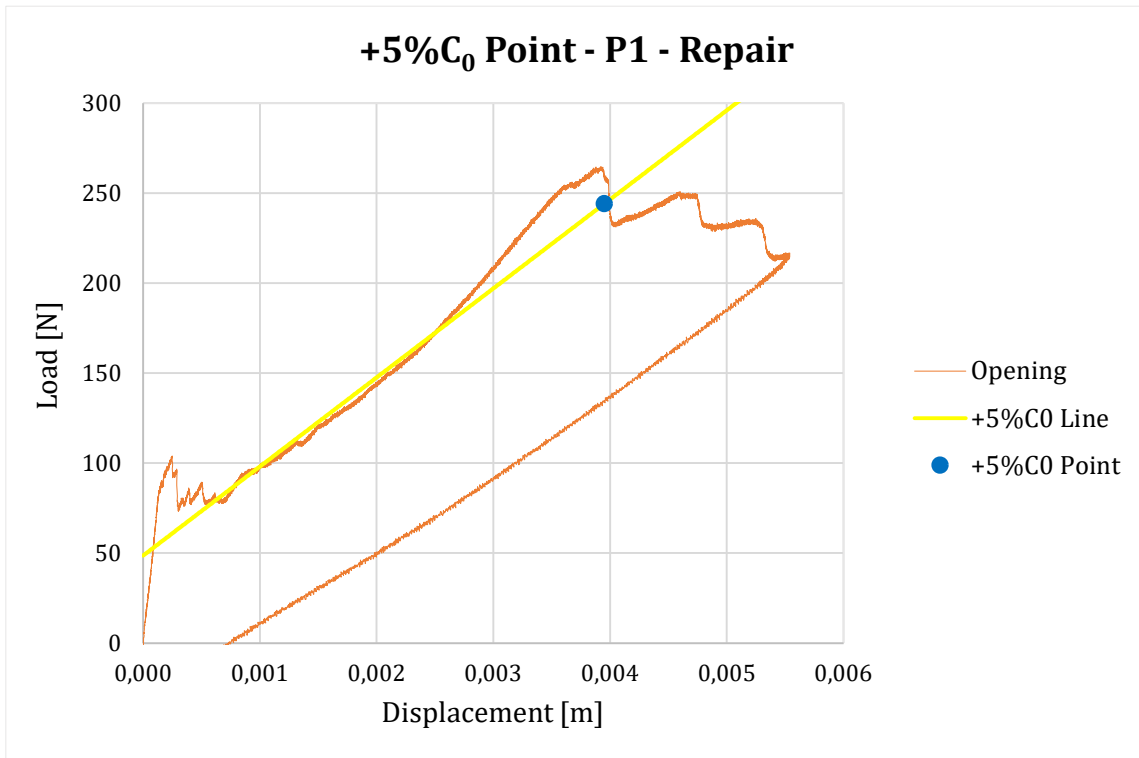
To conclude the mechanical assessment, the  $NL$ ,  $+5\%C_0$  and  $P_{MAX}$  critical points were evaluated again and compared with the ones previously found for pristine P1 specimen. The critical points results are showed in the table below, while their identification is depicted in the following graphs.

Specimen	$NL$		$+5\%C_0$		$P_{MAX}$	
	$P_C$ [N]	$\delta_C$ [m]	$P_C$ [N]	$\delta_C$ [m]	$P_C$ [N]	$\delta_C$ [m]
<b>P1</b>	463.313	0.0010	468.569	0.0011	479.513	0.0011
<b>P1 - Repair</b>	253.881	0.0037	244.179	0.0040	264.588	0.0039

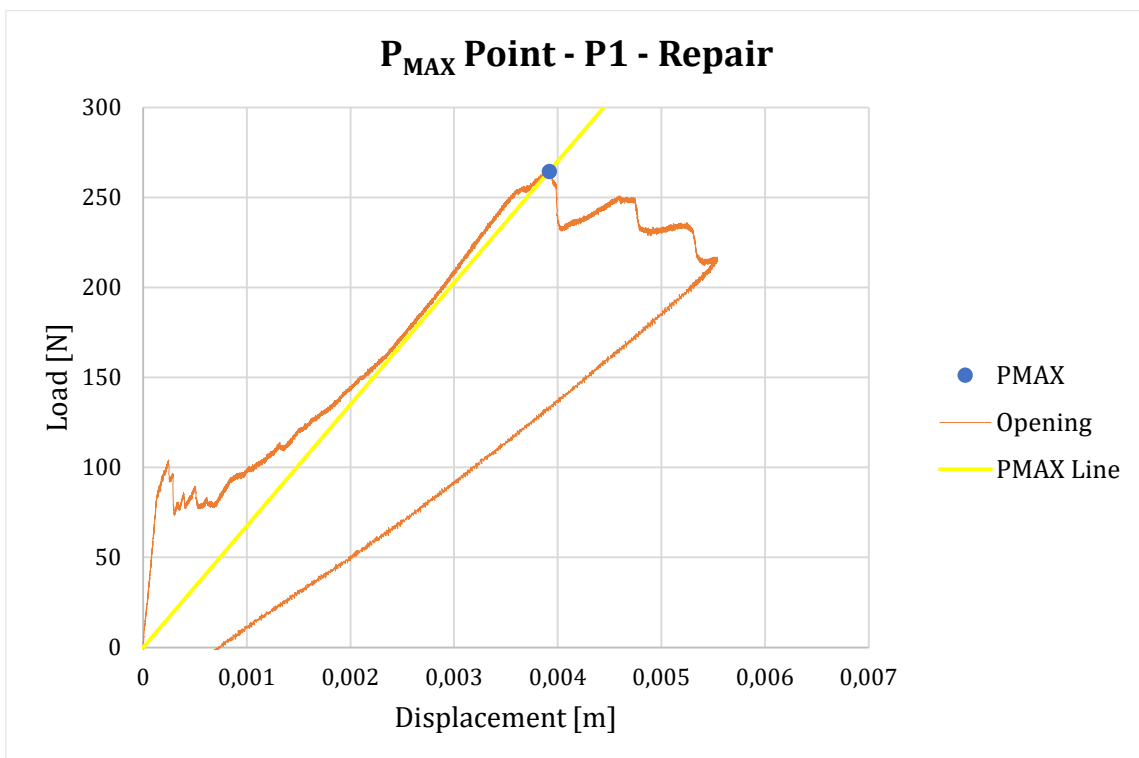
Table 35: Critical points comparison between pristine and repaired specimen.



Graph 45: NL point for repaired P1 specimen.



*Graph 46: +5% $C_0$  point for repaired P1 specimen.*



*Graph 47:  $P_{MAX}$  point for repaired P1 specimen.*

To conclude this last analysis, the average values of the critical interlaminar fracture toughness ( $G_{IC}$ ) for the previous critical points are evaluated and presented in the Table below.

<b>Critical Interlaminar Fracture Toughness <math>G_{IC}^{NL}</math> [J/m<sup>2</sup>]</b>				
<b>Specimen</b>	<b>BT</b>	<b>MBT</b>	<b>CC</b>	<b>MCC</b>
<b>P1</b>	1609.92	817.19	983.39	835.83
<b>P1 - Repair</b>	3264.08	645.37	1065.72	535.32
$\Delta G_{IC}^{NL}\%$	/	21%	-8%	36%
<b>Critical Interlaminar Fracture Toughness <math>G_{IC}^{+5\%C_0}</math> [J/m<sup>2</sup>]</b>				
<b>Specimen</b>	<b>BT</b>	<b>MBT</b>	<b>CC</b>	<b>MCC</b>
<b>P1</b>	1791.00	909.11	1094.00	904.16
<b>P1 - Repair</b>	3393.89	671.04	1108.11	535.33
$\Delta G_{IC}^{+5\%C_0}\%$	/	26%	-1%	41%
<b>Critical Interlaminar Fracture Toughness <math>G_{IC}^{P_{MAX}}</math> [J/m<sup>2</sup>]</b>				
<b>Specimen</b>	<b>BT</b>	<b>MBT</b>	<b>CC</b>	<b>MCC</b>
<b>P1</b>	1832.83	930.34	1119.55	932.43
<b>P1 - Repair</b>	3585.62	708.95	1170.71	585.84
$\Delta G_{IC}^{P_{MAX}}\%$	/	24%	-5%	37%

Table 36: Interlaminar fracture toughness decay after healing cycle.

Excluding the Beam Theory Approach, Compliance Calibration methods has found similar values with respect to the pristine specimen test, with an error < 10%, while MBT and MCC results for every critical point are relatively close to each other. Finally, Modified Beam Theory approach seems again to be the most reliable method, with a moderate reduction of  $G_{IC}$ , as suggested by Standard Test Method for Mode I Interlaminar Fracture Toughness of Unidirectional FRPMCs (D5528-01). [52]

A resume of the main results for what concerns P1 specimen, which underwent a complete mechanical assessment before and after the repair cycle is shown in Table 37.

<b>MBT</b>	<b>Pristine P1</b>	<b>Repaired P1</b>	<b>Relative error</b>
$G_I$ [J/m <sup>2</sup> ]	871.19	291.11	67%
$G_{IC}^{NL}$ [J/m <sup>2</sup> ]	817.19	645.37	21%
$G_{IC}^{+5\%C_0}$ [J/m <sup>2</sup> ]	909.11	671.04	26%
$G_{IC}^{P_{MAX}}$ [J/m <sup>2</sup> ]	930.34	708.95	24%

Table 37: Final G assessment for P1 specimen (MBT).

## 5 CONCLUSIONS

### 5.1 MANUFACTURING PROCESS

Regarding the entire manufacturing process which led to the design and the production of the composite panels, all the technological problems encountered during the experimental part of the thesis work have been successfully solved. In detail:

- The excessive resin leakage upon the production of the first composite panel has been widely reduced from 30% to 11% thanks to the modification on the aluminium mould size and the implementation of plasticine strips to contain the material loss. A clear image of the panel-containing mould just removed from the hot press is shown for demonstration;

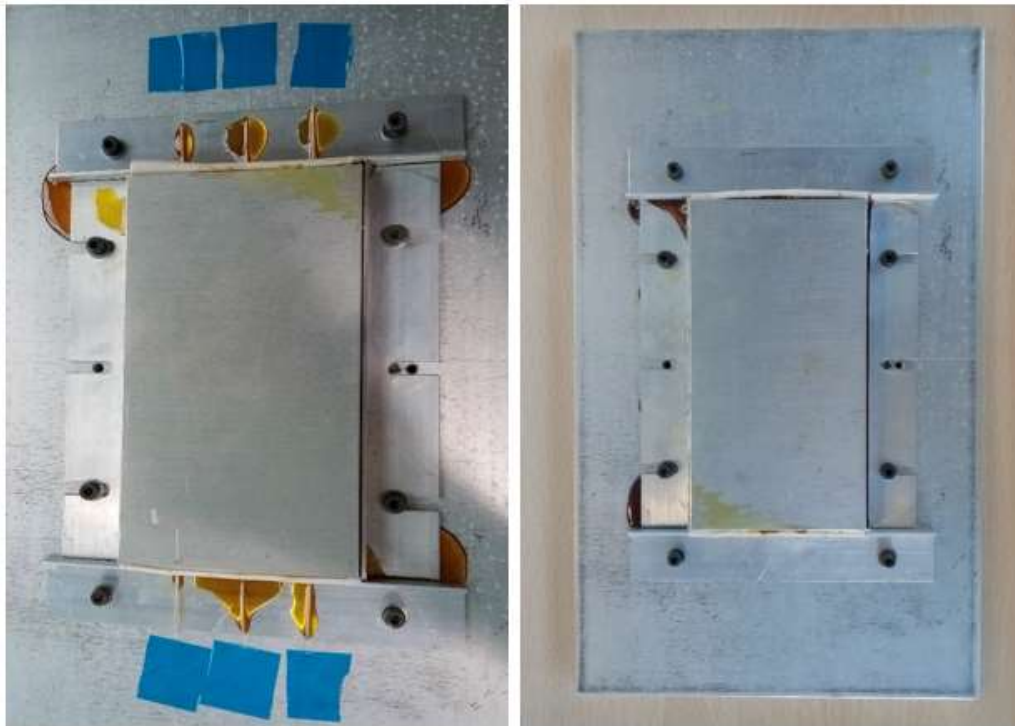


*Figure 72: First panel (on the left) and second panel (on the right) inside the aluminium mould.*

- The scarce interfacial adhesion between epoxy resin and Ergal aluminium stiffening plates has been improved with the employment of an autoclave cycle and the inclusion of peel-ply sheets inside the laminate in order to rise the surface roughness;
- An accurate step-by-step method has been refined to assure a strong bonding between the hinges and the specimens for DCB tests, thus showing that sandblasting bore higher load levels and for this reason it has been denoted as the most efficient technique.

## **5.2 SEM AND DENSITY TESTS: VOIDS AND DEFECTS ASSESSMENT**

The Scanning Electron Microscopy analysis has proved to be a valid tool to visually investigate the real quality of the produced composite material. As can be seen from the various presented micrographs, even though there are two main regions where defects are more concentrated, the voids occur mostly at the ply interface. As commonly known from theoretical studies, the differences in the morphology of the voids are determined by the process parameters and physical properties of the resin. For example, the resin viscosity affects the resin flow, the formation, growth and transport of voids. This brief premise is here used to suggest that the defects detected were almost all a consequence of the unavoidable problems and limits related to the manufacturing hand lay-up process, especially the scarce control on the amount of resin and the geometry and positioning of the dry fabrics sheets inside the panel. In light of the above, the first appeared compact and homogeneous, with no damages worthy of note. Moreover, the fact that the integrity of the optical fibres has been preserved with such a scarce-controlling manufacturing process is surely promising for future implementation of sensors.

For what concerns the density assessment, it was already declared that, as this technique is non-visual, the total void volume fraction of the sample is the only quantitative data obtained. For this reason, it requires accurate knowledge of the densities and mass fractions of the material constituents, this being an inherent disadvantage of the method and limiting its application. Even though the obtained results clearly suffered from the different factors at play, they are overall coherent with the values presented with the rule of mixtures. Then, it is worth mentioning that in the manufacturing of polymer composites, among all defects, voids are arguably the greatest issue because they are difficult to avoid, particularly at the corners of composite components, and are detrimental to the mechanical properties. Voids are formed because of a number of reasons, including the formation of bubbles from volatile by-products produced during the cure reaction of the polymeric matrix, the use of a high-viscosity resin combined with closely packed fibres that are not completely wetted by resin, or the entrapment of air in the material system. In conclusion, by considering the position of the panel from where the specimens were extracted, the tests averagely confirmed the macroscopic and microscopic homogeneity of the composite material despite the inaccuracy of the manufacturing process.

More complete and precise techniques for an in-depth characterization of voids dimension, shape and density are available in the literature [50], which best consider all the possible variables, including the curing and post-curing cycles. Considering the required preparation and testing processes, the characterisation information available, cost and the overall reliability, it is concluded that micro-CT analysis, matrix burn-off and digestion are the most accurate and reliable techniques for characterising voids in composite materials.



### 5.3 DOUBLE CANTILEVER BEAM (DCB) MECHANICAL ANALYSIS

The main purpose of the mechanical assessment conducted with DCB tests was to process the MTS machine data to obtain the interlaminar fracture toughness by means of the methods proposed by ASTM D 5228-01 Standard [52]. The comparison between the values obtained from pristine and repaired specimens would serve as a model for the understanding of the epoxy resin healing ability in terms of efficiency per number of repair cycles. Here follows a list of the main results and considerations:

- The inadequacy of the Beam Theory (BT) approach suggested by ASTM Standard has been confirmed as the  $G_I$  related values were overestimated with respect to the other methods;
- Modified Beam Theory (MBT) can be assumed as the most reliable method as it numerically lies in between Compliance Calibration (CC) and Modified Compliance Calibration (MCC) both for the pristine and the repaired specimen;
- After a partial repair, the P1 specimen showed an average reduction of  $\sim 65/70\%$  in its interlaminar fracture toughness ( $G_I$ ) and of  $\sim 30/40\%$  in its critical related quantity ( $G_{IC}$ ), which are both representative of the scarce success of the hot press healing cycle.

All the disadvantages related to the manual production process must be taken into consideration as the DCB Mode I opening test dramatically suffer from possible composite inhomogeneities, fibres misalignment and the presence of inclusions or air bubbles, thus allowing the crack to propagate out of the panel mid-plane where the PTFE crack initiator sheet is inserted.

For what concerns the numerical results, these must be surely taken in a qualitative way as the specimens are not representative of the standard dimensions given by ASTM D 5228-01. Despite the inherent technological uncertainties, the current thesis work may be a promising starting point for future studies focused on a more complete mechanical assessment of the DGEBA/4-AFD/E-Glass fibres dynamic system, with possible extension to End-Notched-Flexure (ENF) beam tests.

#### **5.4 SELF-HEALING ABILITY OF THE DYNAMIC EPOXY SYSTEM**

It is known from literature that cross-linked polymer networks possess enhanced mechanical properties as well as thermal and chemical resistance with respect to their not cross-linked counterpart. Despite this, the high cross-links density and consequent stiffness increase the susceptibility to mechanical damage. Stimuli-responsive systems are achieved by incorporating some dynamic covalent functionalities into the matrix backbone or in sidechains, so as to improve service life, energy efficiency and impact resistance, as explained in Par. 2.2.3.

The dynamic epoxy system studied in this thesis work had been already characterized, thus showing both vitrimer-like and mechanochromic behaviour. An additional comparative study on the repair efficiency linked to repair cycles and mechanical interlaminar properties has been conducted. An initial qualitative visual inspection had confirmed the success of the resin healing ability, but further mechanical tests have conversely demonstrated that several technological external factors related to the mending cycle could badly affect its efficiency, including the pressure applied and the homogeneity of the temperature reached. First, a better control on the entire manufacturing process is needed to ensure good compaction and enhanced quality. Then, a DCB test on the specimen belonging to the central area of the composite panel can be implemented to understand if the repair ability can depend on material homogeneity and size of delaminated area, in addition to damage entity. Moreover, as the number of possible autonomic repairs is undefined, further DCB openings can be performed to assess an acceptability level for the self-healing behaviour. Even though the DCB comparative study was averagely consistent with the quality of the repair, surely a further improved assessment can be done by means of in-depth Scanning Electron Microscope analyses not only for what concerns voids volume fraction, size and dimensions, but also to study the role of reinforcement fibres.

## **5.5 MECHANOCROMISM**

As explained in the work of *Luzuriaga et al.* [37], since the most widespread methods to detect internal stresses in elastomeric materials are usually invasive or destructive and cannot be used for real-time in situ applications, mechanochromic materials, which can vary their colour upon external stimuli, can be monitored in a non-destructive way, allowing for a better internal damage assessment. 4-AFD has constituted a first example of hardener endowing a dual smart functionality, as explained in Par. 2.2.4. In the context of this work, mechanochromism was visually investigated while performing the DCB tests, focusing on the possible formation of green areas at the crack tip. However, the experimental set up did not allow to find evidence of this behaviour in response of Mode I opening DCB tests. So, this phenomenon was only detectable with accidental scratches during the manufacturing processing, thus being unable to establish similarities and differences between responses of the glass-fibre reinforced epoxy network and the same epoxy system by itself.

## **5.6 FBG SENSORS INCORPORATION FOR DAMAGE MONITORING**

As depicted in Par. 4.2.2.2 the crack has propagated out of the mid-plane where PTFE sheet acts as initiator, thus following a non-linear and non-planar growth path. Local investigations for a more sophisticated in-depth crack analysis can be carried out by incorporating optical fibres equipped with FBG sensors, introduced in Par. 2.6.2. In this perspective, a reliable and complete structural health monitoring system can effectively support the production of further composite panels and their ongoing mechanical assessment. As stated in the literature and explained in Section I, delamination is beyond doubt the main cause of life reduction in fibre-reinforced polymer structures. A suitable study of the delamination phenomenon must take into account all the related parameters, including the toughening mechanisms, such as fibre bridging. Embedded FBG sensors are deeply affected by these phenomena and when interacting with cracks, they give a global and accurate response to the delamination behaviour.

Despite the high cost of the materials, especially the curing agent which is responsible of its functional properties, the dynamic epoxy system object of this study turned out to be very promising in the context of fibre-reinforced-polymer composites, which are expected to grow exponentially in sectors such as automotive, aerospace and biomedicine. Moreover, the renewable energy industry takes great advantages from this kind of smart materials, with great interest toward recyclability and reprocessability. For this reason, further research should be conducted to gain a broader and focused insight into the benefits of dynamic covalent chemistry, allowing these smart materials to become cheaper and therefore their clearly innovative properties can be widely exploited to create more sustainable engineering products.

# 6 APPENDIX

## 6.1 E-glass fabric data sheet



**HexForce® 01102 1000 TF970**  
E GLASS FABRIC

*Product Data*

### Textile Reinforcement for High Performance Composite

HexForce® reinforcements are available in a range of weave styles – from woven fabrics to multiaxials and specialties that offers a range of globally certified aerospace / industrial products in carbon, glass and aramid and specialty fibers that we sell under the HexForce® trademark.

DESCRIPTION		April / 2015	
Type of yarns	Warp : [EC9 68] X 3 Weft : [EC9 68] X 3		
Nominal weight	290 g/m <sup>2</sup>	8.55 oz/sqy <sup>2</sup>	
Weave style	TWILL 2/2		
Width	1000 mm	39.4 in	
Finish type	TF970		
Finish description			

CHARACTERISTICS			
Nominal construction	Warp : 7 yarn/cm Weft : 7 picks/cm	17.9 yarn/in 17.9 picks/in	
Weight distribution	Warp : 50 % Weft : 50 %		
Thickness (*)	0.23 mm	0.009 in	

\*NB : The above average values are obtained with epoxy laminate at 55% of fibres in volume.

#### IMPORTANT

All information is believed to be accurate but is given without acceptance of liability. Users should make their own assessment of the suitability of any product for the purpose required. All sales are made subject to our standard terms of sales which include limitations on liability and other important terms.

© Copyright Hexcel



For European sales office telephone numbers and a full address list, please go to : <http://www.hexcel.com/contact/salesoffices>

## 6.2 CLT analysis for composite stiffness

The Classical Lamination Theory (CLT) analysis was carried out for the composite panel by means of Autodesk Heliuss Composite software. The main characteristics of the basic used materials (introduced in Par. 3.5) are partly present in the software library. The fabric was created from E-glass fibre and dynamic epoxy resin data with a specific software function, with the following features.

	<b>E-Glass Fibre</b>	<b>Dynamic Epoxy Resin</b>	<b>Ergal Aluminium</b>
$E_{XX} = E_{YY}$ [MPa]	$7.24 \cdot 10^4$	$3.83 \cdot 10^3$	$7.00 \cdot 10^4$
$G_{XY}$ [MPa]	$3.03 \cdot 10^4$	$1.45 \cdot 10^3$	$2.69 \cdot 10^4$
$\nu_{XY}$	0.2	0.32	0.3
$\rho$ [g/cm <sup>3</sup> ]	2.60	1.20	2.88
$V_{\%}$	0.55	0.45	/

Table 38: Initial data needed for CLT.

	<b>Fabric</b>
$E_{XX} = E_{YY}$ [MPa]	$2.64 \cdot 10^4$
$G_{XY}$ [MPa]	$4.35 \cdot 10^3$
$\nu_{XY}$	0.14
$\rho$ [g/cm <sup>3</sup> ]	1.97

Table 39: Fabric obtained with Autodesk Heliuss Composite.

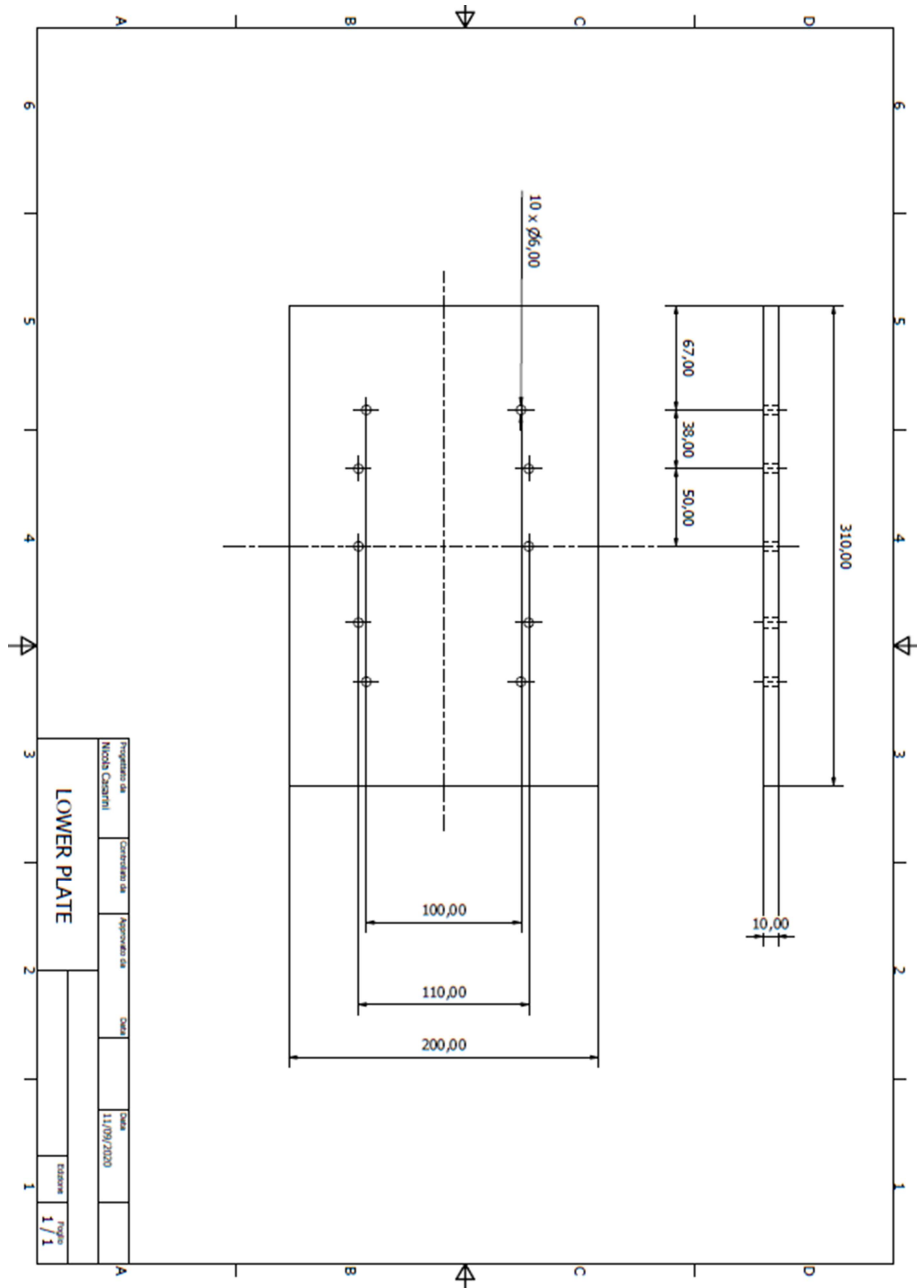
At this point, CLT analysis was applied considering  $n = 6$  used fabrics for the laminate itself and  $n = 8$  for the stiffened panel for both cases of Ergal 3 mm thick and 5 mm thick (the matrices obtained are omitted for simplicity). The three case are showed in Table 40.

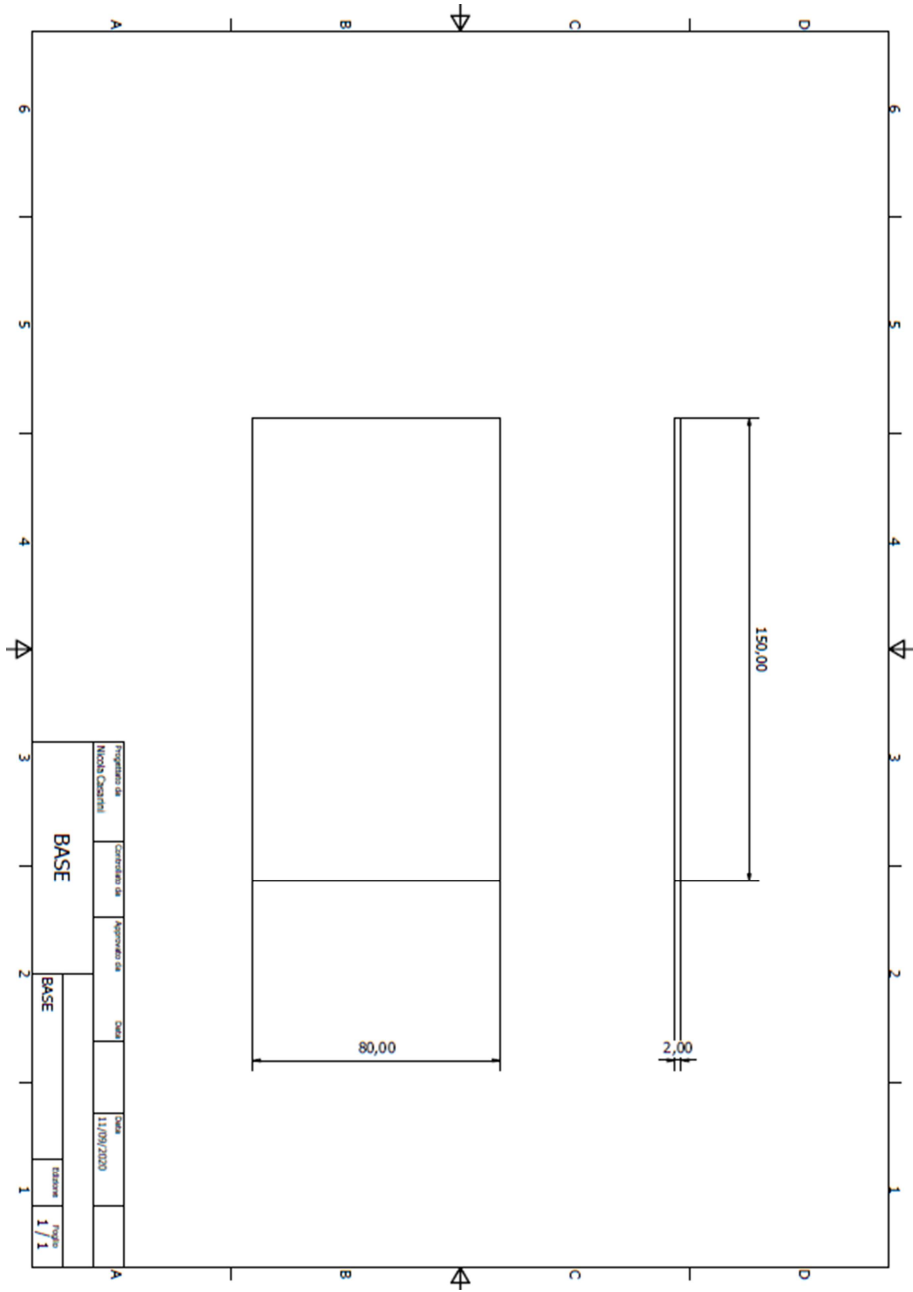
	<b>Laminate</b>	<b>3 mm Ergal</b>	<b>5 mm Ergal</b>
$E_{XX} = E_{YY}$ [MPa]	$2.64 \cdot 10^4$	$6.20 \cdot 10^4$	$6.48 \cdot 10^4$
$G_{XY}$ [MPa]	$4.35 \cdot 10^3$	$2.27 \cdot 10^4$	$2.42 \cdot 10^4$
$\nu_{XY}$	0.14	0.29	0.29
$\rho$ [g/mm <sup>3</sup> ]	1.97	2.71	2.77

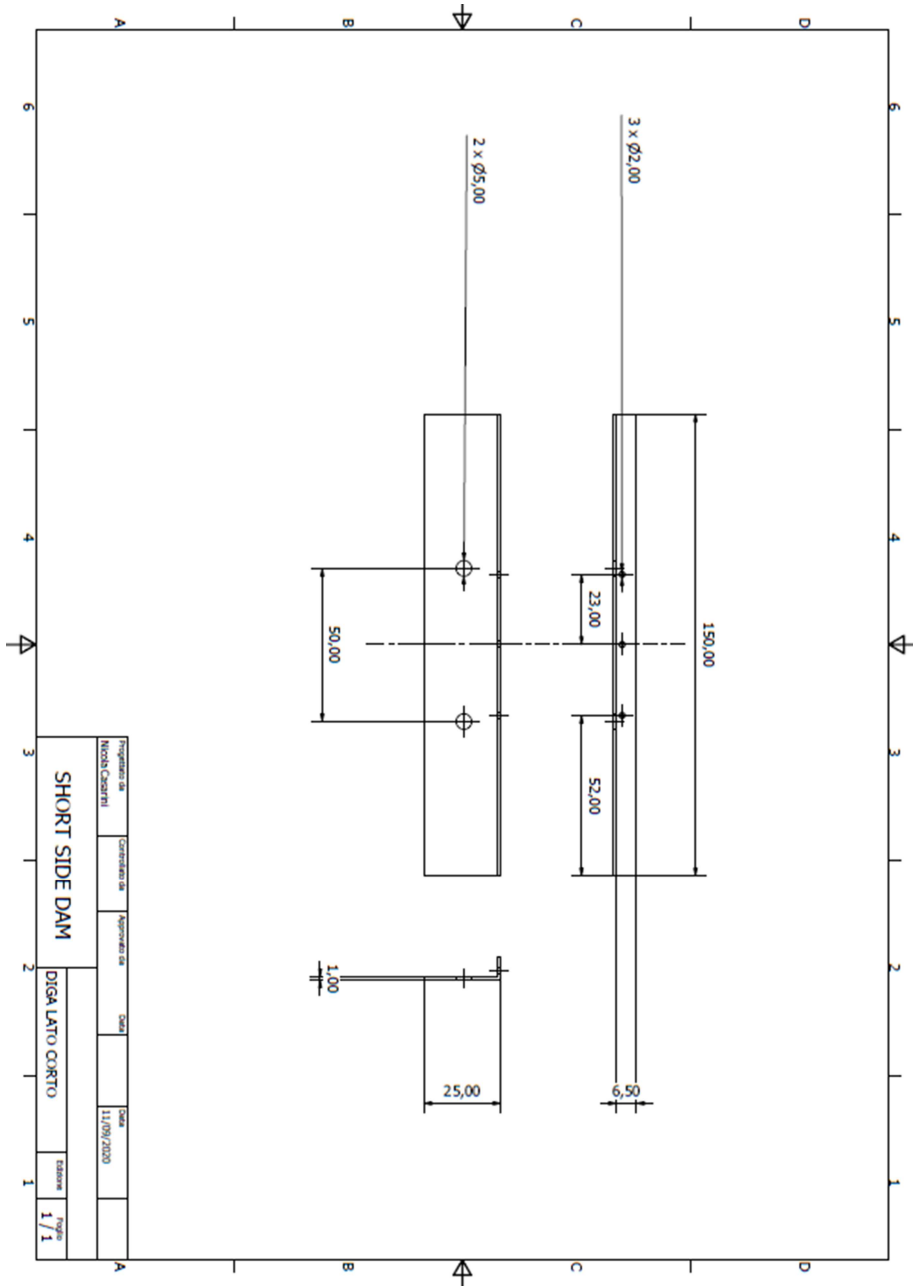
Table 40: Stiffness results obtained with CLT analysis.

The final results necessarily show the symmetry and homogeneity of the produced panels, moreover the increase in stiffness is demonstrated with the implementation of Ergal plates, and slightly enhanced in the case of thicker plates, allowing for the conduction of DCB mechanical tests.

### 6.3 Aluminium mould CAD representation

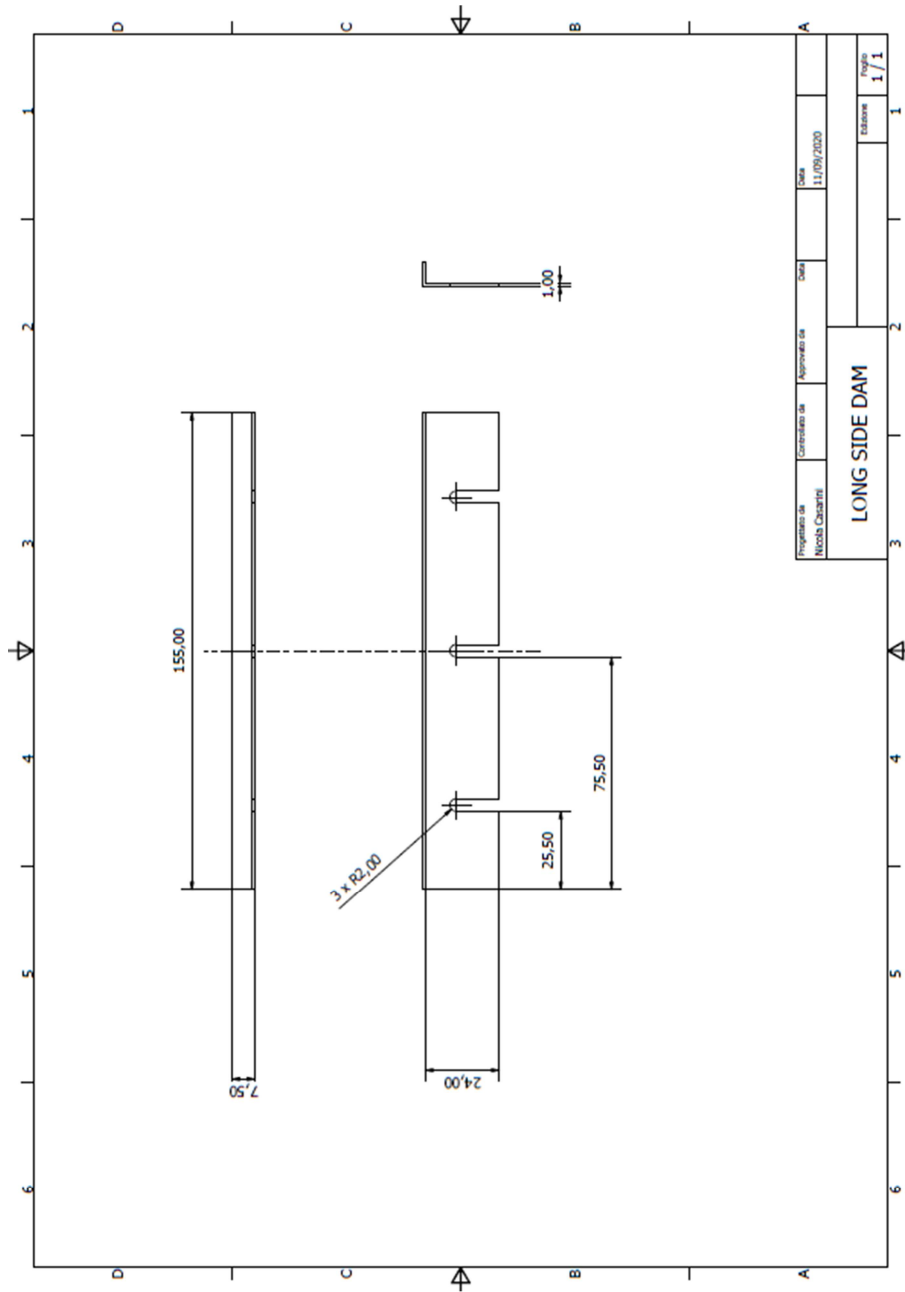




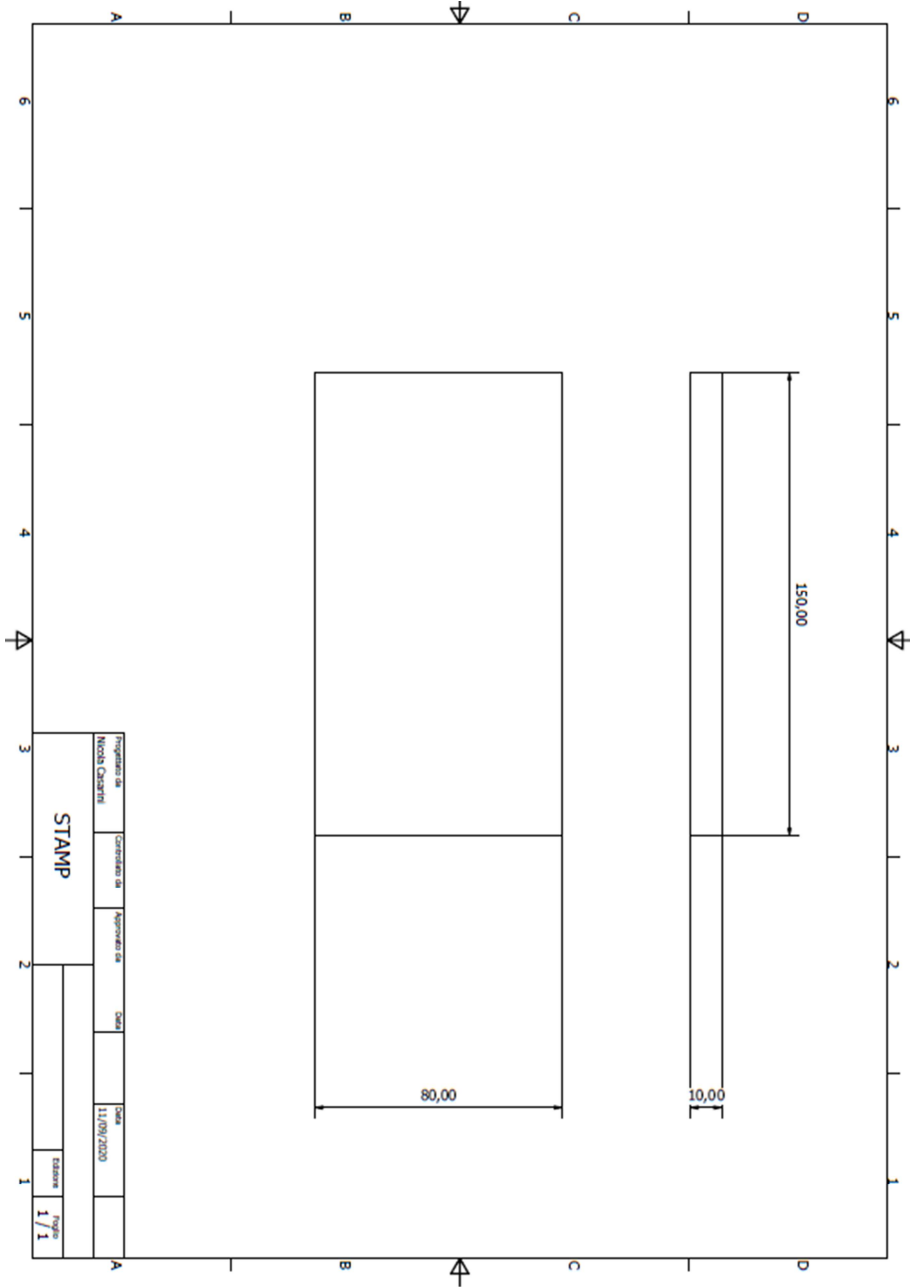


Projectato da		Consultado da		Aprovado da		Data		Data		Edição		Folha	
Nelson Cesarini						11/09/2020				1 / 1		1 / 1	
<b>SHORT SIDE DAM</b>										<b>DIGA LATO CORTO</b>			





Progettato da Nicola Casarini	Completato da	Approvato da	Data 11/09/2020
<b>LONG SIDE DAM</b>			Progetto 1/1



# BIBLIOGRAPHY

- [1] I. P., Trask, R. S., & Williams, H. R. (2008). Self-healing fibre-reinforced polymer composites. *MRS bulletin*, 33(8), 770-774.
- [2] Sih, G. C., & François, D. (Eds.). (2014). *Progress in Fracture Mechanics: Fracture Mechanics Research and Technological Activities of Nations Around the World*. Elsevier.
- [3] Greenhalgh, E. (2009). *Failure analysis and fractography of polymer composites*. Elsevier.
- [4] Ghosh, S. K. (Ed.). (2009). *Self-healing materials: fundamentals, design strategies, and applications* (pp. 138-217). Weinheim: Wiley-vch.
- [5] Arienti, M. A. (2010). *Modellazione del danno in pale di elicottero per lo sviluppo di sistemi di monitoraggio strutturale*, Politecnico di Milano.
- [6] PAOLILLO, S. (2018). *Characterization of a dynamic epoxy network: curing and functional properties*, Politecnico di Milano.
- [7] Soutis, C. (2005). Fibre reinforced composites in aircraft construction. *Progress in aerospace sciences*, 41(2), 143-151.
- [8] Ellis, B. (1993). *Chemistry and Technology of Epoxy Resin*, Blackie Acad. Prof., Glasgow, 1993.
- [9] Dutton, S., Kelly, D., & Baker, A. (2004). *Composite materials for aircraft structures*. American Institute of Aeronautics and Astronautics.
- [10] Saba, N., Jawaid, M., Alothman, O. Y., Paridah, M. T., & Hassan, A. (2016). Recent advances in epoxy resin, natural fibre-reinforced epoxy composites and their applications. *Journal of Reinforced Plastics and Composites*, 35(6), 447-470.
- [11] Jin, F. L., Li, X., & Park, S. J. (2015). Synthesis and application of epoxy resins: A review. *Journal of Industrial and Engineering Chemistry*, 29, 1-11.
- [12] Liu, T., Hao, C., Zhang, S., Yang, X., Wang, L., Han, J., ... & Zhang, J. (2018). A self-healable high glass transition temperature bioepoxy material based on vitrimer chemistry. *Macromolecules*, 51(15), 5577-5585.
- [13] Chrzanowski, W., & Khademhosseini, A. (2013). Biologically inspired 'smart' materials. *Advanced drug delivery reviews*, 65(4), 403.
- [14] Kamila, S. (2013). Introduction, classification and applications of smart materials: an overview. *American Journal of Applied Sciences*, 10(8), 876.
- [15] White, S. R., Sottos, N. R., Geubelle, P. H., Moore, J. S., Kessler, M. R., Sriram, S. R., ... & Viswanathan, S. (2001). Autonomic healing of polymer composites. *Nature*, 409(6822), 794-797.
- [16] Banshiwal, J. K., & Tripathi, D. N. (2019). Self-Healing Polymer Composites for Structural Application. In *Functional Materials*. IntechOpen.
- [17] SIMÓN GARCÍA, C. (2019). *Characterization of a self-healing composite: mechanical and functional properties*, Politecnico di Milano.
- [18] Blaiszik, B. J., Sottos, N. R., & White, S. R. (2008). Nanocapsules for self-healing materials. *Composites Science and Technology*, 68(3-4), 978-986.
- [19] Pang, J. W., & Bond, I. P. (2005). A hollow fibre reinforced polymer composite encompassing self-healing and enhanced damage visibility. *Composites Science and Technology*, 65(11-12), 1791-1799.
- [20] Hamilton, A. R., Sottos, N. R., & White, S. R. (2010). Self-healing of internal damage in synthetic vascular materials. *Advanced Materials*, 22(45), 5159-5163.

- [21] Kessler, M. R., & White, S. R. (2001). Self-activated healing of delamination damage in woven composites. *Composites Part A: applied science and manufacturing*, 32(5), 683-699.
- [22] Hayes, S. A., et al. "A self-healing thermosetting composite material." *Composites Part A: Applied Science and Manufacturing* 38.4 (2007): 1116-1120.
- [23] Das, R., Melchior, C., & Karumbaiah, K. M. (2016). Self-healing composites for aerospace applications. In *Advanced composite materials for aerospace engineering* (pp. 333-364). Woodhead Publishing.
- [24] Van der Zwaag, S., Grande, A. M., Post, W., Garcia, S. J., & Bor, T. C. (2014). Review of current strategies to induce self-healing behaviour in fibre reinforced polymer-based composites. *Materials science and technology*, 30(13), 1633-1641.
- [25] Zhang, M., & Rong, M. (2012). Design and synthesis of self-healing polymers. *Science China Chemistry*, 55(5), 648-676.
- [26] Sordo, F., Mougner, S. J., Loureiro, N., Tournilhac, F., & Michaud, V. (2015). Design of self-healing supramolecular rubbers with a tunable number of chemical cross-links. *Macromolecules*, 48(13), 4394-4402.
- [27] Herbst, F., Döhler, D., Michael, P., & Binder, W. H. (2013). Self-healing polymers via supramolecular forces. *Macromolecular rapid communications*, 34(3), 203-220.
- [28] Hayes, S. A., Zhang, W., Branthwaite, M., & Jones, F. R. (2007). Self-healing of damage in fibre-reinforced polymer-matrix composites. *Journal of the Royal Society Interface*, 4(13), 381-387.
- [29] Meure, S., Wu, D. Y., & Furman, S. (2009). Polyethylene-co-methacrylic acid healing agents for mendable epoxy resins. *Acta Materialia*, 57(14), 4312-4320.
- [30] Varley, R. J., & van der Zwaag, S. (2008). Towards an understanding of thermally activated self-healing of an ionomer system during ballistic penetration. *Acta Materialia*, 56(19), 5737-5750.
- [31] Garcia, S. J., & Fischer, H. R. (2014). Self-healing polymer systems: properties, synthesis and applications. In *Smart Polymers and their Applications* (pp. 271-298). Woodhead Publishing.
- [32] Post, W., Cohades, A., Michaud, V., Van Der Zwaag, S., & Garcia, S. J. (2017). Healing of a glass fibre reinforced composite with a disulphide containing organic-inorganic epoxy matrix. *Composites Science and Technology*, 152, 85-93.
- [33] Park, J. S., Kim, H. S., & Hahn, H. T. (2009). Healing behaviour of a matrix crack on a carbon fibre/mendomer composite. *Composites science and technology*, 69(7-8), 1082-1087.
- [34] García, S. J., Fischer, H. R., & Van Der Zwaag, S. (2011). A critical appraisal of the potential of self-healing polymeric coatings. *Progress in Organic Coatings*, 72(3), 211-221.
- [35] Cohades, A., Branfoot, C., Rae, S., Bond, I., & Michaud, V. (2018). Progress in self-healing fiber-reinforced polymer composites. *Advanced Materials Interfaces*, 5(17), 1800177.
- [36] de Luzuriaga, A. R., Matxain, J. M., Ruipérez, F., Martin, R., Asua, J. M., Cabañero, G., & Odriozola, I. (2016). Transient mechanochromism in epoxy vitrimer composites containing aromatic disulphide crosslinks. *Journal of Materials Chemistry C*, 4(26), 6220-6223.
- [37] G. Sala, L. Di Landro, A. Airoidi, and P. Bettini, 'Tecnologie e Materiali Aerospaziali - 37. Tecnologie di formatura in pressa, in forno ed in autoclave con sacco da vuoto'.

- [38] de Luzuriaga, A. R., Martin, R., Markaide, N., Rekondo, A., Cabañero, G., Rodríguez, J., & Odriozola, I. (2016). Epoxy resin with exchangeable disulphide crosslinks to obtain reprocessable, repairable and recyclable fibre-reinforced thermoset composites. *Materials Horizons*, 3(3), 241-247.
- [39] Sastry, A. M. (2002). Impregnation and consolidation phenomena. *ChemInform*, 33(39), 280-280.
- [40] Laffan, M. J. (2012). Testing the toughness of polymer matrix composites. In *Failure Mechanisms in Polymer Matrix Composites* (pp. 110-128). Woodhead Publishing.
- [41] G. Sala, L. Di Landro, A. Airoidi, and P. Bettini, 'Tecnologie e Materiali Aerospaziali - 42. Attrezzi di formatura e materiali di consumo per le tecnologie dei compositi'.
- [42] Chanda, M. (2017). *Plastics technology handbook*. CRC press.
- [43] Dixit, D., Pal, R., Kapoor, G., & Stabenau, M. (2016). Lightweight composite materials processing. In *Lightweight ballistic composites* (pp. 157-216). Woodhead Publishing.
- [44] Sridharan, S. (Ed.). (2008). *Delamination behaviour of composites*. Elsevier.
- [45] Farrar, C. R., & Worden, K. (2007). An introduction to structural health monitoring. *Philosophical Transactions of the Royal Society A: Mathematical, Physical and Engineering Sciences*, 365(1851), 303-315.
- [46] Epaarachchi, J. A., & Kahandawa, G. C. (Eds.). (2016). *Structural health monitoring technologies and next-generation smart composite structures*. CRC Press.
- [47] Zhou, G., & Sim, L. M. (2002). Damage detection and assessment in fibre-reinforced composite structures with embedded fibre optic sensors-review. *Smart Materials and Structures*, 11(6), 925.
- [48] Menczel, J. D., & Prime, R. B. (Eds.). (2009). *Thermal analysis of polymers: fundamentals and applications*. John Wiley & Sons.
- [49] Sawyer, L., Grubb, D. T., & Meyers, G. F. (2008). *Polymer microscopy*. Springer Science & Business Media.
- [50] Little, J. E., Yuan, X., & Jones, M. I. (2012). Characterisation of voids in fibre reinforced composite materials. *NDT & E International*, 46, 122-127.
- [51] Patranabis, D. (2011). *Instrumentation and Control*. PHI Learning Pvt. Ltd..
- [52] 'ASTM D5528-01: Standard Test Method for Mode I Interlaminar Fracture Toughness of Unidirectional Fibre-reinforced Polymer Matrix Composites'. ASTM, Philadelphia Pennsylvania, 2009.
- [53] Vignelli, C. (2007). Caratterizzazione delle Proprietà Interlaminari di Laminati Ibridi Metallo-Composito, Politecnico di Milano.
- [54] Domenichini, P. (2008). Invasività di Attuatori Piezoceramici inglobati in laminati in composito: influenza sulla tenacità interlaminare, Politecnico di Milano.